NASA Technical Memorandum 110418

Turbulence Measurements in the Near Field of a Wingtip Vortex

Jim Chow, Greg Zilliac, and Peter Bradshaw

February 1997

National Aeronautics and
Space Administration

NASA Technical Memorandum 110418

Turbulence Measurements in the Near Field of a Wingtip Vortex

Jim Chow, Institute of Defense Analyses, Alexandria, Virginia
Greg Zilliac, Ames Research Center, Moffett Field, California
Peter Bradshaw, Stanford University, Stanford, California

February 1997

National Aeronautics and
Space Administration

Ames Research Center
Moffett Field, California 94035-1000

ACKNOWLEDGMENTS

The research work upon which the present study is based was supported by and performed in the Fluid Mechanics Laboratory, which is part of the Fluid Dynamics Research Branch of the NASA-Ames Research Center (Grant NCC-2-55). I am indebted to Greg Zilliac of the Fluid Mechanics Laboratory at NASA/Ames Research Center for his illuminating discussions and his continued help. Thanks also to the Chief of the Fluid Dynamics Research Branch (RFR), Dr. Sanford S. Davis, for his interest and support. Finally, I would like to thank my advisor Peter Bradshaw for his invaluable contributions and support throughout the project.

I benefited from stimulating discussions with my colleagues at NASA-Ames Research Center, especially Dr. Rabindra Mehta, Dr. James Bell, Dr. James Weygandt and Dr. Jennifer Dacles-Mariani. Finally, conversations with Dr. Otto Zeman at the Center for Turbulence Research were extremely helpful in gaining an understanding of the turbulence structure of the tip-vortex flow field.

ABSTRACT

The roll-up of a wingtip vortex, at Reynolds number based on chord of 4.6 million, was studied with an emphasis on suction side and near wake measurements. The research was conducted in a 32 in. x 48 in. low-speed wind tunnel. The half-wing model had a semi-span of 36 in., a chord of 48 in. and a rounded tip.

Seven-hole pressure probe measurements of the velocity field surrounding the wingtip showed that a large axial velocity, of up to 1.77 U_∞, developed in the vortex core. This level of axial velocity has not been previously measured. Triple-wire probes have been used to measure all components of the Reynolds stress tensor. It was determined from correlation measurements that meandering of the vortex was small and did not appreciably contribute to the turbulence measurements.

The flow was found to be turbulent in the near-field (as high as 24 per cent RMS $w-$velocity on the edge of the core) and the turbulence decayed quickly with streamwise distance because of the nearly solid body rotation of the vortex core mean flow. A streamwise variation of the location of peak levels of turbulence, relative to the core centerline, was also found. Close to the trailing edge of the wing, the peak shear stress levels were found at the edge of the vortex core, whereas in the most downstream wake planes they occurred at a radius roughly equal to one-third of the vortex core radius. The Reynolds shear stresses were not aligned with the mean strain rate, indicating that an isotropic-eddy-viscosity based prediction method cannot accurately model the turbulence in the vortex. In cylindrical coordinates, with the origin at the vortex centerline, the radial normal stress was found to be larger than the circumferential.

TABLE OF CONTENTS

Chapter *Page*

LIST OF TABLES

LIST OF FIGURES

Roman Symbols

$A_{m,i}$:	m constant angle calibration coefficients of wire i
$A'_{m,i}$:	m constant angle calibration coefficients of wire i, including temperature dependent effects
$\tilde{A}'_{m,i}$:	m constant angle calibration coefficients of wire i, including temperature dependent effects and skewness factor
AR:	Aspect ratio = $2b^2$/(half-wing surface area)
b:	wing semi-span
b_o:	wing semi-span of constant chord section of wing
B:	Coefficient in King's law equation
c:	chord
C_f:	Skin friction coefficient, $C_f \equiv \tau_w/(\frac{1}{2}\rho U^2)$
d:	Hot-wire diameter
E_i:	Hot wire signal voltage for wire i
E'_i:	Hot wire signal voltage for wire i, modified for temperature dependent effects
E_0:	Hot wire signal voltage at zero velocity
E_{corr}:	Temperature-corrected hot wire signal
k:	Turbulent kinetic energy
k_t:	Thermal conductivity
k_i:	Calibration yaw factor for wire i
K:	Coefficient in inverse King's law equation, $K \equiv 1/B^{1/n}$
l:	Hot-wire active length
OHR:	Overheat ratio = (hot-wire abs. temp.)/(tunnel abs. temp.)
m:	Exponent for constant-angle calibration polynomial
n:	Velocity exponent for constant-angle polynomial fit or for King's law equation
$Nu_{(L)}$:	Nusselt number based on the bracketed reference length, $Nu_{\mathrm{L}} \equiv UL/\nu$
P:	Mean static pressure
p:	Instantaneous static pressure
p':	Fluctuating static pressure
P_T:	Total pressure
P_∞:	Freestream pressure
$\overline{q^2}$:	Twice the turbulent kinetic energy

r, θ, x:	Cylindrical coordinates for radial, tangential and streamwise directions, respectively, with origin at the vortex centerline
R:	Wire resistance
R_0:	Cold wire resistance
$Re_{(L)}$:	Reynolds number based on the bracketed reference length, $Re_{\mathrm{L}} \equiv UL/\nu$
t:	Time
T:	Current tunnel temperature
T_0:	Cold wire temperature
T_{cal}:	Tunnel temperature at calibration
U, V, W:	Mean velocity in the x, y, z directions respectively
$\hat{u}, \hat{v}, \hat{w}$:	RMS velocity components in the x, y, z directions respectively
u', v', w':	Fluctuating velocity components in the x, y, z directions respectively
u, v, w:	Instantaneous velocity in the x, y, z directions respectively, e.g. $u = U + u'$
U_j:	u, v, w, for j = 1, 2, 3 respectively
U_{mag}:	Velocity magnitude = $\sqrt{U^2 + V^2 + W^2}$
$U_{eff,i}$:	Effective velocity measured by hot-wire for wire i
$U'_{eff,i}$:	Effective velocity measured by hot-wire for wire i, including temperature dependent effects
$\tilde{U}'_{eff,i}$:	Effective velocity measured by hot-wire for wire i, including temperature dependent effects and skewness factor
u_τ:	Friction velocity, $u_\tau \equiv \sqrt{\tau_w/\rho}$
U_{cf}:	Crossflow velocity = $\sqrt{V^2 + W^2}$
U_∞:	Freestream velocity
V_r, V_θ, V_x:	Mean velocity in the r, θ, x directions respectively
$\hat{v}_r, \hat{v}_\theta, \hat{v}_x$:	RMS velocity components in the r, θ, x directions respectively
v'_r, v'_θ, v'_x:	Fluctuating velocity components in the r, θ, x directions respectively
v_r, v_θ, v_x:	Instantaneous velocity in the r, θ, x directions respectively, e.g. $v_r = V_r + v'_r$
x, y, z:	Tunnel fixed cartesian coordinates for streamwise, normal, and spanwise directions, respectively, with origin at root of trailing edge of wing

Greek Symbols

α:	Angle of attack or temperature coefficient of resistivity
β:	Yaw angle
$\beta_{i,j}$:	Wire direction cosines for wire i
γ:	Tip circumferential angle, zero at top of tip
γ_i:	Angle between wire i and freestream velocity vector
Γ_x:	Circulation of streamwise vortex
ϑ:	Coefficient of diffusivity
ν:	Kinematic viscosity of air
ν_t:	eddy viscosity of air
ρ:	Density of air
τ_w:	Wall shear stress
Ω:	Tangential velocity
Ω_x:	Streamwise component of mean vorticity, $\Omega_x \equiv \frac{\partial W}{\partial y} - \frac{\partial V}{\partial z}$
Ω_z:	Spanwise component of mean vorticity, $\Omega_z \equiv \frac{\partial V}{\partial x} - \frac{\partial U}{\partial y}$
θ:	Pitch angle

Subscripts and Superscripts

$\overline{\ }$:	(overbar) Time-averaged quantity
$(\ )_{calc}$:	Calculated value
$(\ )_{cl}$:	Value on center-line
$(\ )_{max}$:	Maximum value over a given range
$(\ )_{meas}$:	Measured value

1. INTRODUCTION

1.1 BACKGROUND

The wingtip vortex flow is one of great importance because of its effect on practical problems such as landing separation distances for aircraft, blade/vortex interactions on helicopter blades, and propeller cavitation on ships. It also continues to be a perplexing problem for the computational scientist because of the presence of turbulence and because of large gradients of velocity and pressure in all three directions, especially in the near field at high Reynolds number. In the case of a wing with nearly-constant loading, a discrete vortex forms at the tip (Figure 1.1), fed by vorticity from the boundary layer near the tip. As the vortex moves downstream, it rolls up more and more of the wing wake, until its circulation is nominally equal to that of the wing. The rollup distance is small compared to the separation of aircraft on the approach path, but not necessarily small compared to the distance between interacting lifting surfaces, such as the strake or foreplane and the main wing on a close-coupled fighter or consecutive blades on a helicopter rotor. The flow in the near-field rollup region is therefore important in its own right as well as in providing a possible means of control of the far-field vortex. Controlling a single vortex however only changes the virtual origin (by a few tens of chord lengths) leaving the only possibility of airplane vortex wake control as stimulation of the Crow instability (Crow, 1970).

To be able to meet some of these practical considerations, designers need not only a better understanding of the flow physics in the near-field tip vortex rollup process, but also a better feel for the limitations in current computational abilities and in current turbulence models.

A literature review indicates that the tip vortex has been the subject of hundreds of experimental studies, concentrating almost entirely on the far-field. There seems to have been no study of the tip flow and near-field vortex rollup process detailed enough to be used in developing or testing a prediction method or for putting the design of tip modifications on a firm fundamental basis. The lack of

experimental studies in this area is related to the difficulty in measuring a highly turbulent flow with large gradients in all three directions, near a curved solid body surface.

1.2 PREVIOUS WORK

1.2.1 Analytic Studies

Analyses of a tip vortex have generally been more successful in the far-field than in the near-field. Assumptions that are often made in simplifying the far-field analysis may not hold in the near-field. The main assumption that has been made in all previous analytic studies is that of axisymmetric flow. In the early stages of roll-up, however, this is obviously not a good assumption. Other assumptions that are often made are that the axial velocity perturbation is small with respect to U_∞ ("light loading") and that the apparent eddy viscosity, defined in a given plane as (Reynolds stress)/(mean strain rate), is well-behaved, i.e. the same in all planes ("isotropic"). Again, in the near field, both of these conditions are violated. In the present experiment, the axial velocity excess in the core can reach levels as high as 77% of the freestream velocity while the Reynolds stress contours are not consistent with well-behaved eddy viscosity.

These approximations have had some success in predicting the far-field behavior of the tip vortex. In particular, similarity solutions have given accurate estimates of the decay rate of a tip vortex far downstream of the trailing edge of a wing. These types of analysis are most useful in analyzing the wake vortex encounter problem, and better models, founded on reliable experimental data, are needed for the near field.

1.2.1.1 Analysis of Laminar Vortices

A few authors have analytically investigated the structure of laminar trailing vortices. Although at the Reynolds numbers found in most practical applications

trailing vortices are turbulent, many features of a laminar trailing vortex are still present in a turbulent tip vortex.

The simplest analytic model for a 2-D line vortex assumes solid body rotation of a viscous core surrounded by an irrotational (potential) field:

$$V_\theta = \frac{\Omega a^2}{r}, \; r \geq a \tag{1.2.1}$$

$$V_\theta = \Omega r, \; r < a \tag{1.2.2}$$

where Ω is the angular velocity of the solid body rotation and a is the radius of the viscous core region, also defined here as the point of maximum tangential velocity. This is a simple approximation to the well known solution for the growth of a laminar 2-D line vortex which can be found in Lamb (1932). The velocity distribution is given as follows:

$$V_\theta = \frac{\Gamma_x}{2\pi r}\left[1 - exp\left(-\frac{r^2}{4\nu t}\right)\right] \tag{1.2.3}$$

Batchelor (1964) did an analysis on axial flow in a laminar trailing vortex starting with the steady axisymmetric incompressible momentum equations (see Appendix B, Equations B3-B6). Assuming axial gradients are of smaller magnitude than radial gradients, boundary-layer type approximations can be made:

$$\frac{\partial}{\partial x} << \frac{\partial}{\partial r}, \; V_r << V_x \tag{1.2.4}$$

which reduces equation (B.5) to the familiar Euler's n-equation:

$$\frac{\partial P}{\partial r} = \rho \frac{V_\theta^2}{r} \tag{1.2.5}$$

Bernoulli's equation including total pressure loss, ΔH, is written as:

$$\frac{P}{\rho} + 1/2(V_x^2 + V_\theta^2 + V_r^2) = \frac{P_\infty}{\rho} + 1/2U_\infty^2 - \Delta H \tag{1.2.6}$$

Neglecting radial velocities, the axial velocity can be derived from (1.2.5) and (1.2.6) as:

$$V_x^2 = U_\infty^2 + \int_r^\infty \frac{1}{r^2}\frac{\partial (rV_\theta)^2}{\partial r} dr - 2\Delta H \tag{1.2.7}$$

Using the vortex model of Eqns. 1.2.1 and 1.2.2, the axial velocity is found to be:

$$V_x = U_\infty, \; r > a \tag{1.2.8}$$

$$V_x = \left(U_\infty^2 + 2\Omega^2(a^2 - r^2) - 2\Delta H \right)^{1/2}, \; r \leq a \tag{1.2.9}$$

This equation shows that, as the roll-up of the vortex generates larger and larger tangential velocities, pressure forces produce a strong downstream flow in the core of a trailing vortex, provided only that total head losses are not large. Similarly, as the tangential velocities decay in the far-field part of the flow, pressure forces will act to decelerate the axial flow in the core.

Moore and Saffman (1973) sought to improve upon Batchelor's analysis and studied the influence of viscosity on the axial flow in a laminar trailing vortex. They noted that although Batchelor's primarily inviscid arguments suggested a large axial velocity excess, "wind-tunnel tests and free-flight observations show that there is usually a deficit of axial velocity in the core, although some cases of a velocity increase have been reported". They solved 2-D unsteady versions of Eqns. B.4-B.6 with boundary-layer type approximations using boundary conditions found from previous inviscid analysis with adjustments made for wing boundary layers. Using the light load approximation, their solution for a semi-infinite rectangular wing gives two different axial profiles for the vortex centerline and the outer edge of the viscous core respectively:

$$\frac{V_{x,cl} - U_\infty}{U_\infty} = -2.4 \times 10^{-5} \alpha^2 Re_c^{1/2} \left(\frac{c}{x} \right)^{1/2} + 0.28 \left(\frac{c}{x} \right)^{1/2} \tag{1.2.10}$$

$$\frac{V_x(r) - U_\infty}{U_\infty} = \left[0.93\times10^{-4}\alpha^2 - 0.32Re_c^{-1/2}\right]\left(\frac{c}{r}\right) \qquad (1.2.11)$$

where α is in degrees, and Re_c is the Reynolds number based upon chord. Eqn. 1.2.10 suggests an axial velocity deficit on the vortex centerline which increases with Re_c and with angle of attack. Eqn. 1.2.11 can give an axial velocity excess or deficit at the outer edge of the viscous core. Comparisons with available experimental data are poor although the measurements of Logan (1971) showed a qualitatively similar axial flow, with a velocity deficit at the centerline and an axial velocity excess at the edge of the viscous core. The radius of the core (whose edge was defined as the point of maximum tangential velocity) for an elliptically loaded wing was found to be:

$$\frac{a}{c} = 2.92\left(\frac{x}{c}\right)^{1/2} Re_c^{-1/2} \qquad (1.2.12)$$

Although their analysis is claimed to be valid for the near-field, the assumptions made in the analysis (axisymmetry, light loading, laminar boundary layers) make comparisons to near-field experimental data difficult.

1.2.1.2 Analysis of Turbulent Vortices

Quite apart from possible transition in the vortex itself, or boundary layer transition due to a strong adverse pressure gradient (which can occur at relatively low Reynolds number), surface roughness due to rivet heads, dirt or impact damage is likely to cause transition of the tip boundary layer upstream of the start of vortex formation. All past analytical studies done on a turbulent tip vortex have assumed an isotropic eddy viscosity to represent the behavior of the turbulence. We shall see that this sort of approximation fails badly, because for a vortex flow-field, the shear stress vector will not align itself with the mean strain rate.

Squire's (1954) analysis of a turbulent line vortex augmented the laminar viscosity in Equation 1.2.3 by a turbulent eddy viscosity whose value was proportional to the total circulation:

$$V_\theta = \frac{\Gamma}{2\pi r}\left[1 - exp\left(-\frac{r^2}{4(\nu+\nu_t)}\right)\right] \tag{1.2.13}$$

where $\nu_t = c\Gamma$ and c is a constant.

The analysis by Hoffmann & Joubert (1963) on a turbulent line vortex predicted a constant eddy viscosity and a logarithmic radial variation of circulation in regions where the inertial forces in the tangential momentum equation are small in comparison to the Reynolds stresses (near the point of maximum tangential velocity). By dimensional reasoning the functional form of this behavior was written as:

$$\frac{\Gamma}{\Gamma_a} = \frac{1}{C}\ln\left(\frac{r}{a}\right) + 1 \tag{1.2.14}$$

Govindaraju and Saffman (1971) predicted an overshoot of circulation for a fully-rolled-up turbulent vortex under light loading conditions. Their model allows for $\Gamma_a/\Gamma_\infty = 1.2$, where most investigators have found values ranging from 0.37 to 0.6. Convincing experimental evidence of the existence of an overshoot of circulation is lacking, however.

Lezius (1974) noticed that in towing tank tests between 100 and 1000 chords downstream of an airfoil set at 8 degrees, the vortex decayed at a rate proportional to $t^{-7/8}$, not the usually predicted $t^{-1/2}$. The towing tank tests had Re_c ranging from 2.2×10^5 to 7.5×10^5. It was reasoned that the increased decay rate was due to turbulence that had not yet reached equilibrium. The inferred eddy viscosity (estimated by decay rate of tangential velocity) increased with time (distance) implying that the initial turbulence levels in the boundary layers on his wing were low and increased with time (production>dissipation). An analytical model was made adding time dependence to the eddy viscosity in Squire's solution.

Phillips (1981) analyzed the near-field roll-up of a turbulent vortex. With the exception that the boundary layers were considered to be initially turbulent, the analysis was similar to that of Moore and Saffman, with the same assumptions of light loading and axisymmetry of the vortex core. Phillips noted that the phe-

nomenon of overcirculation hypothesized by Govindaraju and Saffman was most unlikely during the roll-up process.

1.2.1.3 Other Related Analytic Studies

Lezius (1991) studied the influence of spanwise lift-tailoring on the stability of vortex roll-up. He used Rayleigh's stability criterion for a two-dimensional vortex, which states that the flow is stable if:

$$\frac{\partial \Gamma_x^2}{\partial r} > 0 \tag{1.2.15}$$

For a vortex modeled by Eqns. 1.2.1 and 1.2.2, the viscous core is stable and the inviscid region has

$$\frac{\partial \Gamma_x^2}{\partial r} = 0$$

and is marginally stable. For a spanwise lift distribution that continually increases the circulation in the radial direction, a stable roll-up ensues. Lezius reasoned that a lift distribution which created a radially decreasing circulation at some point would create an instability in the roll-up and hence increase the rate of decay of the velocities. Small scale experimental studies were done which qualitatively demonstrated the validity of the idea.

Widnall and Wolf (1980) analytically studied the effect of the tip vortex structure on helicopter noise due to blade-vortex interaction. Under certain flight conditions (usually descent), an impulsive noise called blade slap is generated at the blade passage frequency due to the passage of a blade through the preceding blade's tip vortex. The sources of this impulsive noise have been thought to be due to two sources: shock formation due to local transonic velocities induced upon the following blade; and unsteady lift fluctuations generated by the blade-vortex interaction. Their analysis was for incompressible flow, however, which ruled out consideration of noise generated by the unsteady transonic velocities. The inviscid roll-up model of Betz was used to calculate the velocity profile in the vortex and the unsteady lift on the blades due to the blade-vortex interaction was calculated using linear

unsteady aerodynamic theory. They concluded that substantial reduction in blade slap intensity could be obtained through the use of a tapered blade tip. More generally, varying the slope of the spanwise load distribution near the tip was found to greatly influence noise levels generated by the blade-vortex interaction.

1.2.2 Experimental Studies

Past experimental work on tip vortices have mainly concentrated on mean flow measurements in the far field. Wind tunnel measurements of the far-field vortex flow are complicated by low-frequency unsteadiness (also known as "meandering") in flow directions which can give large sources of measurement error especially in regions of large velocity gradients. The crux of the meander problem is that low frequency motion of a vortex will make any time-averaged Eulerian point measurement a weighted average in both time and space. Meander can also be misinterpreted as true turbulence, e.g. $u' \approx l' \partial U / \partial y$, where l' is some $y-$wise displacement amplitude. Westphal and Mehta (1989) made turbulence measurements in a vortex forced to oscillate laterally and compared them with results for a stationary vortex. They found that RMS v' increased by a factor of two and that contours of the Reynolds shear stresses were altered considerably. The meander displacement amplitude is small within a few chords downstream of the generating wing. Experimentalists have also used conditional sampling techniques (Corsiglia, Schwind and Chigier, 1973, McAlister and Takahashi, 1991) or instantaneous flowfield measurement techniques (Green, 1991) to obtain meaningful turbulence measurements in the presence of meander.

To measure the flow a large number of chord lengths downstream of the wing model in a wind tunnel, low Reynolds numbers may have to be accepted in order to reduce chord size. However, the resulting increase in the ratio of probe diameter to chord, can also increase the effect of probe interference and of vortex bursting. Although these effects are less apparent in measuring a near-field vortex flow, this regime has its own difficulties. Generally, flow velocities, gradients, angles, and turbulence levels all attain their highest levels in the near-field and the limits of applicability of various measurement probes are often reached (regions of flow reversal/separation can become a factor). Another difficulty in previous experiments has been the uncertainty about which trends were due to boundary layer transition and Reynolds number effects, and which were due to other flow variations (angle

of attack, downstream distance, tip shape, etc.). Fully turbulent boundary layers (occurring in laboratory experiments with a transition trip, or in most real-life flight conditions) will separate farther downstream and will create higher levels of initial turbulence in a tip vortex than the laminar boundary layers found in small scale experiments. Hence, roll-up behavior will be strongly influenced by the condition of the wing boundary layers.

The two following subsections describe previous experimental work relevant to the present study on the near-field roll-up of a tip vortex, which is summarized in Tables 1.1. A sketch of the most basic tip geometries studied is shown in Figure 1.2. The literature has been separated into sub-categories of studies without turbulence measurements and studies with turbulence measurements.

1.2.2.1 Near-Field Experiments Without Turbulence Measurements

Grow (1969) made near-field measurements of the mean flow in a tip vortex for various wing shape parameters, using a five-hole pressure probe and a vorticity meter. It was found that 90% of the measurable circulation enters the tip vortices within one chord of the trailing edge. McCormick, Tangler & Sherrieb (1968) reduced Grow's data to get the following linear empirical formula for the maximum tangential velocity in the near-field at $Re_c \approx 3.5\times10^5$:

$$\frac{V_{\theta,max}}{U_\infty} = 0.7C_L,\ 2 < AR < 4 \tag{1.2.1}$$

$$\frac{V_{\theta,max}}{U_\infty} = 0.625C_L,\ AR > 4 \tag{1.2.2}$$

The surface pressure measurements of Spivey and Morehouse (1970) showed a characteristic suction peak on the tip, denoting the approximate location of the primary vortex as it rolls-up on the suction side of the wing. Occasionally, a second suction peak was measured outboard and downstream of the primary peak, which they hypothesized to be due to a secondary vortex.

Orloff (1974) used a two-dimensional laser velocimeter to measure the mean flow two chords downstream of a NACA 0015 wing with square tip at a variety of angles of attack and freestream velocities. For this model, $\partial(\frac{V_\theta}{U_\infty})/\partial\alpha = 0.05$ /deg and $V_{x,cl}/U_\infty$ varied from a defect value of 0.88 to excess values of 1.05 and 1.18 at $\alpha = 8, 10, 12^o$ respectively. Batchelor's arguments for increasing axial velocity with increasing tangential velocity are a possible explanation for these trends.

Thompson (1983) used dye and hydrogen bubble flow visualization techniques in a water tunnel to study the effects of various tip shapes on the vortex formation process on a rectangular NACA 0012 wing. Round, square and bevelled tip shapes (in axial view) were studied at $Re_c = 2.2\times10^4$ and at various angles of attack. The separation process of the tip boundary layers, and hence the location and number of vortices forming, was highly dependent upon tip shape. For the square and bevelled tip shapes, separation was fixed by their sharp-edged boundaries. The primary vortex due to a rounded wingtip was located on the rear portion of the suction side of the wing. Outboard of the primary vortex, a secondary vortex of the opposite sense was induced by the effect of the primary vortex on the tip boundary layer. Likewise, a tertiary vortex was seen outboard of the secondary vortex. As these secondary vortices became wrapped up into the primary vortex a rapid change of direction of the vortex core was seen in plan view. This "vortex kink" has been observed by other researchers but the reason why it is present is not well understood. The path of the vortex centerline undergoes a sudden spanwise crossflow acceleration at the beginning of the kink and then at the end of the kink, it resumes its original direction. Although the boundary layers in the experiment were laminar, turbulent boundary layers would probably not change the locations of separation at the sharp edges of the square and bevelled tip. The rounded-tip separation location, however, would definitely be affected by the presence of turbulent boundary layers.

The work done by Higuchi, Quadrell and Farell (1986) and Ikohagi, Higuchi and Arndt (1986) addressed the inability of available analytic models to accurately predict the near-field roll-up, particularly for cavitation prediction. LDV was used

to measure the mean flow up to 3.9 chords downstream of an elliptic wing. The vortex cross-section was far from circular. The maximum tangential velocity was found to be 10% larger on the suction side than the pressure side. It was found that vortex core size was highly dependent upon angle of attack although previous analytic studies had found no such dependence. A semi-empirical model for a near-field tip vortex was constructed by using their data to patch together Squire's analytic model of the core and potential region with Hoffman & Joubert's analytic model for a logarithmic buffer region. Although this semi-empirical model fit the experimental data better (by definition), it still did not allow for asymmetries in the flow, and errors of up to 25% occurred because of this.

Francis & Katz (1988) used a dye/laser sheet combination in a towing tank to visualize the formation of a tip vortex on a rectangular NACA-66 hydrofoil. The location of the vortex core was tracked along the chordline and empirical formulas were developed for $10^5 < Re_c < 5 \times 10^6$, $0^o < \alpha < 12^o$, and $-0.52 < x/c < 0.0$. The formulas predicted the vortex to increase in core diameter with increasing x/c, while the path of the vortex centerline was found to move up and inboard. Opposite trends were predicted for increasing Re_c. For increasing angle of attack, the core diameter decreased, while the vortex moved up and inboard. Note that their empirical formulas were derived for a square tipped rectangular wing and may be less accurate when applied to other wing shapes.

McAlister & Takahashi (1991) used two-component LDV to measure the mean flow behind a NACA 0015 wing with square and rounded tips at various conditions (chord size, chord Reynolds number, circulation, and downstream distance were varied). A maximum core axial velocity of $1.5U_\infty$ and a maximum tangential velocity of $0.84U_\infty$ were measured at $x/c = 0.1$ and at 12 degrees angle of attack. A single parameter was varied and and all other parameters were held constant to find trends in flow structure. Increased chord size or circulation level increased tangential and axial velocities. Increased Reynolds number however decreased tangential and axial velocities. The round tipped wing showed smoother separation characteristics and greater velocities than the square tipped wing.

Shekarriz, Fu and Katz (1993) used Particle Displacement Velocimetry to measure the flow over a square-tipped rectangular wing at various chord Reynolds number and angles of attack. They also noticed crossflow velocities on the suction side to be 40% higher than the velocities on the pressure side, a marked difference from Higuchi's 10% difference. Contradicting the data analysis by McCormick et al. (1968), the increase of $V_{\theta,max}/U_\infty$ with lift coefficient was not linear at some of the Re_c studied; this was attributed to transition effects.

1.2.2.2 Near-Field Experiments With Turbulence Measurements

Poppleton (1971) studied the effect of air injection into the core of trailing vortex. The jet/vortex system was generated by airfoils set at equal and opposite angles of attack separated by a jet-pipe. Pitot probes, normal wires, and inclined wires were used to measure far downstream of the vortex. As might be expected, the jet increased the levels of turbulence in the core and the rate of decay of the vortex was increased also.

Chigier & Corsiglia (1971, 1972) used triple wires to measure up to 9 chords downstream of a square-tipped rectangular wing with NACA 0015 section. At 12 degrees angle of attack and $Re_c = 9.5 \times 10^5$, a maximum core axial velocity of $1.4U_\infty$ was measured at $x/c = -0.25$. Afterwards, the core axial velocity decayed at the trailing edge, to a value of $1.1U_\infty$, and then showed the disturbing trend of accelerating slightly to a value of $1.2U_\infty$ at $x/c = 4.0$. At $x/c = -0.50$, the maximum crossflow velocity was measured to be $0.42U_\infty$ and it decayed axially thereafter. The decay in crossflow velocity with axial direction should produce an adverse axial pressure gradient near the axis (Eq. 1.2.5). Instead, their measurements showed an acceleration of the fluid on the core centerline. The turbulence fluctuations were measured to be at their highest levels in the core. Maximum turbulence intensity was roughly found to increase linearly with angle of attack. At 12 degrees angle of attack, a maximum turbulence intensity of 12.2% was found on the core centerline. Similar to Thompson's study of a rectangular tipped wing, they found a secondary vortex, of the same sense of rotation as the primary vortex, on the tip face.

Corsiglia, Schwind, and Chigier (1973) later repeated the previous tests using a rotating triple-wire traverse to eliminate the effects of meandering. Only traverses that passed through the vortex center were later analyzed. At $x/c = 26.7$, the maximum tangential velocity was measured to be $0.72U_\infty$. This was almost 75% larger than the maximum tangential velocity measured using their old technique at $x/c = -0.50$. They attributed this major discrepancy to the effects of meandering, but it is highly doubtful that meandering could have this sort of effect so early in the development of the vortex. Clearly, some other sort of measurement error has impacted one or both of the measurement techniques used.

Singh (1974) used quad-wires and single-wires to measure the mean and turbulent flow quantities up to 85 chords downstream of a square-tipped rectangular wing with NACA 64_3-618 section. He found a large axial velocity excess immediately downstream of the trailing edge for wings with large L/D ratios (>40), while at lower L/D ratios, the vortex had a small axial velocity defect. A vortex with an axial jet was shown theoretically to be unstable, and a wing with a L/D ratio of 60 also developed laminar instabilities at $40 > x/c > 13$. The airfoil section was claimed to minimize the initial wake turbulence levels so that these laminar instabilities could be measured far downstream. The high L/D ratio wing measured a peak axial velocity of $1.6U_\infty$ at $x/c = 0.8$. Curiously, the axial velocity decelerated quickly to freestream level at $x/c = 2.4$, and then to an extreme velocity defect of $0.52U_\infty$ at $x/c = 5.0$. The crossflow velocities and core size measured at these locations were subject to error because the large flow angles in the initial roll-up of the wing were outside the range of their calibration. Their core size as a fraction of chord, a/c, was roughly twice what had been measured previously in similar flow conditions. Initially, the turbulence intensity was highest some distance from the vortex center (around 15% freestream velocity), but it was claimed that, far downstream the turbulence diffused into the vortex center and the profiles showed a broad peak at the center. The "instabilities" which developed downstream were analyzed by studying the axial velocity fluctuations and correlations. It was found at $x/c = 30$ that about 50% of the fluctuation energy was due to low frequency pe-

riodic components. A wing with a low L/D ratio (equal to 20) was found to have a small axial velocity defect and a maximum crossflow velocity of about $0.5U_\infty$ whose value showed a self-similar decay rate of $x^{-1/2}$ for $x/c > 30$. Turbulence levels also showed a self-similar decay rate. As the vortex became fully rolled-up, a small overshoot of circulation was found, although nowhere near the levels postulated by Govindaraju and.Saffman.

Phillips and Graham (1984) used single normal and inclined hot-wires rotated to several orientations (7 are needed) to measure the full Reynolds stress tensor in the far-wake of a vortex generated by a differential airfoil (two joined wings at equal and opposite angles of attack) with trip ($Re_c = 7.4 \times 10^4, \alpha = 9°$). Three crossflow planes were studied, at 45, 78, and 109 chords downstream of the wing. The effect on turbulence of an axial velocity excess/deficit in the vortex core was simulated by placing a round jet or wake-enhancing nacelle in the center of the vortex generator. The profiles of the Reynolds stresses are close to what might be expected from mean flow considerations. The change of sign of $\overline{v_r' v_\theta'}$ at some r_1 is different from Singh's results. For the round jet in the vortex, $\hat{v}_r > \hat{v}_\theta > \hat{v}_x$ for some $r < r_1$ and $\hat{v}_r > \hat{v}_x > \hat{v}_\theta$ for some $r > r_1$. They attributed the larger $\hat{v}_r$ to turbulence diffusion being larger than turbulence production. The jet had much faster turbulent decay than the wake, and they attributed this to the effect of the radial velocity, V_r. The jet had positive radial velocity which meant that the vortex core was being compressed axially and widened. This, they claimed, had the effect of suppressing turbulence. The wake-enhanced vortex had negative radial velocity, which meant that the vortex core was being stretched ($\partial V_x/\partial x > 0$) and turbulence production therefore enhanced. A momentum balance along radial lines was calculated for each of the momentum equations and it was found that in the r-equation, the $\partial \overline{v_r'^2}/\partial r$ term cannot always be ignored, although V_r could be. In the θ-equation and the x-equation however, the radial velocity was found to be important.

Lee & Schetz (1985) used a five-hole pressure probe and single normal wires to measure behind a slightly swept NACA 0012 wing (whose tip shape was not

stated in the paper). They measured up to 6 chords downstream of the wing at up to 10 degrees angle of attack and found some confusing trends. At 5 degrees angle of attack, normalized tangential velocity increased with freestream velocity. Correspondingly, normalized axial velocity in the core also increased with freestream velocity. Surprisingly though, at 10 degrees angle of attack, the normalized axial velocity and axial turbulence intensity in the core decreased with freestream velocity. They did not display tangential velocities at this angle of attack, however.

Mehta & Cantwell (1988) measured two of the three Reynolds shear stresses in a turbulent vortex generated by a half-delta wing, at relatively low Reynolds number. Distributions of Reynolds shear stresses were found to be consistent with the isotropic eddy viscosity concept, and the distributions of the anisotropy parameter, $\overline{v'^2} - \overline{w'^2}$, were aligned such that their contribution to vorticity production was negligible.

Stinebring, Farrell, & Billet (1990) used three-component LDV to study the tip vortex structure of a swept wing hydrofoil with particular interest in cavitation inception. At an unspecified angle of attack and $Re_c = 8.5 \times 10^5$, an axial velocity defect was found just downstream of the trailing edge. In the core center, $v' > w' > u'$ and the maximum fluctuating velocity was 2.3% of freestream velocity. From the fluctuating velocities, they defined a dimensionless fluctuating pressure:

$$\frac{2\sqrt{p'^2}}{\rho {U_\infty}^2} = k \frac{u'^2 + v'^2 + w'^2}{{U_\infty}^2} \tag{1.3.1}$$

where the constant k ranged from 0.39 to 3.6. The fluctuating pressure was found to be an important factor in cavitation inception. They also defined a roll-up parameter:

$$K_r = \left(\frac{V_{\theta,max,1}}{V_{\theta,max,2}} \right)^2 \tag{1.3.2}$$

where the indices 1 and 2 represent maximum tangential velocities separated by 180 degrees. As the tangential velocities become independent of the tangential direction, roll-up is complete and K_r approaches 1. They found in their experiment that:

$$\frac{\partial K_r}{\partial(log(x/c))} = 0.33 \tag{1.3.3}$$

Bandyopadhyay, Stead, & Ash (1991) investigated the turbulence structure in a turbulent trailing vortex generated by a double-branch vortex generator (aerofoils at equal and opposite angles of attack). They used a seven-hole pressure probe and single wires to measure up to 40 chords downstream of the trailing edge at various freestream turbulence levels (generated by screens). They concluded that for their range of test conditions, the Rossby number (core centerline axial velocity defect or excess divided by maximum tangential velocity) was the controlling parameter for the turbulence structure, not the vortex Reynolds number (circulation/viscosity). A lower Rossby number was found to promote re-laminarization. They also concluded that the inner core is not, as suggested previously, a region in nearly solid-body rotation that does not interact significantly with the outer vortex region, but a re-laminarizing region where patches of turbulent fluid are intermittently brought in from the outer region. Their vortex was created by a differential airfoil, and their measurements were taken far downstream of the trailing edge, so that they may not be quantitatively representative of the near-field rollup region of a wingtip vortex.

Green & Acosta (1991) and Green (1991) measured the instantaneous flowfield up to 10 chords downstream of a rounded-tip rectangular wing with NACA 66-209 section. Double-pulsed holography and the tailored-air-bubble technique were used to measure the instantaneous velocity and static pressure respectively. At $x/c = 2$ and 10 degrees angle of attack, the core axial velocity was measured to be $1.6U_\infty$, with a mean fluctuation of $0.2U_\infty$ (several runs were made to calculate a nominal mean). Green noticed a low frequency instability with peak-to-peak axial amplitudes up to 25% of the freestream velocity. Contrary to the results found by most other researchers, the vortex was found to be axisymmetric at $x/c = 2$. The tangential velocity was also highly unsteady with mean fluctuations of $0.15U_\infty$. At 5 degrees angle of attack, the low frequency instability disappeared, although the axial velocity was still highly unsteady. He hypothesized that in the near field the non-dimensionalization of the axial velocity with the wing lift coefficient was

constant. For all flow conditions, the axial velocity reached freestream velocity for $r/c > 0.04$. Qualitatively, it was noticed that the bubbles were highly deformed near the vortex centerline (although on the centerline they were spherical) implying that either large pressure forces or large shear forces were acting upon them. As was found in the study by Thompson, Green observed a vortex kink for small values of x/c. The flow turned through about 25 degrees before being turned again to its freestream direction shortly thereafter. The similarity of this behavior to the vortex-soliton theory of Hasimoto (Hopfinger et al. 1982) was noted. The core static pressure was found to be adequately modeled by the steady axisymmetric radial momentum equation or the semitheoretical correlation of Dunham (1979):

$$P_{cl} = 3.44\left(\frac{V_{\theta,max}}{U_\infty}\right)^2 \tag{1.3.4}$$

The core fluctuating pressure was found to be predicted rather well by the axial velocity unsteadiness:

$$p'_{cl} = \left(\frac{u_{cl}}{U_\infty}\right)^2 - \left(\frac{U_{cl}}{U_\infty}\right)^2 \tag{1.3.5}$$

Cutler & Bradshaw (1993) used cross-wires and pressure probes to study the interaction of a longitudinal vortex pair, generated by a delta wing, with a turbulent flat plate boundary layer. They observed that lateral convergence of the boundary layer produced a drop in eddy viscosity, dissipation length scale, and skin-friction coefficient. They found high levels of turbulence in the vortex core with $\hat{v}_r > \hat{v}_x > \hat{v}_\theta$. Contours of $\overline{v'w'}$ had the characteristic four lobed pattern (an attribute caused by the rectangular coordinate system), but the planes of symmetry at $\pm 45^o$ to the horizontal were not consistent with well-behaved eddy viscosity.

1.2.2.4 Effects on Practical Problems

There have been several experimental studies where devices have been used to alter or manipulate the tip vortex. The goal has always been to diffuse the vortex so that tangential velocities induced by the vortex are lower (and hence

so are core axial velocities and core pressures). Carlin, Dadone & Spencer (1989) studied the effects of "umbrella" and "tabbed" trailing edge devices on the roll-up of the vortex. It has generally been concluded that tip shape can substantially affect the way the vorticity in the tip vortex is concentrated. However, trade-offs with other performance concerns (weight, drag, lift, etc.) make more experimental work necessary before reliable tip modifications can be made. Heffernan (1985) gives an overview of vortex attenuation devices.

1.2.3 Computational Studies

Although there have been many computational studies of the roll-up of a vortex generated by a delta wing or of the process of vortex breakdown, few Navier-Stokes computational studies of the vortex roll-up process of a conventional wing exist.

The computational work by Srinivasan et al. (1988), used ARC3D, a thin-layer Navier-Stokes solver, with the Baldwin-Lomax turbulence model to study the flow on a helicopter wingtip. It showed good qualitative agreement with the experimental work done by Spivey (1970), but the resolution of the viscous wake and the surface pressure suction peak induced by the vortex was poor.

De Jong, Govindan, Levy, and Shamroth (1988) used a forward-marching solver with eddy viscosity turbulence model to solve the flow around a NACA 0012 wing with rounded wingtip. 225,000 grid points were used at a Re_c of 7.4×10^5 and angles of attack of 6.18^o and 11.4^o. The location of the vortex roll-up over the suction surface of the wing was accurately depicted, but many key features of the flow were absent. The development of an axial velocity excess was not reproduced.

The computational studies by Dacles-Mariani et al. (1993) and (1994), done in conjunction with the present experimental study, modeled the wind-tunnel walls and used experimentally measured inflow boundary conditions. The grid had 1.5×10^6 points and was more densely spaced in regions of the flow where the gradients were large (e.g. vortex core). An upwind-differencing scheme was used in conjunction with a modified Baldwin-Barth turbulence model. They predicted an excess of axial velocity and showed that it is possible to predict the mean flow of the tip-vortex

near-field rather well using a Reynolds-Averaged Navier-Stokes code; however the turbulence modeling used was not as accurate as desired.

Preliminary work by Zeman (1994) used a full Reynolds stress model to study the far-field nature of the turbulence in an isolated vortex. He predicted a rapid decay of the initial turbulence in the vortex core and his contours of $\overline{v_r' v_\theta'}$ were qualitatively similar to those measured in the present study.

The state-of-the-art in computations still has a long way to go before being able to qualitatively describe the turbulence in the roll-up of a wingtip vortex. Accurate turbulence modeling remains the major stumbling block in computational studies.

1.3 SUMMARY OF UNRESOLVED ISSUES

The key questions that were raised by previous studies and that have been studied in the present experiment are the following:

1) Assuming that the axial velocity excess/deficit exists due to some trade-off between the development of a favorable axial pressure gradient and the wrapping up of low-momentum boundary layer fluid into the vortex core, how can this be correlated by relevant flow parameters? In other words, when should we expect an excess to occur and when should we expect a deficit to occur?

2) What influence does turbulence have on the roll-up of the vortex and what sort of modeling is needed to accurately depict the turbulence in this flow?

3) Based upon answers to the previous questions, what sort of modifications could be made to solve some of the practical problems involved with the roll-up of a tip vortex?

1.4 OBJECTIVES

This experimental study focuses on the initial roll-up region of the turbulent vortex from a generic unswept wingtip at high Reynolds number. The approach is first to reach a basic understanding of the physics involved in the flow near the wingtip, supported by detailed measurements of turbulence structure, before

proceeding to development of prediction methods or tip modifications.

Surface oil-flow visualization, laser-illuminated smoke visualization, surface pressure measurements, velocity-field measurements by use of a seven-hole pressure-probe, 2-point single-wire correlation measurements, and turbulence measurements by use of a triple-wire probe have been completed for the flow over a rectangular wing with rounded tip as far as a half chord downstream of the the trailing edge. The Reynolds number based on chord was 4.6 million. Given the trade-off between taking extensive measurements at one flow condition or taking fewer measurements at several flow conditions, the former option was chosen because measurements at closely-spaced points are needed to resolve the large spatial gradients in the thin tip boundary layer and the rollup region, and because it would give the computational scientist a solid test case for comparison. Wind-tunnel blockage will have some impact on some of the quantitative aspects of the study (if comparisons are to be made with free-flight data), but the measurements will be completely valid for computationalists so long as they include the same boundary conditions used in the experiment (i.e. include wind-tunnel walls). In addition, it is felt that the qualitative aspects of the flowfield are preserved.

Table 1.1 Summary of Previous Experimental Work

Author and Year	Reynolds Number Range	Axial Measurement Range, x/c	Measurement Technique	Tip Shape	Airfoil Type
Grow (1969)	3.5×10^5	6.0	5-hole pressure probe	unknown	rectangular NACA 0015
Logan (1971)	1.5×10^5 to 2.3×10^5	10.0 to 26.0	5-hole pressure probe	1/12 Piper Cherokee	1/12 Piper Cherokee
Chigier and Corsiglia (1971)	9.5×10^5	−0.75 to 4.0	3-wire probe	square	rectangular NACA 0015
Chigier and Corsiglia (1972)	9.5×10^5	9.0	3-wire probe	square	rectangular NACA 0015
Corsiglia, et al. (1973)	3.0×10^5	0.0 to 165.0	rotating 3-wire	square	rectangular NACA 0015
Orloff (1974)	5.0×10^5 to 9.0×10^5	2.0	2D LDV	square	rectangular NACA 0015
Singh (1974)	6.3×10^4 to 1.3×10^5	0.8 to 80.0	4-wire probe 1-wire probe	square	rectangular NACA 64-3-618
Singh and Uberoi (1974)	1.3×10^5	0.8 to 80.0	4-wire probe 1-wire probe	square	rectangular NACA 64-3-618
Thompson (1983)	2.2×10^4	−1.0 to 0.0	dye, hydrogen bubble	square, bevel, round	rectangular NACA 0012
Lee and Schetz (1985)	2.1×10^5 to 1.5×10^6	3.0 to 6.0	5-hole pressure probe		swept NACA 0012
Higuchi et al. (1986)	4.7×10^4	0.79 to 3.93	LDV	N/A	elliptic NACA 66-2-415
Francis and Katz (1988)	2.6×10^4 to 1.3×10^6	−0.5 to 0.0	dye	square	rectangular NACA 66 series
McAlister and Takahashi (1991)	1.5×10^6	0.1 to 6.0	LDV	square, round	rectangular NACA 0015
Green (1991)	7.9×10^5	10.0	Double-Pulsed Holography	round	rectangular NACA 66-209
Green and Acosta (1991)	4.1×10^5 to 6.8×10^5	2.0 to 10.0	Double-Pulsed Holography	round	rectangular NACA 66-209
Stinebring et al. (1991)	8.5×10^5	0.07	LDV	square	swept
Shekarriz et al. (1993)	3.6×10^4 to 2.2×10^5	0.0-6.7	PDV	square	rectangular 19% thick

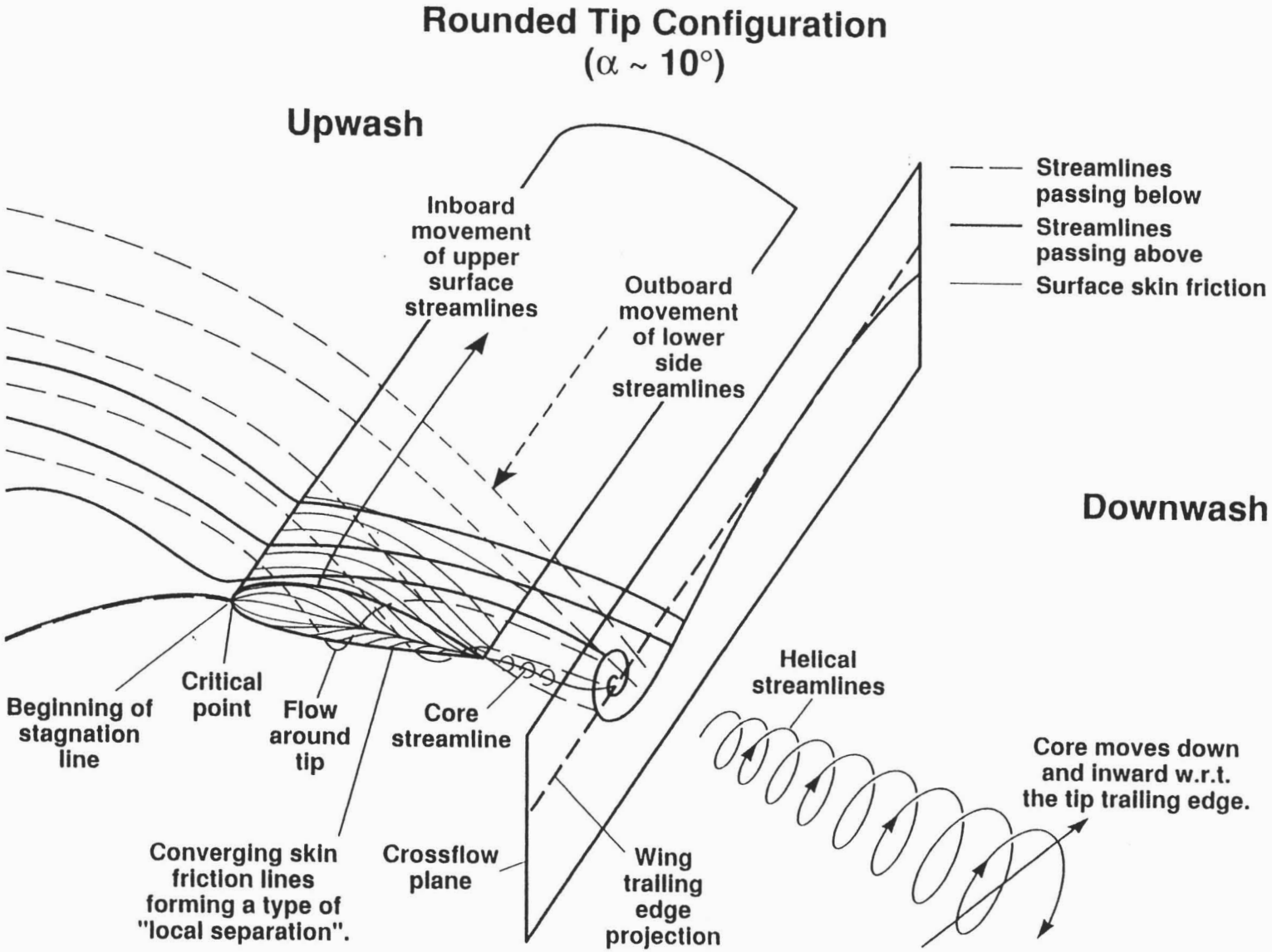

Figure 1.1 Initial Roll-up of a Wingtip Vortex

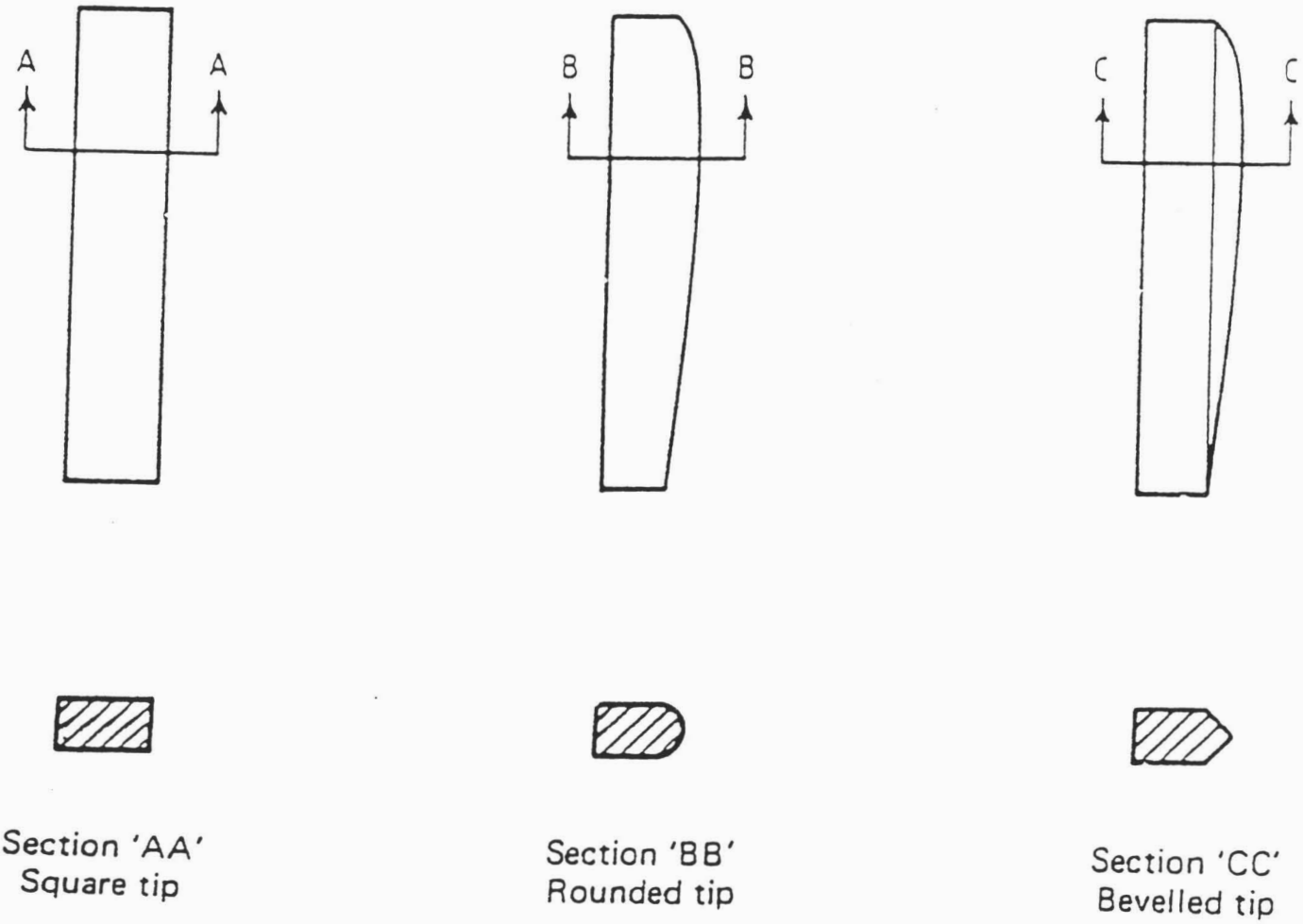

Figure 1.2 Basic Wingtip Shapes

2. EXPERIMENTAL APPARATUS AND PROCEDURES

Flow visualization studies and mean/turbulence flow measurements have been performed in the near-field of a helicopter blade tip at full-scale Reynolds number. Flow visualization studies used the surface oil-flow, naphthalene sublimation and laser-illuminated smoke techniques. Mean flow measurements were performed using surface pressure taps and a seven-hole pressure-probe. Correlation and turbulence measurements were performed using a single-wire and triple-wire probe respectively.

The following chapter describes in detail the experimental facilities and techniques used to perform these measurements.

2.1 EXPERIMENTAL FACILITIES

2.1.1 Wind Tunnel Configuration

The measurements were performed in the 32" $\times$ 48" low speed wind tunnel (Figure 2.1) at the Fluid Mechanics Laboratory (FML) of NASA Ames Research Center. This open-loop wind tunnel, which is powered by a 130,000 cubic feet per minute compressor, has a sonic throat to keep the test section free from the effects of downstream disturbances. The tunnel has a faired inlet, followed by honeycomb straighteners, which are then followed by five screens. The contraction ratio of the wind tunnel is 9 to 1, and the maximum x-component freestream turbulence level as measured by hot wire anemometer is 0.15%. The rectangular test section has a width of 48 inches, a height of 32 inches, and a length of 120 inches. The maximum speed of the wind tunnel is 200 feet/second although the experiment was conducted entirely at a freestream velocity of 170 feet/second. Tunnel speed was computer controlled through feedback of tunnel dynamic pressure measurements. A traversing mechanism is contained in a sealed enclosure lying above the test section (so that plenum is at tunnel static pressure), and removable slotted plexiglas ceiling sections allow freedom of movement for the traverse in the axial direction. Plexiglas side walls of 1/2 inch thickness allowed for visual inspection of ongoing tests. Further

information concerning the design of the wind tunnel can be found in Zilliac (1988).

2.1.2 Wing Model Configuration

A half-wing model of 4 foot chord, 3 foot semi-span including rounded (half-body of revolution) wingtip, and NACA 0012 wing section was used, as shown in Figure 2.2. The constant chord section of the wing accounted for 33.12 inches of the span, while the maximum span extension of the tip near the quarter chord measured 2.88 inches. The two coordinate systems used to describe the physical locations of the experiment are also shown in Figure 2.2. Note that the origin is at the wing root trailing edge.

During the design phase of this study, the decision was made to use as large a model as possible while avoiding severe viscous tunnel interference due to excessive growth or separation of the tunnel wall boundary layers. "Inviscid" tunnel interference is, of course, very large and computations have to take into account the presence of tunnel walls.

The model was constructed out of aluminum with a skin thickness of 1/4 inch and precision machining of the surface contour ($\pm$ 0.0005 inches). This skin covered a wing structure consisting of 3 aluminum ribs and a single-tube steel spar. A removable rounded-tip cap and detachable bottom surface allowed access to pressure tap tubing. A steel beam support structure with bearings held the wing structure in place as shown in Figure 2.3. The wing deflected a maximum of 0.005 inches with the tunnel running at the test speed of 170 feet/sec and the angle of attack set at 10^o. The angle of attack could be varied through $\pm 16^o$ by rotating the model about its quarter chord, although, the only test case of interest in the present study was at $+10^o$ angle of attack. The quarter chord point was located in the vertical center of the test section so that geometries at positive and negative angles of attack were identical. "Lower surface" measurements were made on the upper surface at -10^o. The quarter chord point was located 19.0 inches downstream of the test section inlet.

A trip was used to fix transition near the leading edge. Spherical roughness

elements of 0.017 inch diameter were packed closely together to form a 1/8 inch wide strip. The strip was placed across the span of the wing at an arc distance of 2.0 inches from the leading edge. The location of the trip was at the nominal location of natural transition on the suction side of the wing which was determined by naphthalene flow visualization. The trip extended around the tip and along the bottom surface of the wing. Naphthalene sublimation and microphone techniques were used to confirm that the boundary layers on the suction side of the wing and the wingtip region were turbulent after the trip.

2.1.3 Traverse Mechanisms

Probe traversing for the seven-hole and triple hot-wire probe was done using NASA/FML built rails and slides driven by Compumotor LE-Series drive units and Model 372 indexers (25000 microsteps/rev). The five-degree-of-freedom traversing system had the capability of translation in three directions, and of pitching and yawing the probe. The traversing gear is shown in Figure 2.4. The pitch and yaw capability was not used with the seven-hole probe (except during calibration). When the triple-wire probe was traversed, pitching and yawing the probe also required translational movement to maintain the sensing portion of the wires at the data point location. By varying the position of the slotted plexiglas ceiling sections, various streamwise locations could be accessed by the traverse. Probe position and orientation was derived from optical encoders on all axes (not from motor step counts). Absolute positioning accuracy of a probe (relative to wing model surface) was within 0.02 inches. Incremental positioning accuracy was determined to be within 0.001 inches for translation, 0.2^o for pitch, and 0.1^o for yaw. Absolute positions were displayed on RSF Electronics Z536 displays.

2.2 DATA ACQUISITION AND REDUCTION

2.2.1 Computer System

Data were acquired using a 32-bit DEC μVAX II computer. The computer had 5 megabytes of RAM, a hard disk with 360 megabytes capacity, and a 90 megabyte capacity tape back-up drive. Connected to the computer were the following: a 15-bit, 10 channel simultaneous sample and hold Tustin X-2100 A/D, a 12-bit, 8 channel A/D, 2 channel D/A AXV-11-C board, 5 Compumotor 372 indexer units, 2 computer terminals, and an Ethernet port. The computer configuration and equipment schematic is shown in Figure 2.5. The core software used for data acquisition was the Fluid Mechanics Data Acquisition System (FMDAS) software which is described by Hooper & Saunders (1985).

Analog signals from the MKS 223B and the FML Hot-Wire Bridges were sent to the Tustin unit. Measurement error due to A/D resolution over a 10 volt range for the Tustin A/D was about ± 0.3 mV and was considered to be negligible compared to instrument error. Tunnel speed was controlled by a D/A channel from the AXV-11-C board with feedback from the Datametrics type 1015 transducer sent to one of the AXV-11-C's A/D channels. The Ethernet port allowed for quick transfer (10 Mbits/second) of raw data using the DECNET protocol, to a separate computer for near-real-time assessments of triple-wire data (see Figure 2.5).

2.2.2 Flow Visualization Technique

To determine the approximate location of transition on the wing surface, the naphthalene sublimation technique was used. Naphthalene mixture was sprayed onto the wing surface and the wind tunnel was set to the reference velocity. Regions of high mixing rate sublime the mixture at a faster rate so that after a certain amount of time has elapsed, the naphthalene is visible only on portions of the surface where the flow is nominally laminar.

To get a qualitative picture of the skin friction lines on the wing, surface-oil

flow visualization was performed using (roughly) a mixture of titanium oxide (1.5 parts), oleic acid (1 drop/tablespoon titanium oxide), kerosene (2 parts), 10 weight oil (1 part), and fluorescent powder (1 part) and photographed using a 2 × 2 inch large format still camera. An ultraviolet lamp was used to illuminate the mixture. This gave more contrast with the background surfaces than with normal lighting. The mixture was simply brushed onto the entire wing surface with the tunnel off, and then allowed to "run" with the tunnel on. Once the kerosene evaporated, the tunnel was turned off again to allow for a clear photographic path.

Laser-illuminated smoke flow visualization using a Rosco 1500 smoke generator, a smoke filament rake, and a 5 Watt Lexel argon-ion laser, was videotaped with a Sony DXC-M3A video camera and also a 35 mm camera. The rake was placed in front of the wind tunnel inlet and aligned so that smoke was wrapped into the vortex. A fan of laser light was generated by passing the laser beam through a cylindrical lens. The fan of light was oriented so that crossflow planes of the smoke filaments could be visualized. Several streamwise stations of the crossflow planes were observed by mounting the lens on the axial traverse.

2.2.3 Pressure Transducer Instrumentation

MKS 223B pressure transducers were used for surface pressure and seven-hole pressure measurements, while a single Datametric Type 1015 transducer was used for tunnel speed control.

The Datametric Type 1015 pressure transducer was calibrated with a linear two point fit over the range of pressures encountered in wind tunnel operation.

For surface pressure measurements, a single MKS 223B pressure transducer was calibrated with a cubic fit of 10 pressures ranging from 6.6 to −6.6 inches of water differential. The digitized pressure was averaged over a 4 second period.

For seven-hole pressure probe measurements, all eight MKS 223B pressure transducers were calibrated at the beginning of every data run with a third-order fit of 12 pressures. The pressures ranged from 7.0 to −26.0 inches of water differential to account for the full range of pressures encountered in the wingtip flow. The

transducers were kept in a temperature controlled box to reduce variation in the transducer calibrations. After allowing time for the pressures to settle, the digitized pressures were averaged, again over a 4 second period.

All calibrations were done using a NASA/FML built automated micro-manometer with a range of up to ± 30 inches of water pressure.

2.2.4 Surface Pressure Measurement System

On the upper half of the wing model surface, 222 static pressure taps were located in 12 chordwise rows at the spanwise locations of $z/b_o = 0.181$, 0.362, 0.725, 0.845, 0.906, 0.936, and 0.966 and at the tip spanwise locations of $\gamma = 0.0^o$, 22.5^o, 45.0^o, 67.5^o, and 80.0^o. Each row had 19 taps at the chordwise locations of $x/c = -1.0$, -0.995, -0.9875, -0.975, -0.95, -0.925, -0.9, -0.085, -0.8, -0.75, -0.7, -0.6, -0.4, -0.2, -0.015, -0.125, -0.075, -0.05, and -0.025. The taps were connected to a six-cap Scanivalve (40 barrels/cap) which in turn was connected to a MKS 223B pressure transducer. Lower surface measurements were made by setting the wing model to negative angle of attack.

2.2.5 Seven-Hole Pressure Probe

A NASA/FML made conical shaped seven-hole pressure probe (Zilliac, 1989) of 0.1 inch diameter was used to measure static pressure and the velocity vector. The primary advantage of a seven-hole probe over a five-hole probe lies in its ability to measure in high flow angle environments. Pressure coefficients are formed, based upon probe holes where the flow remains attached, and large flow angles can be measured even though flow separation may occur on the leeside of the probe. The ability of the seven-hole probe to resolve flow angles up to 65^o was an important attribute for measuring behind the wing where flow angles of up to 50^o were present. Data rate of the probe measurement system was maximized by use of simultaneous sampling of the 8 required pressure measurements at each measurement location (seven for the probe and one for tunnel reference total) with 8 separate MKS 223B

pressure transducers. The pressure transducers were placed in a thermally insulated box to minimize the effects of temperature drift on the calibration of the transducers. Flowfield data using the seven-hole probe were taken at the following cross-flow planes: $x/c = -1.14, -0.59, -0.39, -0.30, -0.20, -0.11, -0.005, 0.005, 0.13, 0.26,$ 0.46, and 0.69. Data planes taken in the wake and in front of the wing model had 21 x 29 data points (23.0 inches vertical, 28.0 inches span). The boundaries of the data planes were at $2z/b_o = 0.33$, $2z/b_o = 1.20$, y/c = -0.11, and $y/c = 0.47$. Data planes taken above the surface of the wing also had 21 x 29 data points. These planes however, were, in essence, half-planes, since they extended exactly half way around the tip, but did not include any points below that line. For data points near the wing surface, an electronic touch sensor was used to find the surface of the model. The first vertical data point above the surface was taken 0.050 inches (about one-half probe diameter) above the location found by the touch sensor. The grids were stretched so that the densest experimental grid spacing was around the center of the core of the vortex. The center of the core was found by taking a small grid (usually 15-20 points) of preliminary measurement data points around an estimated location of the core and then interpolating to the point with the lowest crossflow velocity.

2.2.5.1 Seven-Hole Probe Calibration Procedure

Calibration of the probe was done in situ, prior to installation of the model. The probe was pitched and yawed over 5^o increments for $-30^o < \theta < 80^o$ and $-80^o < \beta < 80^o$. A diagram of the probe stem apparatus during calibration and of the 7-hole pressure probe itself are shown in Figure 2.6. A separate probe stem apparatus was used during actual measurement taking such that $\gamma = 0^o$. The calibration involved forming 28 different non-dimensional pressure coefficients for every pitch and yaw angle combination. For any given measurement point only 4 coefficients are used, but the coefficients which are used are determined by separation criterion. The coefficients were quite insensitive to freestream velocity variations and so long as care was taken to keep the probe tip free of damage or

debris, the probe did not need to be re-calibrated. A more complete description of the calibration procedure and the separation criterion is given by Zilliac (1989).

2.2.5.2 Seven-Hole Probe Uncertainty and Error Analysis

A complete analysis of measurement error of seven-hole probes is given by Zilliac (1989). For high flow angles ($> 30^o$), flow angle measurement uncertainty for the seven-hole probe is within 1^o while velocity magnitude uncertainty is within 1.1% of freestream velocity. For low flow angles ($< 30^o$), flow angle uncertainty is within 0.5^o while velocity magnitude uncertainty is within 0.8%.

2.2.6 Hot-Wire Anemometry System

A Dantec 55P91 triple-wire probe was used to measure turbulence quantities including triple products and all components of the Reynolds stress. The probe consists of three nominally orthogonal 5 micron diameter, 1.25 mm long, platinum-plated tungsten wires which all lie within a 3 mm sphere. The approximate angles and orientation of the wires are shown in Figure 2.7. The exact orientation of the wires was determined through calibration. The outputs of the three wires were connected to custom-built NASA/FML Hot-Wire bridges.

The probe was roughly aligned with the mean flow vector (within 0.2^o of flow angle interpolated from the seven-hole measurements) at each data point location and small samples of measurements were taken (around 500 samples). These samples were processed on-line and the probe was re-aligned to a new approximation to the mean flow velocity vector. This process was repeated until the probe was aligned to within 1^o of the latest approximation to the mean velocity vector. For measurement surveys near the surface of the wing, the geometry of the probe apparatus made alignment with the flow for some points impossible without crashing the apparatus into the wing. Custom software was written to align the probe with the flow as closely as possible, without crashing the probe apparatus (software available upon request from author). When the probe was determined to be aligned, a full

sample buffer of data was taken. The number of eddies of wavelength of the order of δ which are measured per unit time in an Eulerian sense can be estimated by U_∞/δ. For a freestream velocity of 170 feet/sec, and $\delta \sim 0.5$ inch, roughly 4000 eddies pass by the probe per second. At each data point a total of 10000 samples was obtained at a sampling frequency of 500 Hz. This corresponded to a sample spacing of about 8 δ/U_∞ so the samples should be independent. This data was downloaded to another computer to allow for near-real time processing of the data while still having the raw data stored for further post-processing analysis.

Crossflow planes were measured at axial stations identical to those measured by the seven-hole pressure probe. The stretched 20 x 20 grid focused mainly on the immediate region around the vortex, and hence was much smaller in size than planes measured with the seven-hole probe. The 8 $\times$ 8 inch square planes were centered at the nominal core center. The core center was determined by performing a preliminary survey of an area suspected of containing the center and interpolating to find the point of minimum crossflow velocity.

The possibility of meandering of the vortex was investigated by using a pair of single-wire probes placed on opposite sides of the vortex core ($0.07c$ from the center at $x/c = 0.678$), and evaluating measurements between the two. The wires were aligned so that they were primarily sensitive to velocity fluctuations in the y and z direction. Previous researchers have found the tip vortex to meander periodically in a spanwise direction with fc/U_∞ on the order of 0.01 (McAlister & Takahashi[16]). Measurements of the velocity correlation $\overline{u_1' u_2'}$ between the two single wires, positioned on opposite sides of the vortex core, were compared with the correlation computed from an analytical model (to be described in next chapter). The correlation of $\overline{u_1' u_2'}$ was measured by taking a total of 50000 samples at a sampling frequency of 2000 Hz, and a Krohn-Hite Model 3343 Filter was used to low-pass filter the data at a filter frequency setting of 50 Hz.

2.2.6.1 Triple Hot-Wire Apparatus

The complicated geometry of the various rotating and translating axes generally

required simultaneous movement of 5 of the degrees of freedom to keep the sensing portion of the triple-wires at the location of the data point. The triple-wire probe holder also enabled the probe to be rolled manually to within 1^o if needed (an initial guess in the wire orientations was needed during the calibration).

During the investigation it was discovered that the temperature field in the vortex viscous region was spatially varying by up to 2°F/inch. Accurate spatial resolution of the temperature measurements was necessary because the triple-wire data was temperature corrected. A Omega Model TFD temperature sensor was flush-mounted on the body of the probe surface, approximately 1.25 inches downstream of the center of the triple-wire sensors. With the probe aligned to 0^o pitch and 0^o yaw, the only temperature gradient that would give the sensor a different point-measurement from that of the 3 hot-wires would be the axial gradient. The axial gradient was deemed to be negligible and the crossflow gradients were deemed to be important only in the viscous region of the vortex. Hence, for measurement points within 1 inch of the core centerline (the approximate radius of the core viscous region), the probe was initially aligned to 0^o pitch and 0^o yaw, and the temperature was measured before the triple-wire probe aligning process was begun.

2.2.6.2 Triple Hot-Wire Calibration

Calibration was done following an adapted version of the method by LeBoeuf (1990). This method does not assume orthogonality of the wire sensors and avoids measuring the orientation of individual wires by visual procedures. The method is also simplified in that the procedure can be performed simultaneously for all three wires rather than doing a separate normal wire calibration for each wire.

Calibration was completed in two phases; holding constant angle while varying velocity, and holding constant velocity while varying angle. A temperature correction scheme based upon Nusselt-Reynolds number dependence was used. The constant-angle calibration was performed for all three wires simultaneously by aligning the probe apparatus axis with the freestream velocity. Hence the wires were each skewed by approximately 54.7 degrees from the freestream. Angle sensitivity

was modeled by a modified version of Jorgenson's (1974) equations:

$$\left(\frac{U_{eff,i}}{U_{mag}}\right)^2 = 1 + (k_i^2 - 1)\cos^2\gamma_i \tag{2.2.2}$$

where i is the wire index, k is the yaw factor, γ is the angle between wire i and the instantaneous velocity (γ to be solved for later) and $U_{eff,i}$ is the effective normal velocity of wire i. The modified equations assume velocity-independent yaw sensitivity (k_i) and negligible pitch sensitivity for $U_\infty > 5$ meters per second (as in this experiment). In general, the velocity, temperature, and voltage for each wire were made to fit the Nusselt-Reynolds number polynomial:

$$Re_{d,i}^n = \sum_{m=0}^{4} A_{m,i} Nu_{d,i}^{m/2} \tag{2.2.2}$$

where $Re_{d,i}$ is the ambient temperature evaluated Reynolds number based upon the wire diameter, $Nu_{d,i}$ is the Nusselt number based upon wire diameter and evaluated at the film temperature (average of ambient and wire operating temperature), and $A_{l,i}$ represent the calibration coefficients. Given R and R_o (the wire operating resistance and the cold wire resistance respectively), the definition of the overheat ratio, $OHR \equiv \frac{R-R_o}{R}$, and a first (linear) approximation to the dependence of wire resistance with absolute temperature, it can be shown that Equation 2.2.2 can be rewritten as:

$$(U'_{eff,i})^n = \sum_{m=0}^{4} A'_{m,i} (E'_i)^m \tag{2.2.3}$$

with the constants $A'_{m,i}$ containing the wire dimensions and:

$$U'_{eff,i} = \frac{U_eff}{\nu} \tag{2.2.4}$$

$$E'_i = \frac{E_i}{\left[k(\frac{OHR}{\alpha} + T_0 - T)\right]^{1/2}} \tag{2.2.5}$$

where ν is the kinematic viscosity at the ambient temperature, k is the thermal conductivity of the wire at the film temperature, α is the temperature coefficient of resistivity of the wire, E_i is the voltage of wire i, T is the ambient air temperature, and T_0 is the cold wire temperature. Since the wires were calibrated skew to the freestream, the actual constant angle fit was:

$$(\tilde{U}'_{eff,i})^n = \sum_{m=0}^{4} \tilde{A}'_{m,i}(E'_i)^m \tag{2.2.6}$$

where $\tilde{U}_{eff,i}$ represents the velocity magnitude at the angle which the freestream makes with the wire (say $\tilde{\gamma}$ during the constant-angle calibration) which would give the same voltage reading as the true velocity, and the constants $\tilde{A}'_{m,i}$ include the effect of the initial skew angle.

The varying-angle portion of the calibration fit 113 combinations of pitch and yaw angles over a cone half-angle range of 0^o to 30^o (using 5^o increments of pitch and yaw) to the following equation:

$$\left(\frac{\tilde{U}_{eff,i}}{U}\right)^2 = \frac{1+(k_i^2-1)\cos^2\gamma_i}{1+(k_i^2-1)\cos^2\tilde{\gamma}_i} \tag{2.2.7}$$

The non-linear least squares fit of these combinations was done using the IMSL (International Mathematics and Statistics Library) subroutine UNLSJ. For each wire, 5 constant angle coefficients, a yaw coefficient, and 3 wire direction cosines were solved for in the calibration.

One difficulty that was encountered during calibrating the wires was that the maximum speed of the wind tunnel was not high enough to cover the entire range of velocities encountered in our flow (axial velocities reached as high as 300 feet per second in the core). This difficulty was remedied by taking a calibration point in the core of the vortex and then applying King's law to the high speed portion of the constant angle calibration.

Although the triple-wires were temperature corrected, room temperature could change over a day by as much as 15^o F. To remedy any sort of calibration drift, the probe was directed to check a known calibration point after every ten data points.

If the calibration drifted by over 1%, the constant-angle calibration process was repeated and the five constant angle coefficients were re-calculated, before returning to the data measurement process.

Decoding the data involved solving for u_j, for every sample taken, the three simultaneous non-linear modelled equations:

$$(k_i^2 - 1)(\sum_{j=1}^{3} u_j \cos\beta_{i,j})^2 + \sum_{j=1}^{3} u_j^2 - U_{eff,i}^2 = 0 \qquad (2.2.8)$$

where the yaw coefficients k_i, and wire direction cosines $\beta_{i,j}$, were found previously by calibration and $U_{eff,i}$, were determined from a algebraic combination of the wire voltage, ambient temperature, and the calibration coefficients.

2.2.6.3 Triple Hot-Wire Uncertainty and Error Analysis

There were several sources of error in the triple-wire measurements. Curve fit error and calibration drift error (usually temperature related), were minimized through the use of a fourth-order polynomial fit and through constant checking for re-calibration of the probe (every ten traverse points). A typical fit of the constant angle calibration data had a standard deviation of 0.1%. The velocity range of the fit was from 40 to 170 feet per second and errors due to extrapolation of the fit at higher velocities would be larger. A sample fit of typical varying-angle calibration data with RMS error of 0.96% and maximum error of 2.08% is shown in Figure 2.8.

Measurement errors due to mean velocity gradients were corrected using the method described in Appendix A. Pompeo (1992) compared measurements of crossed, triple, and quadruple wires on two-dimensional and three-dimensional boundary layers and found that errors due to instantaneous velocity gradients could be substantial for any multi-sensor probe. Triple wires were found to have errors of up to 20% of maximum levels in measuring $\overline{v'^2}$, and $\overline{w'^2}$, 30% in measuring $\overline{v'w'}$, and up to 10% in the other Reynolds stresses. However, Pompeo did not attempt to align the probe with the mean flow velocity vector.

Paulsen (1982) showed that alignment of the triple-wire probe with the mean

flow velocity vector can greatly influence the accuracy of mean and turbulence measurements. Misalignment of the probe axis to the mean flow vector of 15^o was found to result in mean errors of up to 10% of maximum levels and Reynolds stress errors of up to 30%.

Muller (1992) compared cross-wire and triple-wire measurements on a relaxing flat plate boundary layer. Measurements of $\overline{u'v'}$ by the two methods agreed within 5% and the triple correlation $\overline{u'^3}$ was within 10%.

Gieseke and Guezennec (1993) compared cross-wire and triple-wire measurements on a turbulent flat plate boundary layer. In comparisons to data by Klebanoff (1954), errors were found of up to 5% maximum levels in $\overline{u'^2}$ and $\overline{v'^2}$, up to 10% in $\overline{w'^2}$, and up to 15% in $\overline{u'v'}$. Negligible levels of $\overline{u'w'}$ and $\overline{v'w'}$ were measured which was expected for a two-dimensional boundary layer.

As a result of the previous comparisons, it is estimated that the mean velocities are determined within 2.0% of freestream and 1.0^o of the true velocity vector. The following are the estimated errors of the turbulence measurements: $\overline{u'^2}$ and $\overline{v'^2}$ within 5%, $\overline{w'^2}$ within 10%, shear stresses $\overline{u'v'}$, $\overline{u'w'}$, and $\overline{v'w'}$ within 15%, 15%, and 30% respectively.

2.3 OFFLINE DATA PROCESSING

Near-real time processing of the data was available by transferring sampled data over the Ethernet to another computer for immediate processing. The raw data files containing the A/D counts and the hot-wire calibration data were saved on disk and available for re-processing at a later date.

Offline data processing was done using a MicroVax II with roughly 4 times the processing power of the MicroVax computer used for instrument control. Color and grey-scale contour display of the various scalar quantities were displayed on a Silicon Graphics Iris Workstation using the NASA/Ames developed FAST software (Walatka, et al., 1992). Subsequent editing of saved images was done using PIXEDIT.

2.3.1 Triple Hot-Wire Data Reduction Software

Offline processing of the raw triple-wire data was done using the FORTRAN program written by the author, RETAK3W. The offline processing capability allowed for calculation of all the mean and turbulence velocity statistics (including triple products) and allowed for the user option of including gradient correction (see Appendix A). All raw data files and the source code of RETAK3W are available on IBM floppy disk upon request sent to the author.

2.3.2 Computation of Derived Quantities

Several quantities had to be found by calculation from the triple-wire data. In particular, the vorticity, and all the quantities involved in the transport equation balances, required spatial derivatives of the various basic mean and turbulent quantities.

A script file was written for the NASA/Ames developed FAST software, which calculated the various spatial derivatives and scalar products of the entire data flowfield, and totaled the contributions of the various rate mechanisms. Metric formulation of the grid was necessary because the data grids were not necessarily evenly spaced or rectangular (e.g. data planes over the surface of the wing). A second-order differencing scheme was used on metric derivatives. A central difference was used on scalar quantity derivatives on the interior data points. Forward and backward differences were used on points on the edges of the dataset.

The circulation of the tip-vortex system was found by numerically calculating the line integral of the velocity along a path following the edges of the seven-hole data planes. This plane extended near enough to the root wall to encompass most of the vorticity shed from the wing wake and far enough to the opposite tunnel wall to completely encompass the viscous region shed from the tip portion of the wing.

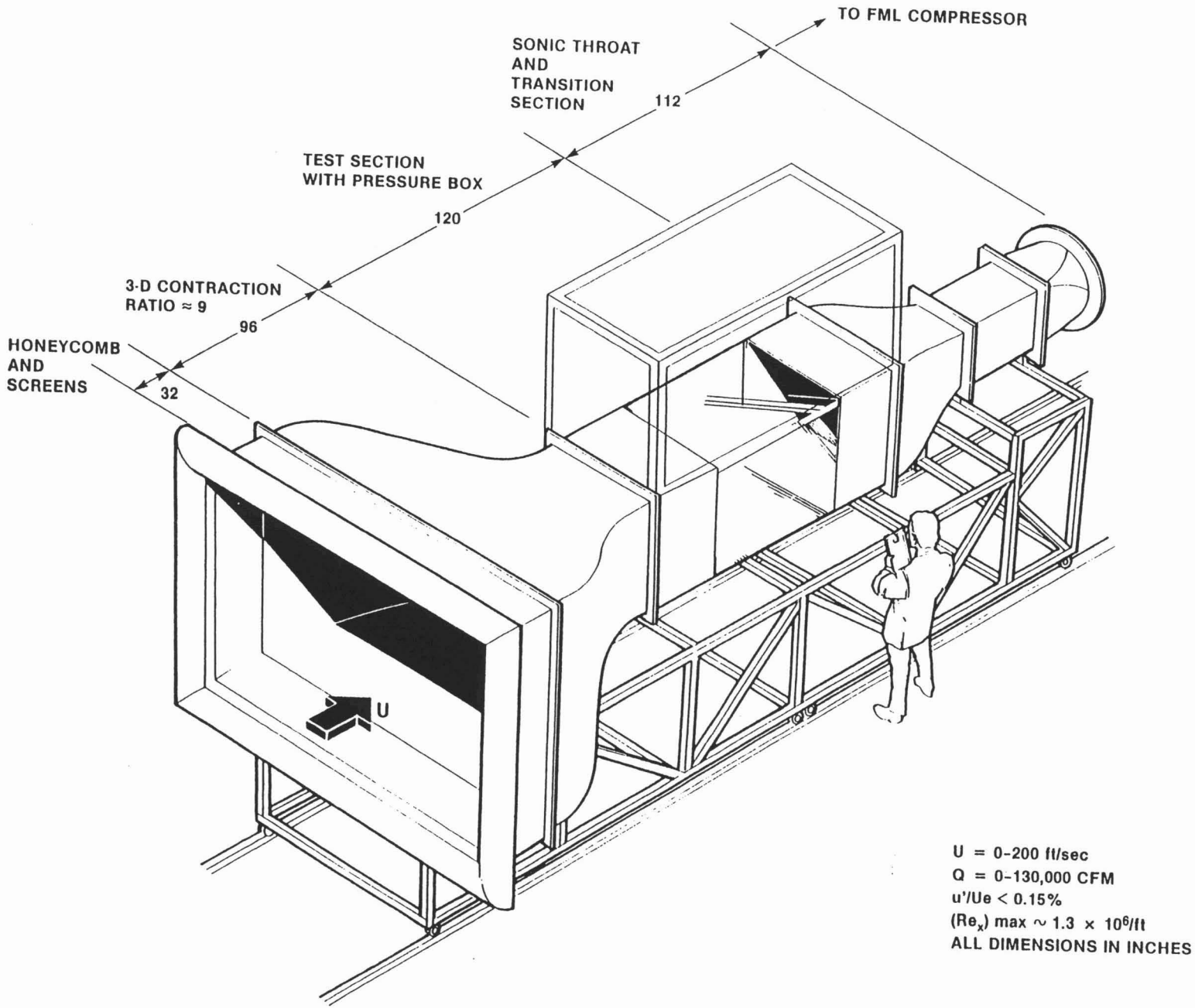

Figure 2.1 $32'' \times 48''$ **Wind Tunnel Facility**

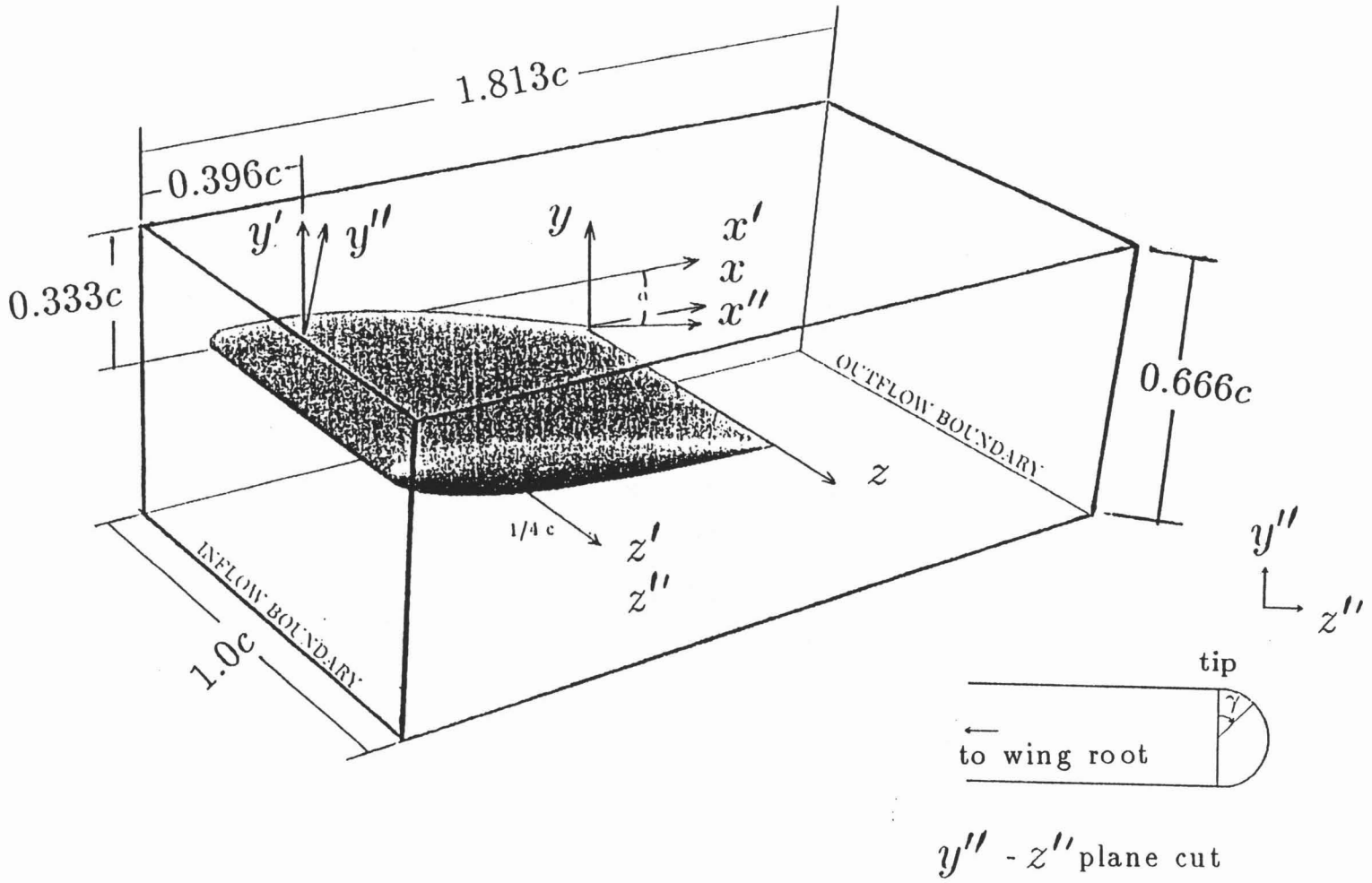

Figure 2.2 Wing Model and Coordinate Systems

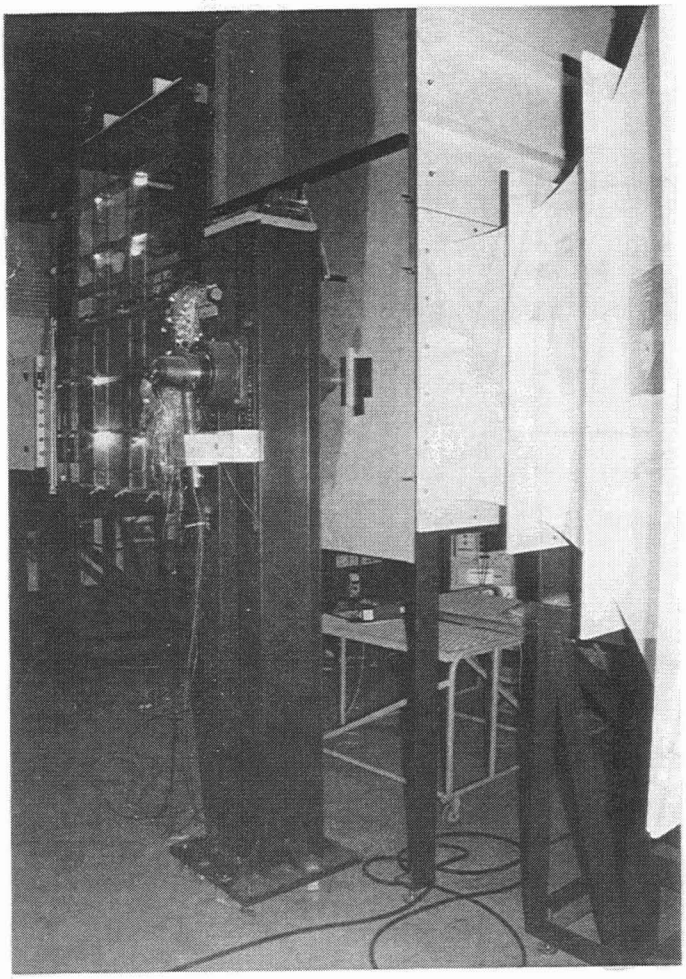

Figure 2.3 Wing Model Support Stand

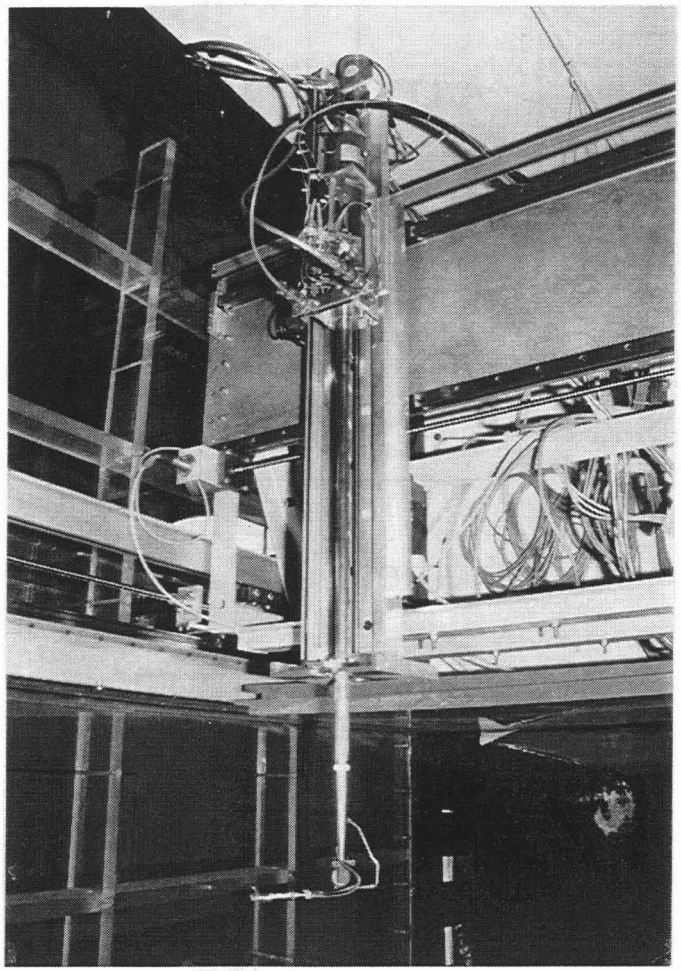

Figure 2.4 Traversing Gear

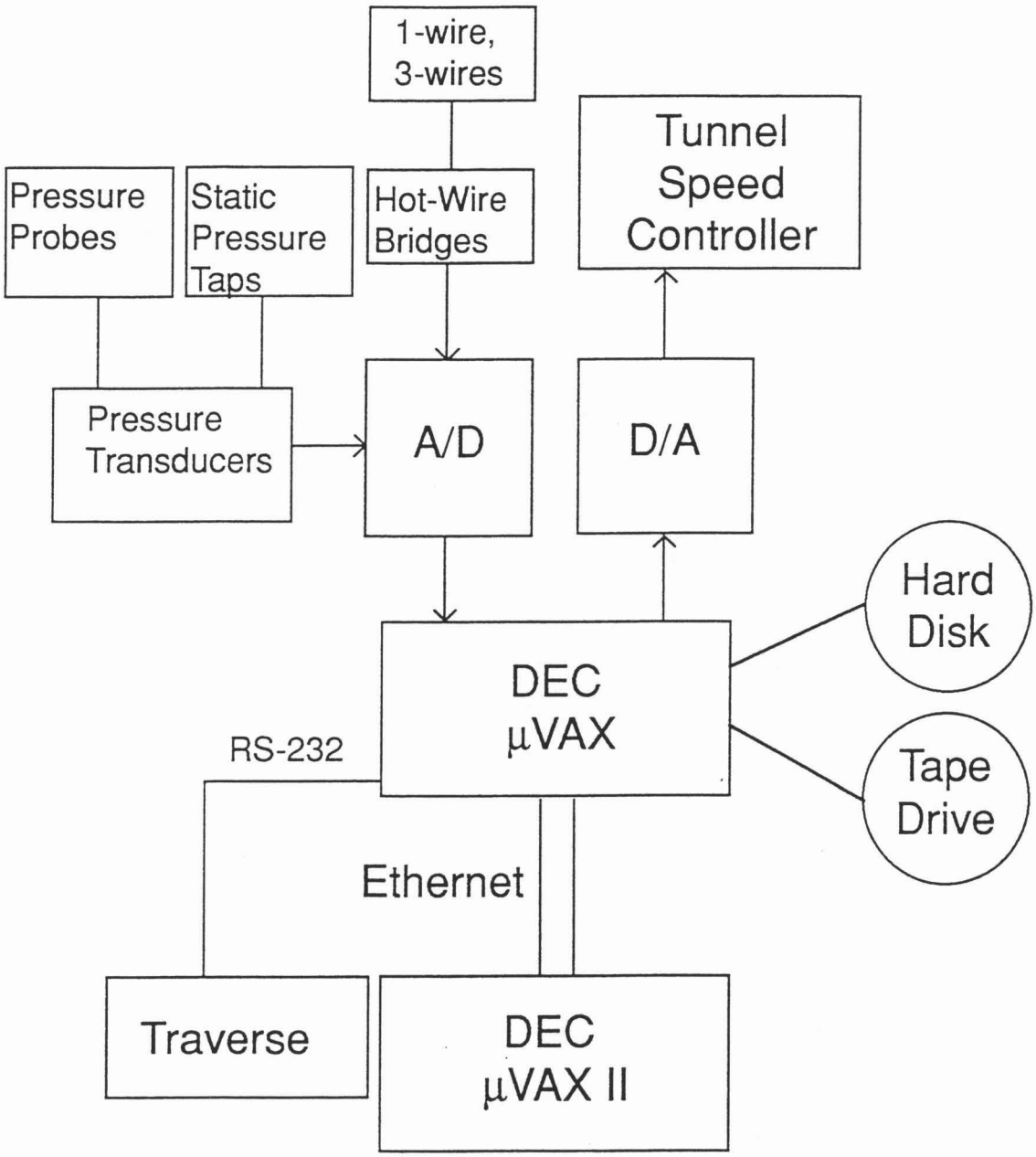

Figure 2.5 Equipment Schematic

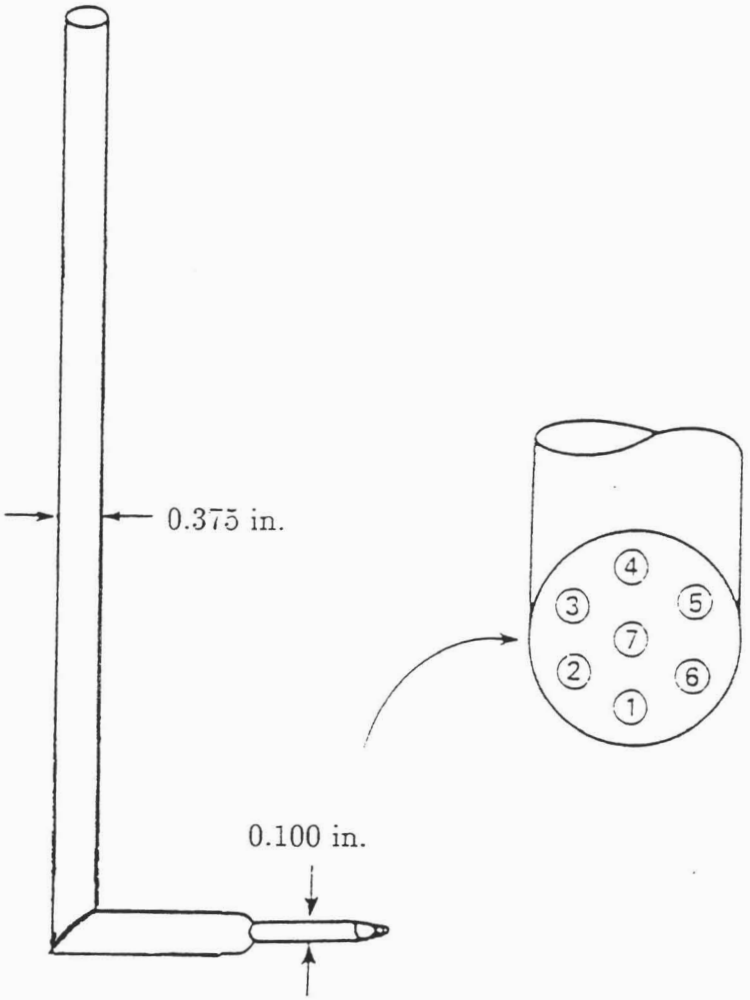

Figure 2.6 Seven-Hole Probe

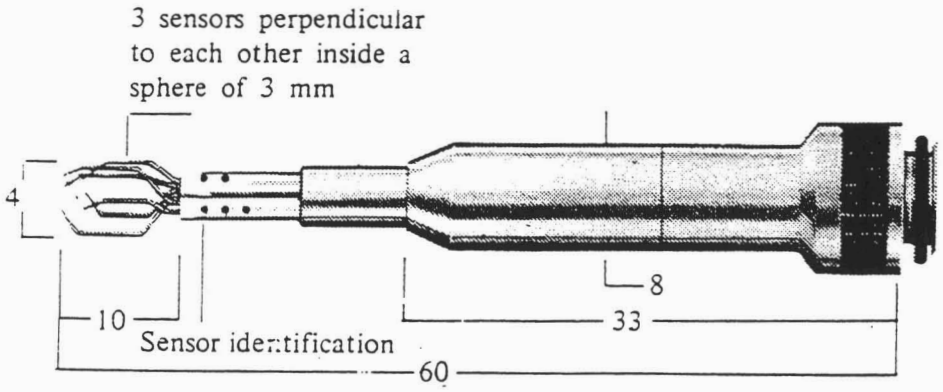

All dimensions in mm.

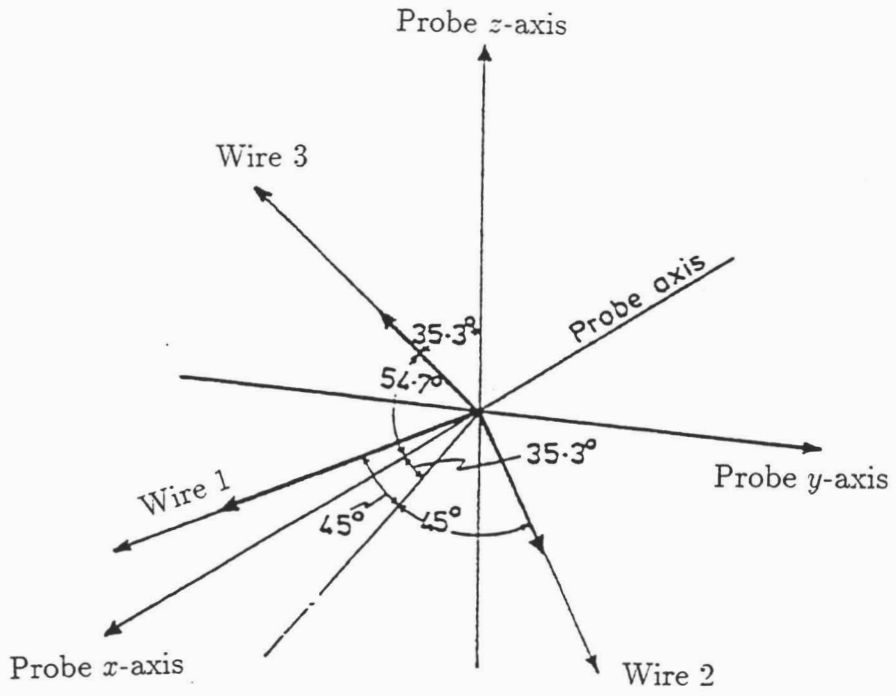

Relative angular positions of wires.

Figure 2.7 Triple-Wire Probe Apparatus

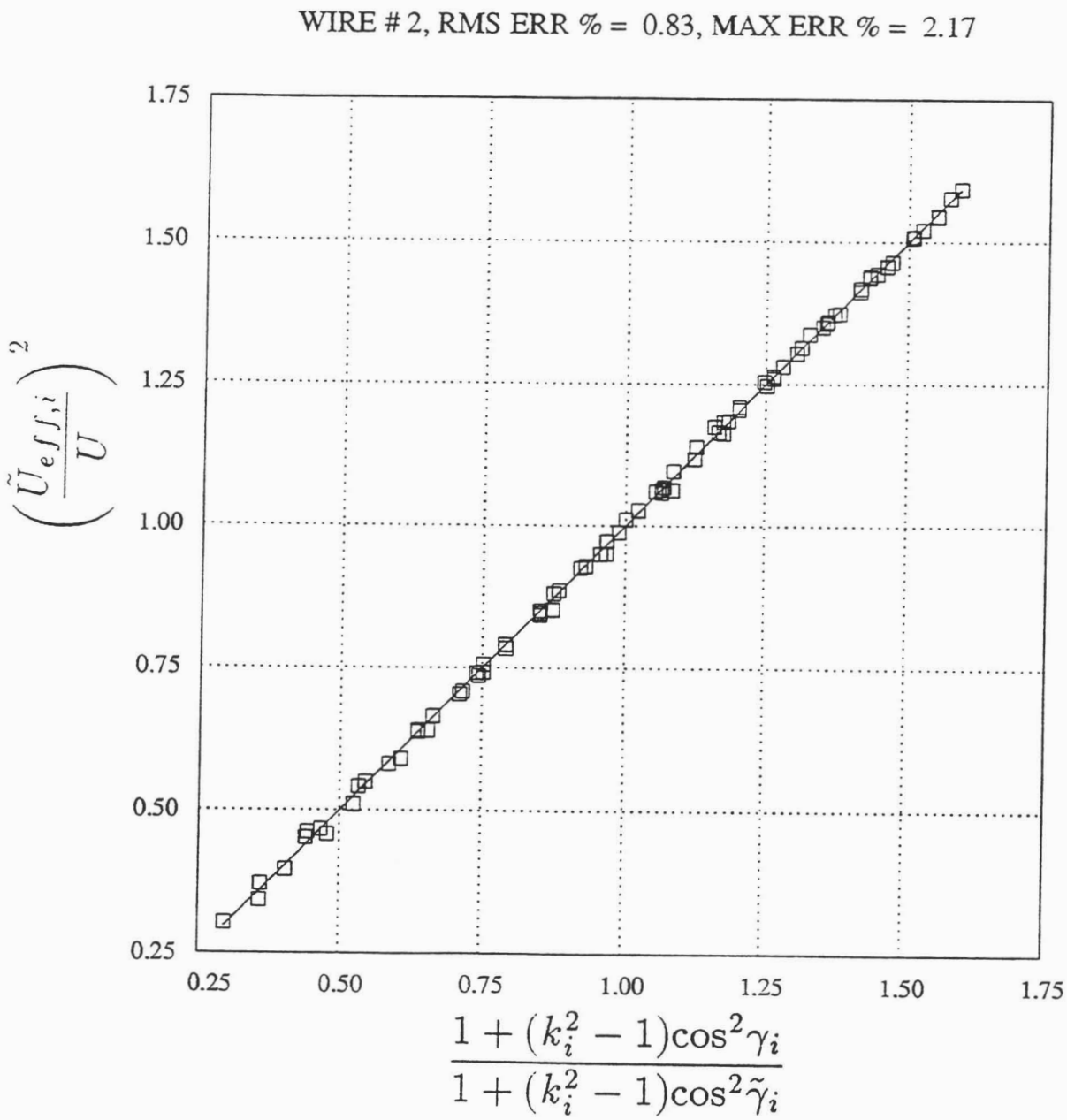

Figure 2.8 Typical Triple-Wire Angle Calibration

3. EXPERIMENTAL RESULTS AND PRELIMINARY DISCUSSION

The following chapter presents the results of the present investigation in chronological order. Flow visualization tests were completed initially to get a qualitative feel for the nature of the flow. The surface pressure and seven-hole measurements are presented next, followed by the turbulence and correlation data as measured by hot-wire anemometry.

The location and size of the data planes for the seven-hole and triple-wire measurements are shown in Tables 3.2-3.3. This chapter presents line and contour plots of the resultant data. The free stream velocity, U_∞, and the wing chord length, c, are used to normalize the data where it is most useful.

3.1 FLOW VISUALIZATION RESULTS

3.1.1 Laser-Illuminated Smoke Flow

Streamwise development of the tip vortex is shown by sheets of laser-illuminated smoke flow photos in Figure 3.1. Each frame visualizes the crossflow plane perpendicular to the x axis. Still photographs of crossflow planes were taken at the following locations: $x/c = -0.39, -0.26, -0.14, -0.01, 0.12, 0.25, 0.37, 0.50$. The spanwise location of the vortex core is nearly constant at $z/b_o = 0.97$. The perpendicular distance to the core from the wing surface increases with chord. At $x/c = -0.39$, the vortex core is located about 0.4 inches above the wing surface, while near the trailing edge ($x/c = -0.01$), the vortex core "sits" approximately 1.5 inches above the wing surface. The first signs of the tip vortex can be seen in the first photo at $x/c = -0.39$. The radial growth in the size of the vortex with axial location is apparent. A small kink in a smoke filament can be seen in the wake photos taken at $x/c = 0.37$ and $x/c = 0.50$. This feature corresponds to what has been observed and described by various authors as a "vortex kink". Green (1991) attributed this effect to the vortex-soliton of Hasimoto (see Hopfinger 1982) theory while Thompson (1983) hypothesized that the "kink" was caused by the merging of

the primary and secondary vortices. The seven-hole probe measurements described later seem to confirm the latter hypothesis.

3.1.2 Naphthalene Sublimation

Photos of naphthalene sublimation on the suction side and pressure side at the experimental test conditions of $V_\infty = 170$ feet per second and 10^o angle of attack were used to determine the placement location of the roughness trip and the photos are shown in Figure 3.2a,b. Natural transition (regions of laminar flow can be seen as lighter shades of grey) occurs near the leading edge (a surface distance of 2.0 inches) on the suction side, while it occurs at roughly half chord on the pressure side of the wing. Transition wedges can be seen on both suction and pressure sides. The suction side transition line was used as the chordwise placement location of the spanwise running roughness elements. Ideally, it would have been preferred to place the elements at different locations on the pressure and suction sides of the wing (at half chord on the pressure side and at the leading edge for the suction side), but since negative angles of attack were used for bottom surface measurements, the compromise location was chosen. Microphone listening tests confirmed that the wing boundary layers were laminar before and turbulent after the trip. The microphone was traversed around suspected re-laminarization areas on the wing but no evidence of re-laminarization was found.

3.1.3 Surface Oil Flow

Surface oil flow results on the pressure side of the model (Figure 3.3a, freestream from top to bottom) show the highly three-dimensional nature of the flow near the tip region. Some "sag" to the oil in the tip region of the trailing edge occurred because of the "tunnel-off" condition at the time of the photographs. In the tip region, the effect of the spanwise pressure gradient causes the skin friction lines to become skewed outboard. Figure 3.3b shows the tip region skin-friction patterns (freestream velocity flows from left to right). Again, the general action of flow

wrapping around the tip from the pressure side to the suction side is evident. The dominant feature, in Figure 3.3b, is a line where other skin-friction lines converge, starting at about 55% chord. The properties of this "convergence line" are hard to quantify. Unlike classical two-dimensional separation, the skin friction magnitude is non-zero along this line (owing to the presence of a streamwise component). In the literature (Tobak and Peake, 1982), this line is often described as indicative of "local separation" or "open separation". The salient characteristic of this type of separation is that there are no singular points in the skin-friction line topology. Additionally, there is no zone of stagnant fluid or reversed x-wise flow which typically occurs in flows which are "globally separated" (for more detail, see Zilliac 1989). The convergence line is indicative of the departure of the shear layer from the surface. This lifting off of vorticity occurs due to the adverse pressure gradient encountered by the crossflow velocities which wrap the flow around the tip. Figure 3.3c shows the suction side skin-friction patterns. The effect of the tip vortex is apparent near the trailing edge of the tip region. Directly beneath the tip vortex, the skin friction lines get swept outboard. Additional converging skin friction lines (two of them) can be seen adjacent to the main line of converging skin friction mentioned previously. These correspond to secondary and tertiary vortices formed by local separation of the crossflow induced by the primary and secondary vortices respectively. Away from the tip, the skin-friction lines are quite two-dimensional, until the root of the wing is reached, where the influence of a wing root horseshoe vortex causes the lines to move outboard slightly.

3.2 MEAN FLOW MEASUREMENTS

3.2.1 Surface Pressure

The flow phenomena described in the oil-flow results are also evident in the surface pressure measurements (Figure 3.4a,b). Here, surface pressure coefficient contours ($C_p \equiv (P - P_\infty)\ /\ .5\ \rho U_\infty^2$) are plotted on the suction and pressure sides

of the wing. The pressure side wing surface contours show the stagnation line, which is nearly straight across most of the wing, at an average arc distance from the leading edge of $s = +0.01c$. Away from the tip of the wing, the flow approaches two-dimensional behavior, and the pressure gradient in the x-direction is favorable for 60% of the chord, only to become slightly adverse for the remaining part of the wing. Near the tip of the wing, the flow and the pressure gradients become highly three-dimensional. The spanwise pressure gradients induce large cross flow velocities around the tip. The large aqua-colored region on the lower rear part of the tip in Figure 3.4b, corresponds to very high velocity air whipping around the tip, only to encounter an adverse pressure gradient after circumventing about half way around the tip. This region corresponds to the main converging-skin-friction line seen in the oil flow photo. In a two-dimensional sense, the flow in this region is similar to crossflow past a circular cylinder, where the shear layer detaches shortly after the onset of an adverse pressure gradient.

The pressure-coefficient contours on the suction side of the wing are fairly two-dimensional on the inboard third of the wing. The leading edge suction peak is evident, and the minimum surface pressure coefficient found here was -2.64. Nearer the tip, in the pre-tip-vortex developing portion of the flow, the surface pressures taper off to gradually equalize themselves with the pressures on the pressure side of the wing. The suction peak, due to the main tip vortex, is also evident in the inset to Figure 3.4b, and a minimum C_p of -1.30 was found in this region. The footprint of the main tip vortex lies at approximately $z/b_o = 0.97$, (assuming the core of the vortex lies directly above the surface of minimum pressure coefficient), and the crossflow pressure gradient becomes adverse as one traverses outboard of this core footprint. This adverse-crossflow-pressure gradient occurs slightly inboard of the secondary converging-skin-friction line shown in Figure 3.3c. It is believed that the vorticity sheet lifting off from this secondary converging-skin-friction line forms a secondary vortex of the opposite sense to the primary vortex. This belief is corroborated by 7-hole pressure probe data shown later. The surface pressure data could not confirm the existence of a suction peak due to this secondary vortex or a

tertiary vortex because of resolution limitations.

The surface pressure distribution was numerically integrated to find the lift of the wing. A total lift coefficient of $C_L = 0.51$ was measured which was consistent with Prandtl's experimental results (1921) of $C_L = 0.55$ for a rectangular wing with aspect ratio of about 1.4. Considering the wind tunnel interference in the present experiment, the comparison of C_L with Prandtl's results should be viewed with caution. The inboard portion of the wing (where pressure taps are not present) was included in the computation by extrapolating the nearly two-dimensional behavior of the pressure distribution inboard.

The actual values of C_p used to map the countours in Figures 3.4a,b are tabulated in Table 3.1.

3.2.2 Mean Flow Measurements with 7-hole Pressure Probe

Perspective views of the various mean flow quantities as measured by 7-hole pressure probe (the wing model is also shown) are displayed in Figures 3.5(a-e). Data planes at $x/c = -0.591, -0.394, -0.197, -0.010, 0.125, 0.246, 0.452$, and 0.678 are shown.

Figures 3.6-3.10 display scalar quantities at various crossflow planes as measured by 7-hole pressure probe. Each figure set, 3.X(a-k) (consisting of 6380 data points), presents the data in order from the farthest upstream plane to the farthest downstream plane. The x-axis is oriented coming out of the page. It should be noted that each plot contains its own separate legend so that the maximum detail in each separate data plane can be observed, whereas Figures 3.5(a-e) are meant to show more general trends evident in the whole flow field. In addition, thin solid lines were used to help the reader contrast the contour gray-scale shading changes. In regions of slowly varying levels, the plotting package displayed the lines as thick solid lines (usually dark), which may cause confusion, and it should be emphasized that these solid lines are merely demarcation borders to aid the reader. Fortunately, because these solid lines appear in regions of slowly varying levels, it is generally obvious where this occurs.

Figure 3.11 presents various flow quantities as a function of x/c along the center of the vortex (location of minimum core crossflow velocity). Plotted are axial velocity, static pressure and total pressure coefficient, and position of the core centerline. Also plotted as a function of x/c are the maximum crossflow velocity found on the viscous/inviscid boundary of the vortex and the core radius of the vortex.

3.2.2.1 Crossflow Velocity

Figure 3.6(a-k) displays crossflow velocity magnitude normalized by freestream velocity at various crossflow planes as measured by 7-hole pressure probe. Crossflow velocity, U_{cf}, is defined as the resultant of the V and W components of the velocity vector. At $x/c = -0.591$ (roughly 40% chord), high crossflow velocity fluid circumventing the tip can be seen, but no tip vortex is evident yet. A maximum normalized crossflow velocity of 0.602 is shown in this initial data plane. The first indication of a tip vortex can be seen in the second data plane at $x/c = -0.394$. A simple comparison shows that the approximate location of the vortex centerline matches up with the suction peak on the surface of the wing. As the data planes progress down the chord of the wing, the region of high crossflow velocity increases (both in area and magnitude) as the tip vortex gains strength from the feeding sheet of boundary layer vorticity (this can be most easily seen in Figure 3.5a). The maximum crossflow velocity measured at $x/c = -0.394$ was 0.791 times the freestream velocity. This grew quickly to a level of 1.0 at $x/c = -0.296$ and then more slowly to a level of 1.072 at $x/c = 0.125$. The maximum crossflow velocity decayed slowly to a level of 0.963 at the farthest downstream wake plane at $x/c = 0.678$. The vortex core diameter was estimated by calculating the distance between the peak crossflow velocities on either sides of a vertical cut through the vortex centerline. This admittedly arbitrary definition succeeds in describing a consistent estimate of the growth of the vortex viscous region. The radius of the viscous core of the main tip vortex at $x/c = -0.197$ was found to be about 0.9 inches and it grew steadily to a size of 1.48 inches at $x/c = 0.005$. The growth of the core radius of the vortex

was negligible in the wake planes.

The plot of the vortex core position in Figure 3.11 shows the vortex centerline on separate y/c and z/c paths. The y/c path initially goes downwards, following the surface of the wing, until the wing trailing edge is reached, where the vortex centerline moves slightly upwards and then levels off. In the spanwise direction, the centerline generally follows an inboard path except at the $x/c = 0.125$ location. Here, the centerline moves outboard for a moment and then resumes its inboard path at the $x/c = 0.246$ location. This corresponds to the location in the laser-illuminated smoke flow-visualization where a similar "kink" was observed. Both Green & Acosta (1991) and Thompson (1983) have observed that this "kink" occurs slightly downstream of the trailing edge, as has occurred in this study. The secondary vortex lies outboard of the primary tip vortex and rotates with the opposite sense. The disappearance in the wake of any trace of the secondary vortex is presumably due to it being absorbed by the main tip vortex and this may explain the outboard movement of the "kink".

Small low velocity patches can be seen in between the feeding sheet and the main vortex, corresponding to the approximate location of the secondary line of converging skin friction. These patches of low-crossflow-velocity air are not readily observable in data planes taken in the wake ($x/c > 0$). Maximum crossflow velocity (on the order of the freestream velocity) is found on the nominal viscous/inviscid boundary of the vortex. A better demarcation of this boundary would be regions where $\Omega_x \approx 0$. The axial development of the maximum normalized crossflow velocity is plotted in Figure 3.11.

3.2.2.2 Static Pressure Coefficient

Equation 1.2.5 (Euler's n-equation) gives a rough explanation for the decrease in static pressure in the core of the vortex as it rolls up, and this in turn causes the core centerline axial velocity to increase. As the maximum crossflow velocity of the vortex increases with x/c, an axial pressure gradient also develops and accelerates the core fluid in the axial direction. Figures 3.8(a-k) illustrate the decrease in core

pressure with chord. The core centerline static pressure coefficient, $(P-P_\infty)/\frac{1}{2}\rho U_\infty^2$, drops from a value of -0.64 at $x/c = -0.394$ to a value of -3.43 at $x/c = -0.010$. In the wake, the core pressure actually still decreases very slightly, due to the wind tunnel pressure gradient. It might be expected that further downstream, the core pressure would increase due to the decay of the peak crossflow velocities.

The adverse pressure gradient encountered by the flow traveling around the tip from the suction side to the pressure side of the wing can also be seen in Figures 3.8(a-c). The location and magnitude of these results matches well with the surface oil flow and the surface pressure measurements.

3.2.2.3 Axial Velocity

Figure 3.7a-k shows the axial velocity normalized by the freestream velocity. The axial development of the vortex centerline axial velocity is plotted in Figure 3.11c. The axial velocity in the core of the vortex increases with x. A profile of the axial velocity across a cut through the vortex at $x/c = 0.125$ is plotted in Figure 3.12. At the $x/c = -0.394$ data plane, the normalized axial velocity of the core centerline point is equal to 0.823, a slight freestream deficit. A maximum axial velocity of 1.77 U_∞ was found at $x/c = 0.005$ (slightly downstream of the trailing edge). Chigier and Corsiglia (1972) noted a maximum axial velocity in the core right before the trailing edge of about 1.4 U_∞ (NACA 0015, $\alpha = 12.0^o$, $Re_c = 953{,}000$). Shortly after the trailing edge they observed an axial core velocity reduction to 1.1 U_∞. In the present study, the axial velocity maximum decreases very slowly in the wake to a value of 1.69 U_∞ at $x/c = 0.69$, a marked difference from the results of Chigier and Corsiglia.

In fact, the level of axial velocity excess measured on the core centerline in the present experiment has not been observed previously. Certainly several factors influence the development of this velocity excess, including tip shape, angle of attack, wing section, and Reynolds number. The present experiment was performed at a relatively high angle of attack, at high Reynolds number, and with a tip shape with forgiving separation characteristics. As was discussed previously, a rounded

tip shape has a single primary separation line which detaches from wingtip due to the adverse crossflow pressure gradient. By contrast, a square tip shape would have two primary separation lines; one for each sharp corner. It might be deduced that these two separation lines would serve to decrease the tangential velocity induced by the rollup. Past experiments have not approached the high Reynolds number ($Re_c = 4.6$ million) of the present study. More importantly, because the model was large, the vortex core in the present experiment was much larger than in previous experiments. The probe size relative to the core size was therefore smaller. This resulted in reduced probe gradient errors and in lessened likelihood of probe-induced vortex breakdown. Finally, the measurement of the data planes in the near wake allowed for minimization of the vortex meander problem which has contaminated the bulk of the previous experimental work. It is thought that near the trailing edge of the wing, the amplitude of the meander is reduced. Interestingly, the one study that nearly matched the velocity excess measured in the present study (mean levels of 1.6 times the freestream velocity as opposed to 1.77), was the non-intrusive study by Green (1991). That study was performed at a much lower Reynolds number (based upon chord) which would suggest that higher Reynolds number may have the effect of increasing the axial velocity excess. Looking at it in another way, a low chord Reynolds number may cause an axial velocity deficit on the core centerline. A low Reynolds number would mean that viscosity would play a larger role in the flow than inertial forces. Hence, the low momentum boundary layer fluid which is wrapped into the vortex would have a larger effect, possibly resulting in large enough decelerating forces to counteract the favorable pressure gradient forces and give an axial velocity deficit. A higher angle of attack would work in favor of the development of an axial velocity excess because the added pressure differences on the suction/pressure sides of the wing would increase the acceleration of the crossflow around the wingtip (provided no stalling of the wing occurred). A further analysis of the influence of various parameters on the core centerline axial velocity is left for the next chapter.

The growth of the boundary layer thickness (green-blue area in Figure 3.5b

nearly spanning the wing) with chord, and its development into the wake, are quite vivid. An interesting development is the apparent thinning of the boundary layer in between the main tip vortex and the nearly-two-dimensional section of the flow. As one progresses down the chord, the span of this boundary layer "dip" increases. The crossflow velocity in this region is dominated by v-velocity (a downward component towards the surface). It is believed that the tip vortex induces a flow such that the low momentum fluid in the boundary layer is "pushed aside" and replaced by higher momentum fluid, thus thinning the boundary layer.

3.2.2.4 Total Pressure Coefficient

The gradual loss of total pressure in regions of the flow where viscosity plays an important role can be seen in Figures 3.9(a-k). Total pressure coefficient, $C_{p,tot} \equiv (P_{total} - P_\infty)/\frac{1}{2}\rho U_\infty^2$, is shown in the figures. It can be seen that at $x/c = -0.394$, where the tip vortex is first evident, the core centerline axial velocity is a deficit, at 0.82 U_∞, and the static pressure is about 0.6 dynamic pressures below freestream static. Until the trailing edge plane is reached (data at $x/c = -0.005$ and 0.005 straddle the trailing edge), the general trend of Figure 3.11 shows that total and static pressure fall while the axial velocity increases as x/c increases. The axial velocity increases because the rate at which the static pressure falls is much faster than the total pressure fall. Downstream of the trailing edge, the axial velocity decays slowly and the static pressure levels off. The low absolute level of the total pressure coefficient ($C_{p,tot}$ is significantly less than one and decreasing) implies that the nature of the flow in the vortex core is highly viscous which is not surprising considering that much of the vortex core fluid originates from the separated boundary layers. The largest loss in total pressure occurs in the recirculating region in between the detached tip boundary layer and the main tip vortex ($C_{p,tot} = -0.413$ at $x/c = -0.197$). The highly viscous vortex core also shows a large loss of total pressure ($C_{P,tot} = -0.069$ at $x/c = -0.197$). The increase in the size of the vortex core can also be seen be comparing the area of the dark circular patches from plane to plane (since the white regions indicate approximately no loss of total pressure).

A definition of the vortex core boundaries based upon a criteria of percentage of the freestream dynamic pressure (say 90%) may be more appropriate than the conventional definition of the vortex (based upon maximum tangential velocities) in some instances, however the latter definition will be used in this study because of the popularity of this definition.

3.2.2.5 Axial Vorticity

The existence of secondary vortices, suggested by the surface oil flow and surface pressure measurements, was confirmed by the 7-hole pressure probe measurements and is most easily shown by looking at contours of axial vorticity. Displayed in Figures 3.10(a-k) are x-component of normalized vorticity (normalized by U_∞, resulting units are in^{-1}). As expected, negative levels of vorticity increase rapidly with chord in data planes measured over the wing. The centerline vorticity continues to increase, albeit at a much slower rate in the wake, implying that roll-up of the vortex has not been completed at the farthest wake data plane. A concentrated grid was measured at $x/c = -0.114$ to investigate the existence of secondary vortices and is displayed in Figure 3.13. The x-vorticity contours show an absolute maximum of -8.8 in the feeding sheet and a local maximum value of about -3.2 in the core of the main vortex. The resolution of the concentrated grid allows the core of the secondary vortex to be easily visible and the the value of the x-vorticity, in this core, was about 3.5. The absolute accuracy of these numbers can be questioned due to insufficient grid resolution, but the general trends of positive and negative values of vorticity (clockwise and counterclockwise vortices) are certainly adequately resolved. The superimposed velocity vectors confirm that the rotational sense of the secondary vortex is opposite that of the main tip vortex and they suggest the location of a tertiary vortex further outboard of the secondary vortex with the same sense as the main vortex.

The non-dimensional circulation of the vortex ($\Gamma' \equiv \Gamma \; / \; [U_\infty \times c]$) was found by taking the line integral of the velocity vector over a closed path, in a crossflow plane. The enclosed area formed by this path included 75% of the span, so that much of

the vorticity shed by the viscous wake of the wing is included in this calculation. The value was found to be $\Gamma' = 0.33$ at an $x/c = 0.005$.

3.2.3 Mean Flow Gradients

The mean velocity and pressure gradients were calculated by 2nd order differencing of the 7-hole and 3-wire mean data. These quantities play a role in analyzing the Navier-Stokes equations and the Reynolds stress transport equations. A sampling of the contours of 4 of the 9 mean velocity gradients, $\frac{\partial U}{\partial x}$, $\frac{\partial U}{\partial y}$, $\frac{\partial V}{\partial y}$, and $\frac{\partial V}{\partial z}$, is plotted in Figure 3.14a-d at $x/c = 0.125$. Most of the contours can be understood with a thought-experiment based on the mean velocity profiles that have been described in previous sections. 3 of the mean velocity gradients not plotted, $\frac{\partial U}{\partial z}$, $\frac{\partial W}{\partial y}$, and $\frac{\partial W}{\partial z}$, are roughly analogous to $\frac{\partial U}{\partial y}$, $\frac{\partial V}{\partial z}$, and $\frac{\partial V}{\partial y}$, respectively with the appropriate swapping of coordinate axes. The highest gradient levels were found in the $\frac{\partial V}{\partial z}$ and $\frac{\partial W}{\partial y}$ quantities. Contours of $\frac{\partial U}{\partial x}$ were initially confusing however. One might expect circular contours of $\frac{\partial U}{\partial x}$, with positive levels in planes over the wing and reduced negative levels in the the wake. Instead, the contours were double-lobed and of opposite sign. Apparently, the skewness of the path of the vortex centerline had a large effect on this quantity.

3.3 HOT-WIRE MEASUREMENTS

Crossflow planes of turbulence quantities as measured by triple-wire probe are shown in Figures 3.16-23. As in the figures displaying the 7-hole mean measurements, Figure 3.15a-f show with respect to the wing, a perspective view of various flow quantities as measured by the 3-wire probe. Data planes at x/c $= -0.394, -0.296, -0.197, -0.114, -0.010, 0.125, 0.246, 0.452$, and 0.678 are shown. All planes consisted of 400 data points measured on a stretched rectangular grid, centered upon the vortex centerline. The dimensions of these planes are described in Table 3.3.

Figures 3.16-21 display the individual crossflow planes for the RMS velocities,

$\hat{u}$, $\hat{v}$, $\hat{w}$, and the Reynolds shear stresses, $\overline{u'v'}$, $\overline{v'w'}$, and $\overline{u'w'}$ respectively.

3.3.1 Correlation Measurements

Assuming a periodic meander of the vortex in a spanwise direction (McAlister & Takahashi (1991)), measurement of the velocity correlation, $\overline{u_1' u_2'}$, of two single-wires positioned on opposite sides (spanwise) of the vortex core at positions 1 and 2, will be enhanced. The correlation is generated primarily because of the spanwise gradients ($\partial/\partial z$) of the v-velocity component which are found in a vortex flow-field. The experimentally measured value of $\overline{u_1' u_2'}$ was $-2.8x10^{-7}$. Mean velocity profiles, measured by 7-hole probe, were used to define the steady functions $u(z)$, $v(z)$, and $w(z)$. These steady functions were used in an analytical model which assumed a sinusoidal meander of the vortex in the lateral direction. The model was then used to assess the effects of meander. The z-location which the modeled single-wire "saw" was governed by the following equation:

$$z = z_0 + a\sin\omega t \tag{1}$$

where z_0 is the actual location of the single-wire probe, a is the amplitude of the sinusoidal meander, and ω is the frequency.

Assuming an oscillation with a period of 0.4 second ($fc/U_\infty = 0.01$), a meander amplitude of 0.005 inches, (i.e. about 0.00010 c), gave a correlation equal to the experimentally measured correlation. A rough estimate of the effect of meander was then made by assuming a periodic motion in the lateral direction with an amplitude of 0.005 inches. Given that the velocity gradient in the core of the vortex is approximately 1.0 U_∞ per inch, this level of meander could cause an apparent additional RMS velocity of 0.5% freestream. Using a similar analysis, the influence on apparent additional normalized Reynolds shear stress levels could reach levels on the order of 0.000025. These low levels were considered to be negligible.

3.3.2 RMS Velocities

The largest levels of $\hat{u}$, $\hat{v}$, and $\hat{w}$ RMS velocity normalized by the freestream

velocity were measured to be 0.224, 0.228, and 0.246 respectively. The character of the turbulence structure was markedly different in planes measured over the wing and planes measured in the wake. In planes measured over the wing, peak levels of turbulence were found where the shear layer departed from the wingtip surface. The levels of RMS velocity decrease as this highly turbulent fluid is wrapped into the forming tip vortex. Near the vortex, peak levels of turbulence were measured near the location of maximum tangential velocity. This behavior continued at x/c = 0.005 and x/c = 0.125. Farther into the wake however, the peak levels of RMS velocity were measured in the center of the vortex. The peak $\hat{u}$, $\hat{v}$, and $\hat{w}$, RMS velocity decreased to a level of 0.100, 0.146, and 0.117 respectively at the final x/c = 0.678 station. The stabilizing effects of the solid body rotation of the vortex seem to reduce the turbulence levels very rapidly. However, the peak levels measured at $x/c = 0.678$ indicate that, at least at less than one chord downstream of the trailing edge, the vortex core is still a highly turbulent region. Modelers ignoring this fact will surely predict the roll-up incorrectly.

Contours of $\hat{u}$ shown in Figure 3.16(a-k) are roughly circular in shape which might be expected for a vortical flow. However, contours of $\hat{v}$ and $\hat{w}$, shown in Figures 3.17(a-k) and 3.18(a-k), respectively are not circular. Instead, contours of $\hat{v}$ are roughly elliptical in shape, with the major axes running in the y-direction, while contours of $\hat{w}$ are roughly elliptical with major axes running in the z-direction. In cylindrical coordinates, this would represent levels of the fluctuating radial velocity, $\hat{v}_r$, to be greater than levels of the fluctuating tangential velocity, $\hat{v}_\theta$. To further illuminate this behavior Figures 3.22a-k and 3.23a-k show the RMS radial and tangential velocities. The origin for each plane was chosen to be the vortex centerline (a plot of the vortex centerline path is shown in Figure 3.11). A further analysis of the possible reasons for this behavior is left for the next chapter. It should be pointed out at this time, however, that this behavior can explain various other interesting features of the turbulence in the tip vortex flow, including the orientation of the $\overline{v'w'}$ component of the Reynolds stress.

The boundary layer, and especially the separated regions were so highly turbu-

lent that only the outer edges of the boundary layer fluid were measurable because the limit of the triple-wire angle calibration was reached.

3.3.3 Reynolds Shear Stresses

Large levels of all three Reynolds shear stresses were measured in the vortex, whereas in a time-evolving line vortex with no streamwise gradients, the only component of shear stress that would exist would be $\overline{v'w'}$. Perspective views of contours of $\overline{u'v'}, \overline{u'w'}$, and $\overline{v'w'}$ are plotted in Figure 3.15d-f respectively. Individual planes are plotted in Figures 3.19, 3.20, and 3.21 respectively. Overall peak absolute levels of $\overline{u'v'}$, $\overline{u'w'}$, and $\overline{v'w'}$ normalized by the square of the freestream velocity were found to be 0.0139, 0.0234, and 0.0125 at $x/c = 0.005$, -0.010, and -0.197 respectively. These peak levels decayed with x/c thereafter, with the farthest downstream plane at $x/c = 0.678$, showing peak absolute levels of 0.0029, 0.0004, and 0.0024 for $\overline{u'v'}$, $\overline{u'w'}$, and $\overline{v'w'}$ respectively.

Qualitatively, contours of the $\overline{v'w'}$ stress in the wake planes ($x/c > 0.0$) had a four-leaf clover pattern with alternately changing sign of the stress in between each adjacent pair of leaves. Each leaf was roughly aligned at $\pm$ 45 degrees off the y and z axes, with positive levels of stress found in the first and third quadrants ($+/+$ and $-/-$ values of z and y respectively) and negative levels of stress found in the second and fourth quadrants. In addition, in each leaf there seemed to be two radii at which peak levels of stress occurred. At $x/c = 0.452$, these two peaks occurred roughly at $r/r_1 = 0.33$ and 1.8. The four-leaf clover pattern of $\overline{v'w'}$ and the two-lobe pattern of the $\overline{u'v'}$ and $\overline{u'w'}$ stresses described later is expected for a cartesian coordinate system and this is explained by the kinematic relations described in Appendix C. It should be emphasized that the signs of $\overline{u'v'}$, $\overline{u'w'}$, and $\overline{v'w'}$ in the alternating lobes are entirely dependent upon choice of coordinate system. Therefore, the orientation of the coordinate system in the present study should be kept in mind during any discussion about signs of any of the shear stress quantities. The orientation of the alternatively positive and negative regions does have physical implications however and Appendix C shows how a $+/-$ 45 degrees

orientation of the $\overline{v'w'}$ stress implies that the $\overline{v_r'^2} > \overline{v_\theta'^2}$ and that $\overline{v_r'^2}, \overline{v_\theta'^2} \gg \overline{v_r'v_\theta'}$. In confirmation of these kinematics, the normal stress contours for $\hat{v}$ and $\hat{w}$ were found to be elliptical. In addition, Figure 4.2 displays contours of the Reynolds shear stresses and the negative of their corresponding mean strain rates at $x/c = 0.452$ (e.g. $\frac{\partial V}{\partial z} + \frac{\partial W}{\partial y}$ for the $\overline{v'w'}$ stress), which for isotropic eddy viscosity methods would align themselves in the same orientation. Noticeably, for each stress, the strain rate is aligned almost exactly opposite to what would be expected for an isotropic eddy viscosity. An explanation for the multi-lobed pattern of the stresses and the non-alignment of the stress and strain rate vectors will be given in the following chapter. The structure of the contours of $\overline{v'w'}$ was not so clear in the planes measured over the wing ($x/c < 0.0$). Though the beginnings of the four-leaf clover pattern can be seen, the influence of the stress created by the shear layers heavily distorts it. The fluid departing from the primary line of local separation measured negative levels of stress with a maximum absolute level of stress of -0.012 found at $x/c = -0.114$. Considering the mean strain rate of the boundary layer fluid in this region, the negative levels of stress might be expected. As this fluid is wrapped into the vortex and passes into the first quadrant, the stress changes sign to positive levels of $\overline{v'w'}$.

Contours of $\overline{u'v'}$ in the wake planes had two lobes of opposite sign stress, with the positive lobe rotated about 30 degrees off the z-axis. The peak levels of stress at a $x/c = 0.452$ occurred at a radii of about $r/r_1 = 0.33$ which corresponds with the first peak measured in the $\overline{v'w'}$ stress. In planes measured over the wing, the boundary layer fluid separating from the tip region had negative levels of $\overline{u'v'}$. Contours of $\overline{u'w'}$ in the wake planes had two lobes of opposite sign stress, with the positive lobe rotated about 20 degrees off the negative y-axis. Again peak levels of stress occurred at a radii of about $r/r_1 = 0.33$ for a $x/c = 0.452$ and the separating boundary layer fluid from the tip region had negative levels of $\overline{u'w'}$. Peak levels of all shear stresses at a $x/c = 0.125$ however were measured at a radius of roughly $r/r_1 = 0.67$, a clearly marked difference in behavior to the peaks measured farther downstream.

All the raw data used to create the contour plots of the mean and turbulent flow field have been tabulated and stored in ASCII format on a 3 1/2" floppy disk, formatted for a MS-DOS computer.

Table 3.1 7-hole Measurement Plane Dimensions

Streamwise Location (x/c)	Vertical Range (y/c)	Spanwise Range (z/c)	y/c of core	z/c of core	Grid Size
-1.135	-0.112 to 0.368	0.224 to 0.829	N/A	N/A	21×29
-0.591	0.105 to 0.368	0.224 to 0.829	N/A	N/A	21×29
-0.394	0.070 to 0.368	0.224 to 0.829	0.122	0.699	21×29
-0.296	0.053 to 0.368	0.224 to 0.829	0.103	0.688	21×29
-0.197	0.035 to 0.368	0.224 to 0.829	0.083	0.678	21×29
-0.114	0.020 to 0.368	0.224 to 0.829	0.067	0.675	21×29
-0.010	0.002 to 0.368	0.224 to 0.829	0.052	0.671	21×29
0.005	-0.112 to 0.368	0.224 to 0.829	0.051	0.670	21×29
0.125	-0.112 to 0.368	0.224 to 0.829	0.056	0.672	21×29
0.246	-0.112 to 0.368	0.224 to 0.829	0.064	0.666	21×29
0.452	-0.112 to 0.368	0.224 to 0.829	0.072	0.664	21×29
0.678	-0.112 to 0.368	0.224 to 0.829	0.074	0.660	21×29

Table 3.2 3-Wire Measurement Plane Dimensions

Streamwise Location (x/c)	Vertical Range (y/c)	Spanwise Range (z/c)	Grid Size
-0.394	0.074 to 0.206	0.616 to 0.783	20 × 20
-0.296	0.057 to 0.186	0.605 to 0.771	20 × 20
-0.197	0.039 to 0.166	0.598 to 0.765	20 × 20
-0.114	0.023 to 0.150	0.592 to 0.759	20 × 20
-0.010	0.006 to 0.134	0.587 to 0.754	20 × 20
0.005	-0.039 to 0.132	0.587 to 0.753	20 × 20
0.125	-0.029 to 0.138	0.588 to 0.755	20 × 20
0.246	-0.023 to 0.144	0.583 to 0.750	20 × 20
0.452	-0.013 to 0.154	0.585 to 0.752	20 × 20
0.678	-0.011 to 0.156	0.583 to 0.749	20 × 20

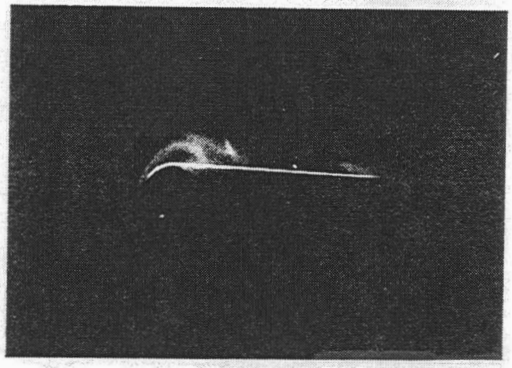

$x/c = -0.39$

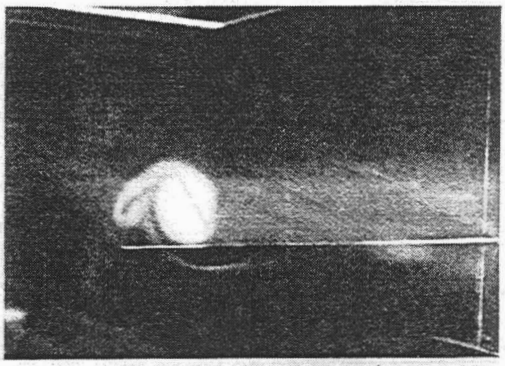

"kink" $x/c = 0.12$

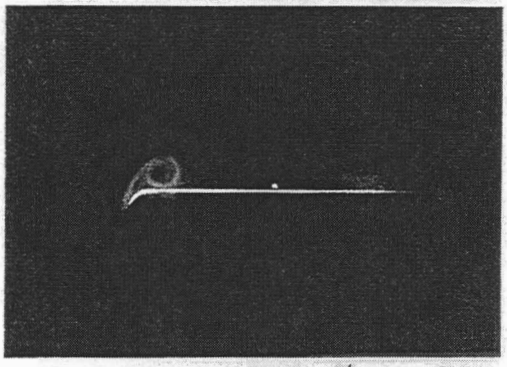

$x/c = -0.26$

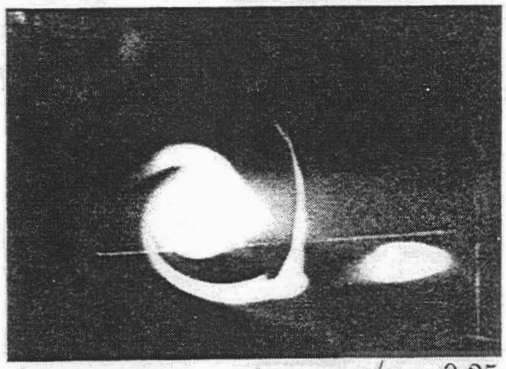

$x/c = 0.25$

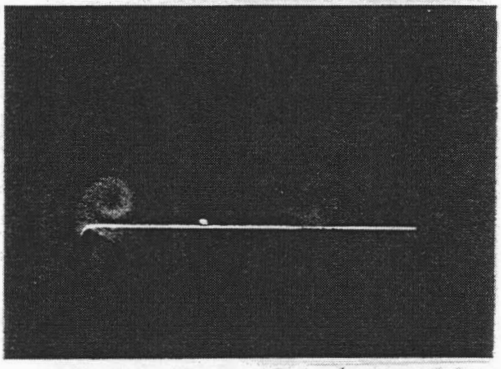

$x/c = -0.14$

$x/c = 0.37$

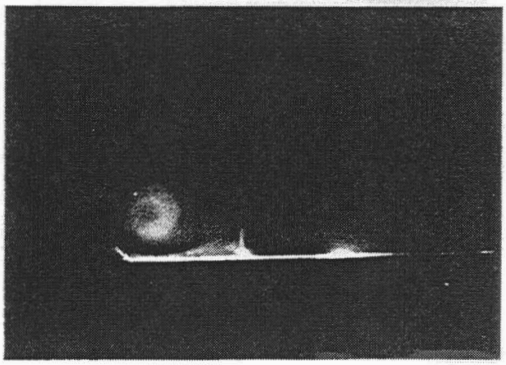

$x/c = -0.01$

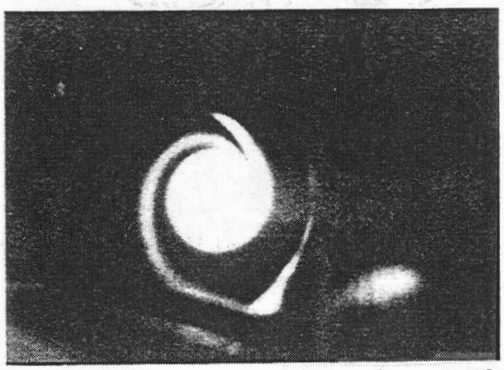

$x/c = 0.50$

Figure 3.1 Laser-Illuminated Smoke Flow

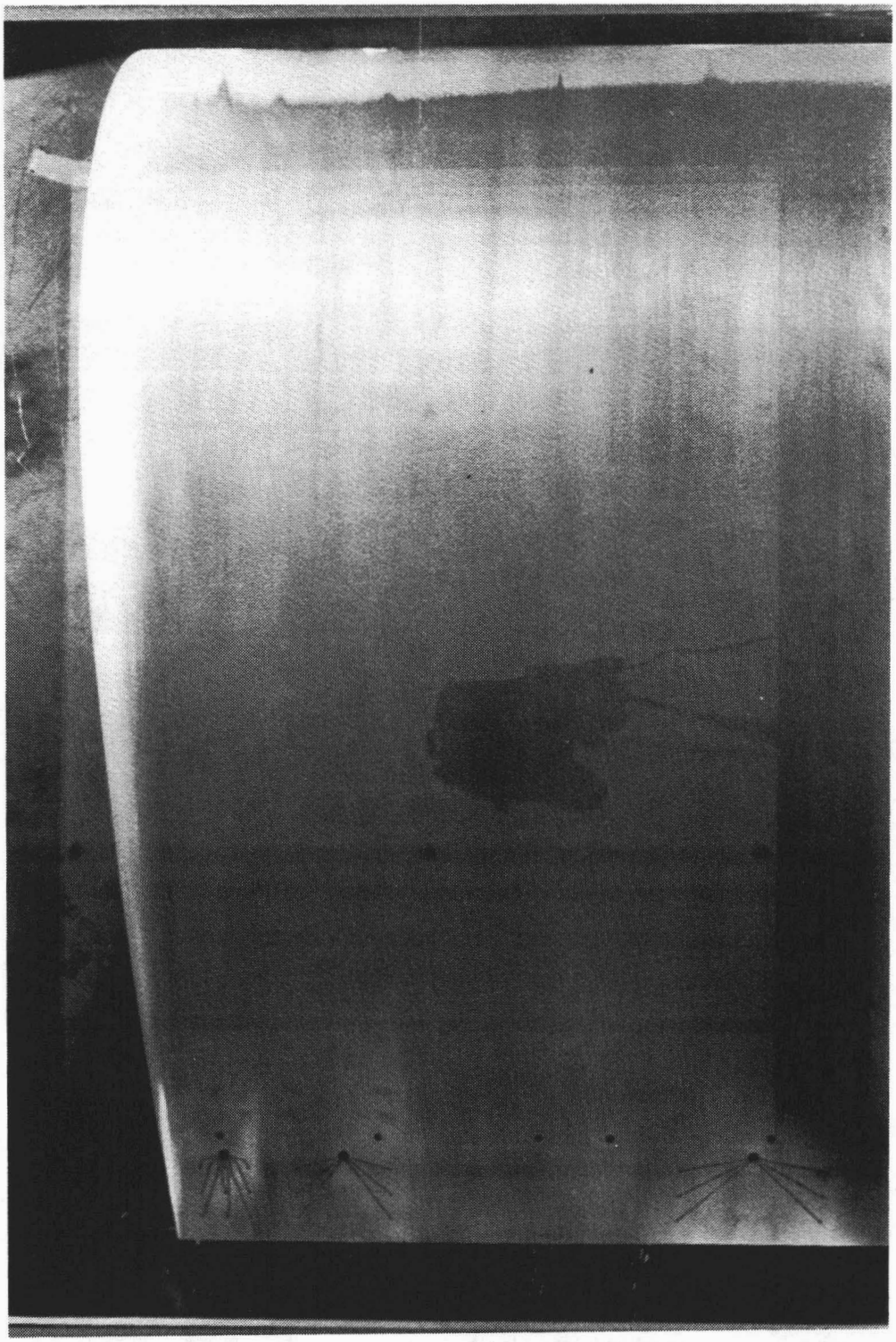

Figure 3.2a Estimated Transition Location through Naphthalene: Suction Side

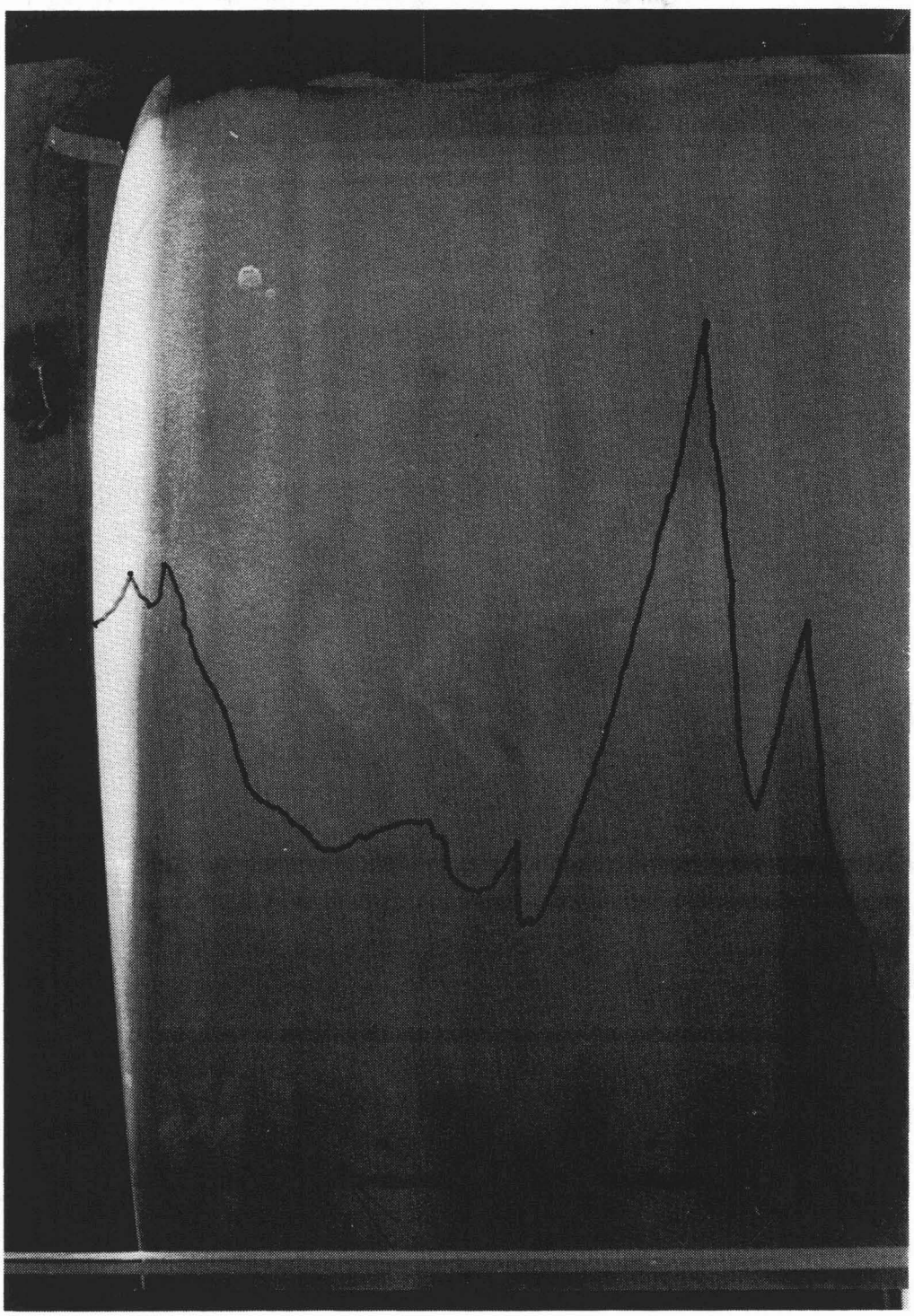

Figure 3.2b Estimated Transition Location through Naphthalene: Pressure Side

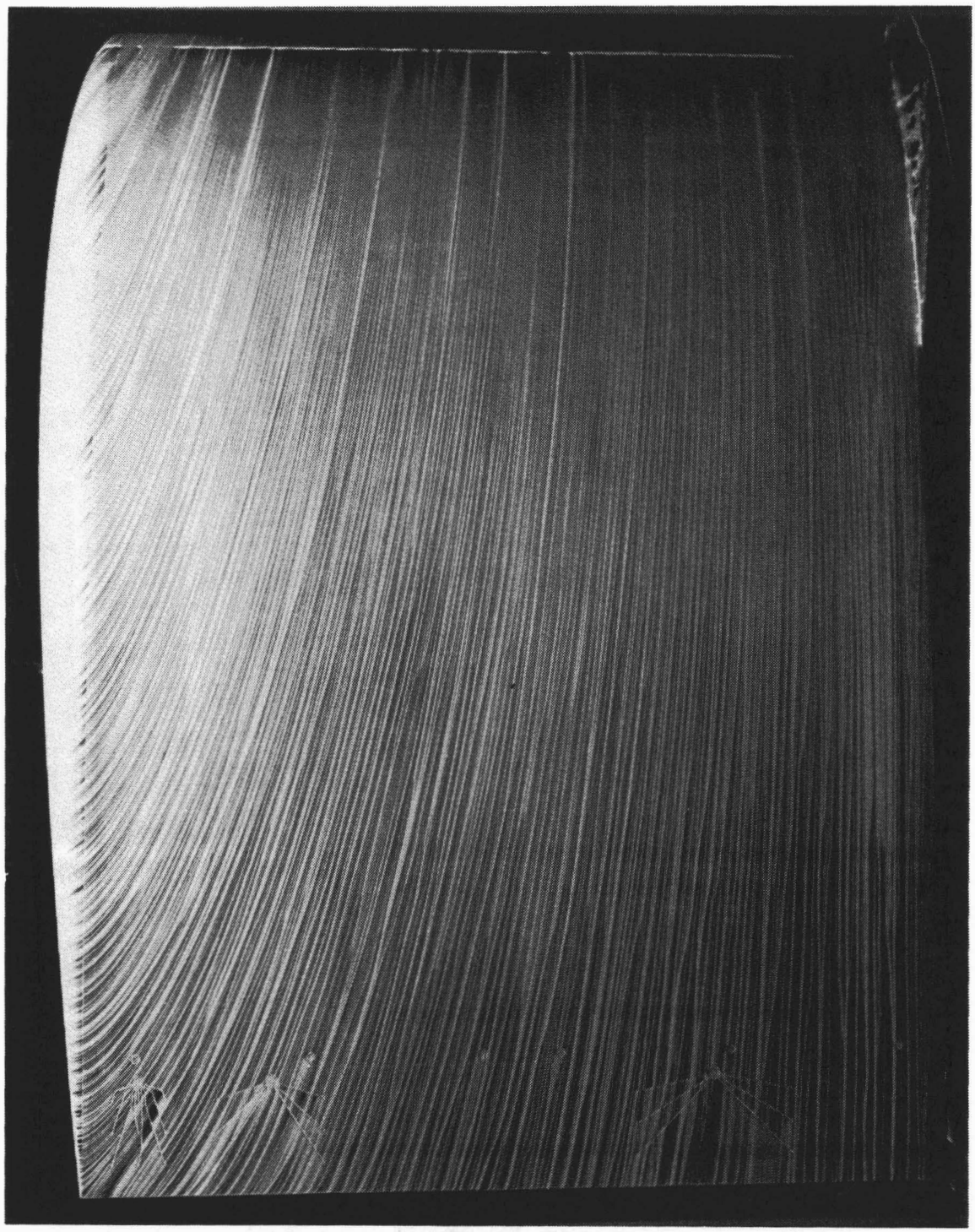

Figure 3.3a Surface Oil-Flow Visualization: Pressure Side

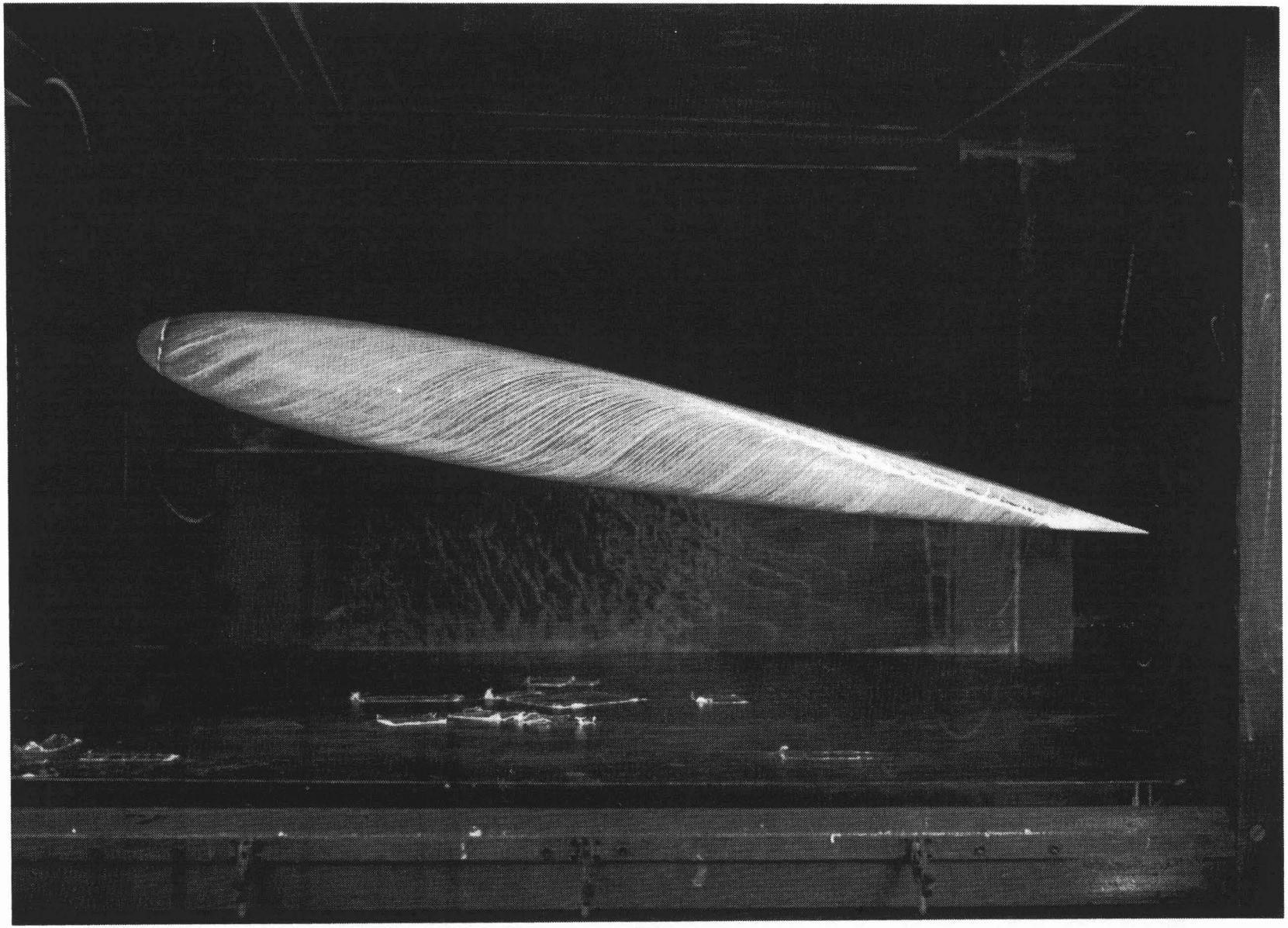

Figure 3.3b Surface Oil-Flow Visualization: Tip View

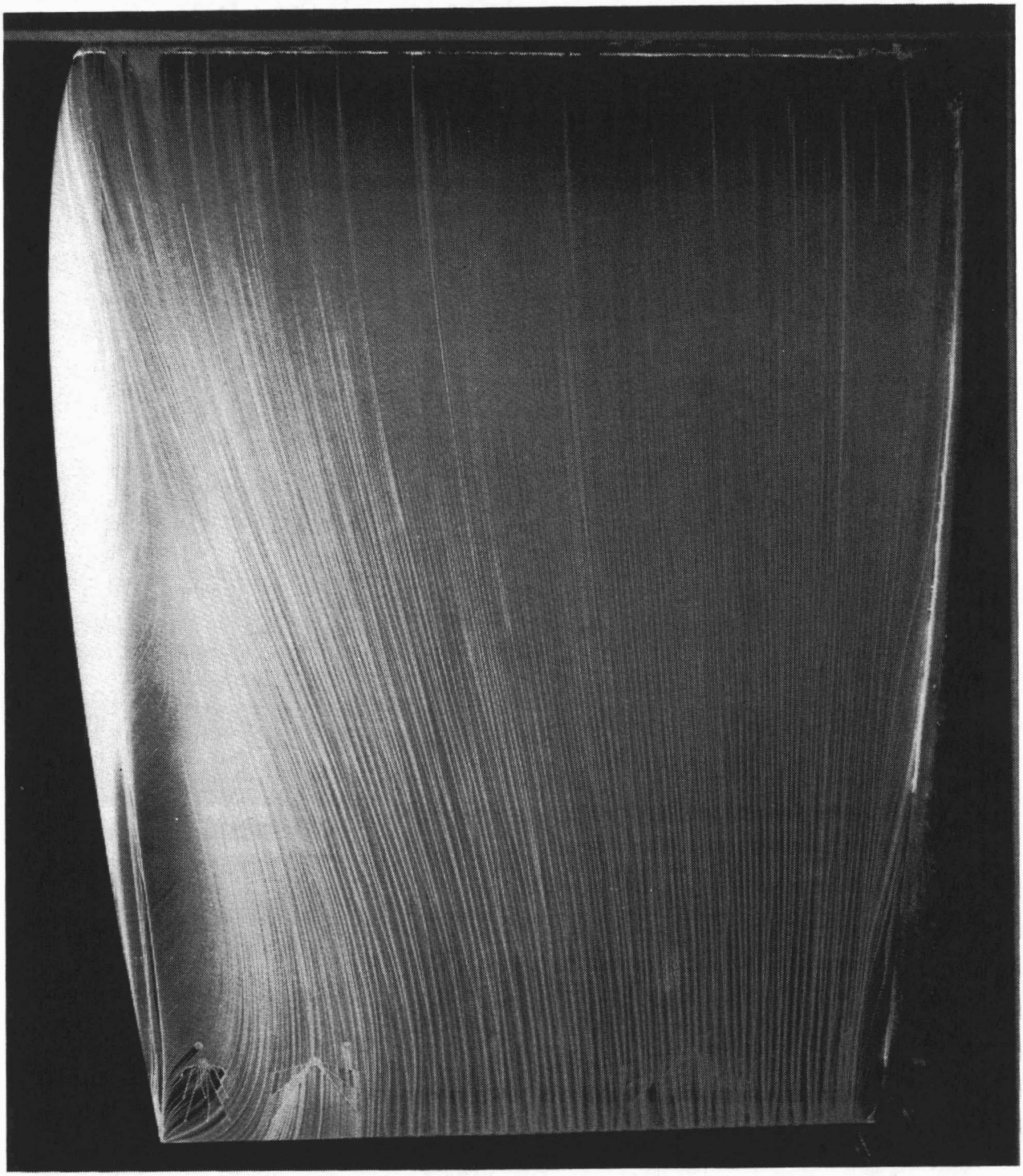

Figure 3.3c Surface Oil-Flow Visualization: Suction Side

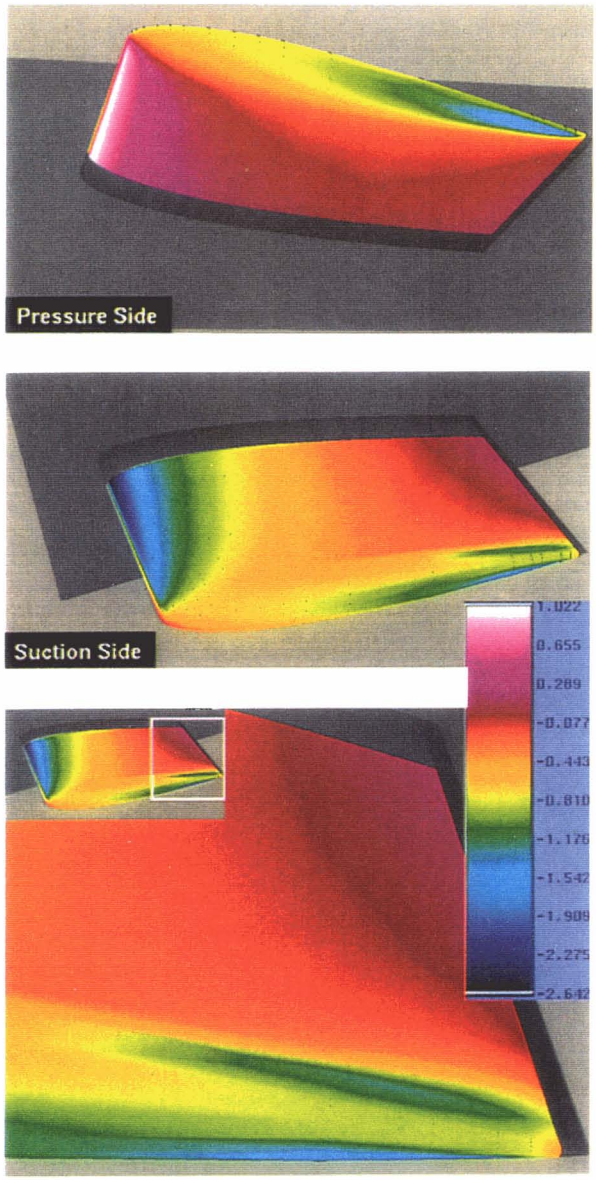

Figure 3.4a,b Surface Pressure Contours: a) Pressure Side (top) b) Suction Side

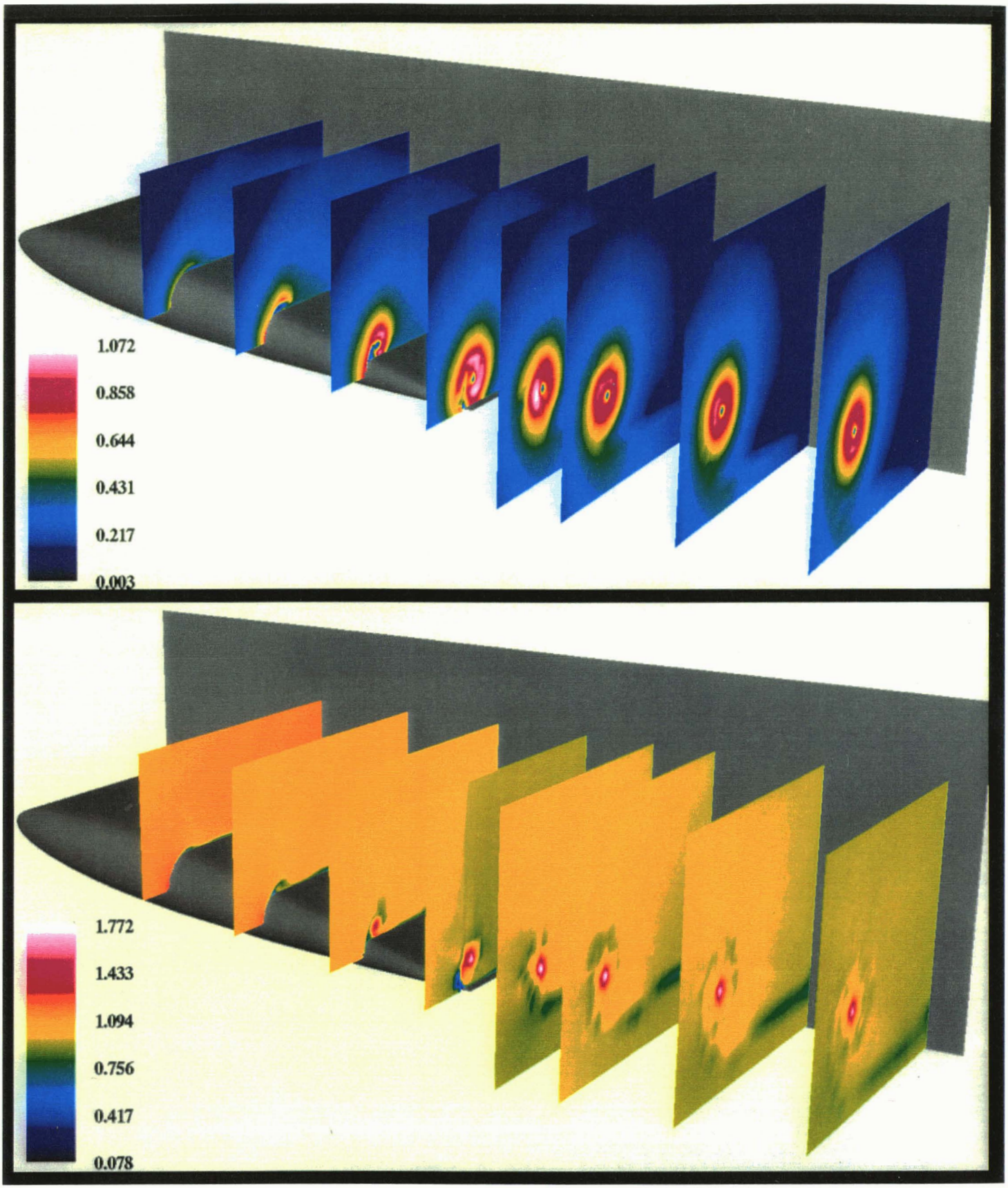

Figure 3.5a,b Perspective Comparison of: a) Crossflow Velocity (top) , b) Axial Velocity

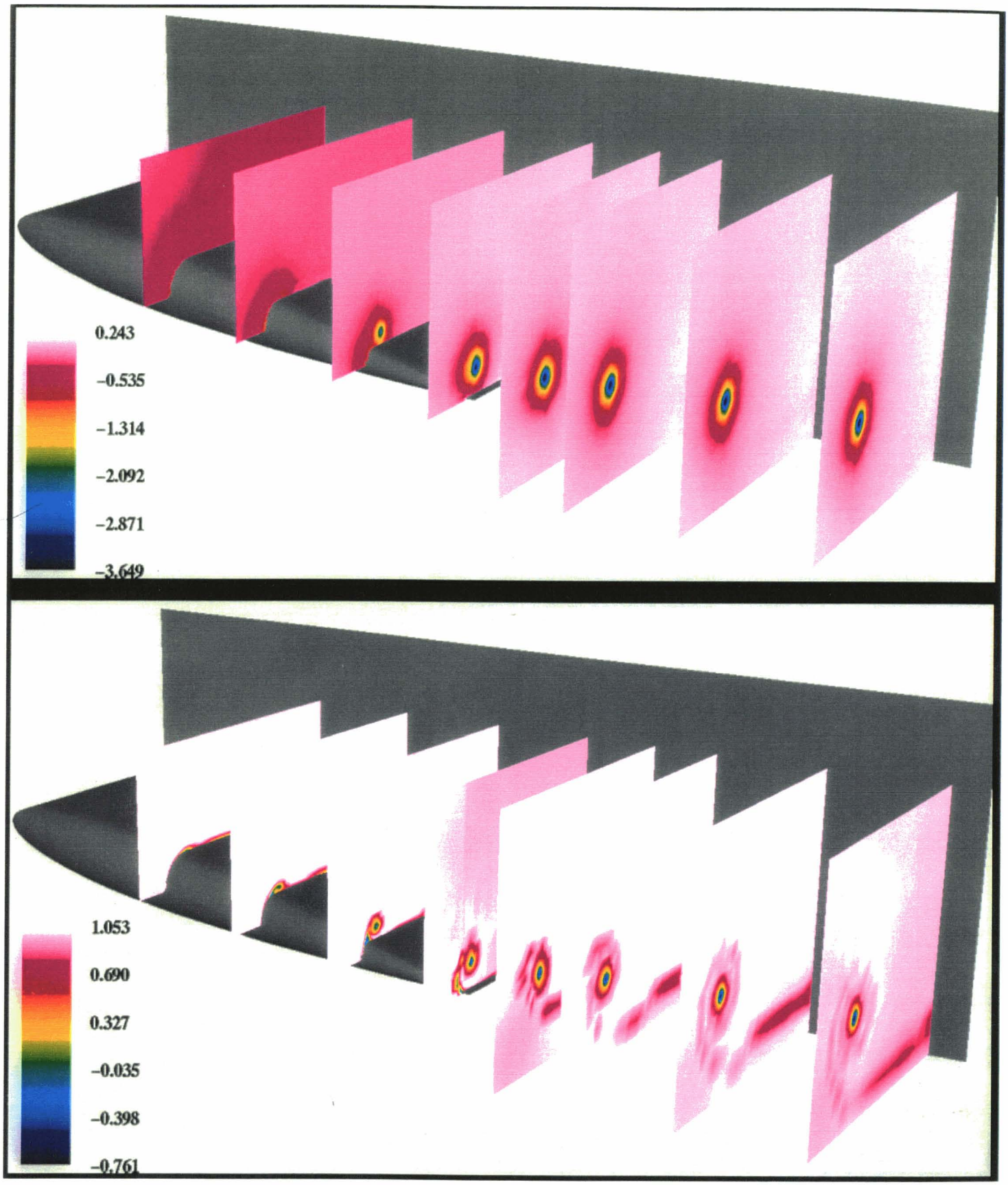

Figure 3.5c,d Perspective Comparison of: c) Static Pressure (top) , d) Total Pressure

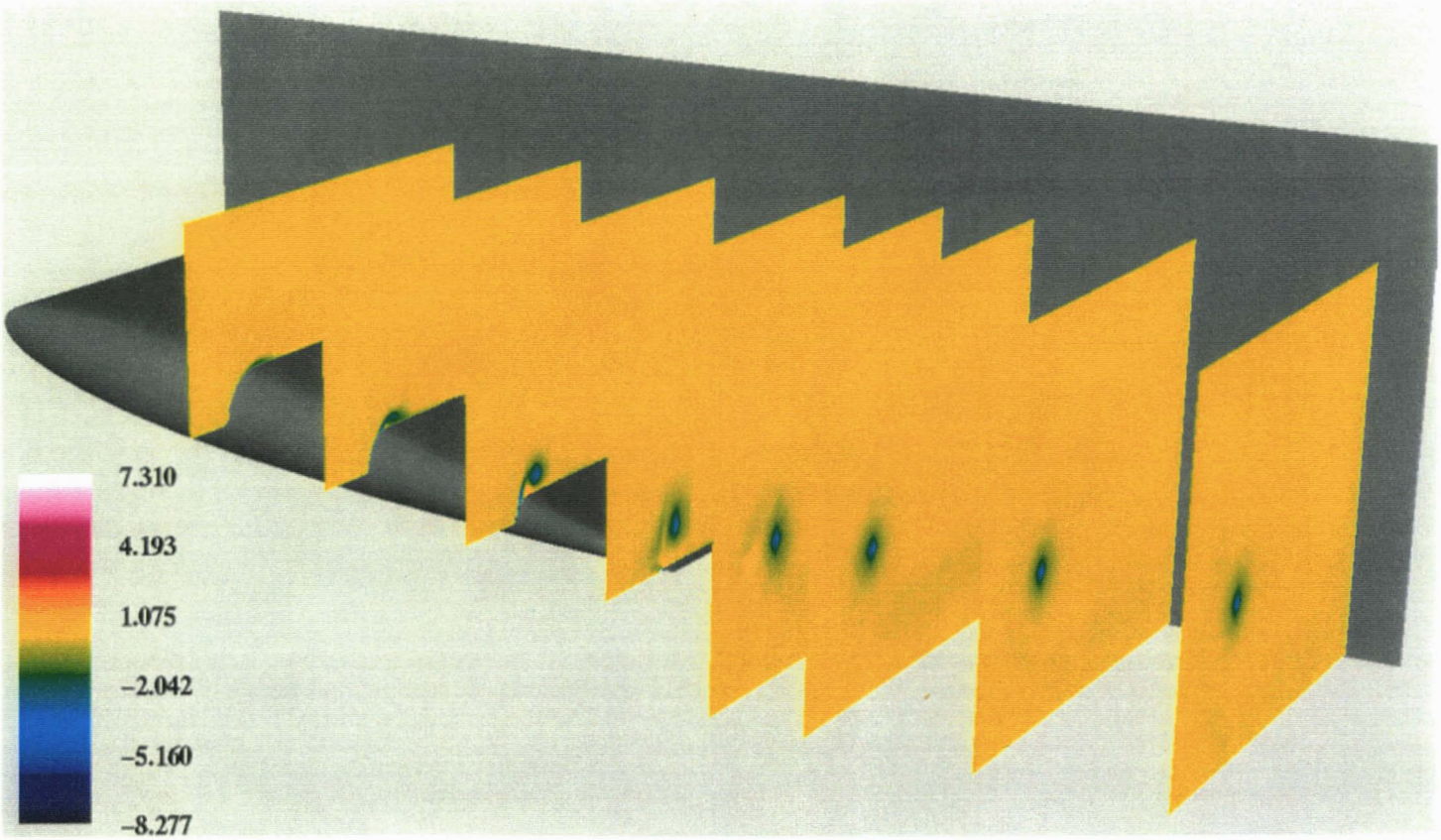

Figure 3.5e Perspective Comparison of: e) Axial Vorticity

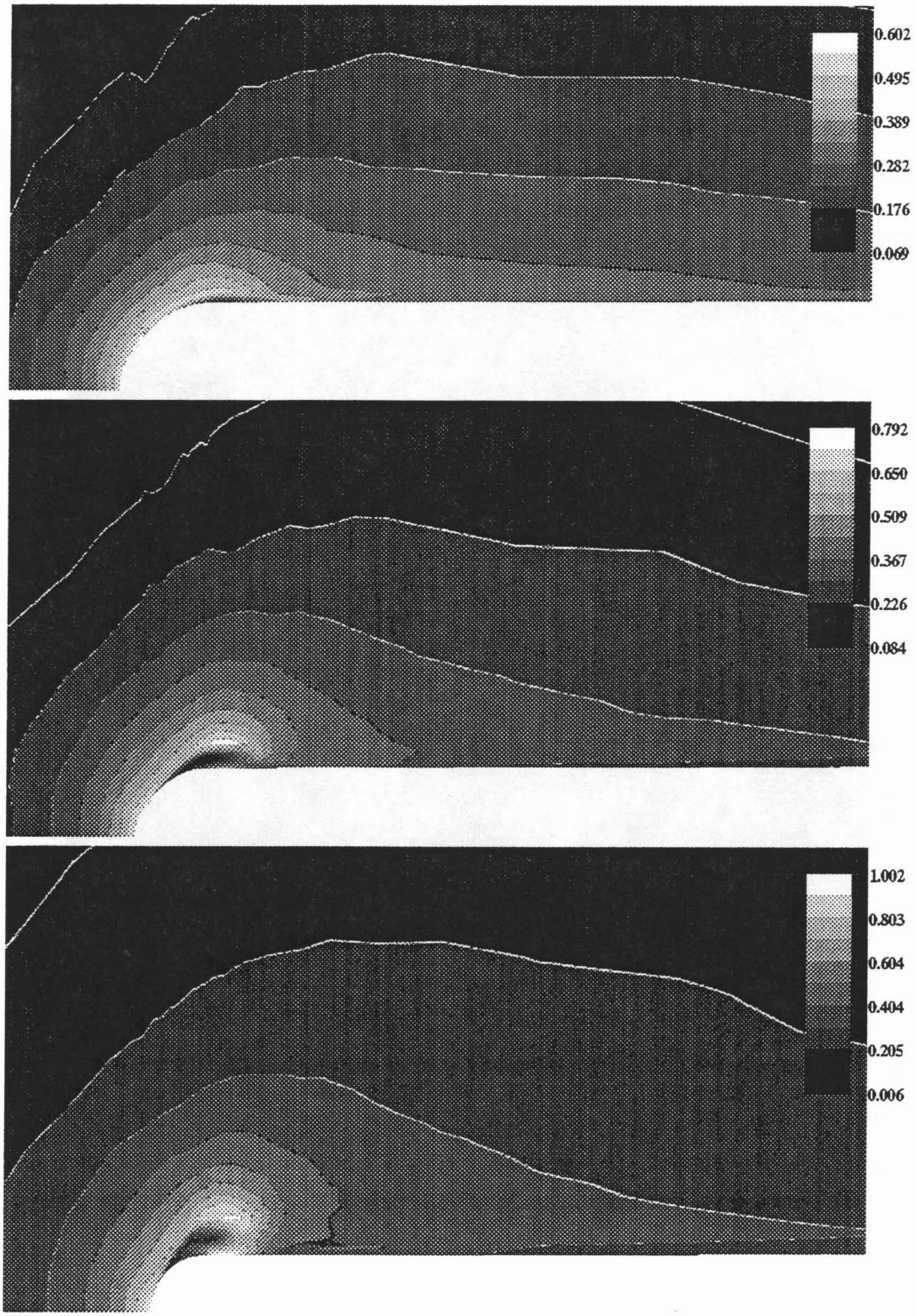

Figure 3.6a,b,c Crossflow Velocity Contours: a) $x/c = -0.591$, **b)** $x/c = -0.394$, **c)** $x/c = -0.296$

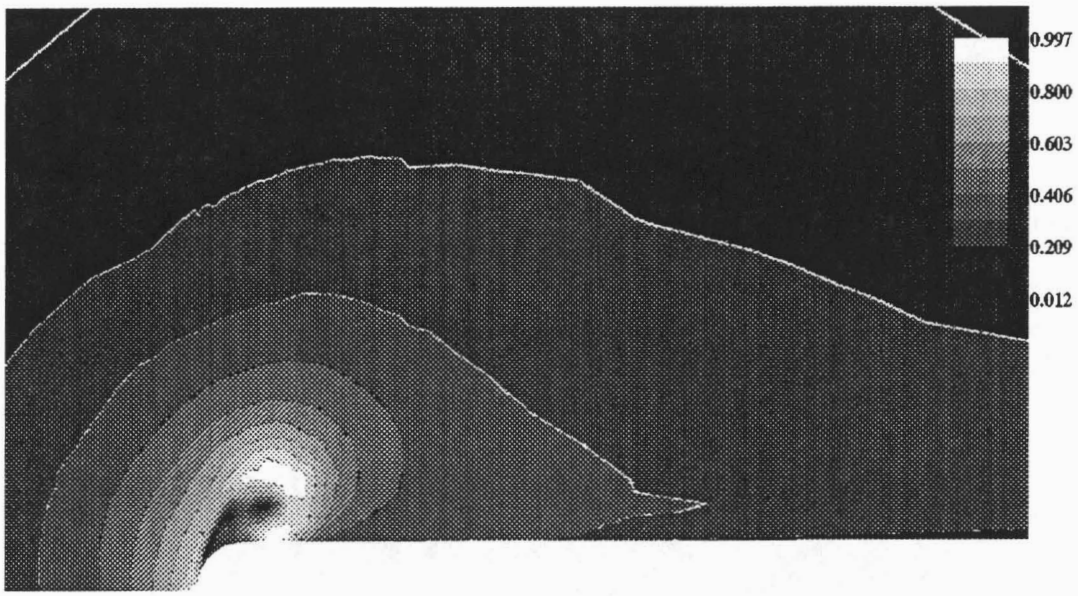

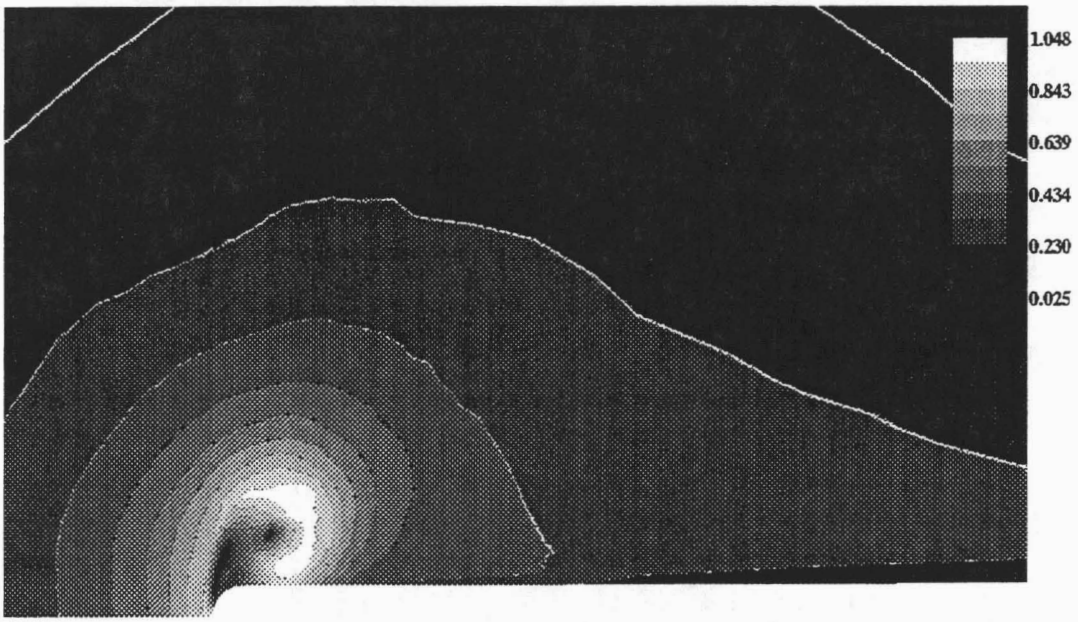

Figure 3.6d,e Crossflow Velocity Contours: d) $x/c = -0.197$, **e)** $x/c = -0.114$

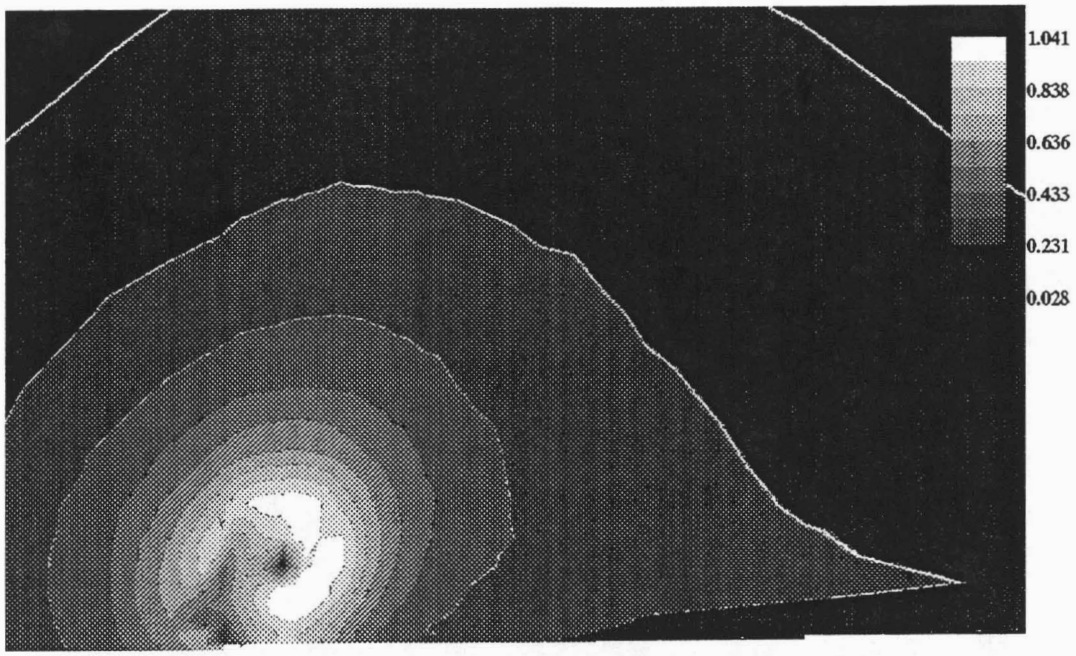

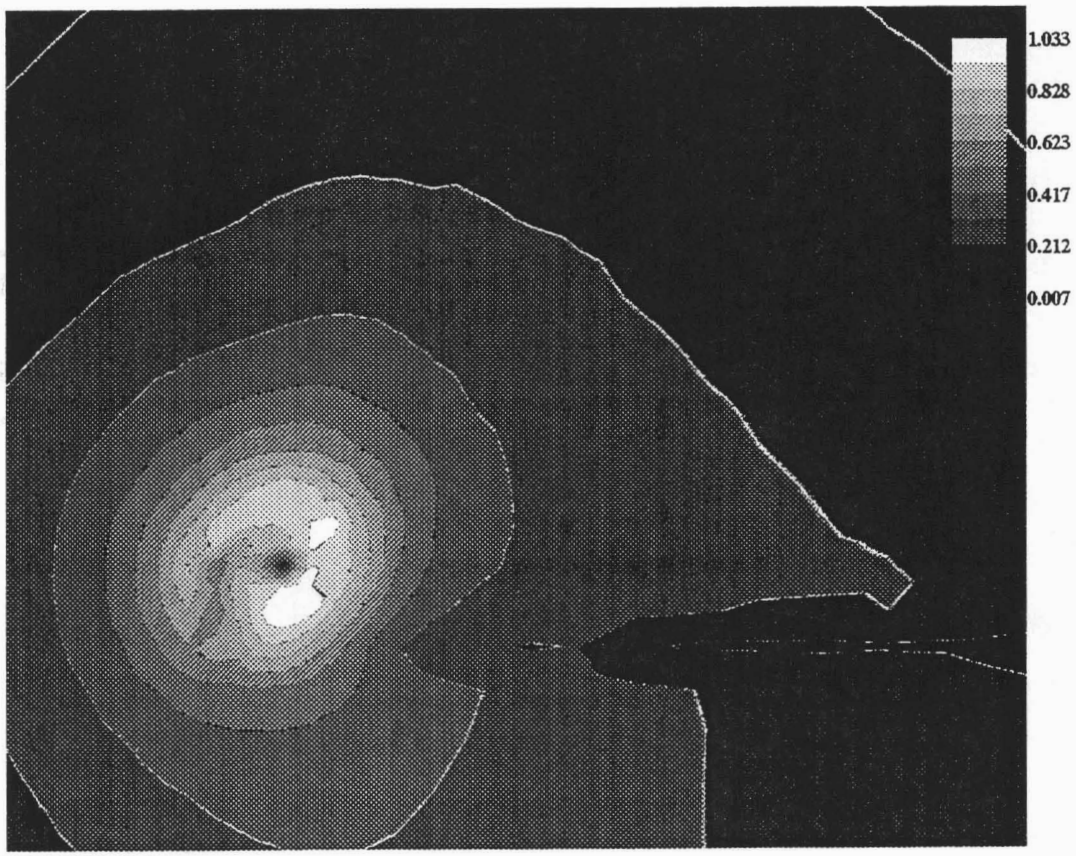

Figure 3.6f,g Crossflow Velocity Contours: f) $x/c = -0.010$, **g)** $x/c = 0.005$

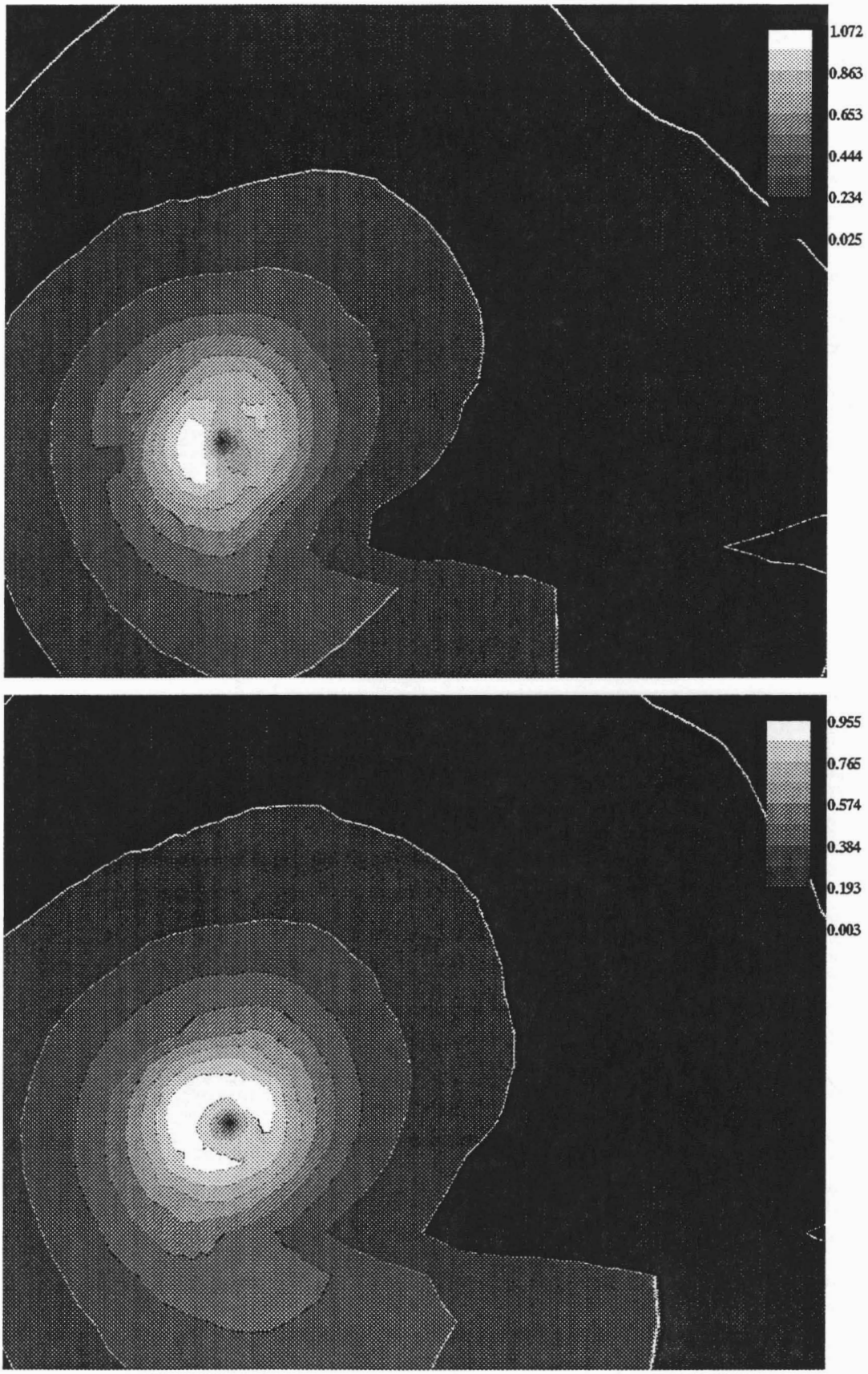

Figure 3.6h,i Crossflow Velocity Contours: h) $x/c = 0.125$, **i)** $x/c = 0.246$

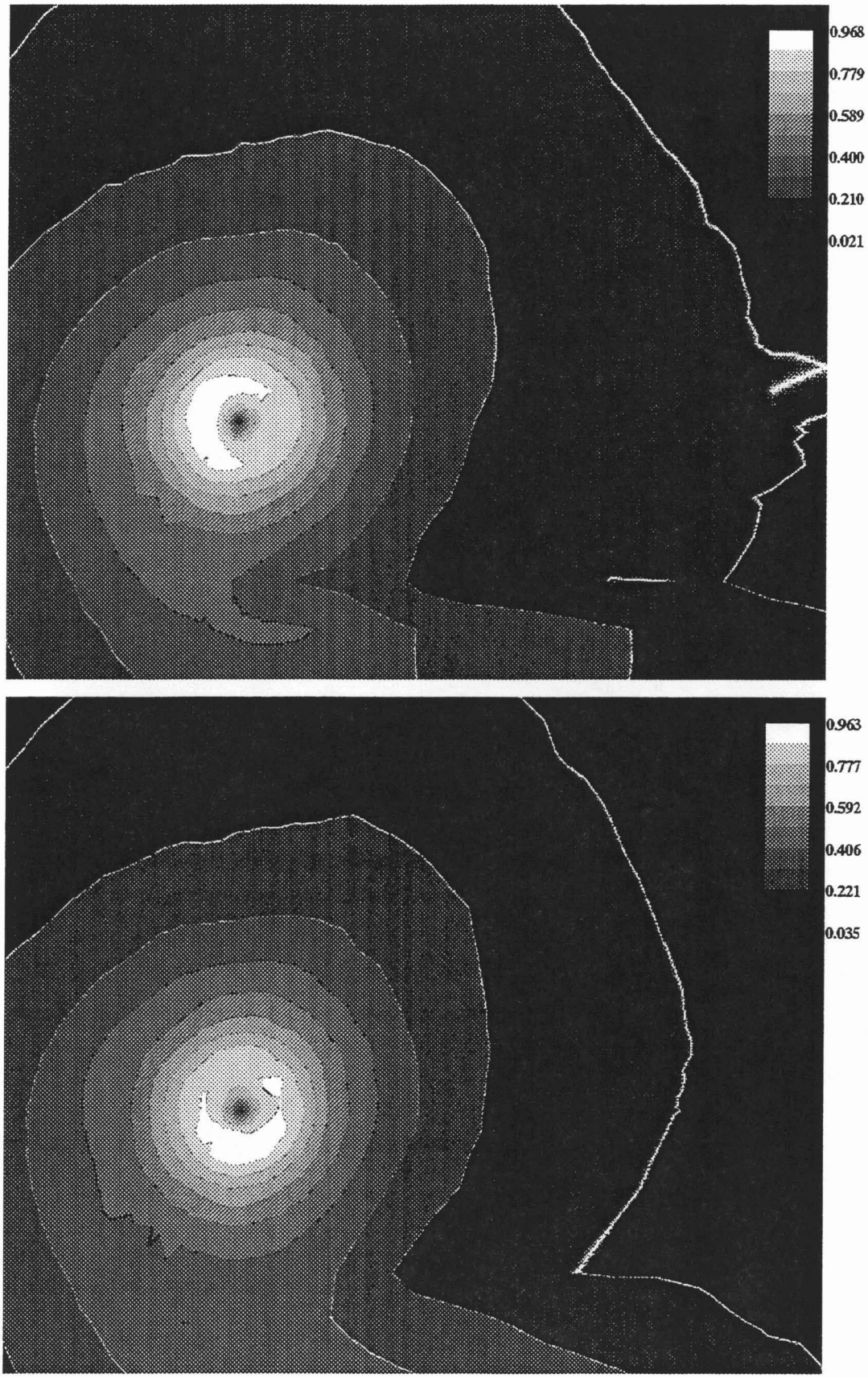

Figure 3.6j,k Crossflow Velocity Contours: j) $x/c = 0.452$, **k)** $x/c = 0.678$

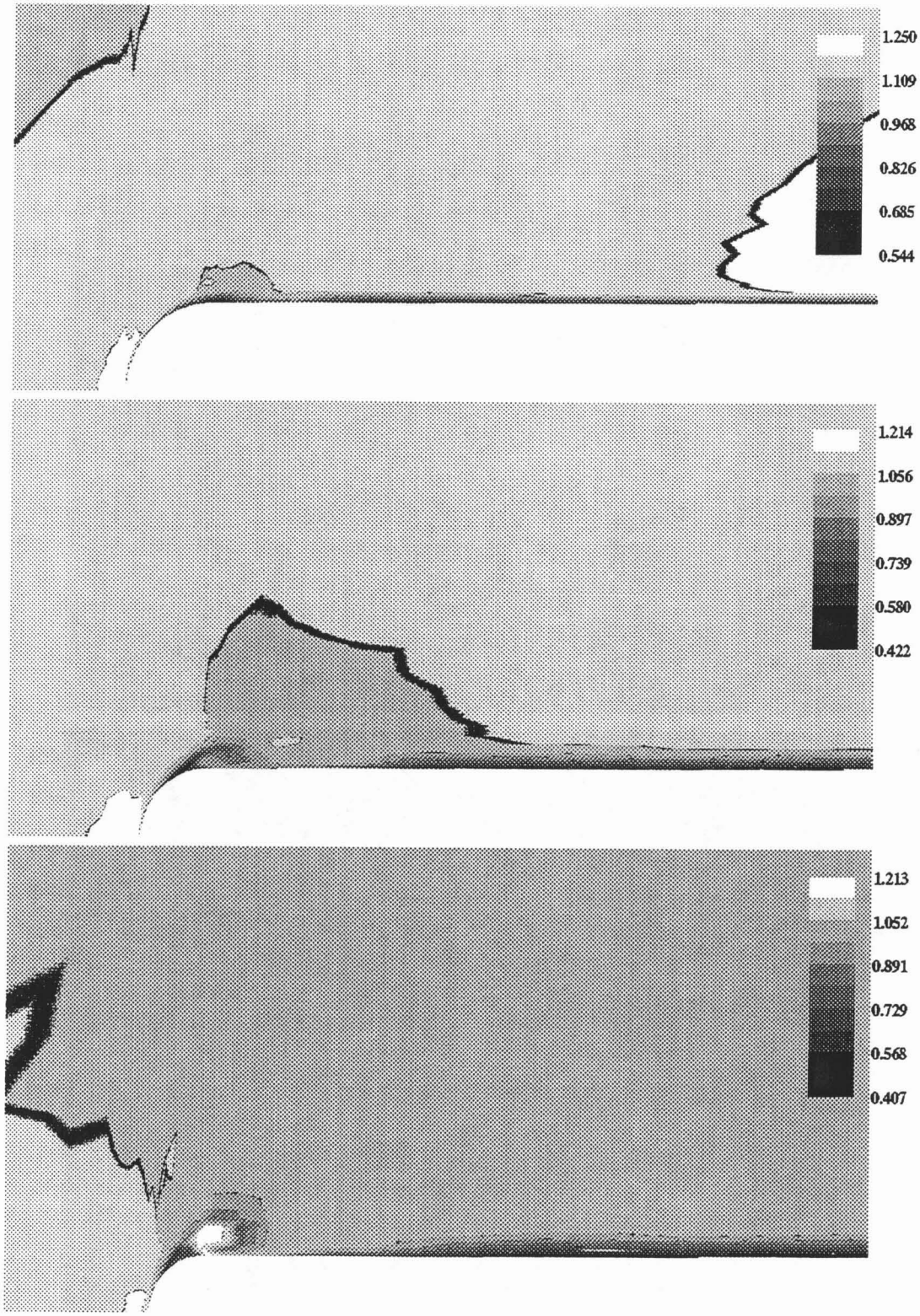

Figure 3.7a,b,c Axial Velocity Contours: a) $x/c = -0.591$, **b)** $x/c = -0.394$, **c)** $x/c = -0.296$

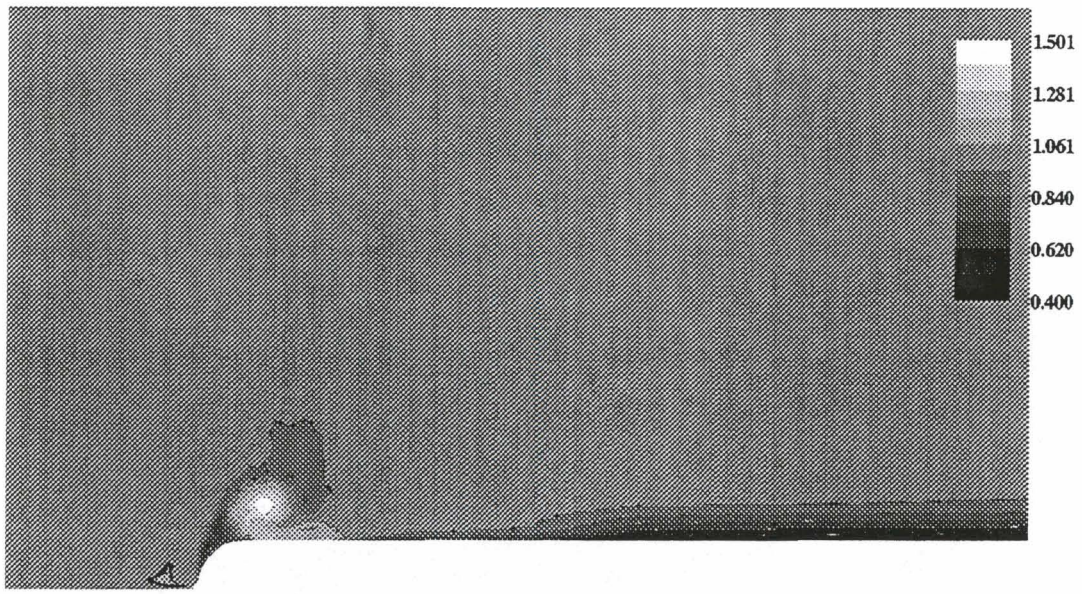

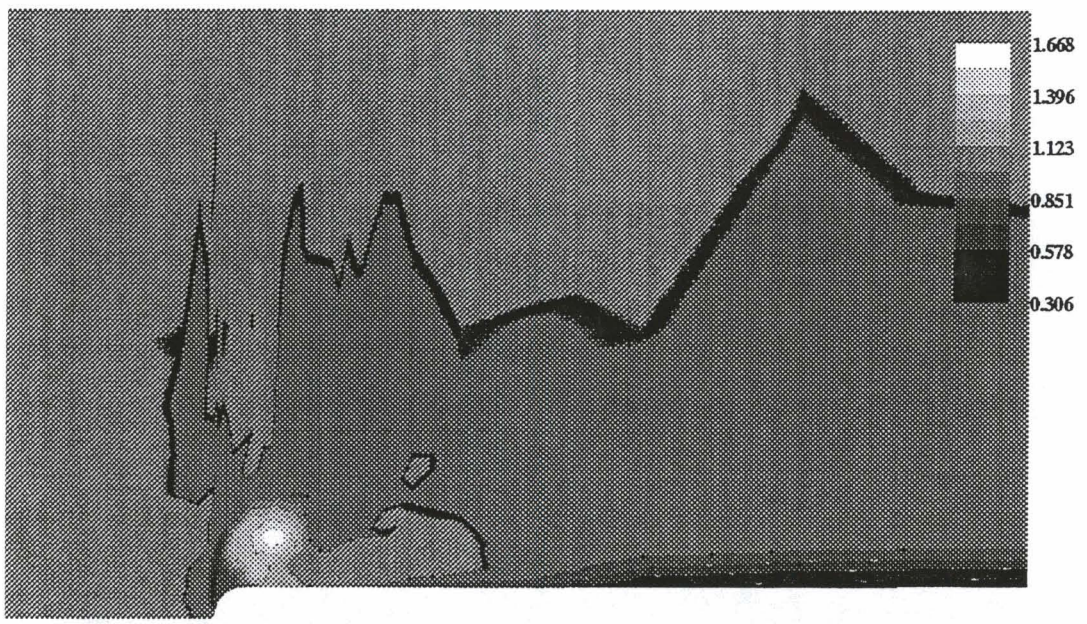

Figure 3.7d,e Axial Velocity Contours: d) $x/c = -0.197$, **e)** $x/c = -0.114$

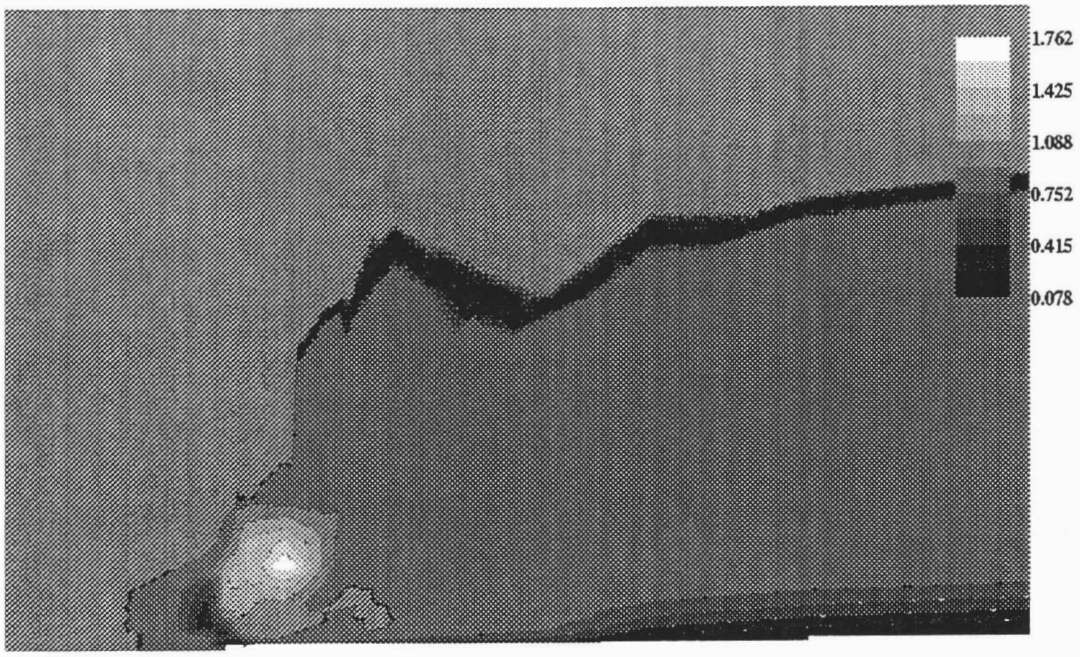

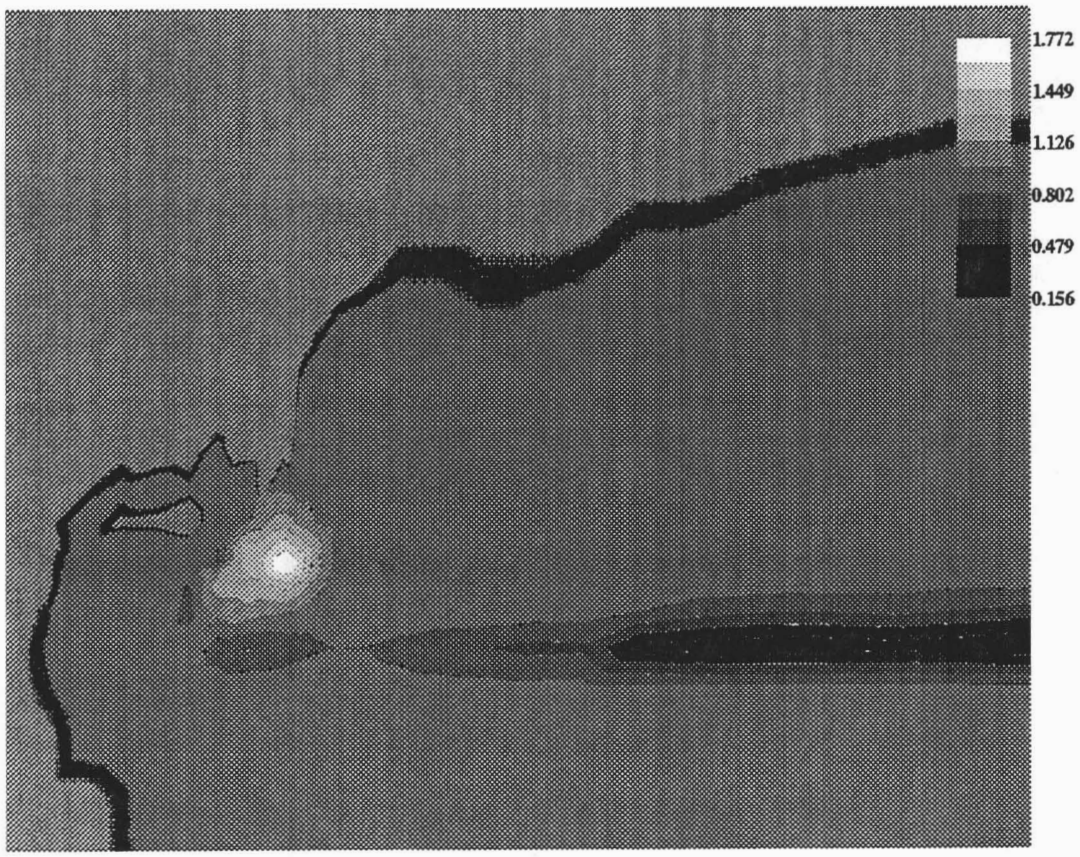

Figure 3.7f,g Axial Velocity Contours: f) $x/c = -0.010$, **g)** $x/c = 0.005$

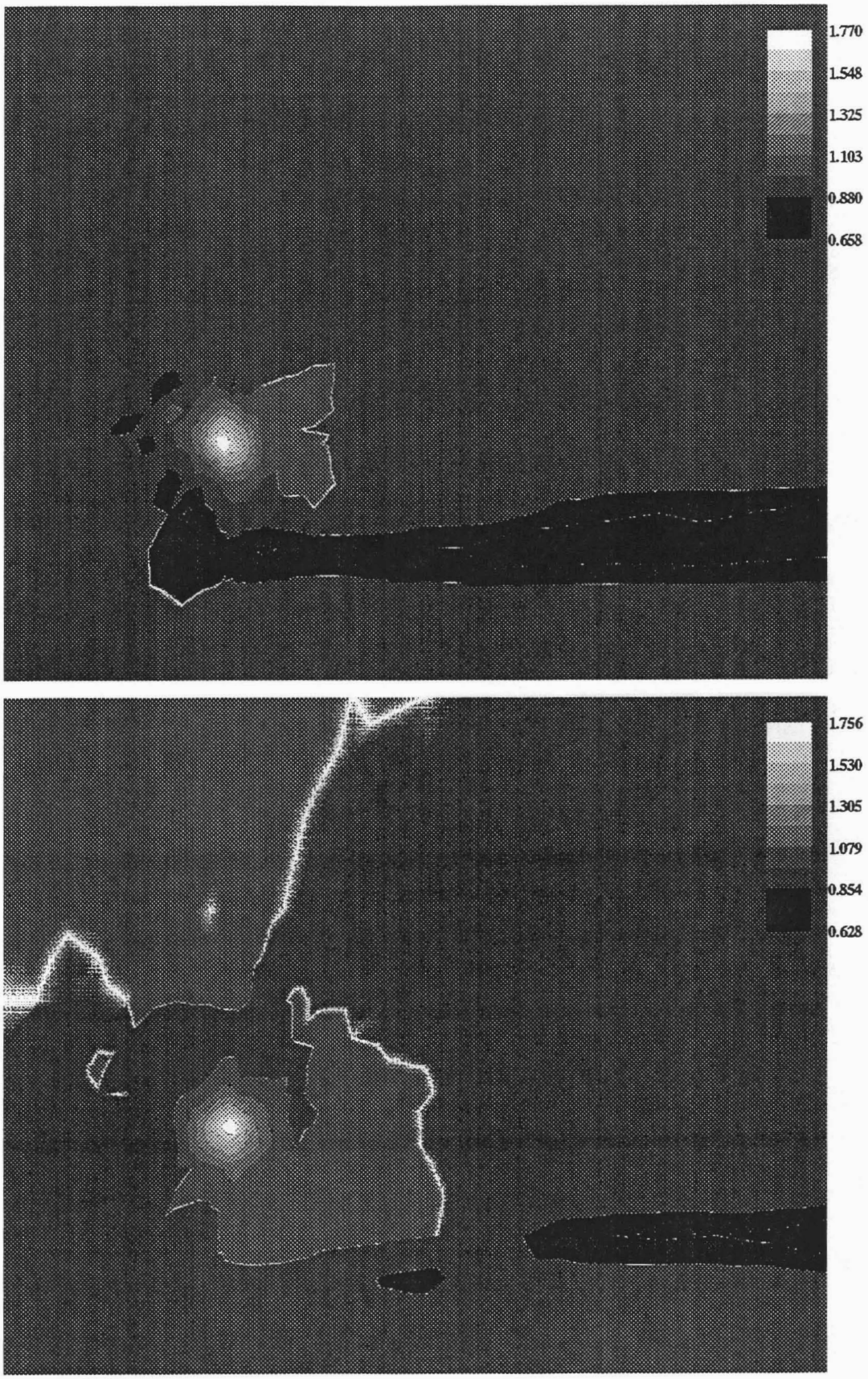

Figure 3.7h,i Axial Velocity Contours: h) $x/c = 0.125$, **i)** $x/c = 0.246$

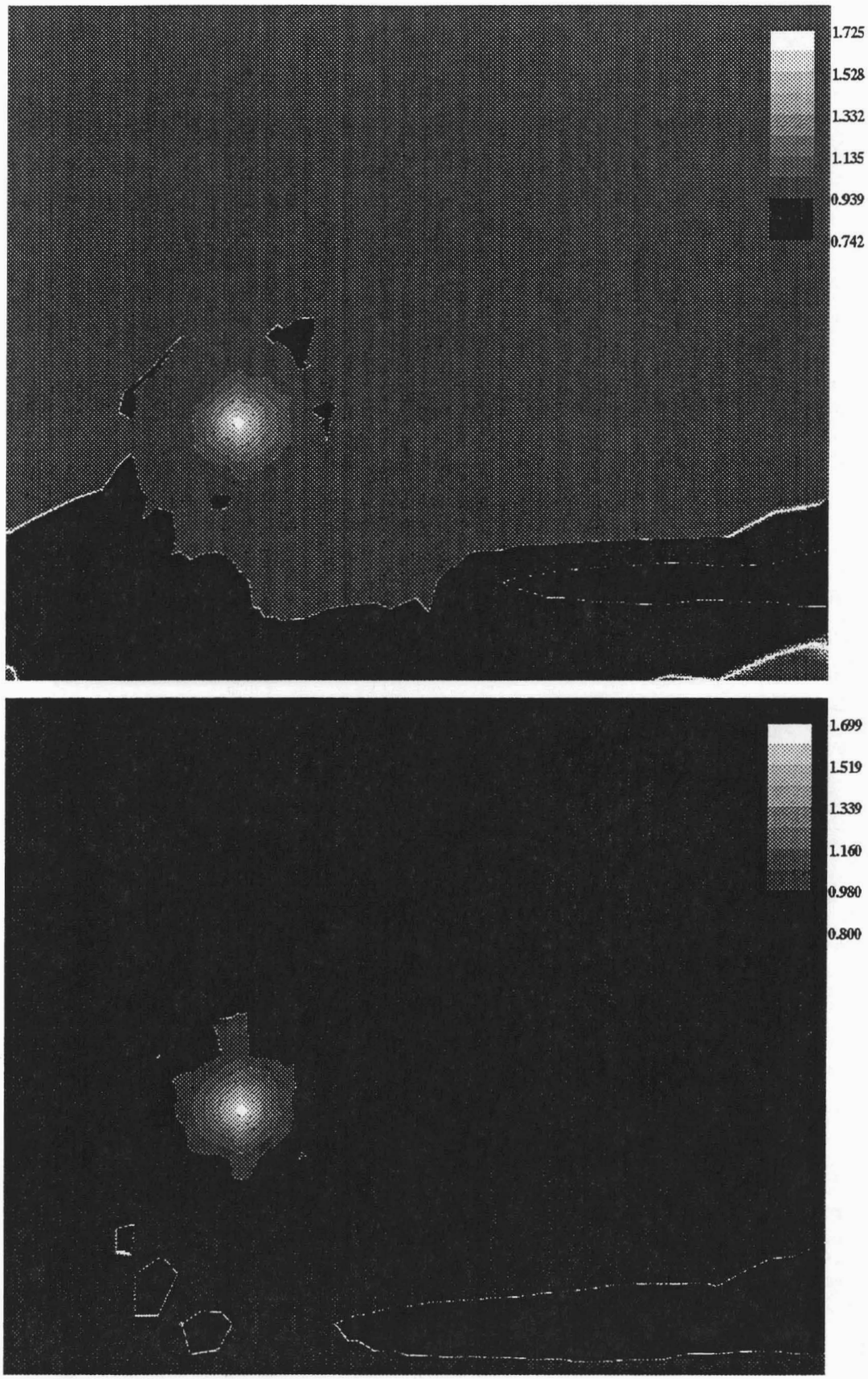

Figure 3.7j,k Axial Velocity Contours: j) $x/c = 0.452$, **k)** $x/c = 0.678$

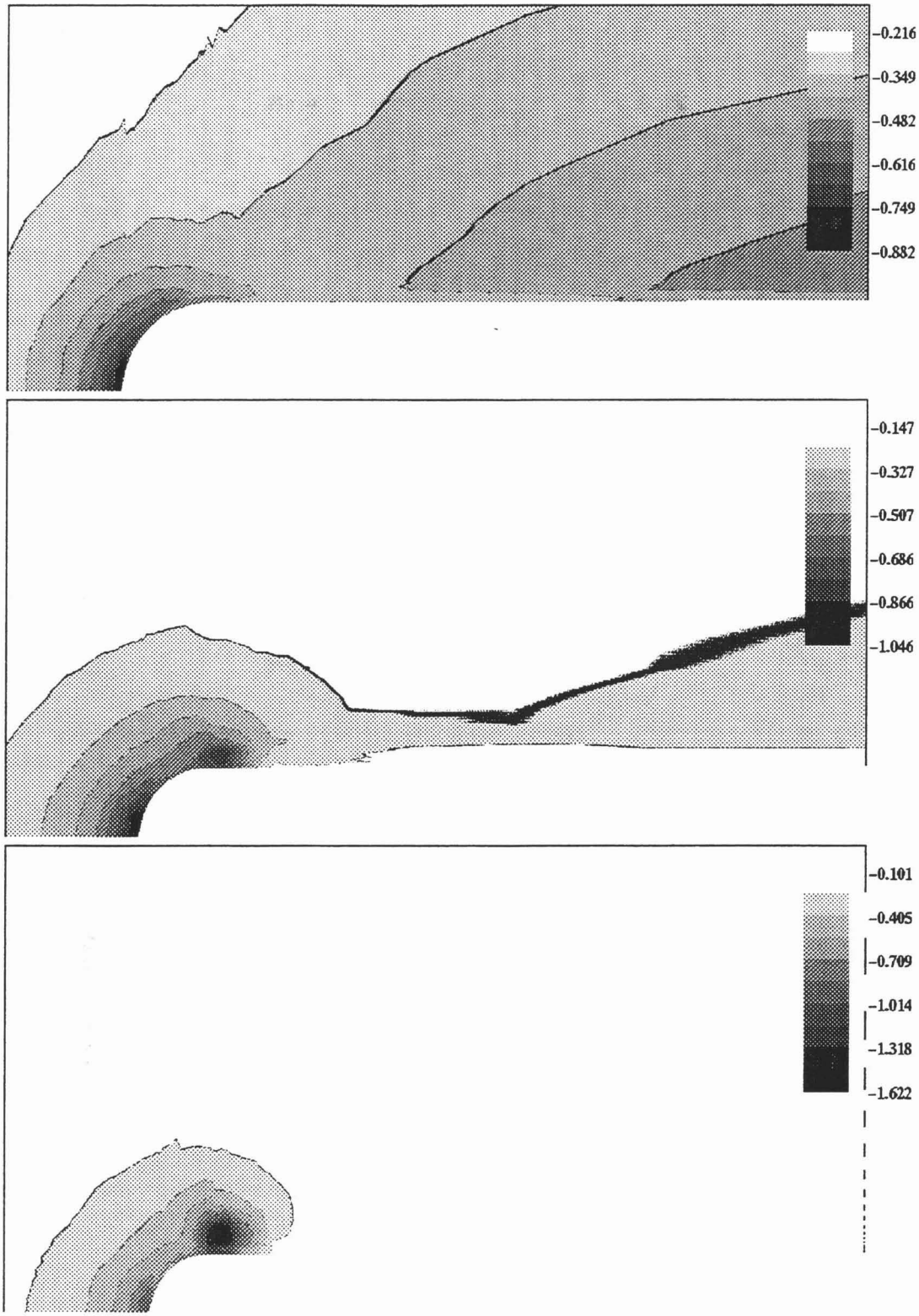

Figure 3.8a,b,c Static Pressure Contours: a) $x/c = -0.591$**, b)** $x/c = -0.394$**, c)** $x/c = -0.296$

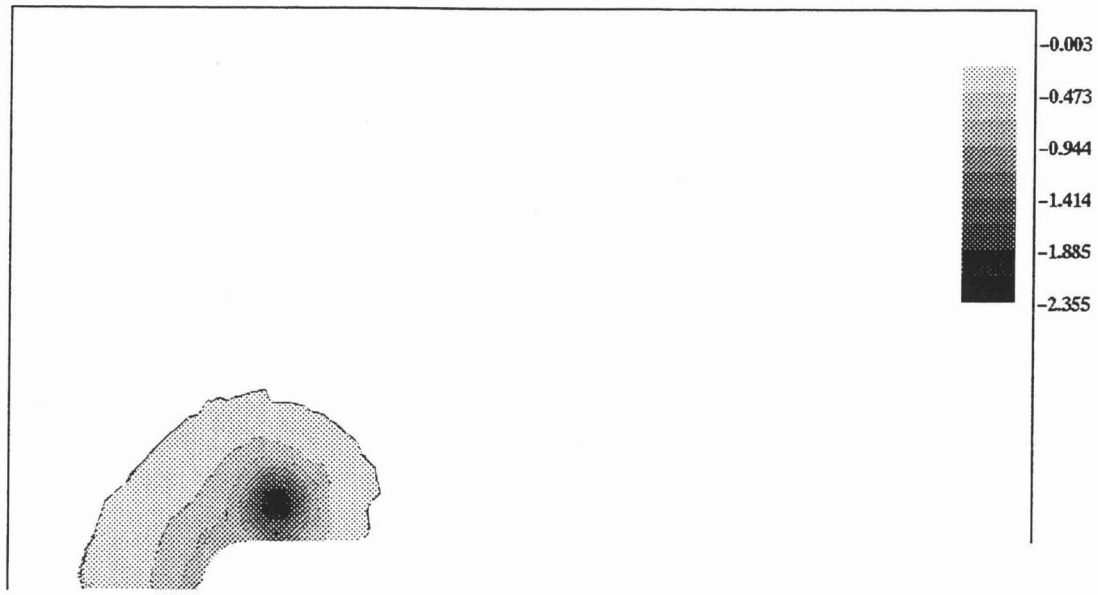

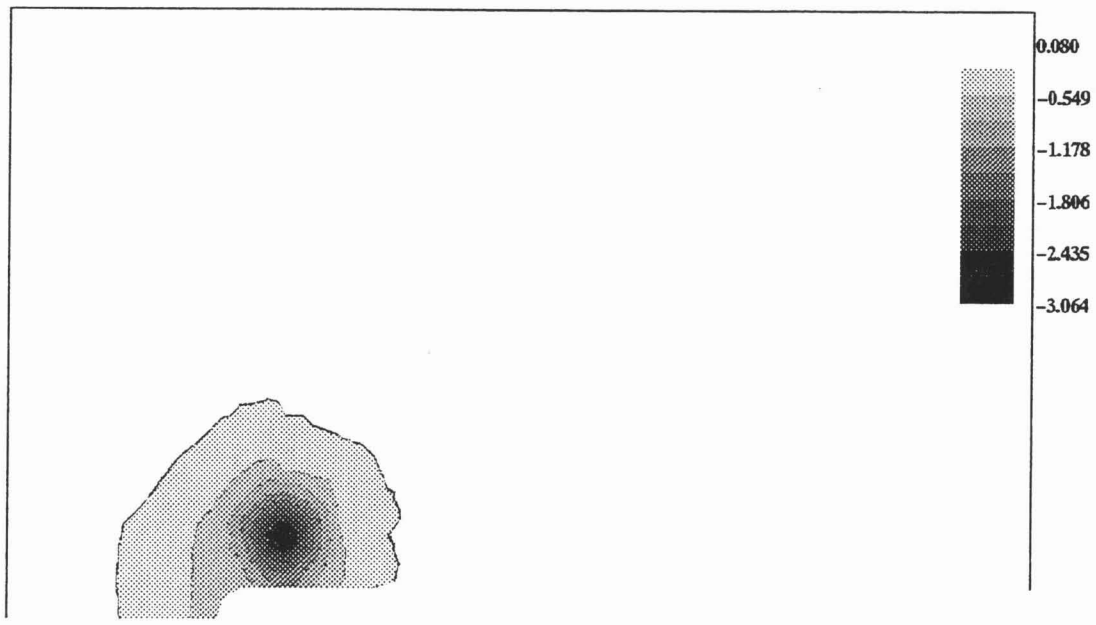

Figure 3.8d,e Static Pressure Contours: d) $x/c = -0.197$, **e)** $x/c = -0.114$

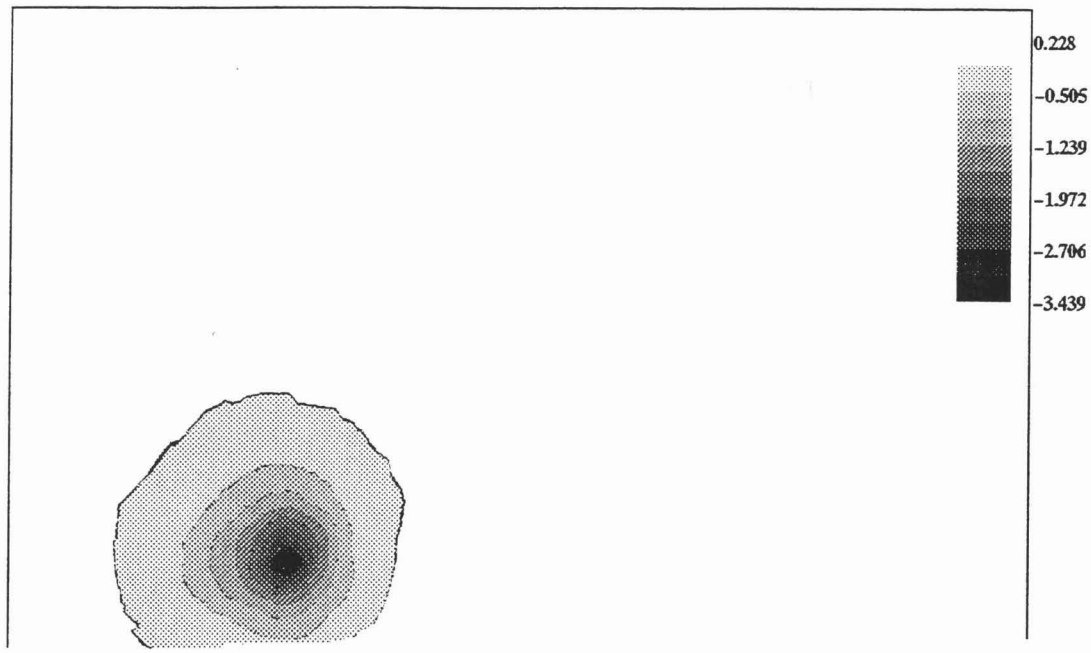

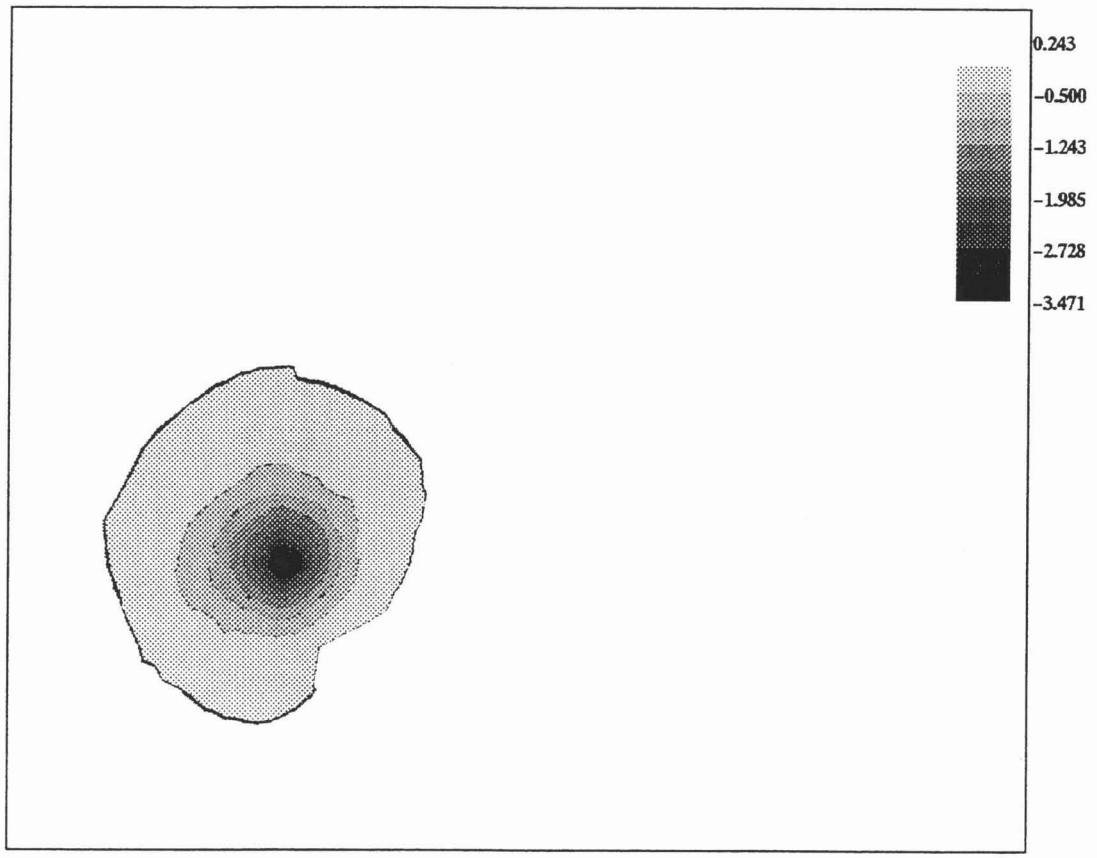

Figure 3.8f,g Static Pressure Contours: f) $x/c = -0.010$, **g)** $x/c = 0.005$

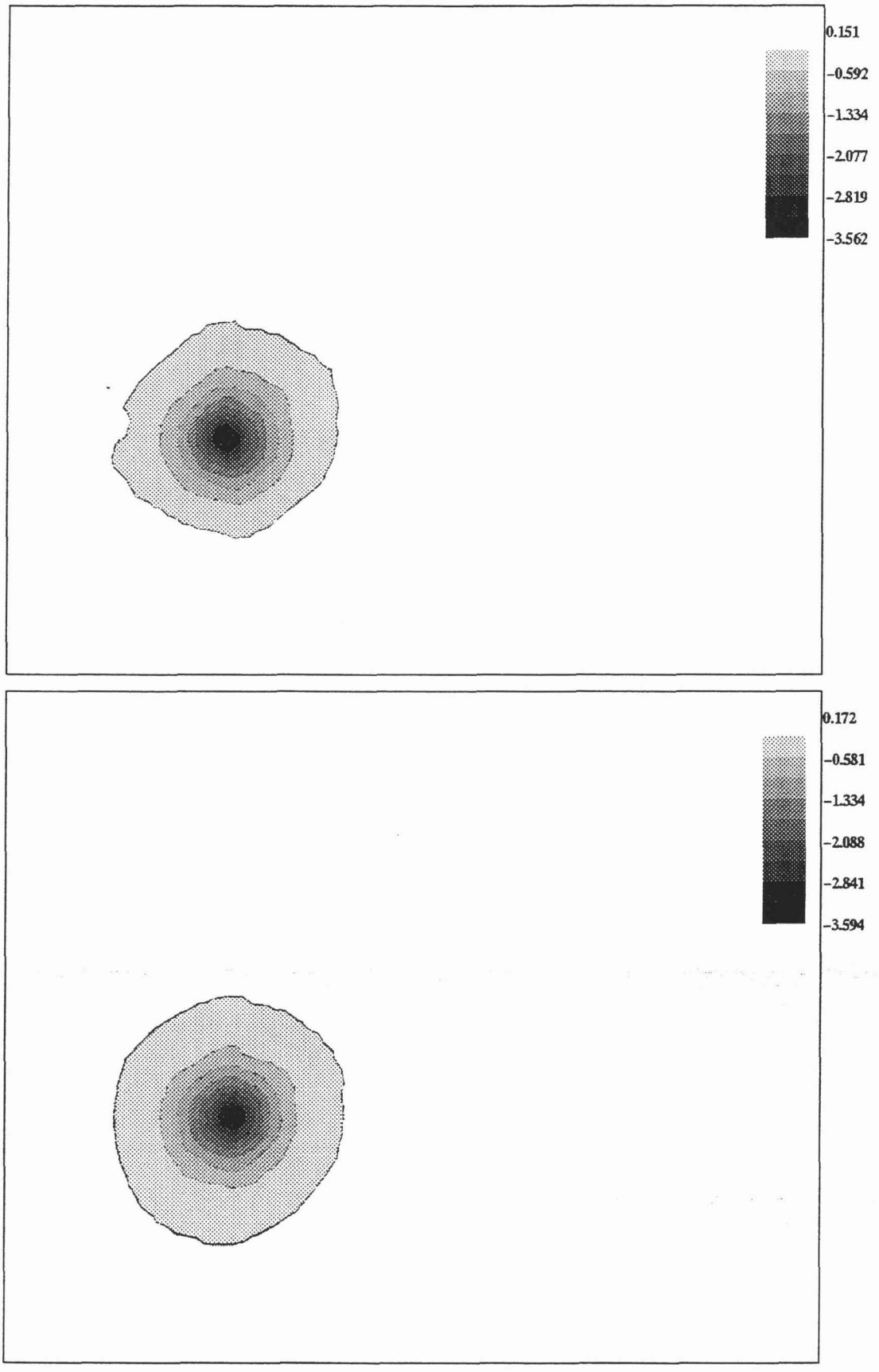

Figure 3.8h,i Static Pressure Contours: h) $x/c = 0.125$**, i)** $x/c = 0.246$

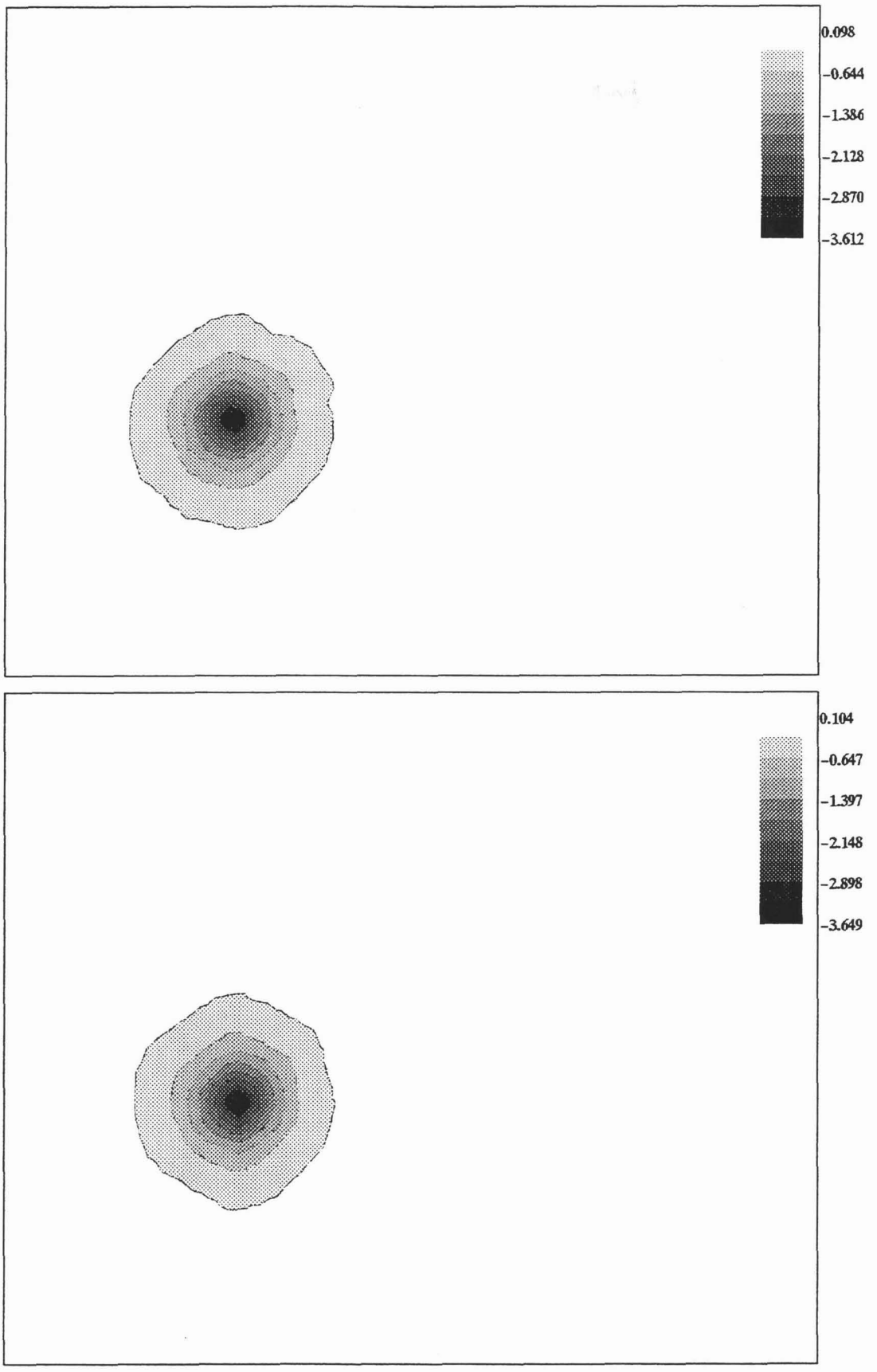

Figure 3.8j,k Static Pressure Contours: j) $x/c = 0.452$**, k)** $x/c = 0.678$

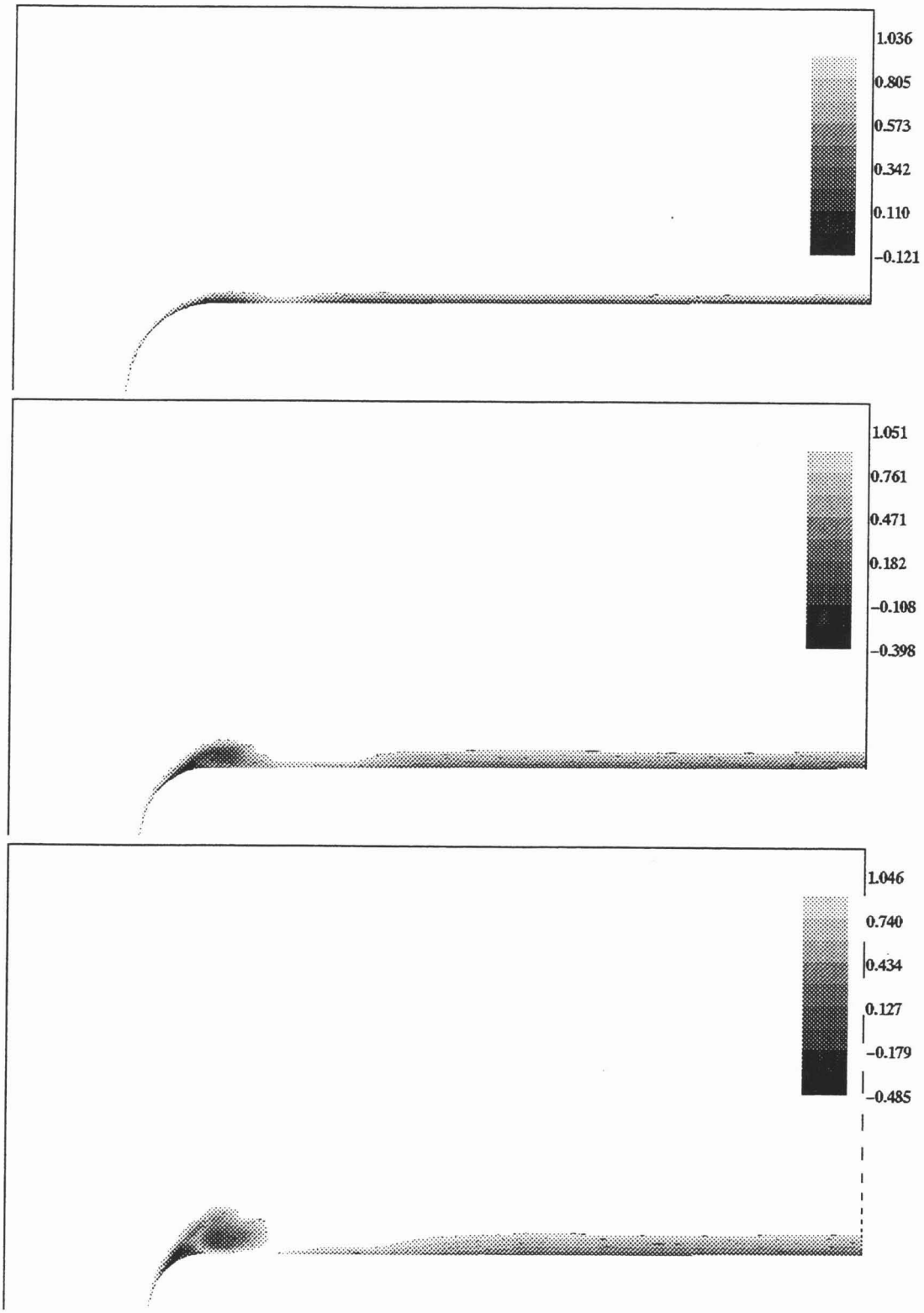

Figure 3.9a,b,c Total Pressure Contours: a) $x/c = -0.591$, **b)** $x/c = -0.394$, **c)** $x/c = -0.296$

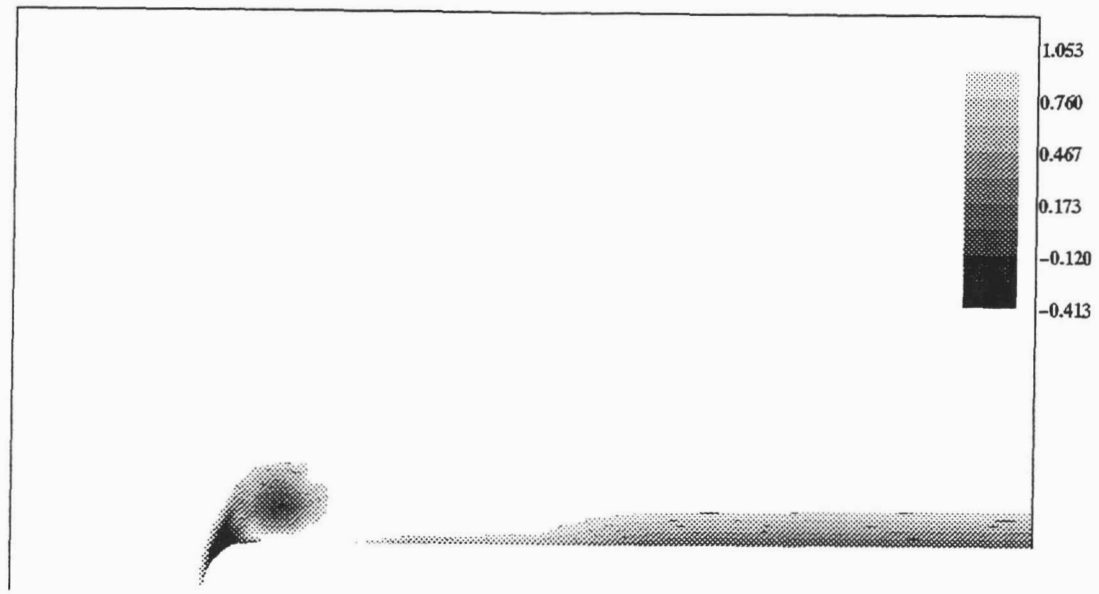

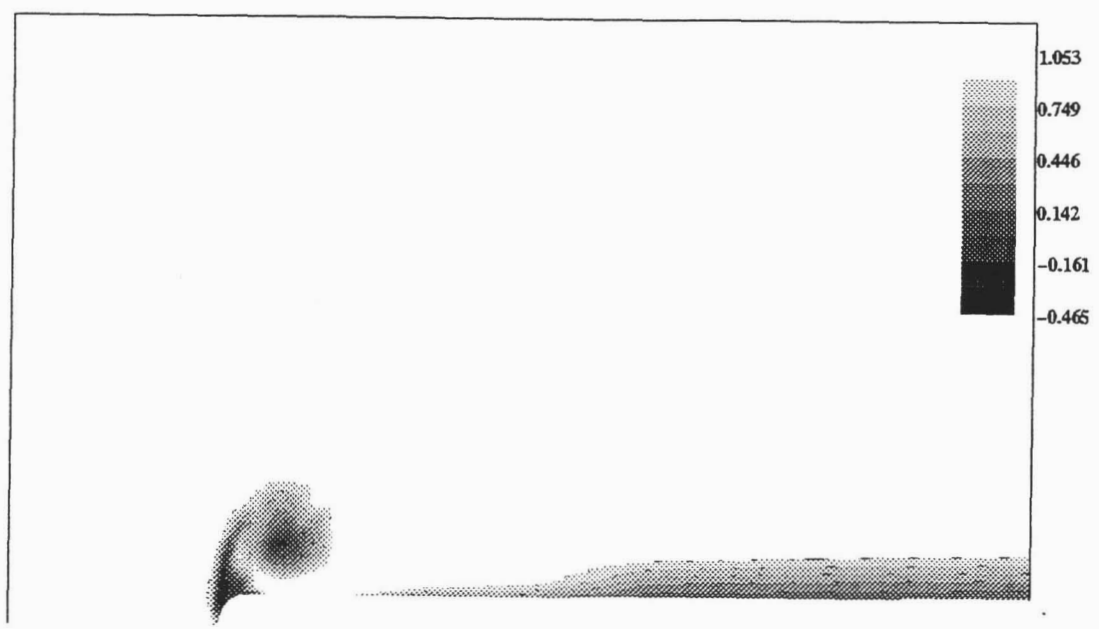

Figure 3.9d,e Total Pressure Contours: d) $x/c = -0.197$**, e)** $x/c = -0.114$

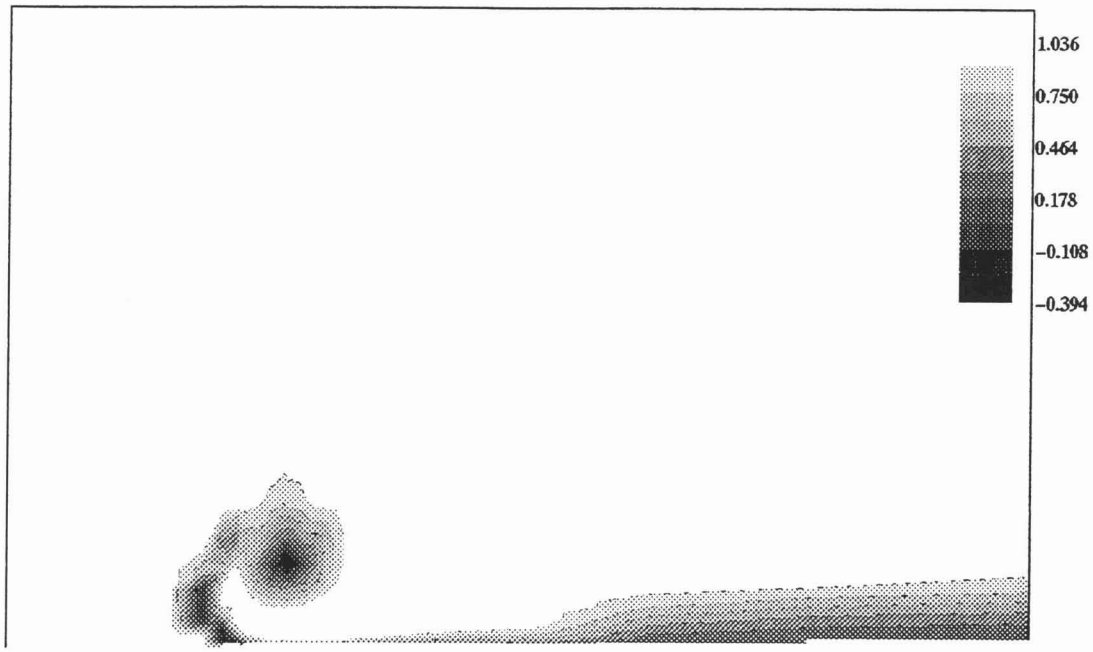

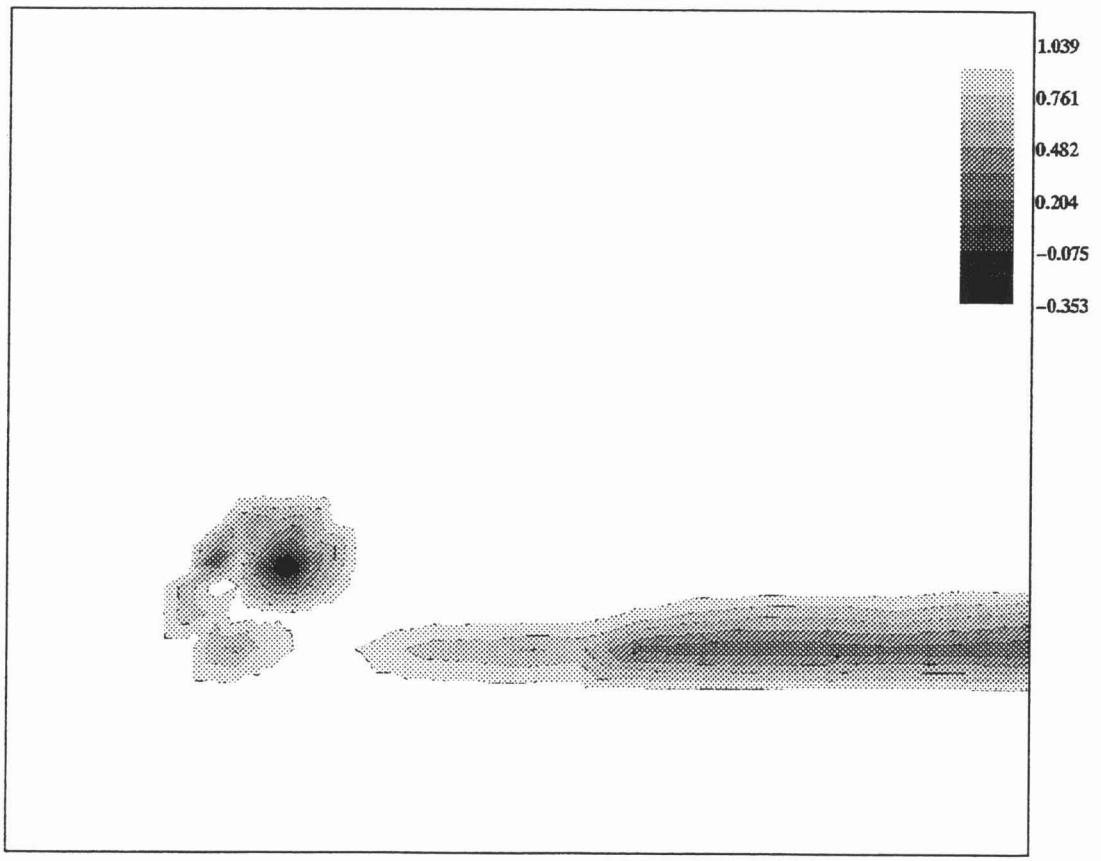

Figure 3.9f,g Total Pressure Contours: f) $x/c = -0.010$, **g)** $x/c = 0.005$

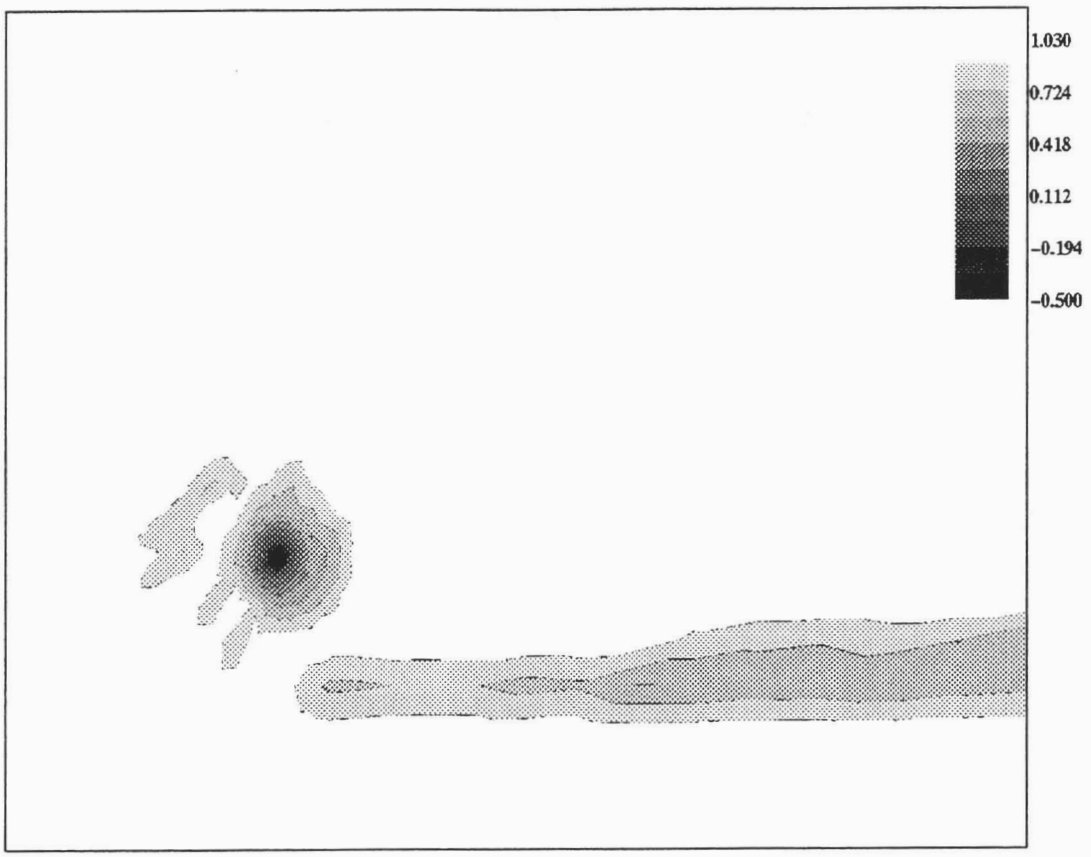

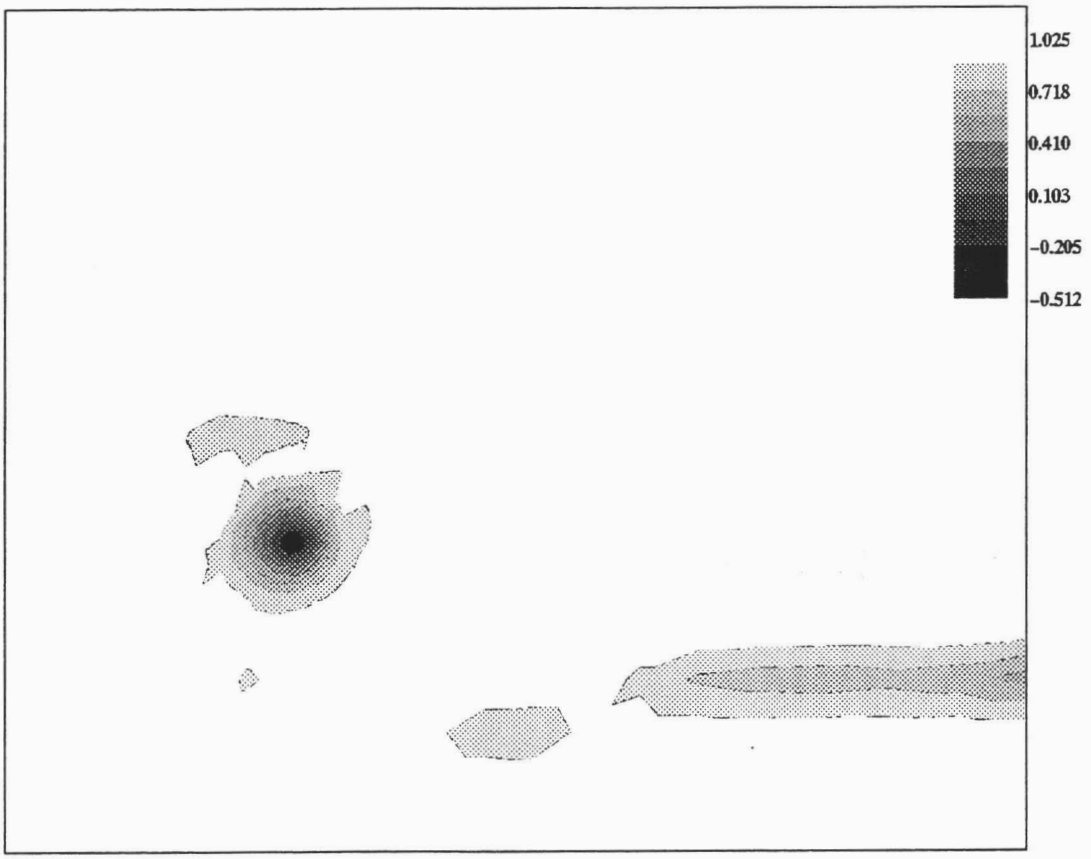

Figure 3.9h,i Total Pressure Contours: h) $x/c = 0.125$**, i)** $x/c = 0.246$

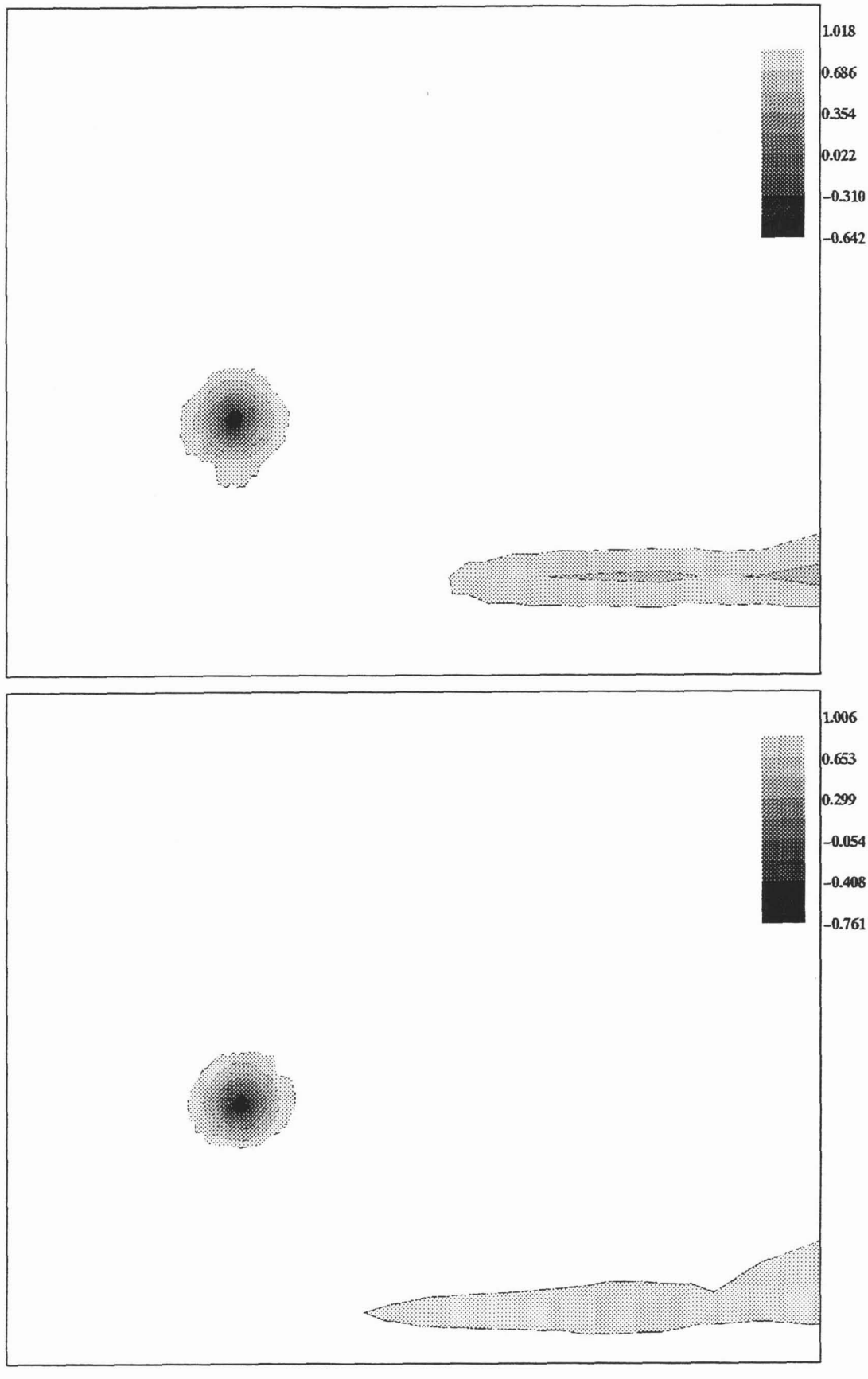

Figure 3.9j,k Total Pressure Contours: j) $x/c = 0.452$, **k)** $x/c = 0.678$

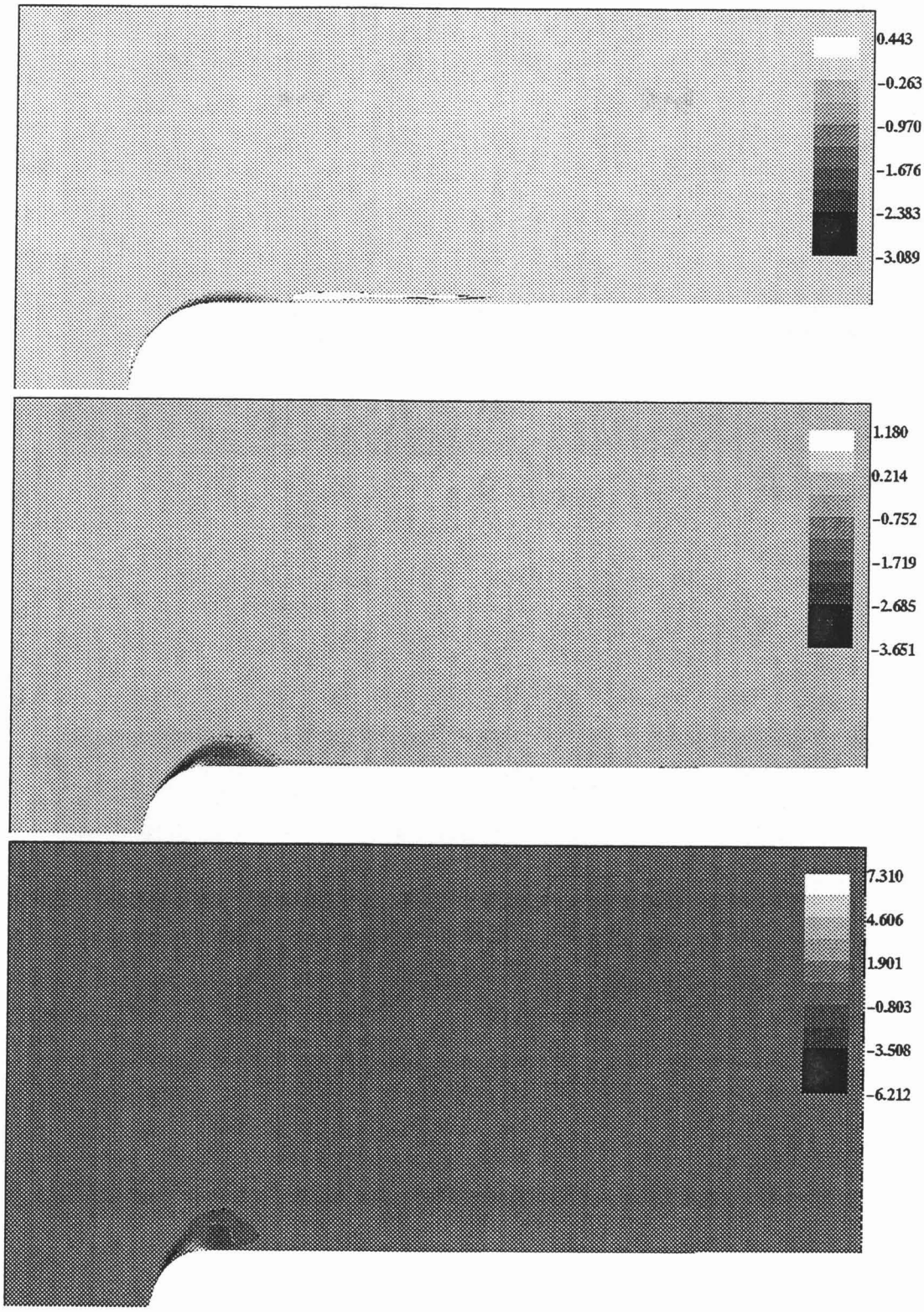

Figure 3.10a,b,c Axial Vorticity Contours: a) $x/c = -0.591$, **b)** $x/c = -0.394$, **c)** $x/c = -0.296$

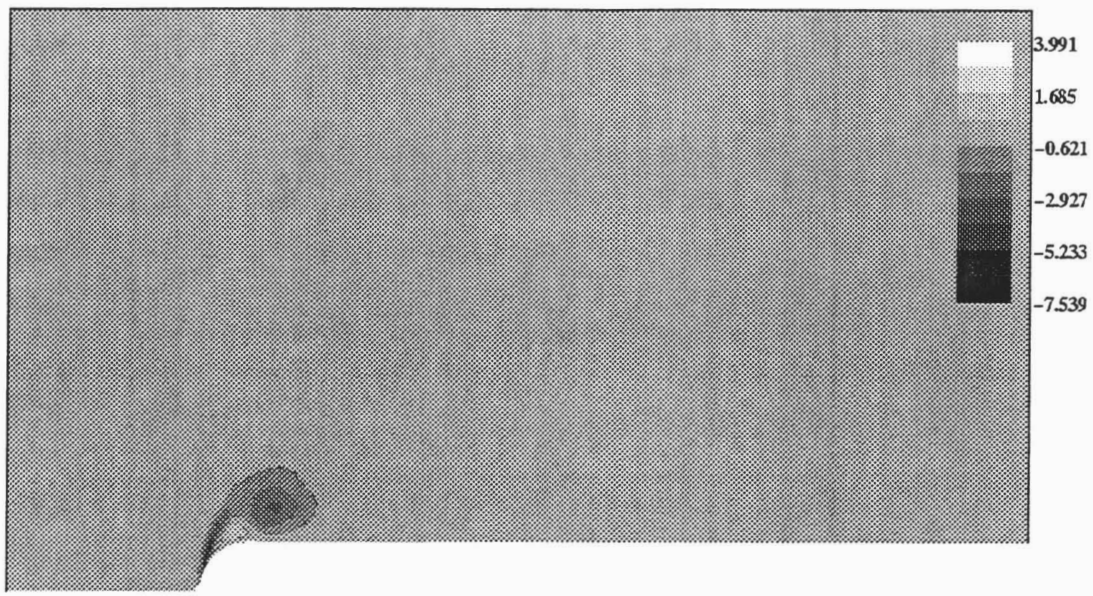

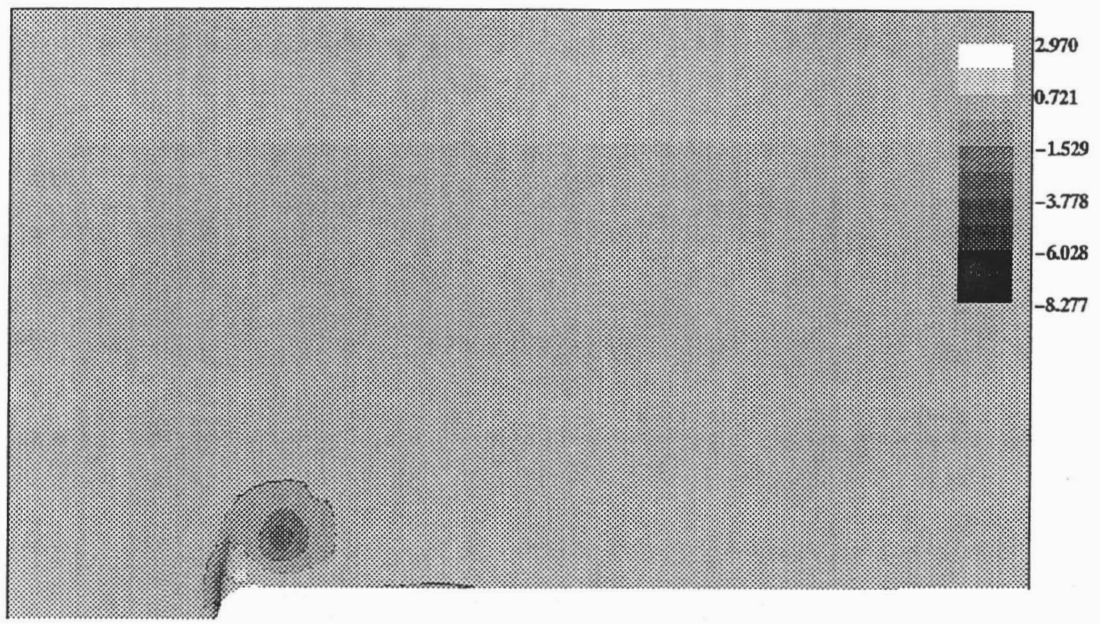

Figure 3.10d,e Axial Vorticity Contours: d) $x/c = -0.197$**, e)** $x/c = -0.114$

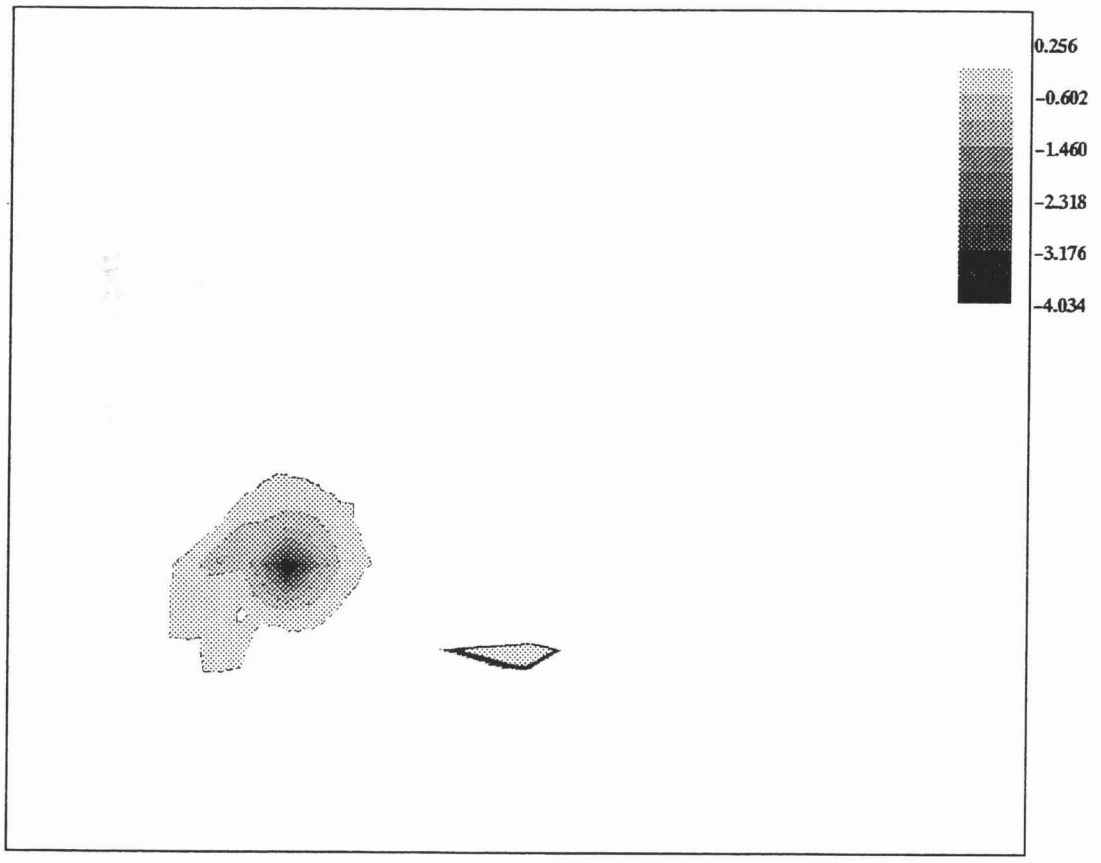

Figure 3.10f,g Axial Vorticity Contours: f) $x/c = -0.010$, **g)** $x/c = 0.005$

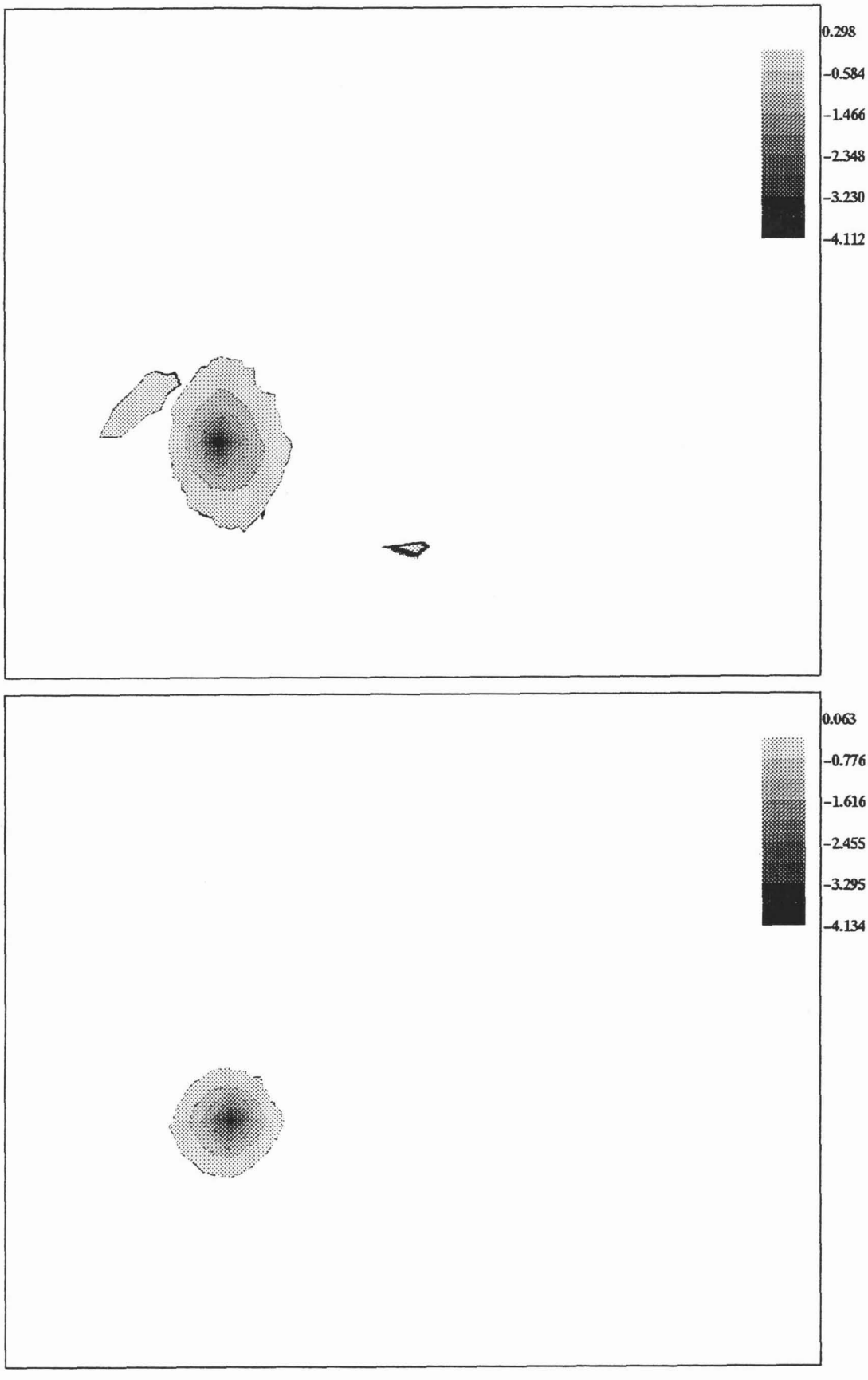

Figure 3.10h,i Axial Vorticity Contours: h) $x/c = 0.125$**, i)** $x/c = 0.246$

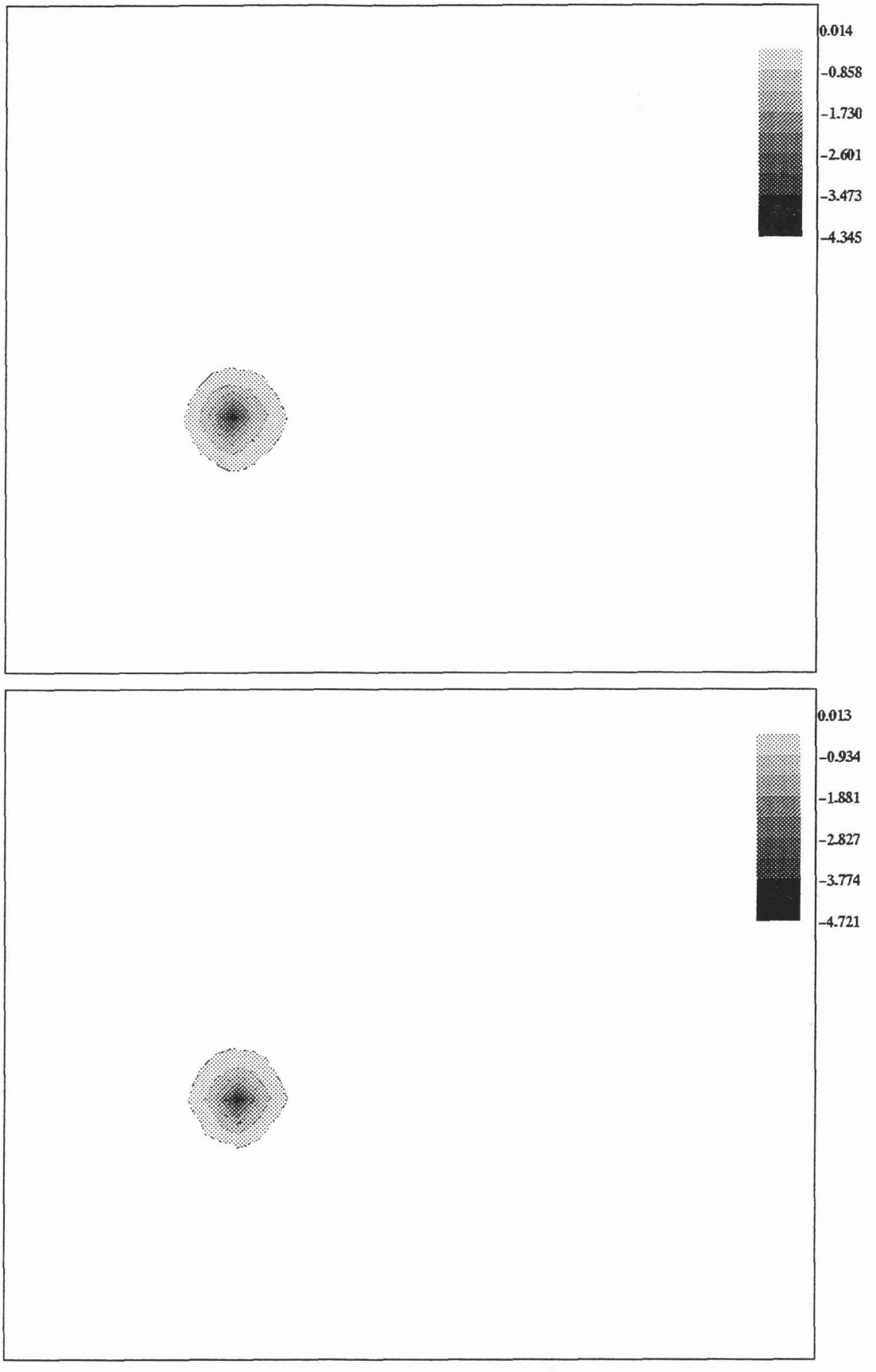

Figure 3.10j,k Axial Vorticity Contours: j) $x/c = 0.452$**, k)** $x/c = 0.678$

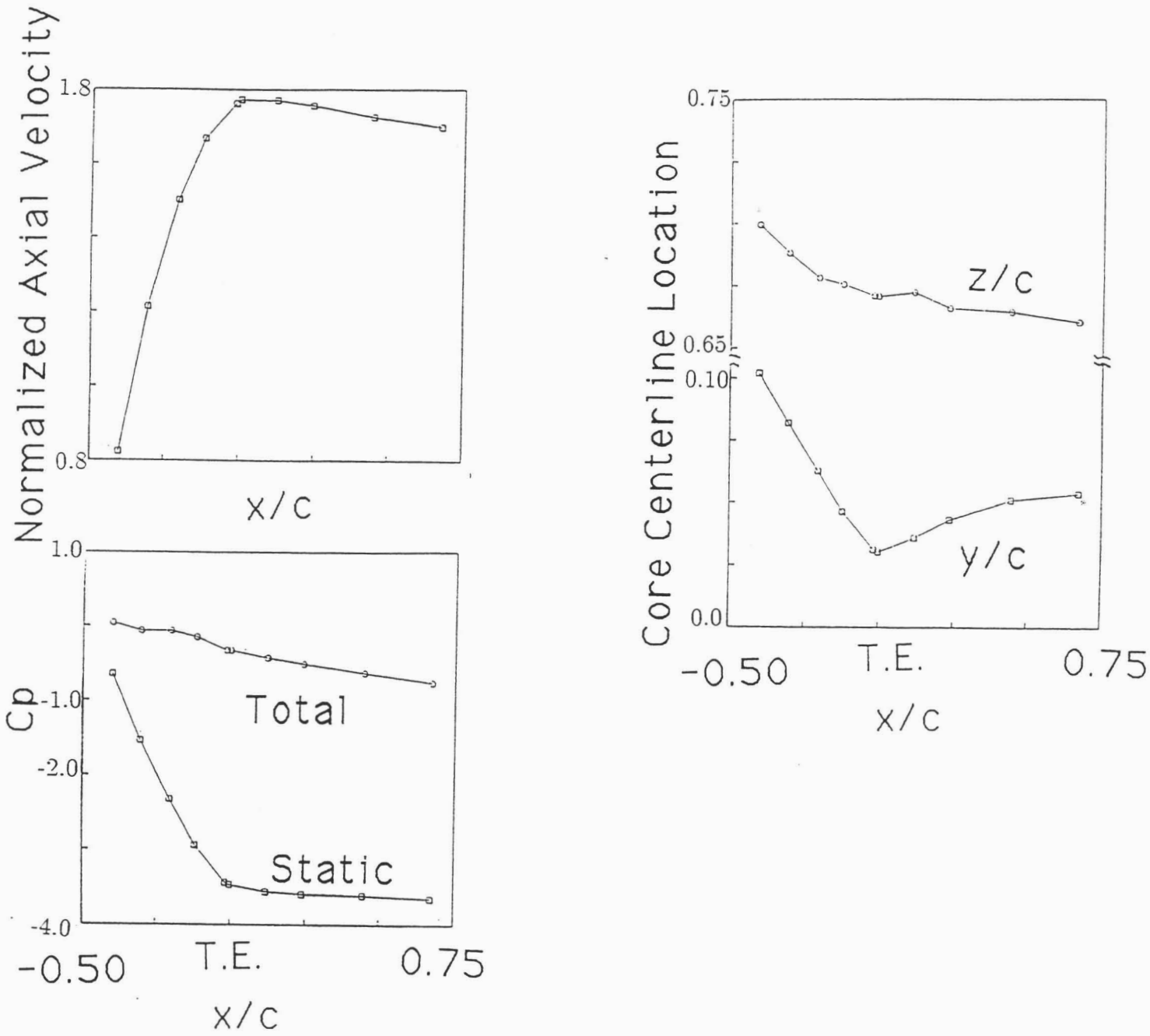

Figure 3.11 Axial Progression of Various Flow Quantities Along Vortex Centerline

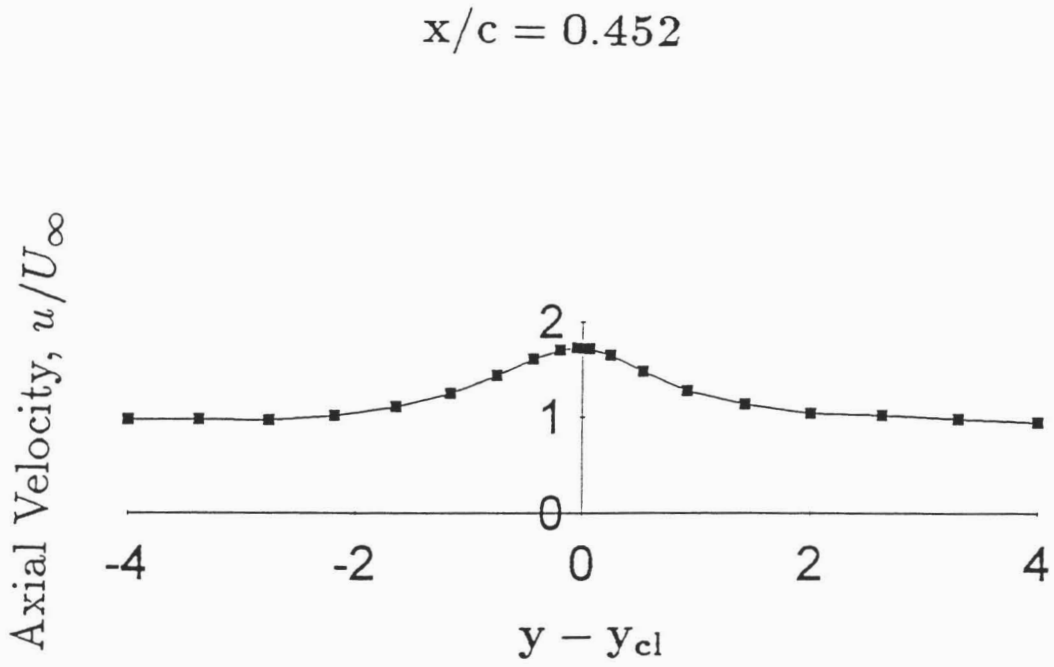

Figure 3.12 Axial Velocity Profile vs y-Distance from Vortex Centerline

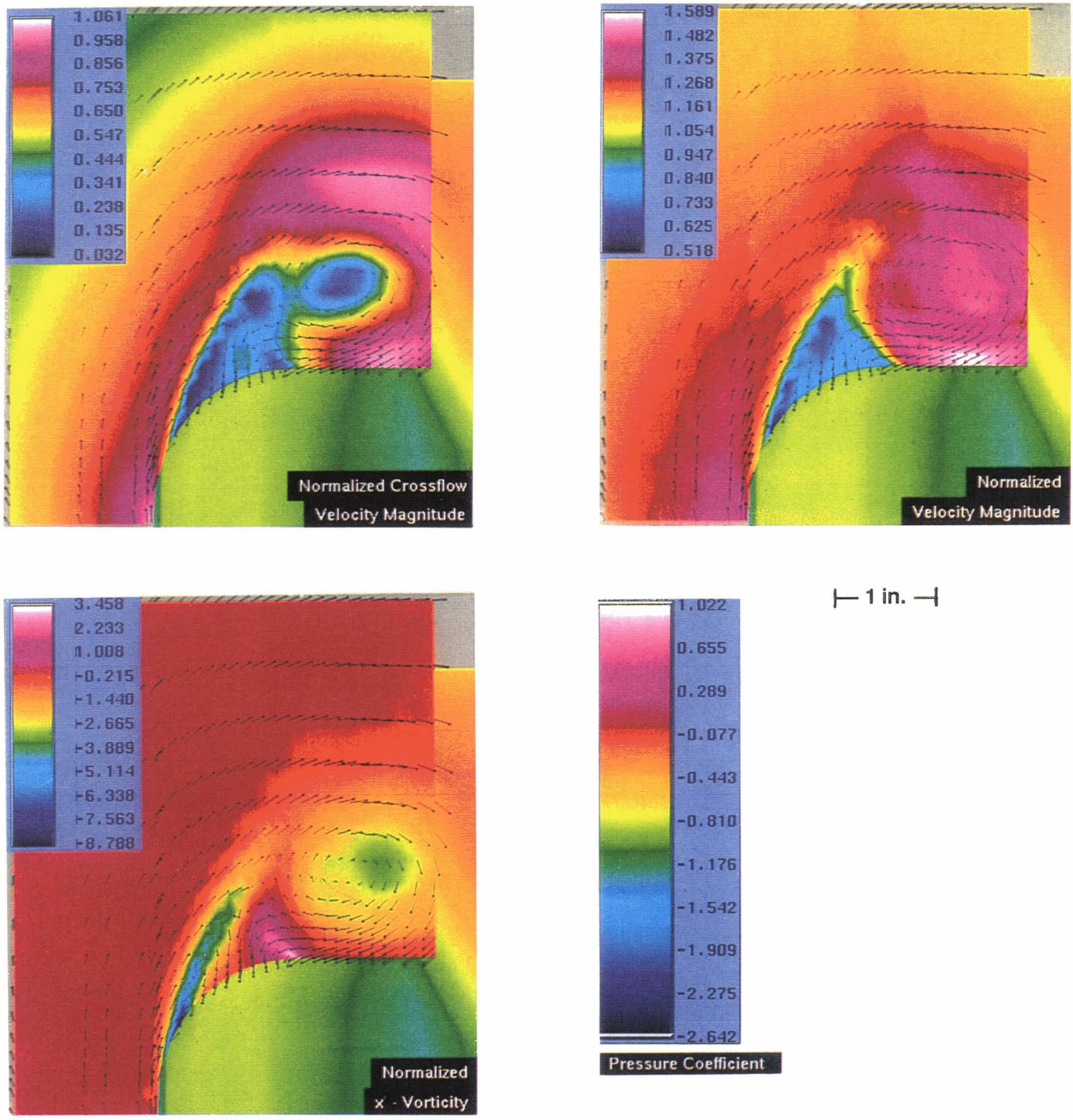

Figure 3.13 High Resolution Crossflow Plane at $x/c = -0.114$

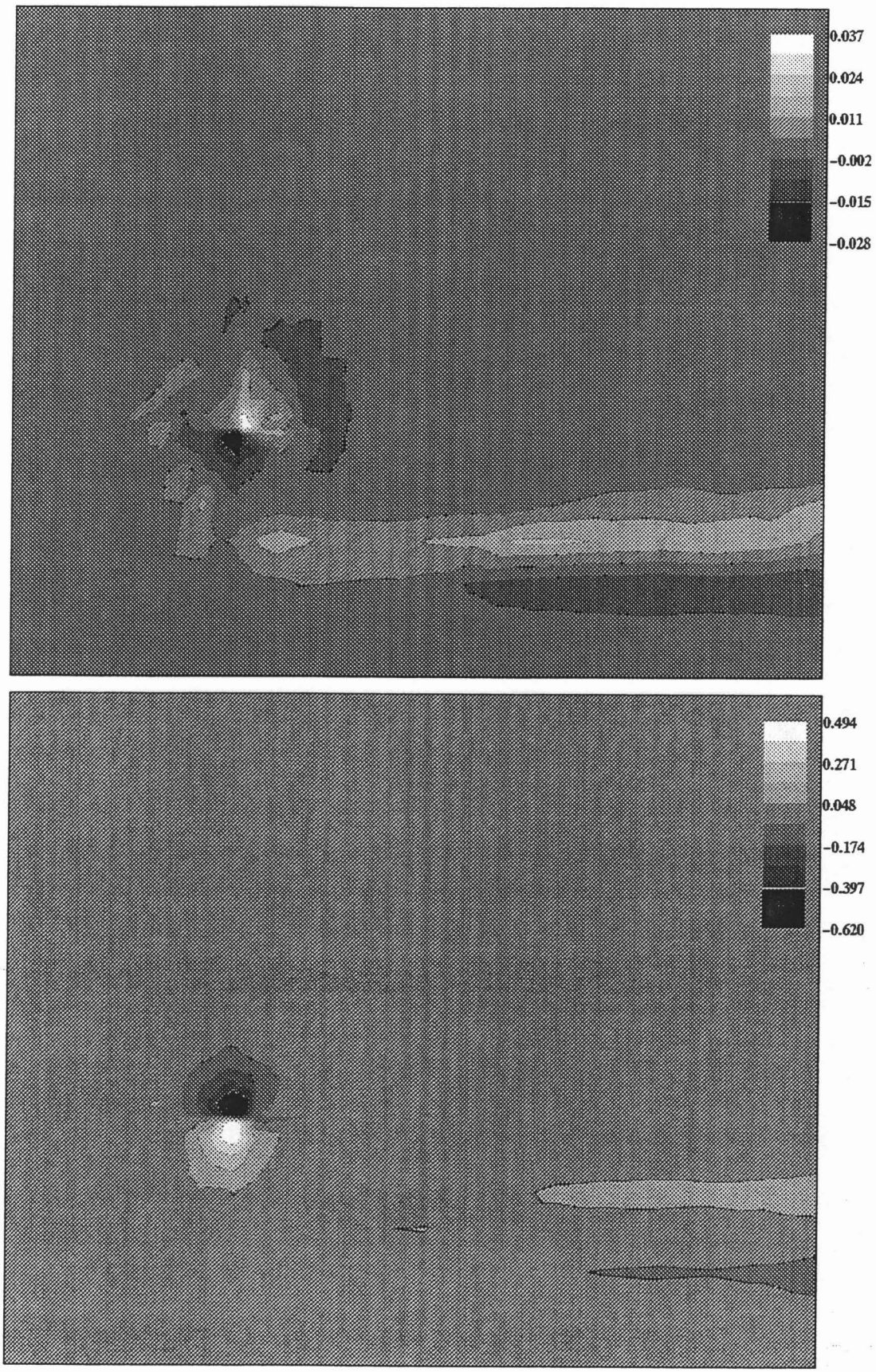

Figure 3.14a,b Mean Velocity Gradients ($x/c = 0.125$)**: a)** $\partial U/\partial x$**, b)** $\partial U/\partial y$

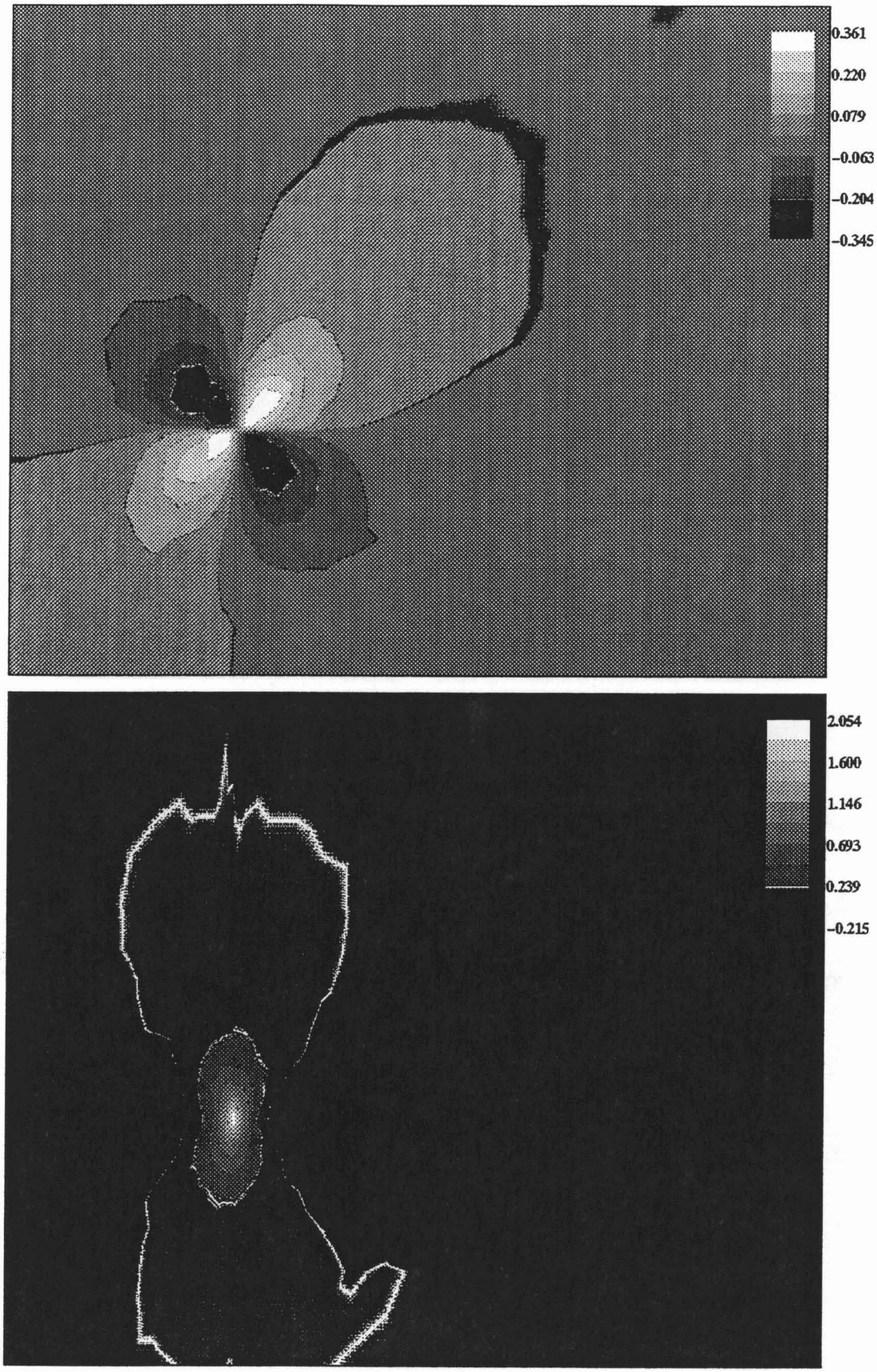

Figure 3.14c,d Mean Velocity Gradients ($x/c = 0.125$): a) $\partial V/\partial y$, b) $\partial V/\partial z$

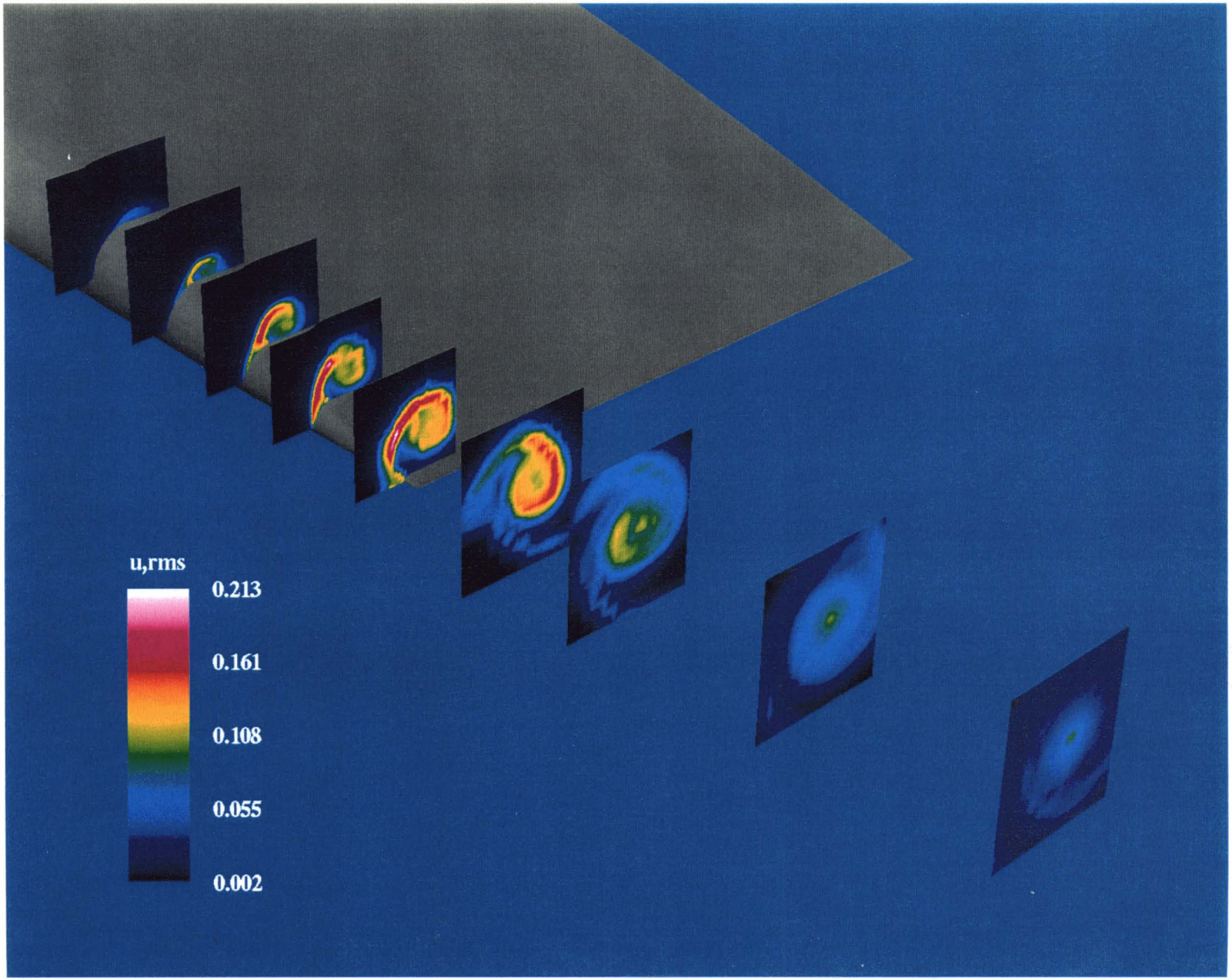

Figure 3.15a Perspective View of $\hat{u}$

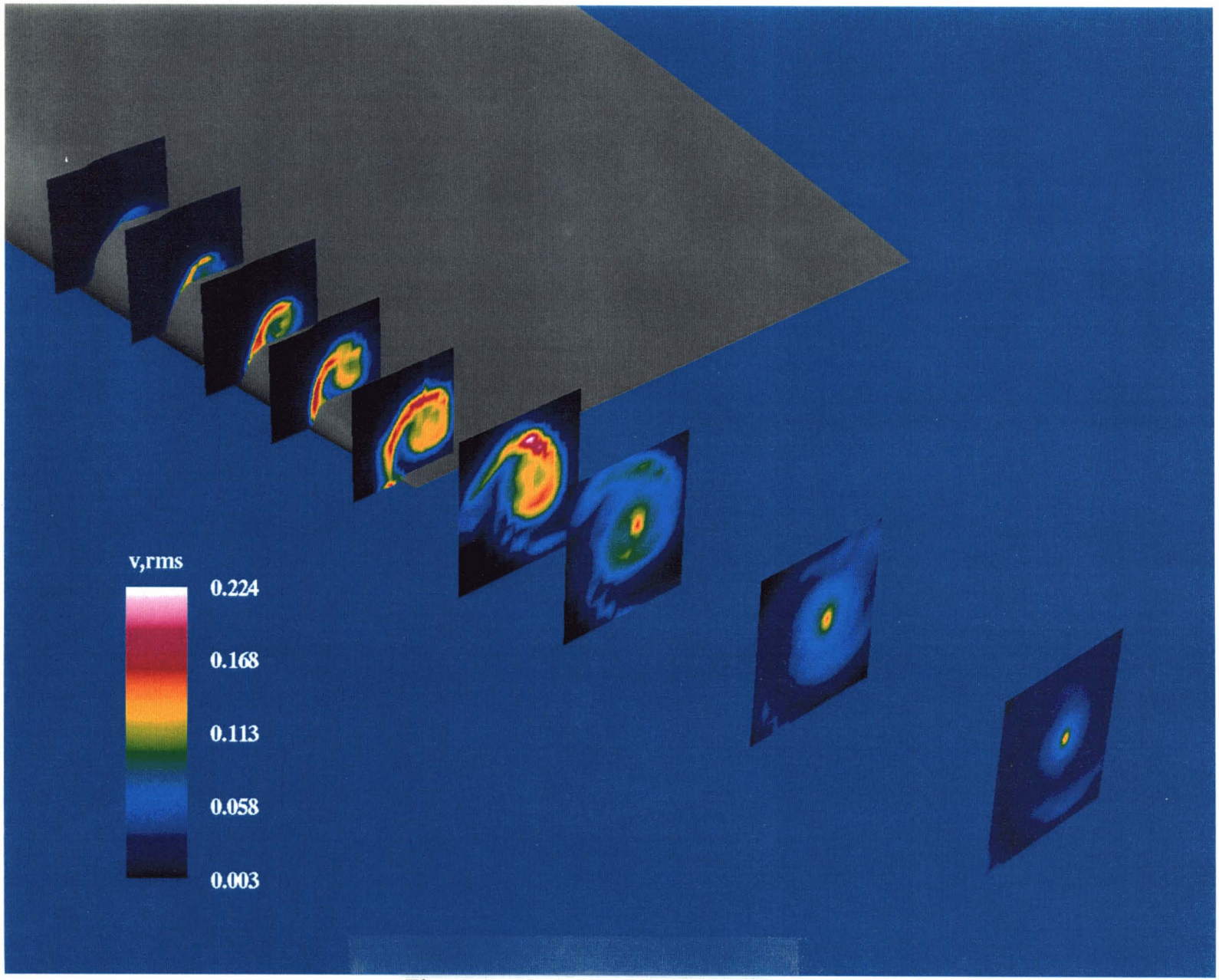

Figure 3.15b Perspective View of $\hat{v}$

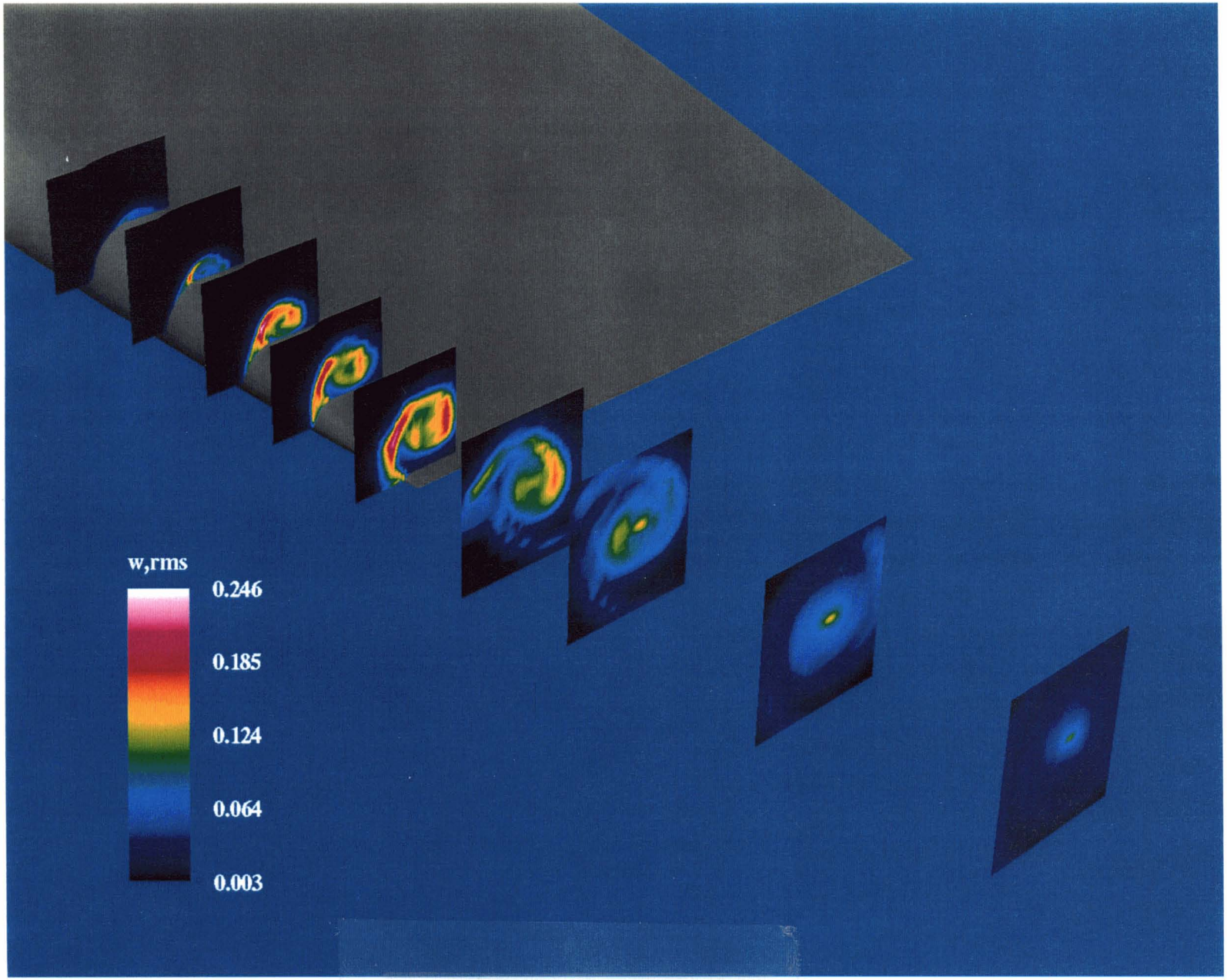

Figure 3.15c Perspective View of $\hat{w}$

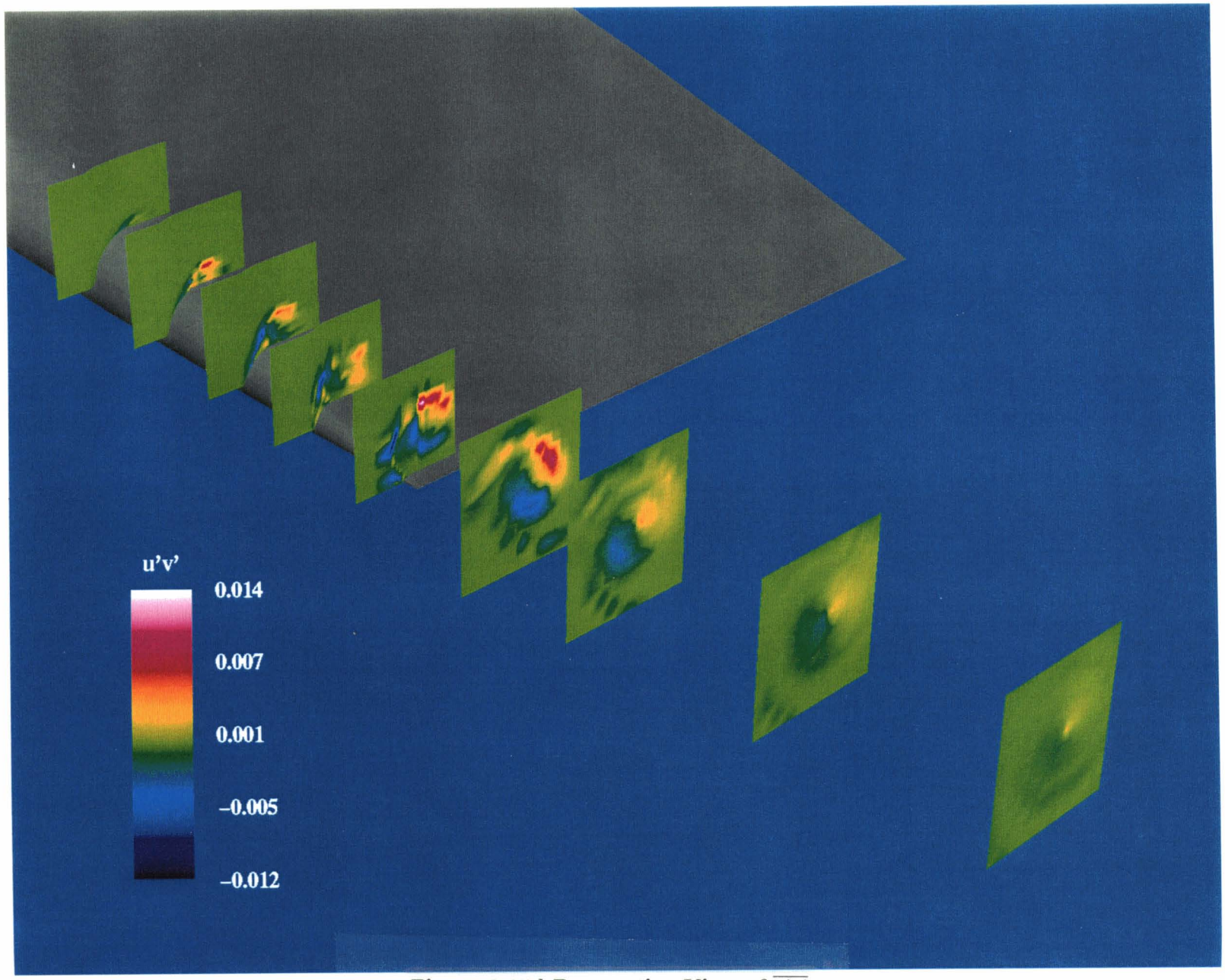

Figure 3.15d Perspective View of $\overline{u'v'}$

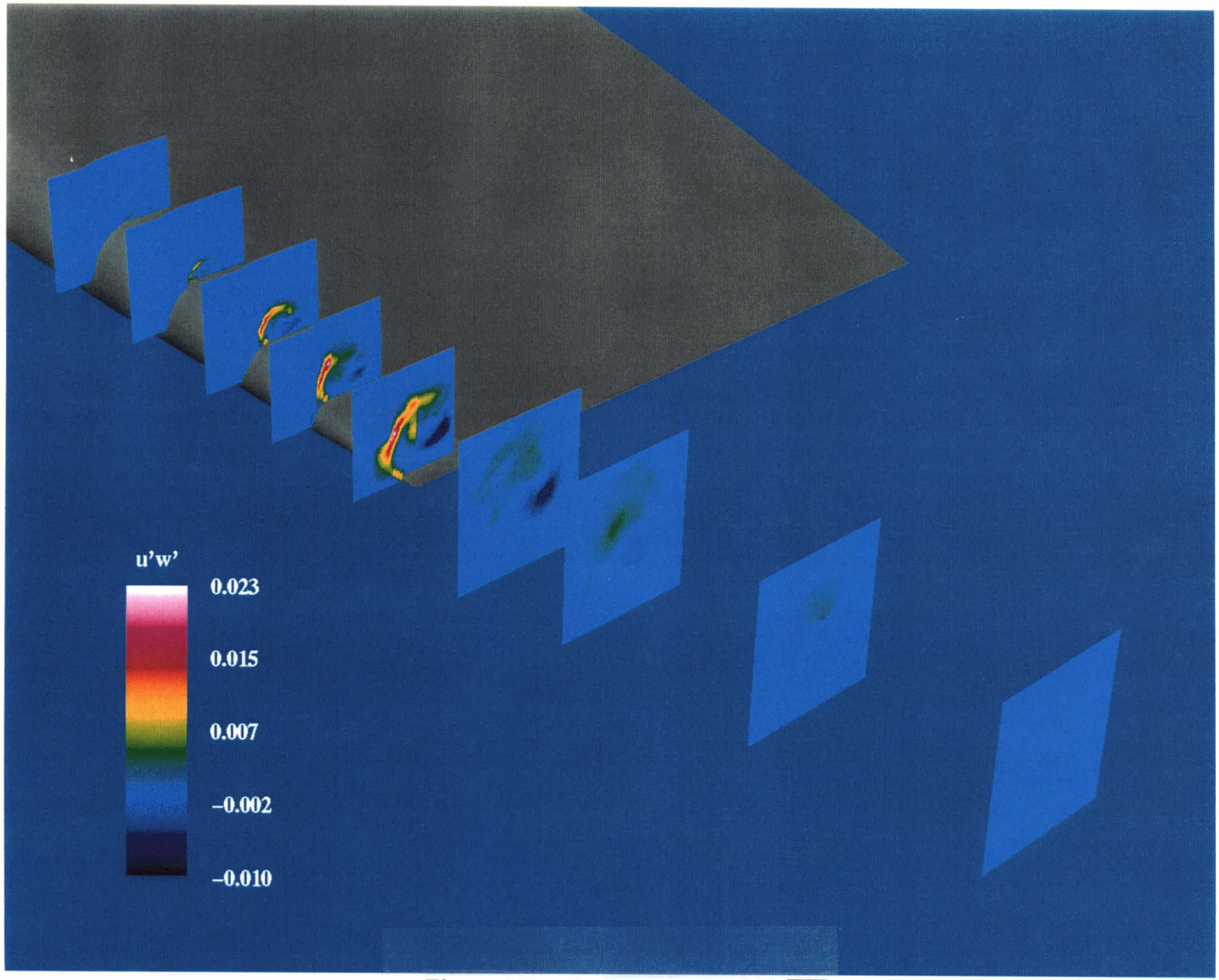

Figure 3.15e Perspective View of $\overline{u'w'}$

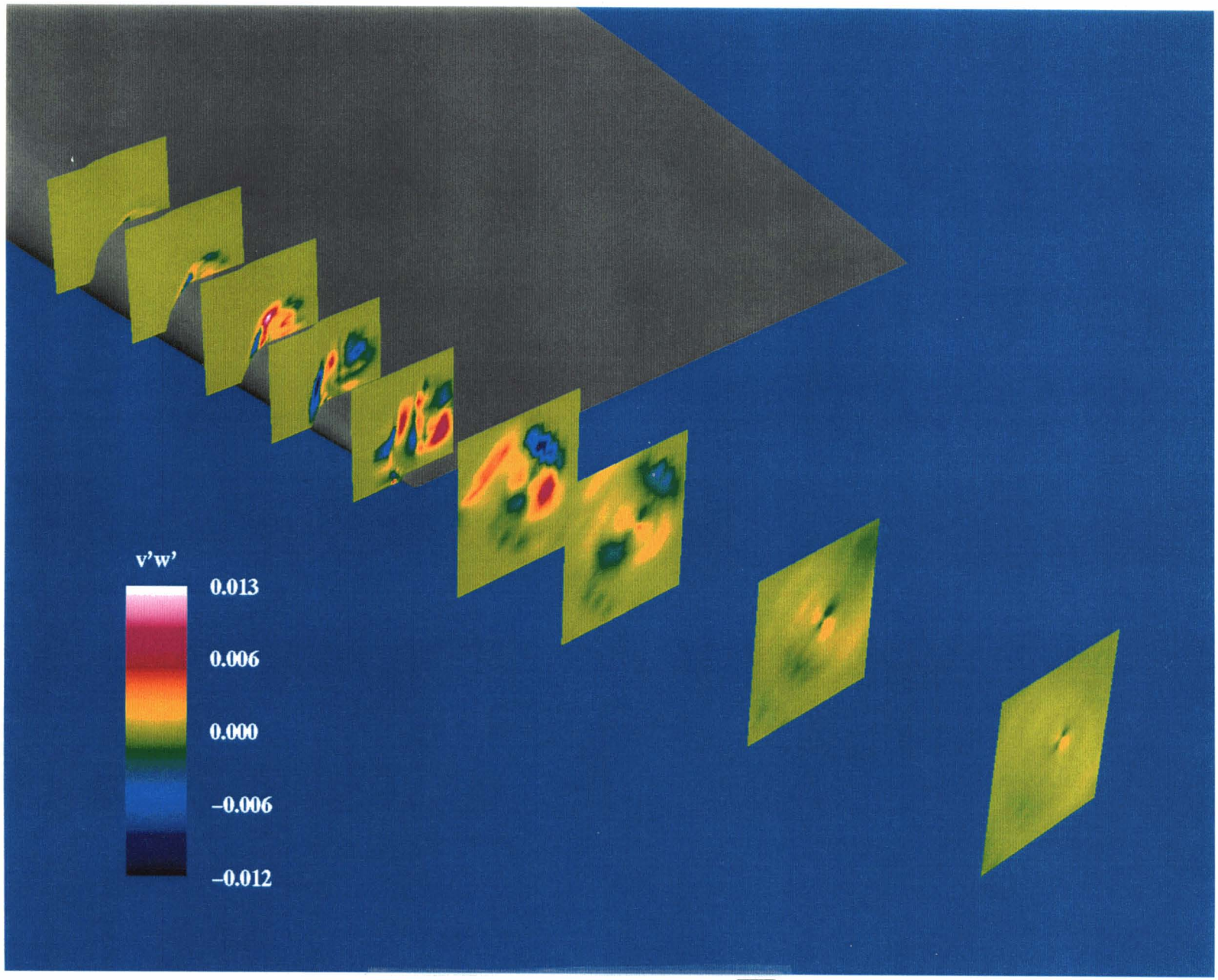

Figure 3.15f Perspective View of $\overline{v'w'}$

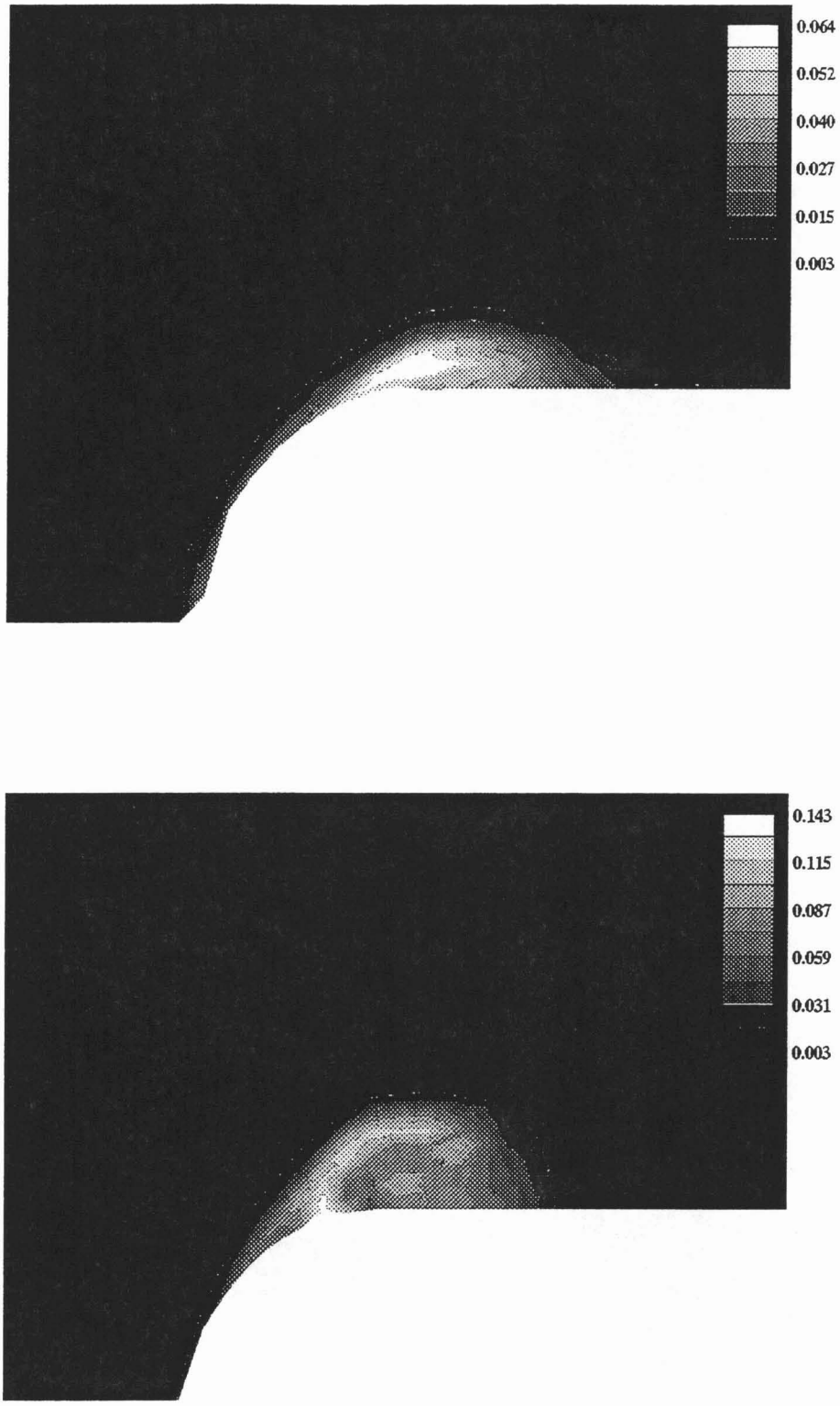

Figure 3.16a,b Contours of $\hat{u}$: a) $x/c = -0.394$, b) $x/c = -0.296$

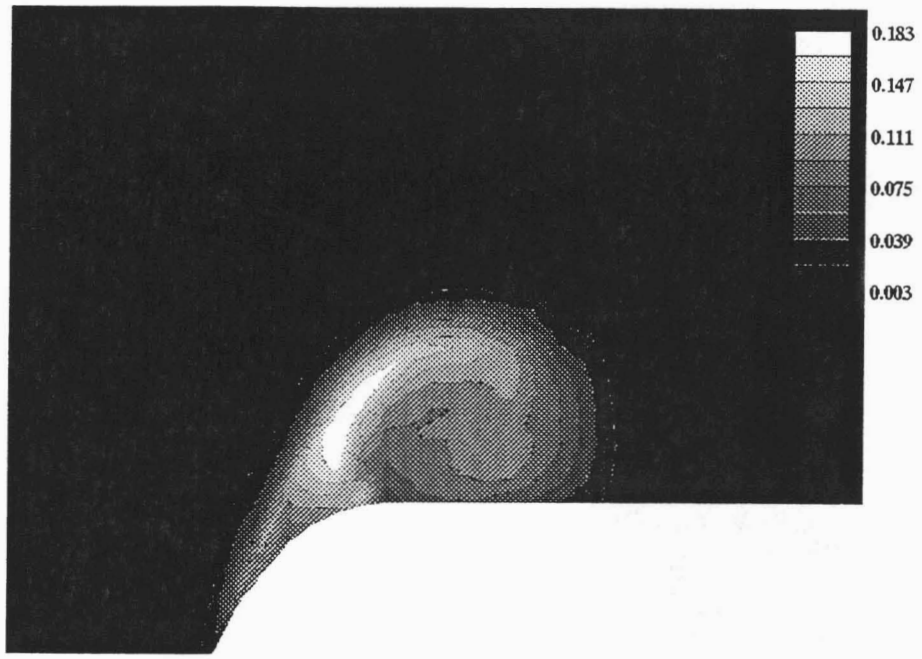

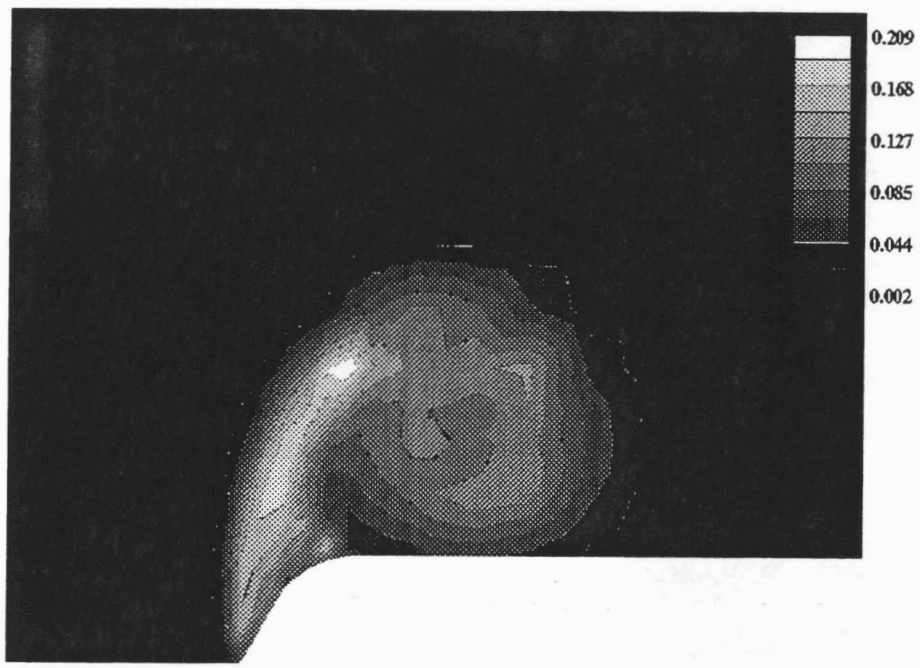

Figure 3.16c,d Contours of $\hat{u}$: c) $x/c = -0.197$, d) $x/c = -0.114$

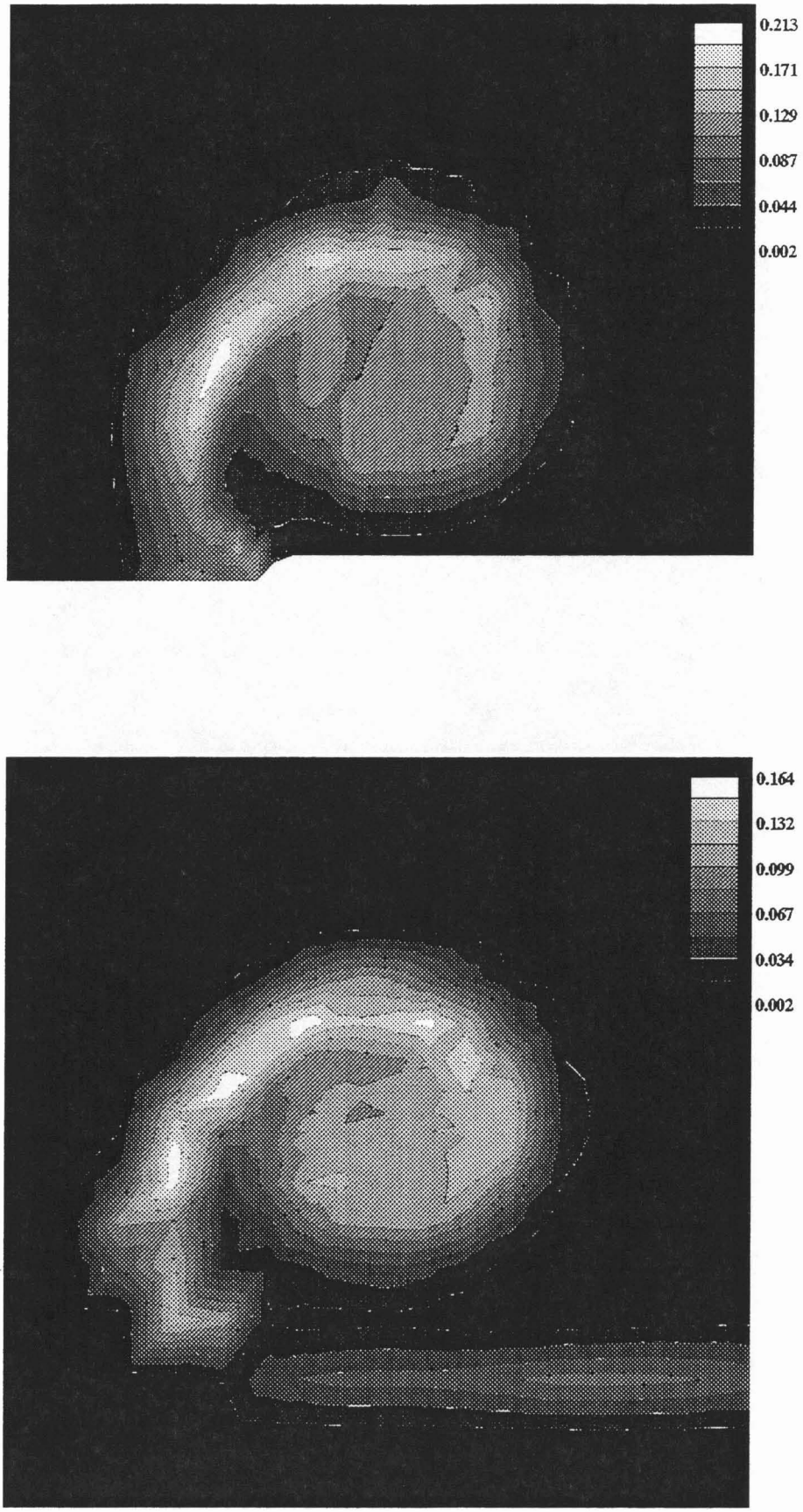

Figure 3.16e,f Contours of $\hat{u}$: e) $x/c = -0.010$, f) $x/c = 0.005$

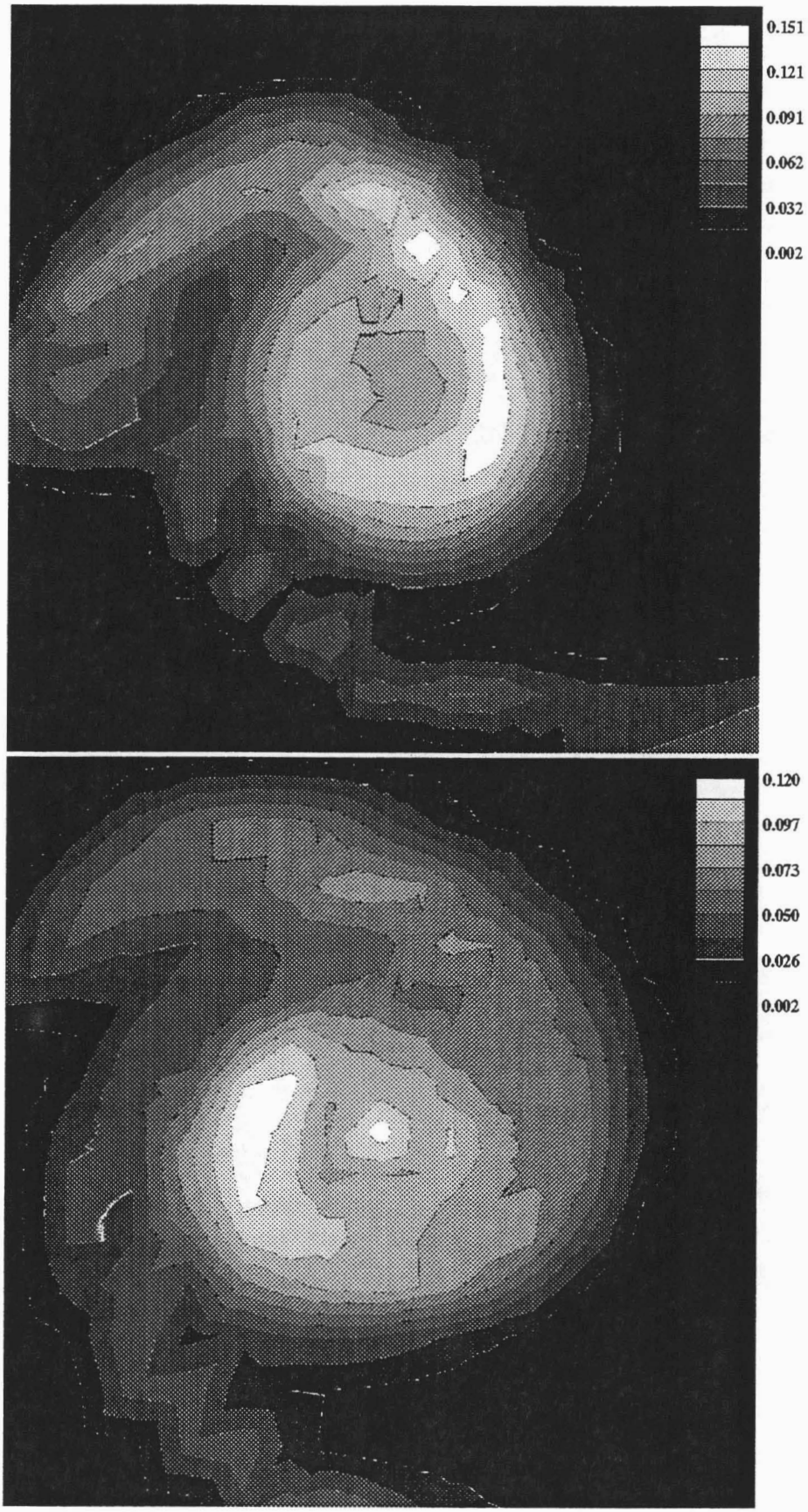

Figure 3.16g,h Contours of $\hat{u}$: g) $x/c = 0.125$, h) $x/c = 0.246$

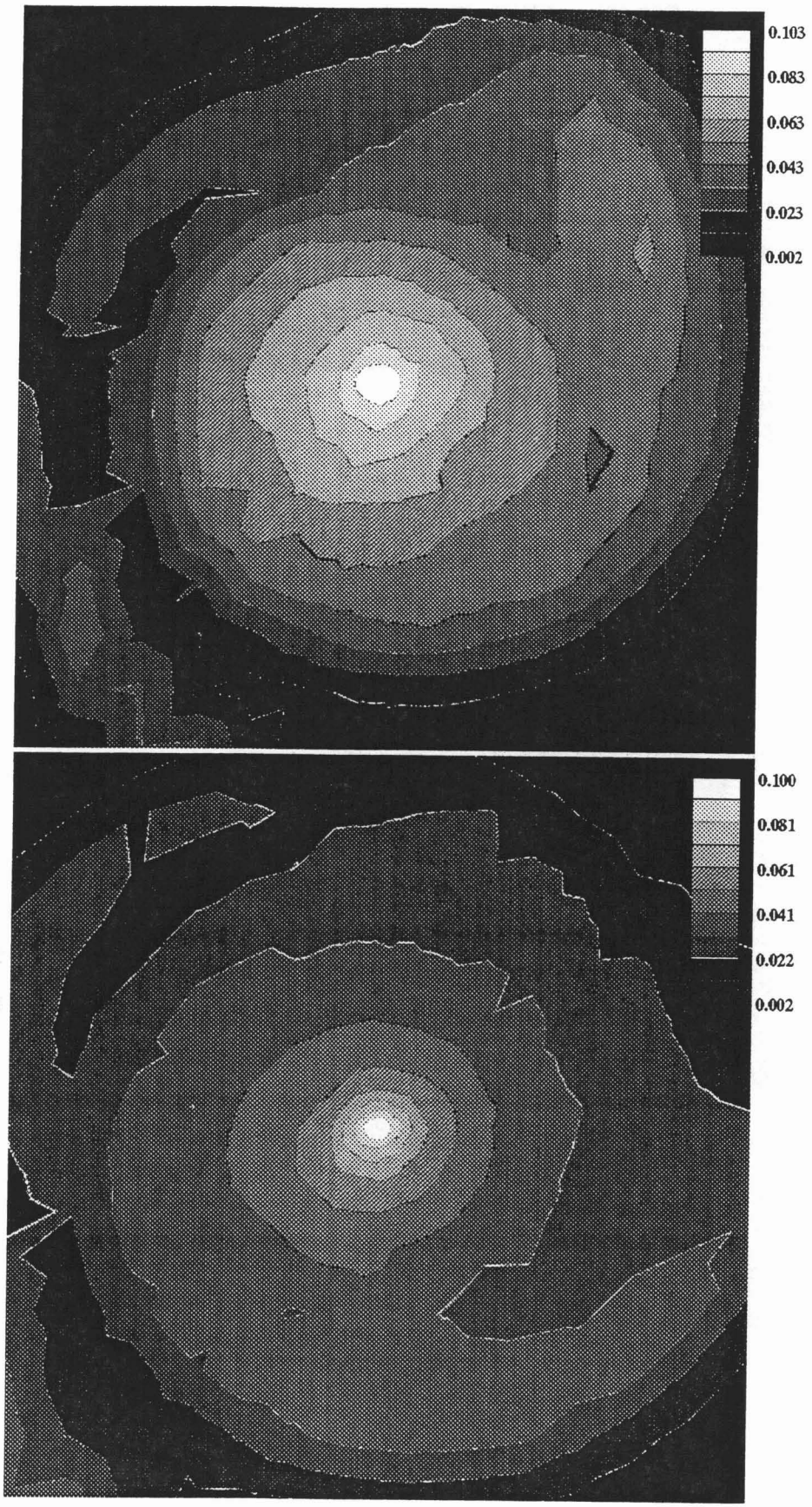

Figure 3.16i,j Contours of $\hat{u}$: i) $x/c = 0.452$, j) $x/c = 0.678$

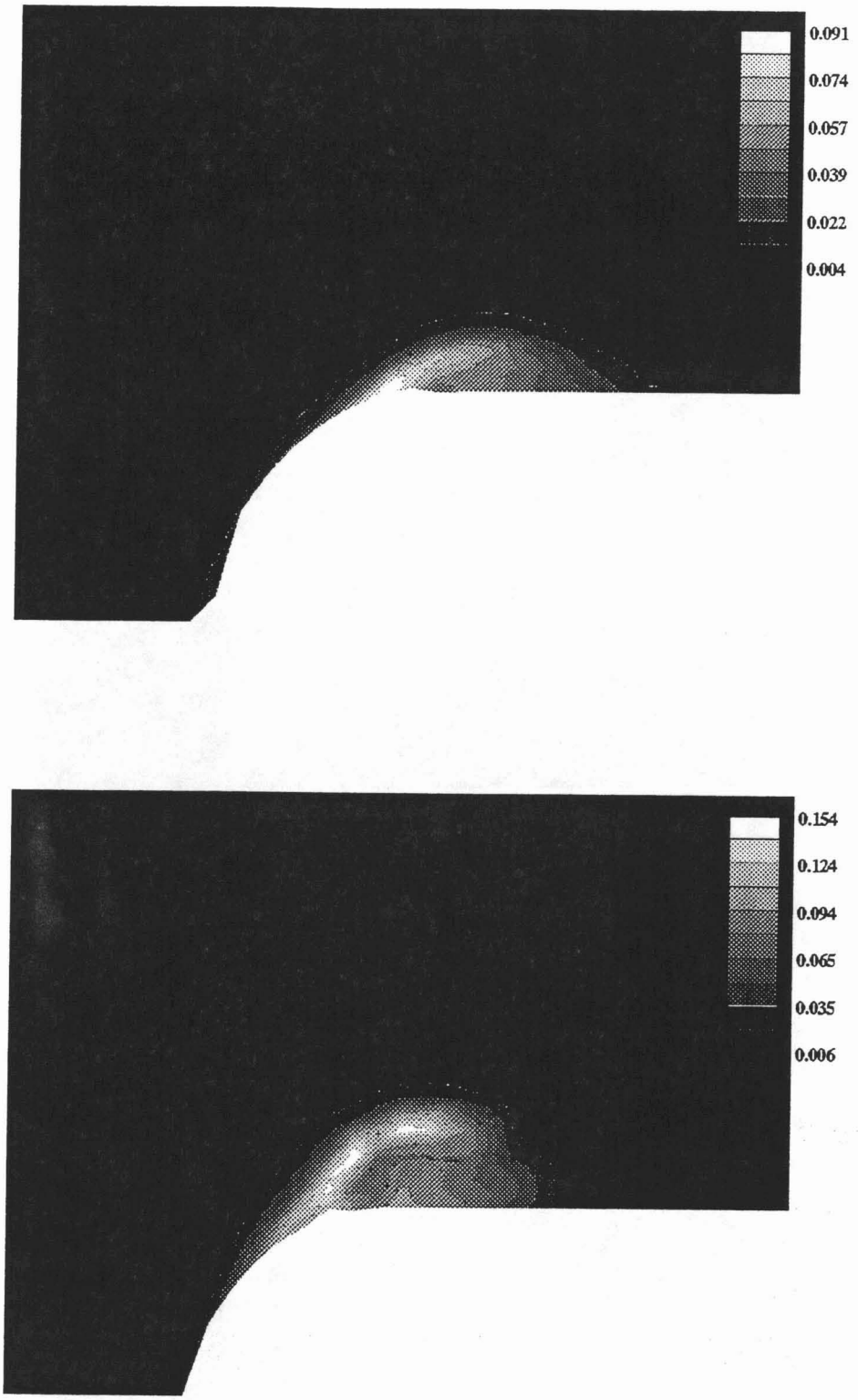

Figure 3.17a,b Contours of $\hat{v}$: a) $x/c = -0.394$, b) $x/c = -0.296$

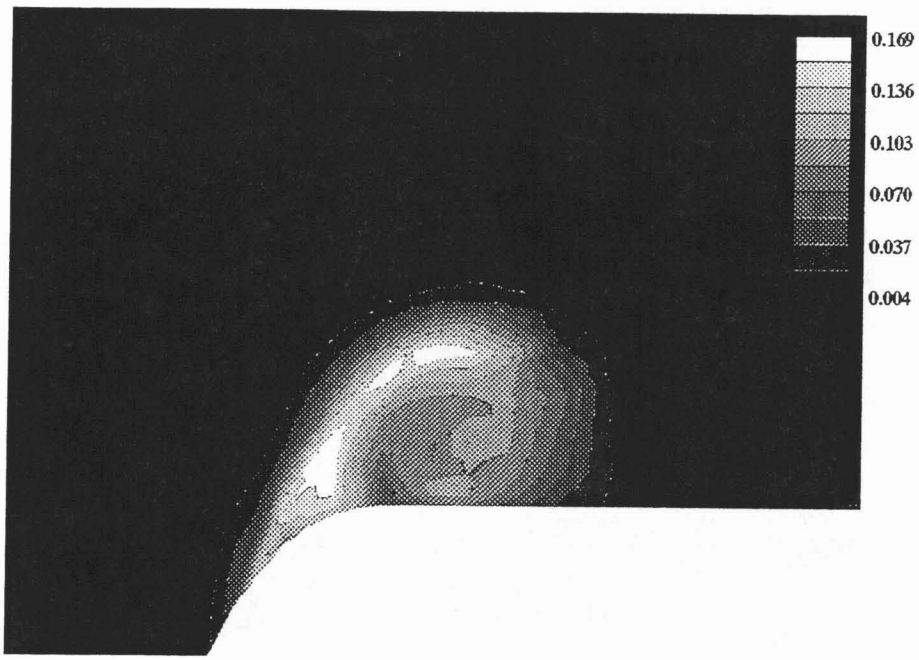

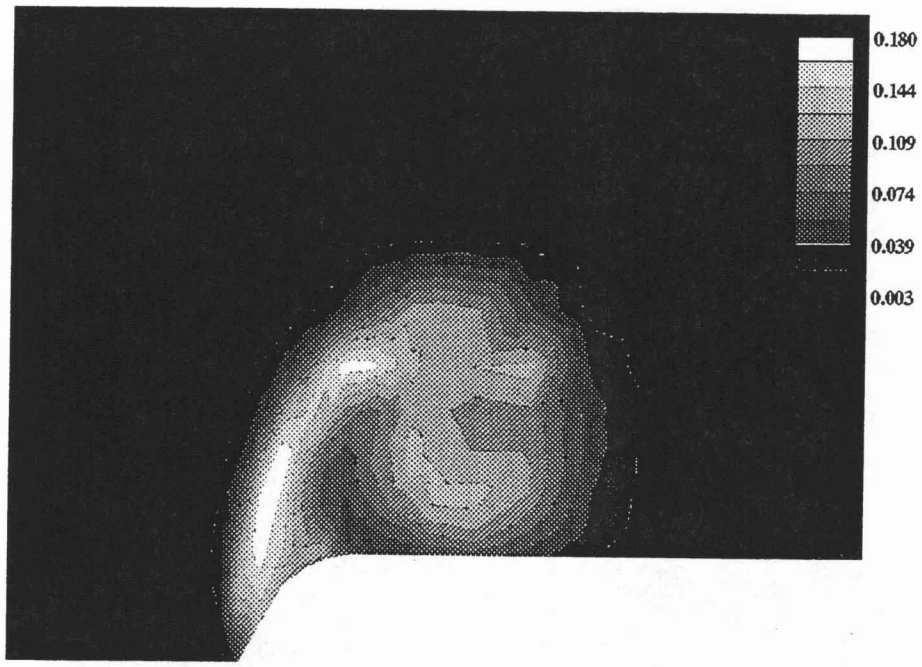

Figure 3.17c,d Contours of $\hat{v}$: c) $x/c = -0.197$, d) $x/c = -0.114$

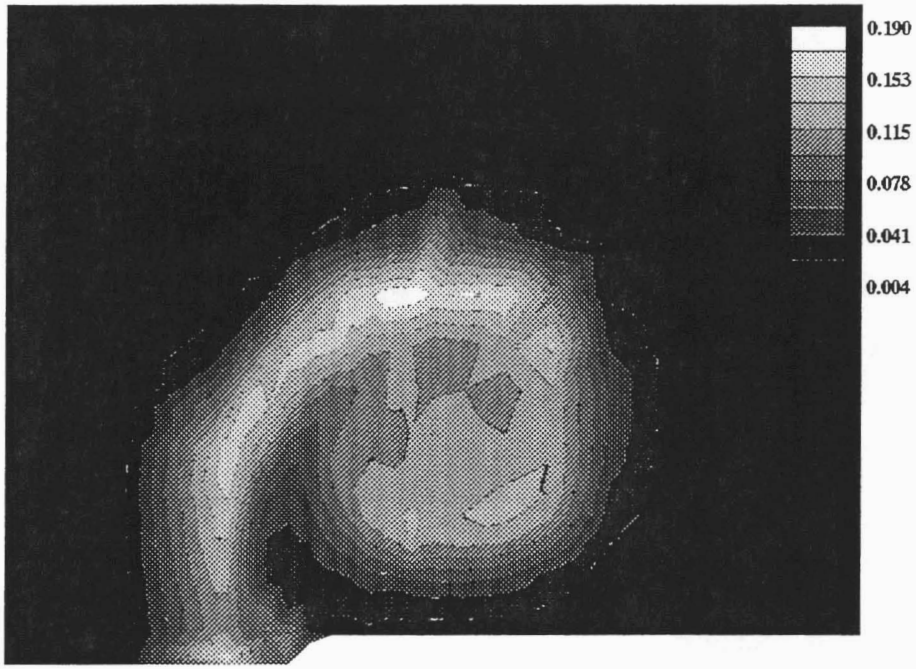

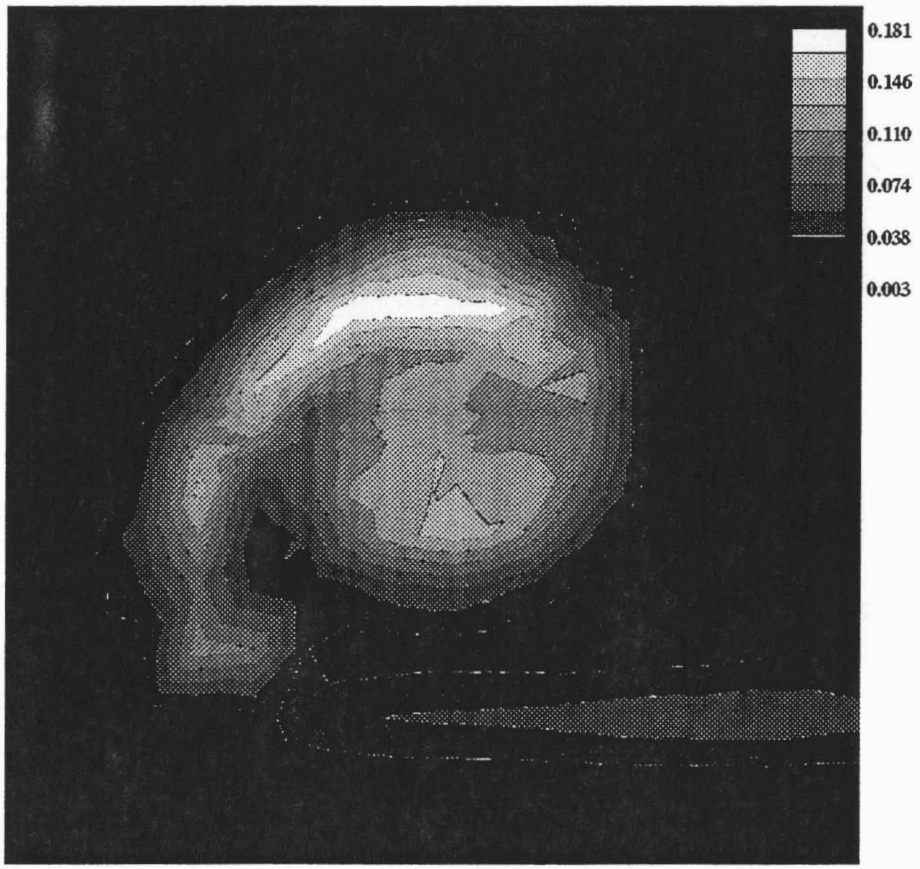

Figure 3.17e,f Contours of $\hat{v}$: e) $x/c = -0.010$, f) $x/c = 0.005$

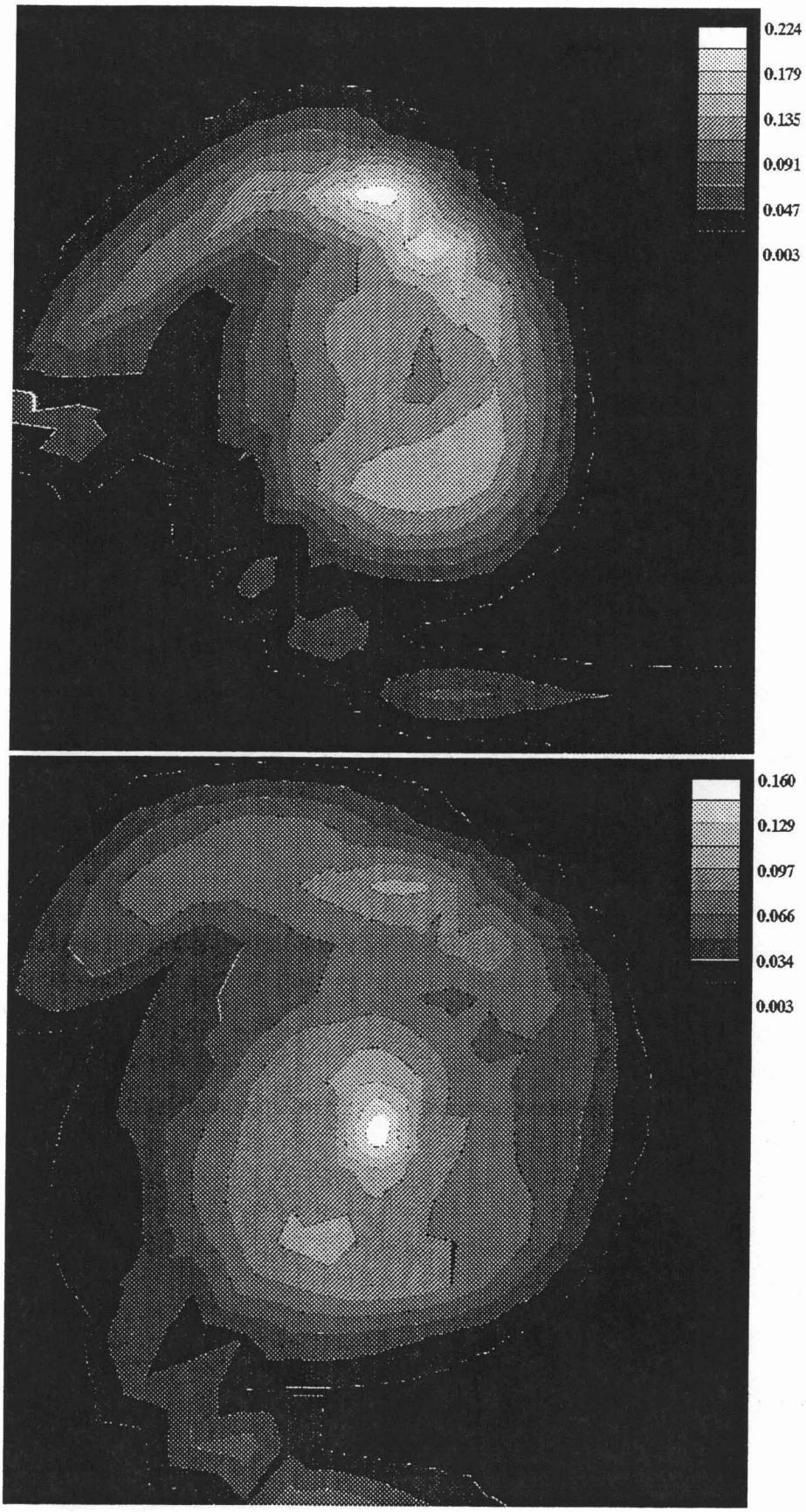

Figure 3.17g,h Contours of $\hat{v}$: g) $x/c = 0.125$, h) $x/c = 0.246$

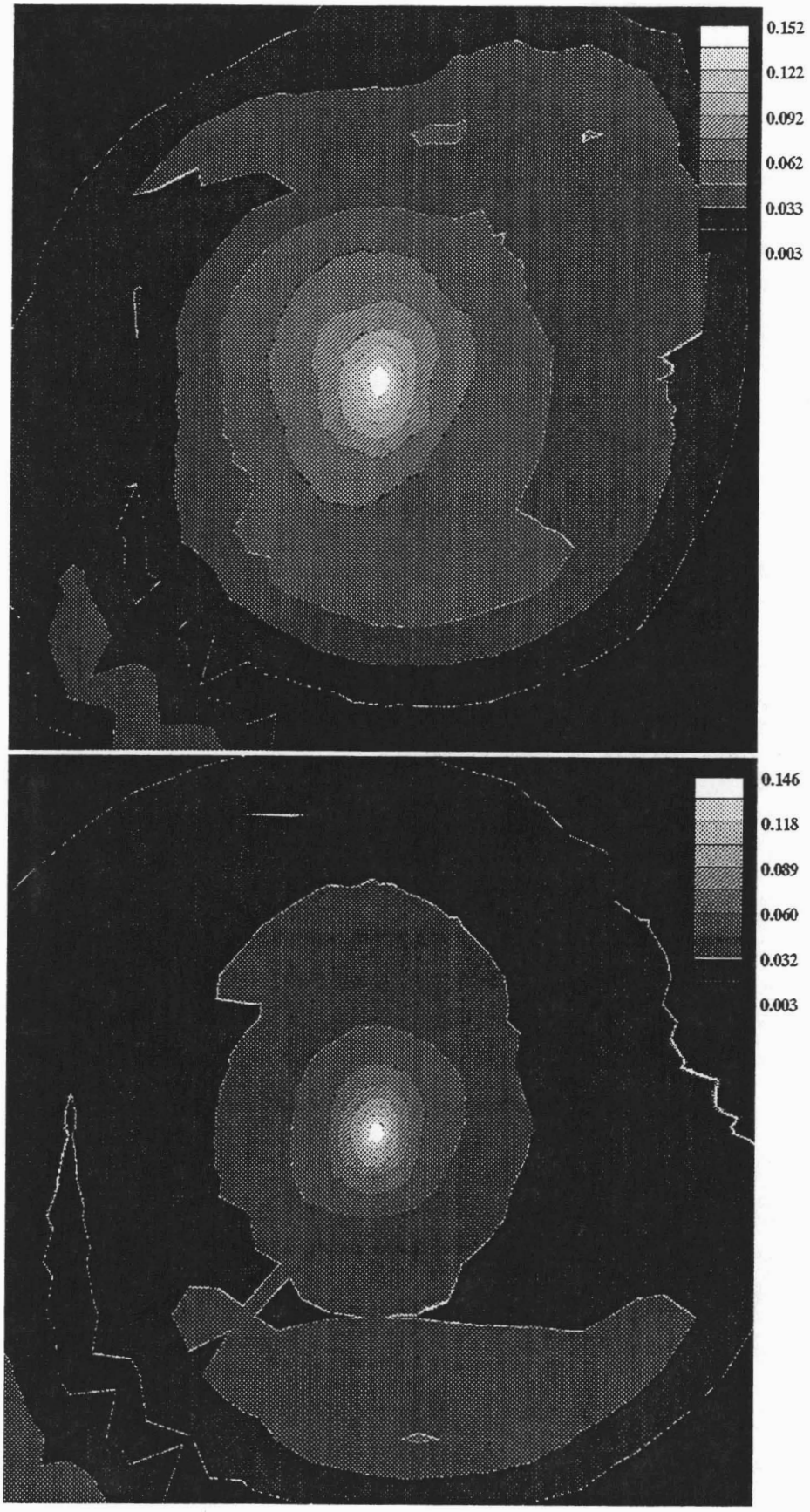

Figure 3.17i,j Contours of $\hat{v}$: i) $x/c = 0.452$, j) $x/c = 0.678$

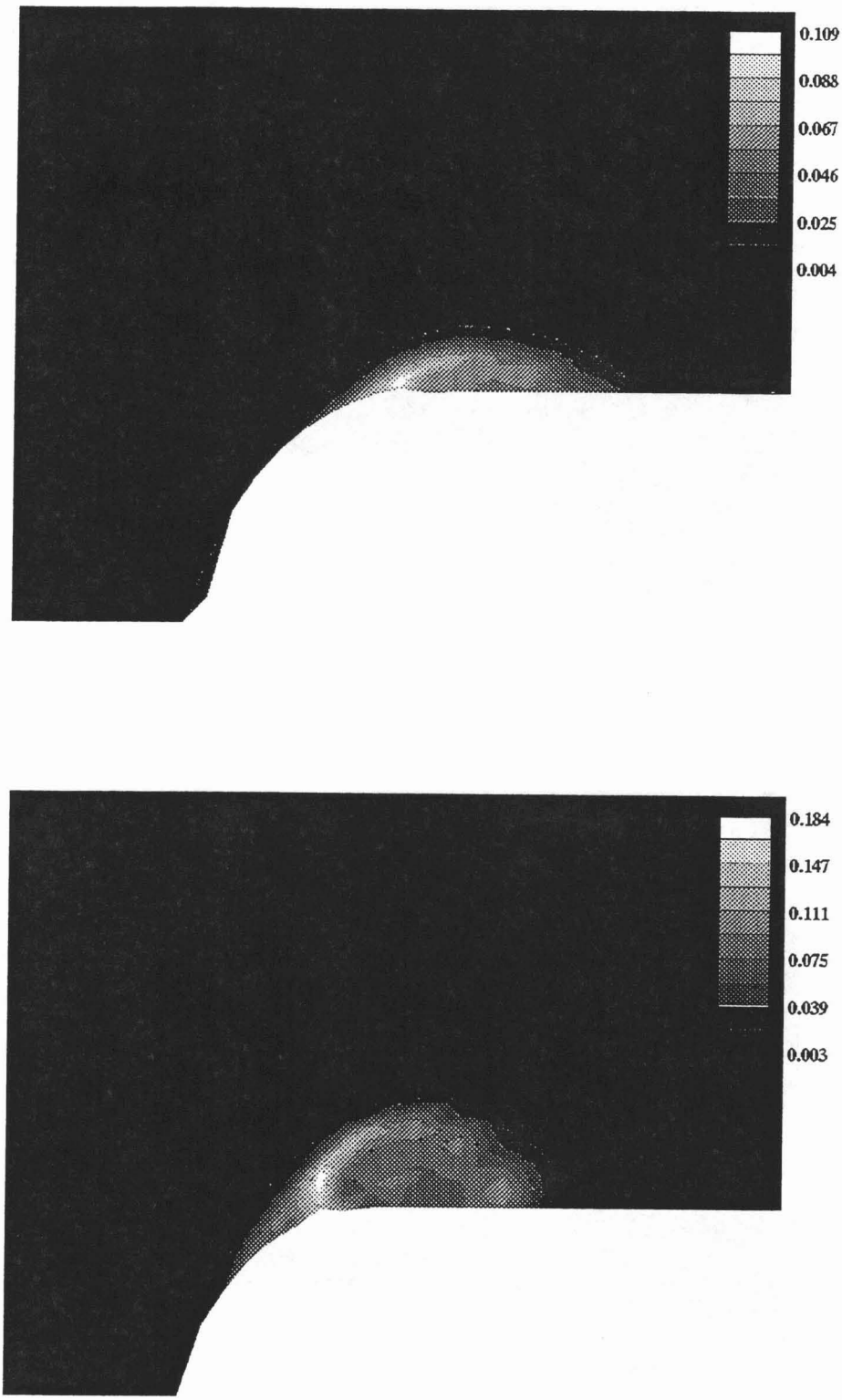

Figure 3.18a,b Contours of $\hat{w}$: a) $x/c = -0.394$, b) $x/c = -0.296$

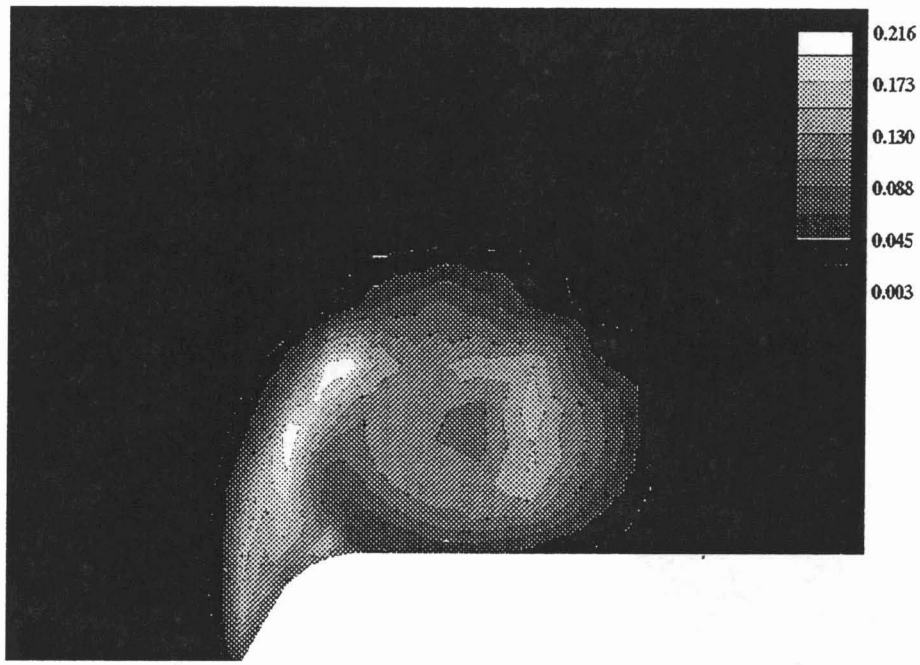

Figure 3.18c,d Contours of $\hat{w}$: c) $x/c = -0.197$, d) $x/c = -0.114$

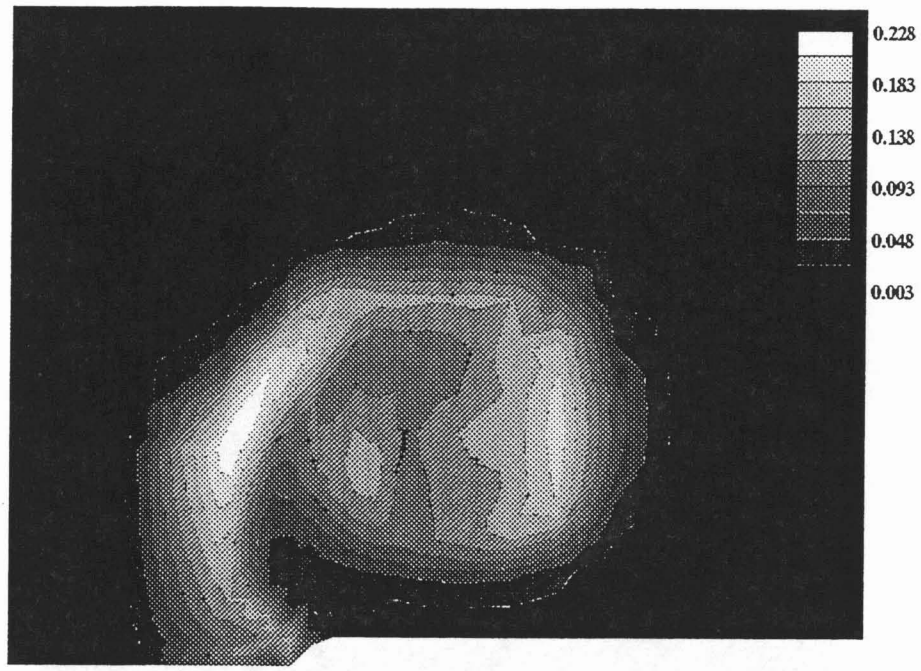

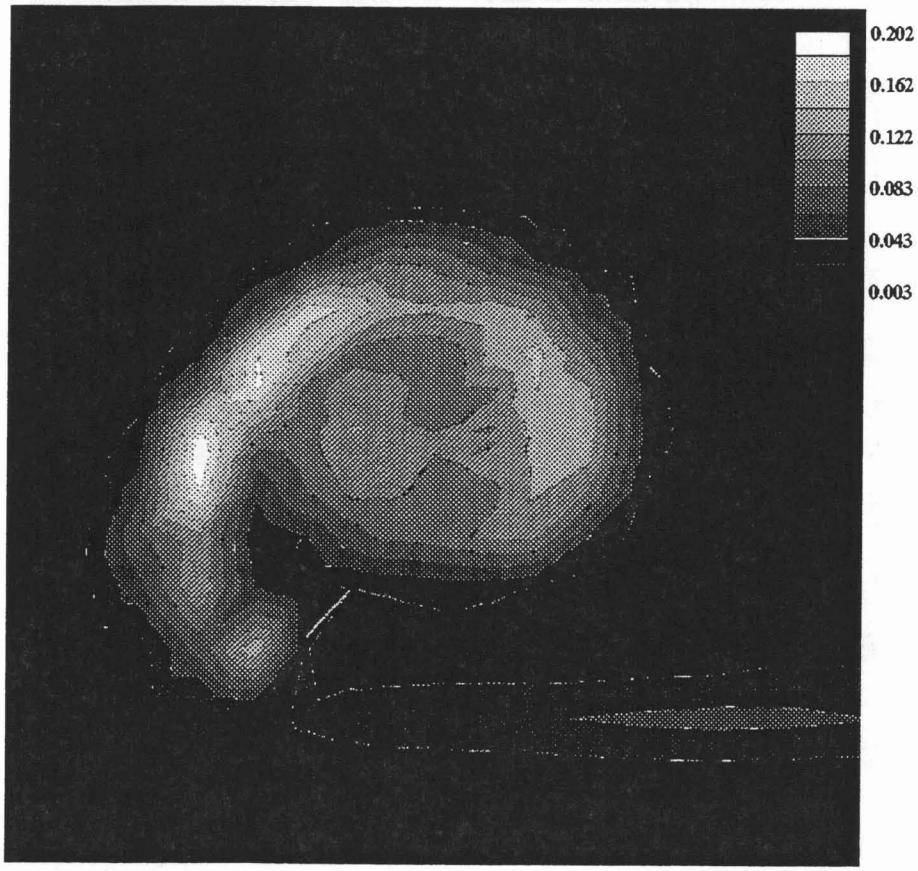

Figure 3.18e,f Contours of $\hat{w}$: e) $x/c = -0.010$, f) $x/c = 0.005$

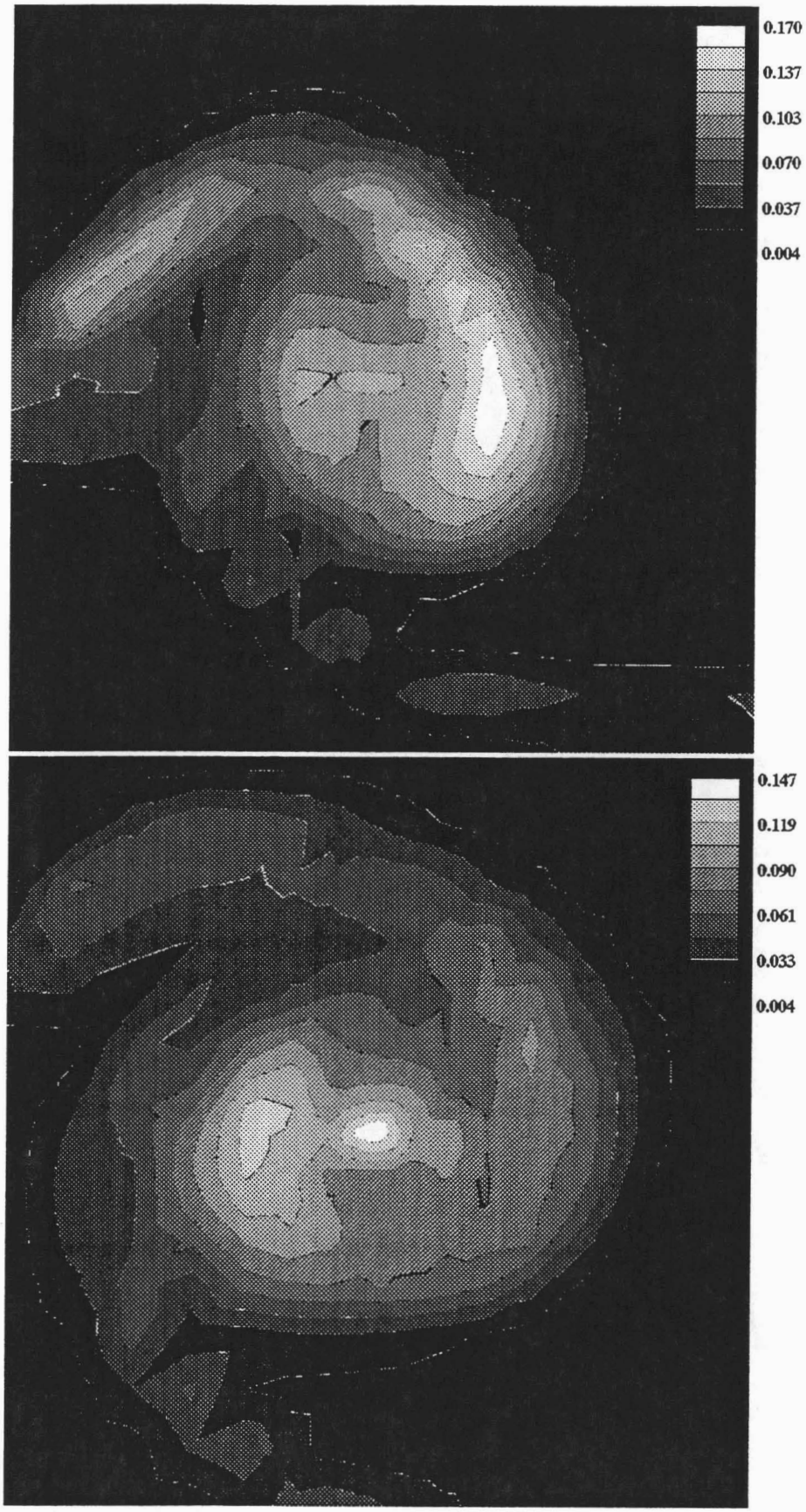

Figure 3.18g,h Contours of $\hat{w}$: g) $x/c = 0.125$, h) $x/c = 0.246$

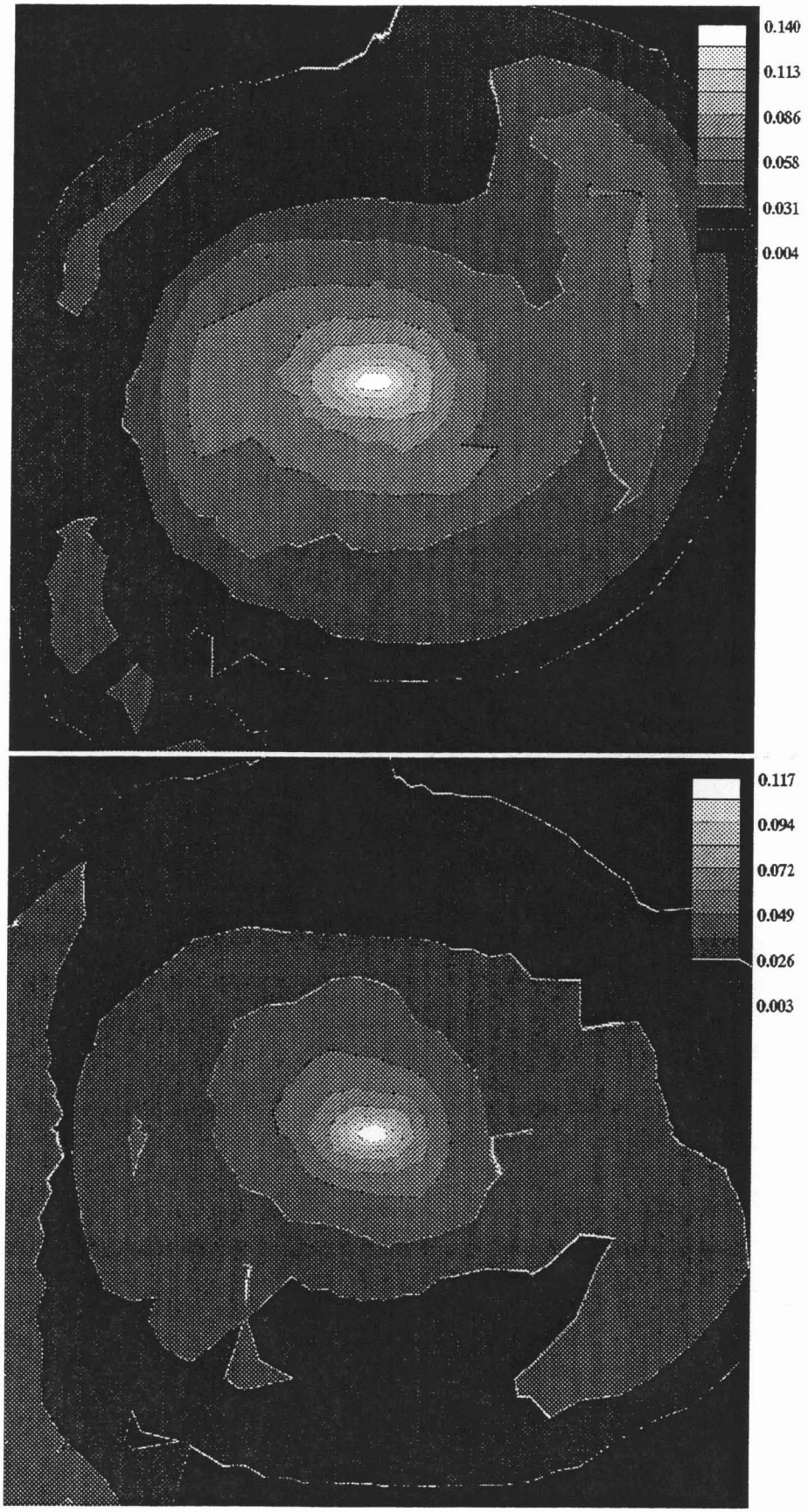

Figure 3.18i,j Contours of $\hat{w}$: i) $x/c = 0.452$, j) $x/c = 0.678$

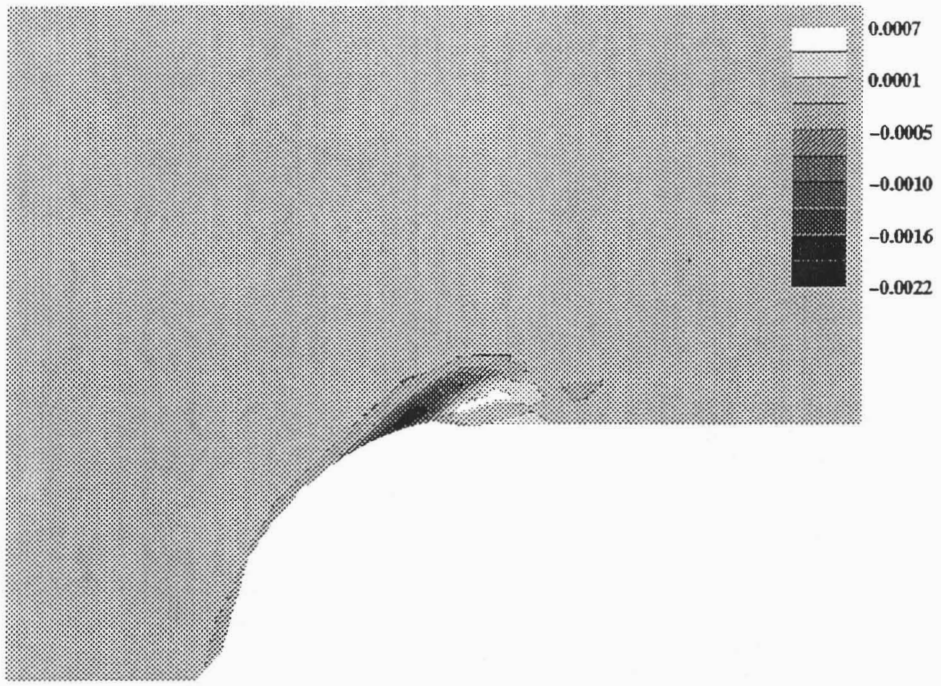

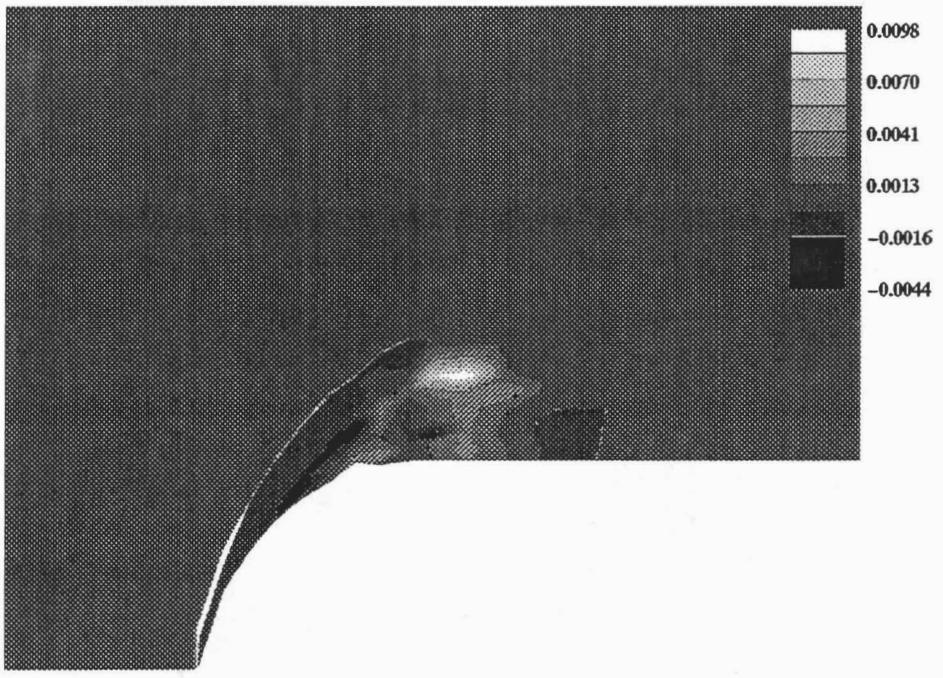

Figure 3.19a,b Contours of $\overline{u'v'}$: a) $x/c = -0.394$, b) $x/c = -0.296$

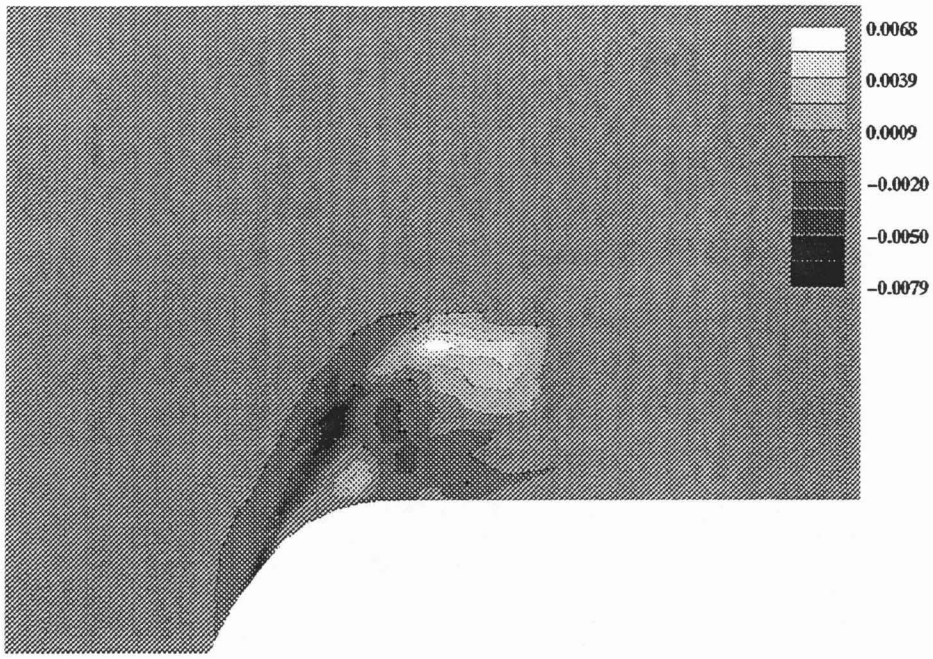

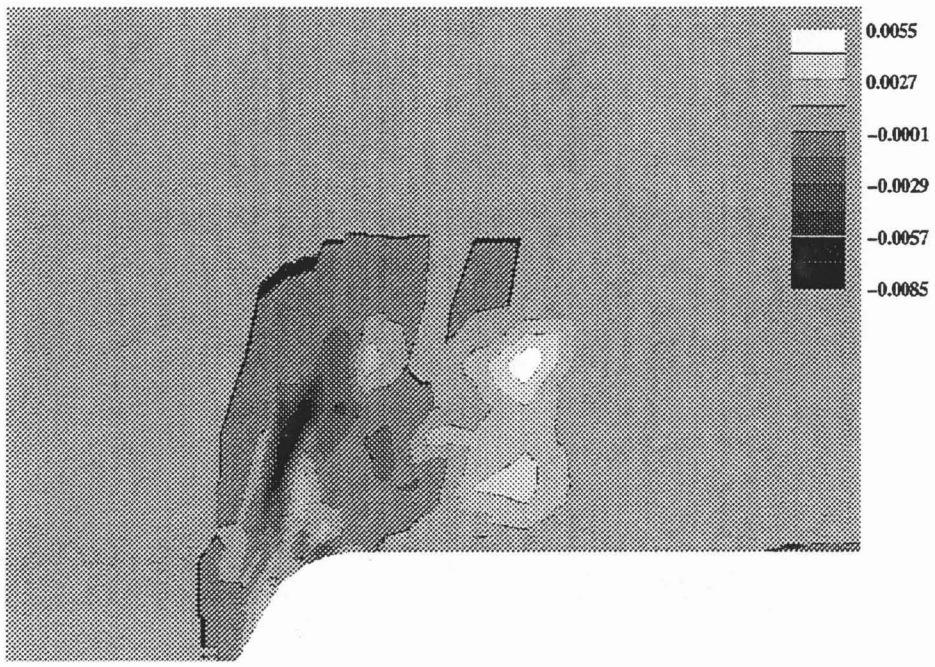

Figure 3.19c,d Contours of $\overline{u'v'}$: c) $x/c = -0.197$, d) $x/c = -0.114$

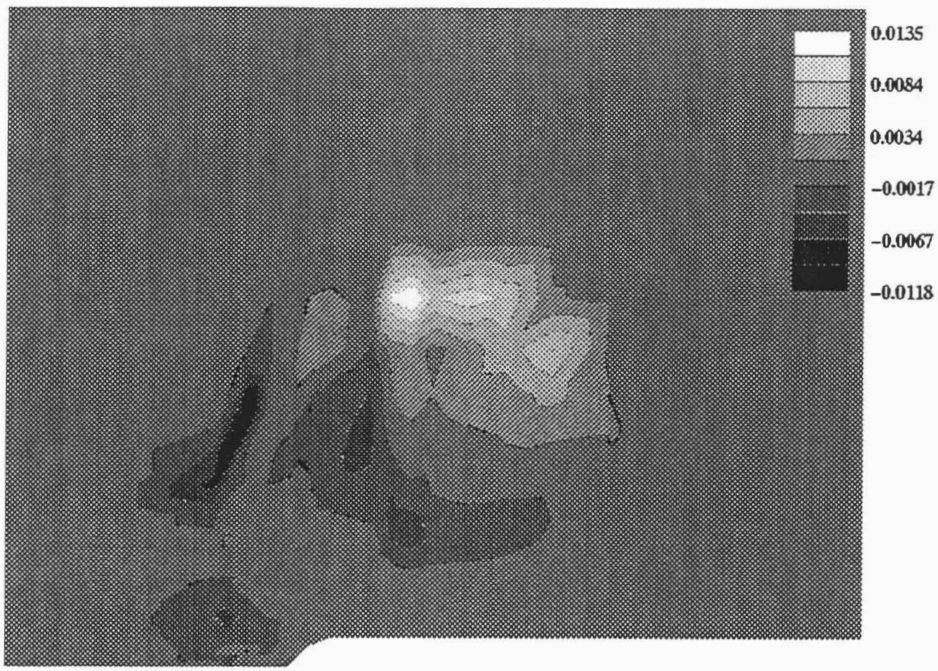

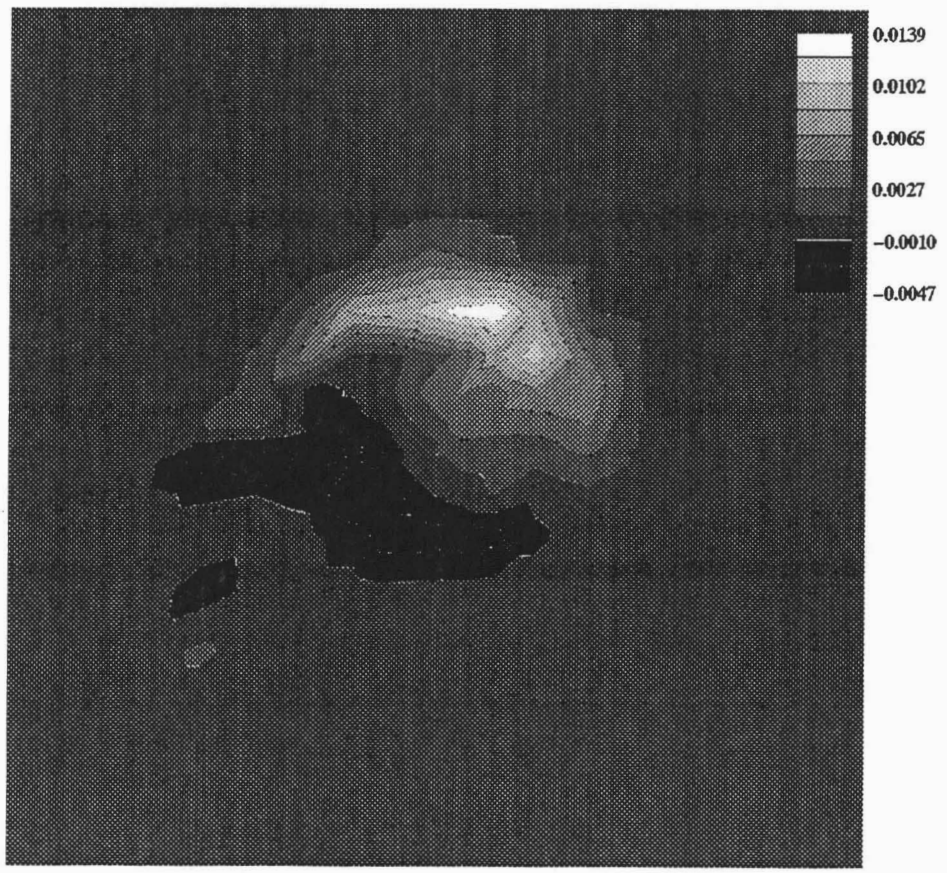

Figure 3.19e,f Contours of $\overline{u'v'}$: e) $x/c = -0.010$, f) $x/c = 0.005$

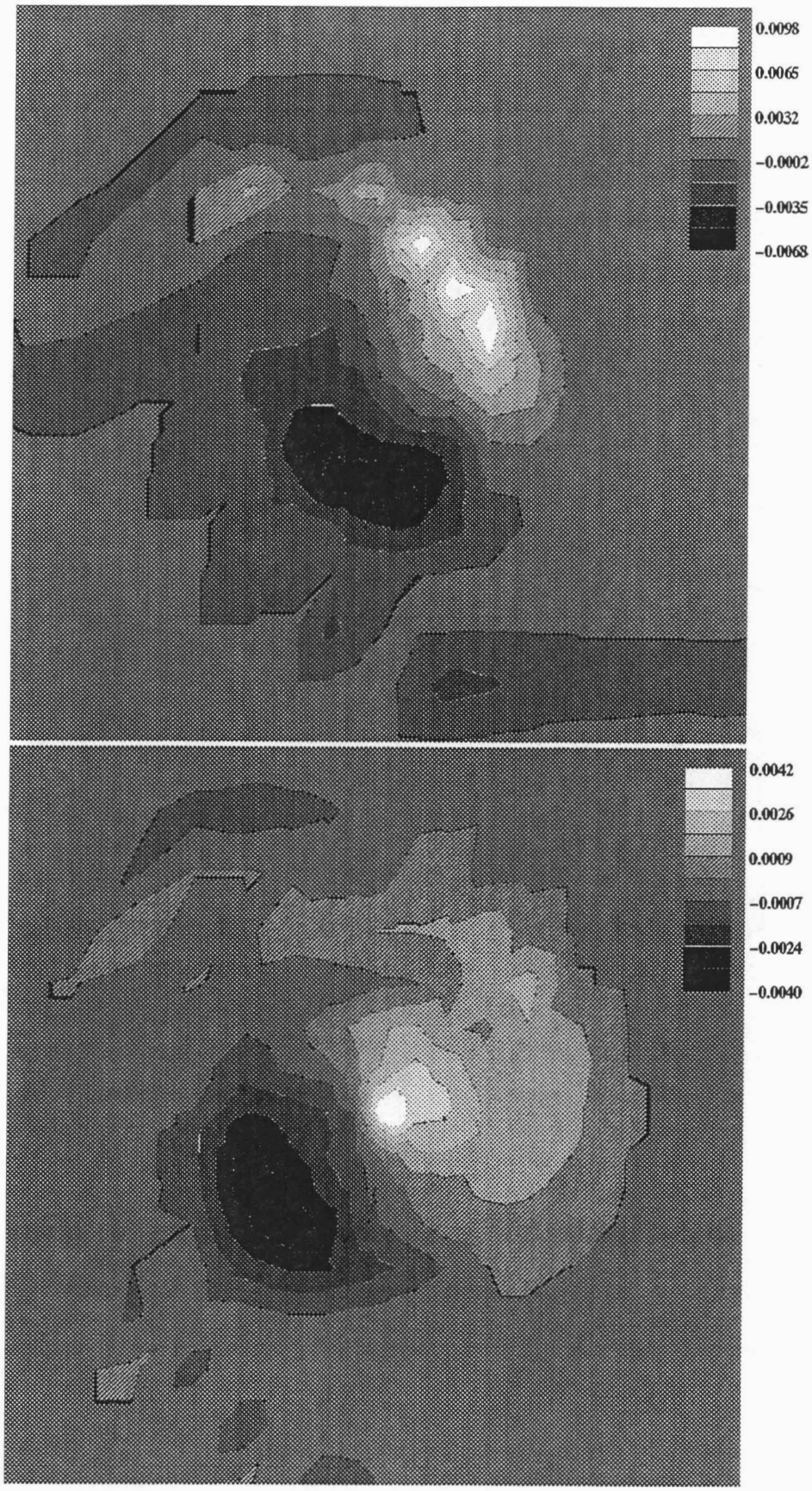

Figure 3.19g,h Contours of $\overline{u'v'}$: g) $x/c = 0.125$, h) $x/c = 0.246$

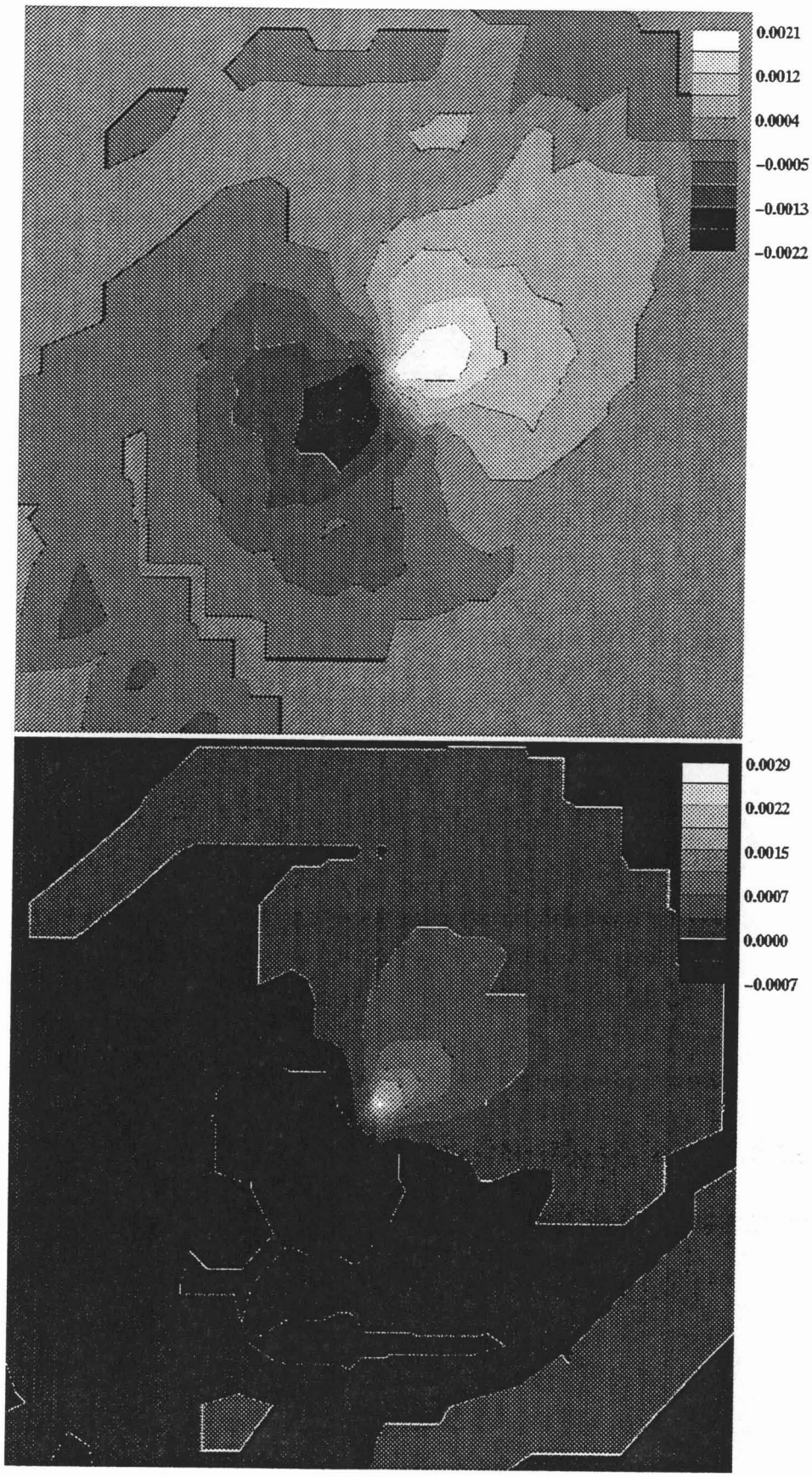

Figure 3.19i,j Contours of $\overline{u'v'}$: i) $x/c = 0.452$, j) $x/c = 0.678$

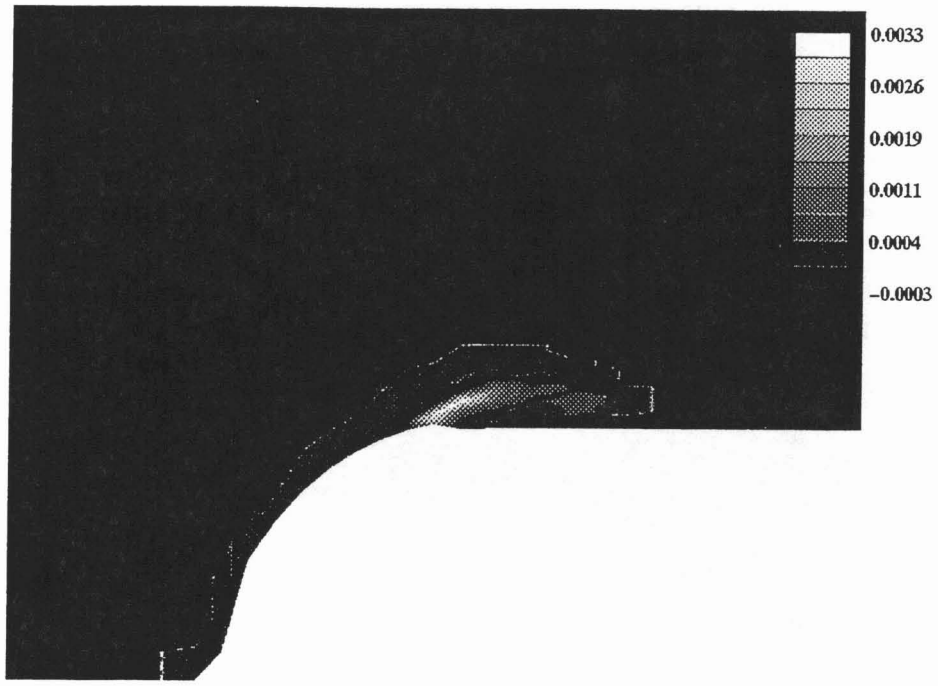

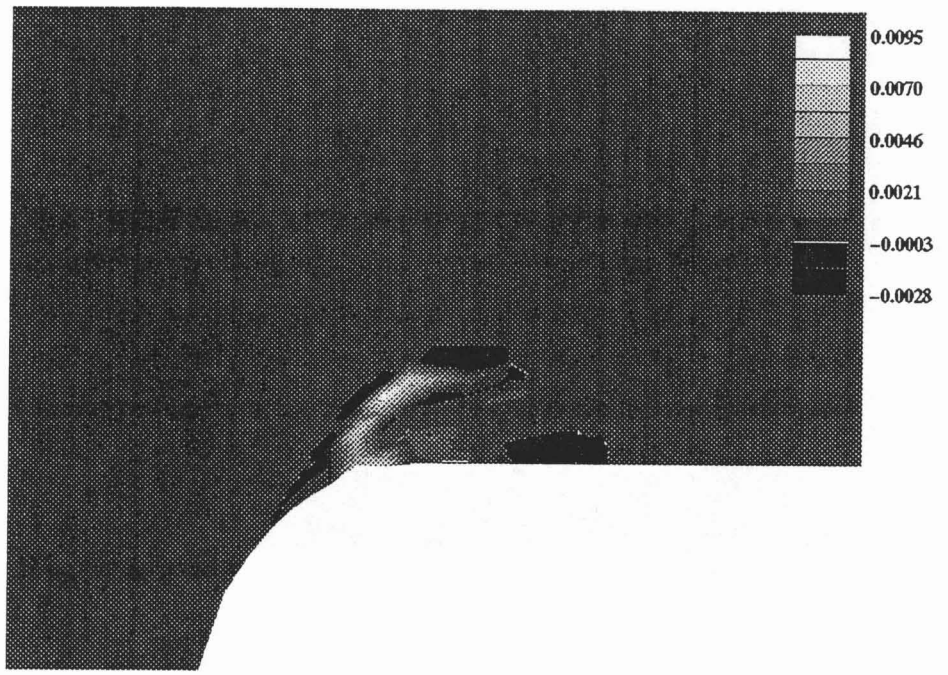

Figure 3.20a,b Contours of $\overline{u'w'}$: a) $x/c = -0.394$, b) $x/c = -0.296$

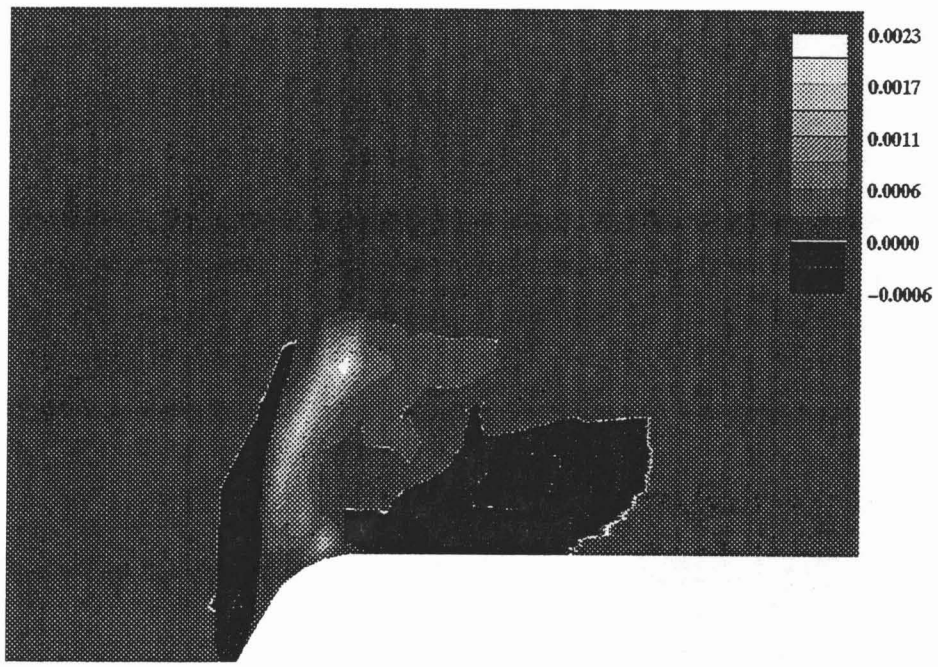

Figure 3 $\overline{u'w'}$: **c)** $x/c = -0.197$, **d)** $x/c = -0.114$

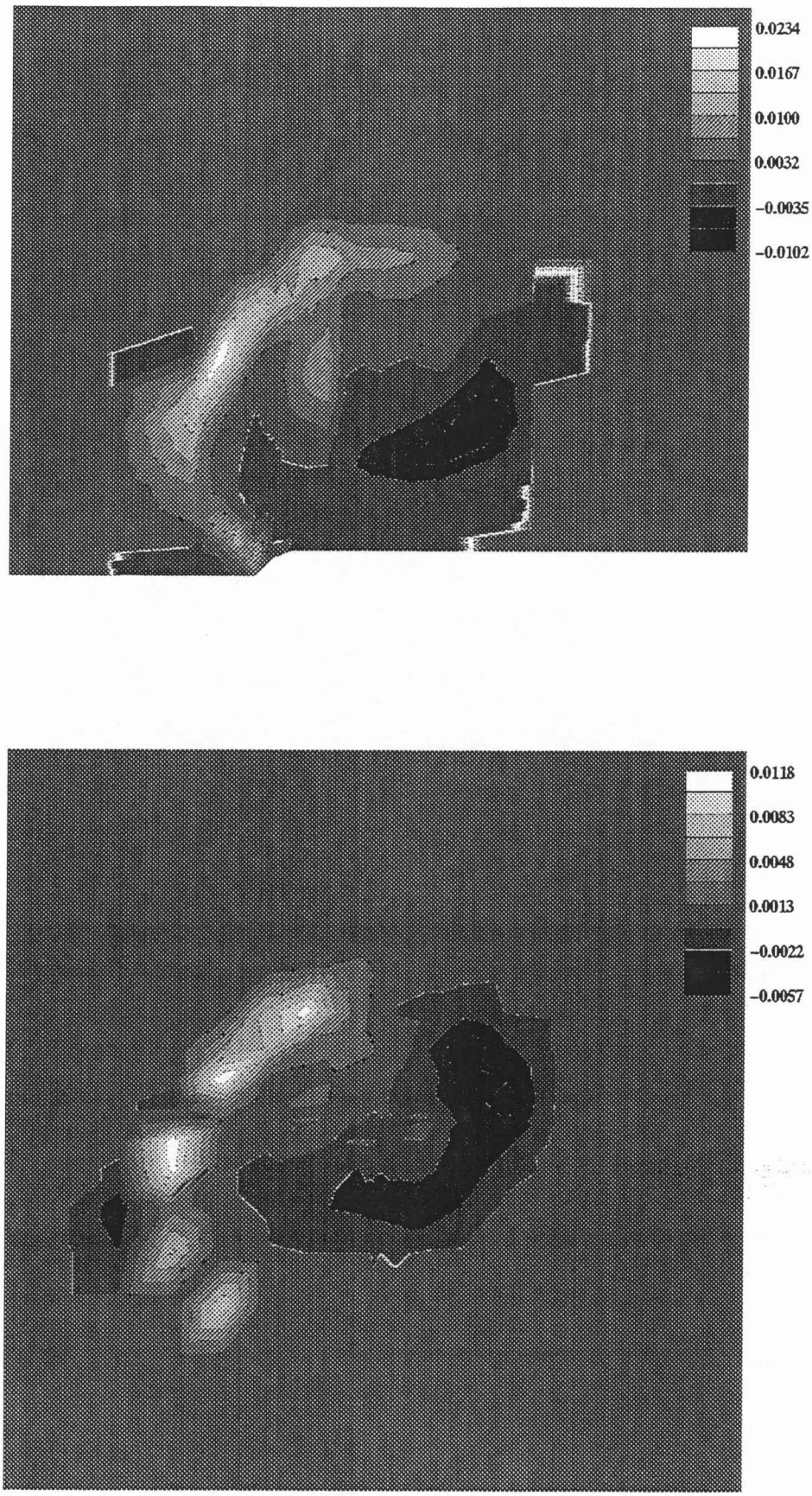

Figure 3.20e,f Contours of $\overline{u'w'}$: e) $x/c = -0.010$, f) $x/c = 0.005$

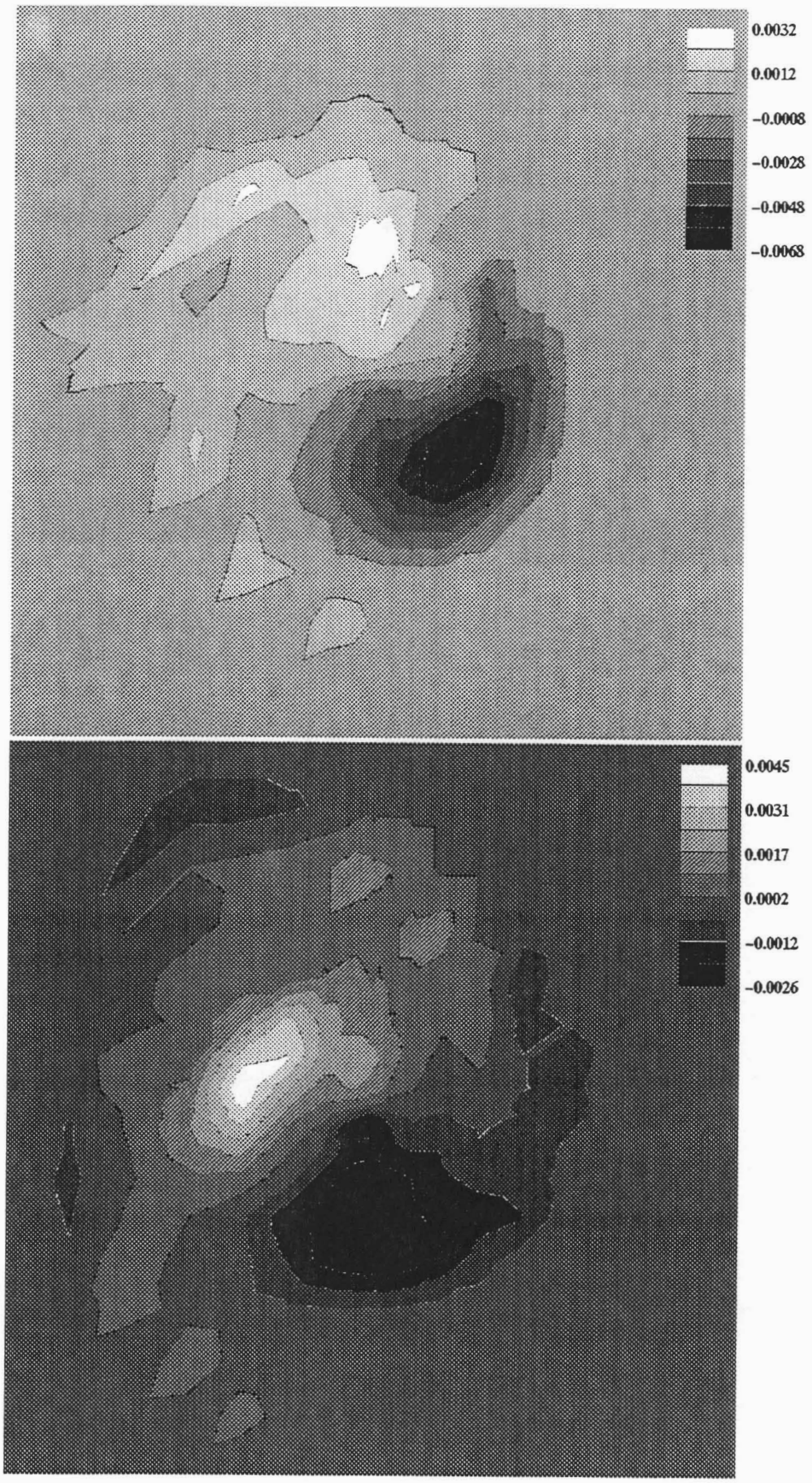

Figure 3.20g,h Contours of $\overline{u'w'}$: g) $x/c = 0.125$, h) $x/c = 0.246$

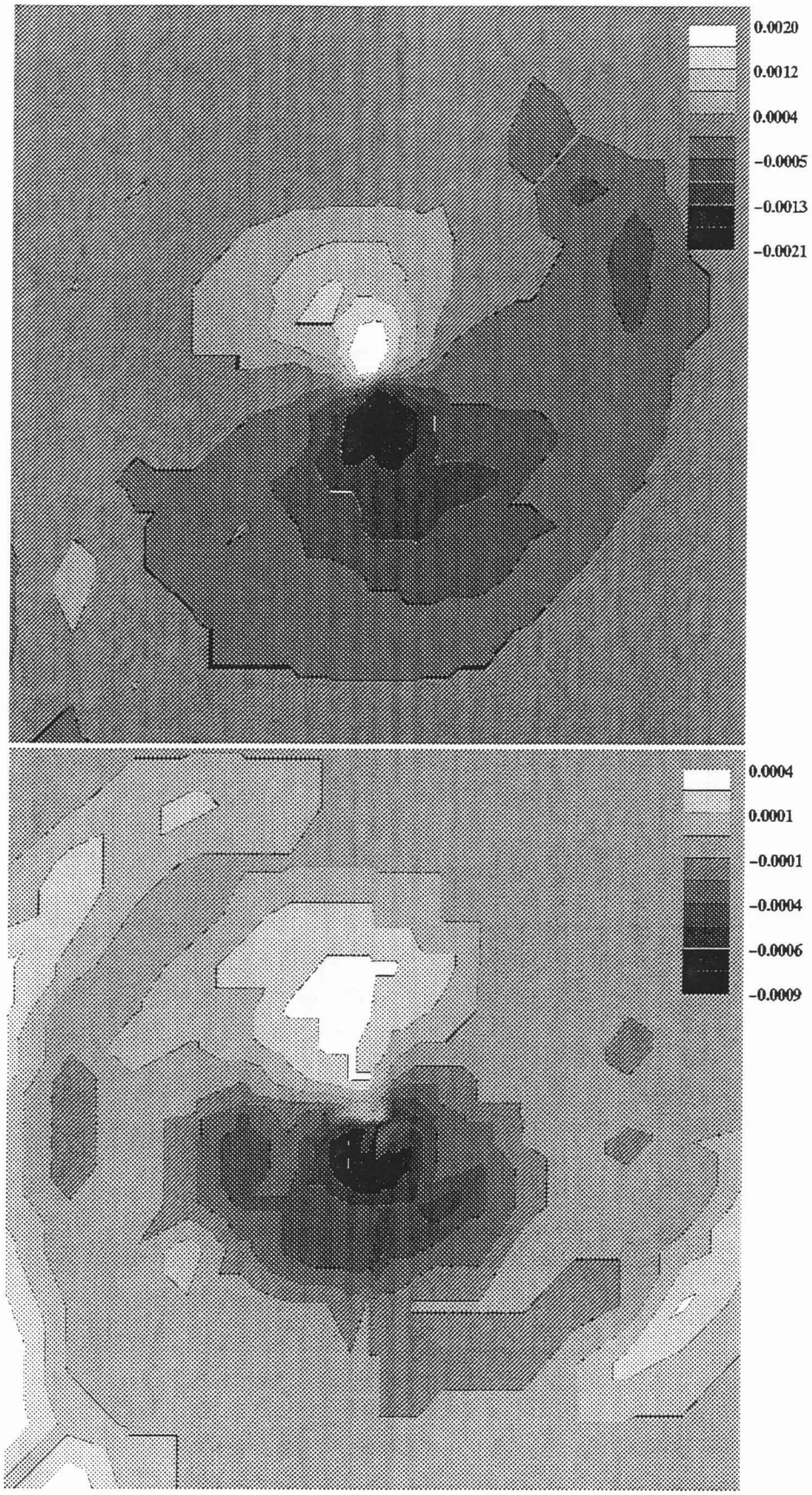

Figure 3.20i,j Contours of $\overline{u'w'}$: i) $x/c = 0.452$, j) $x/c = 0.678$

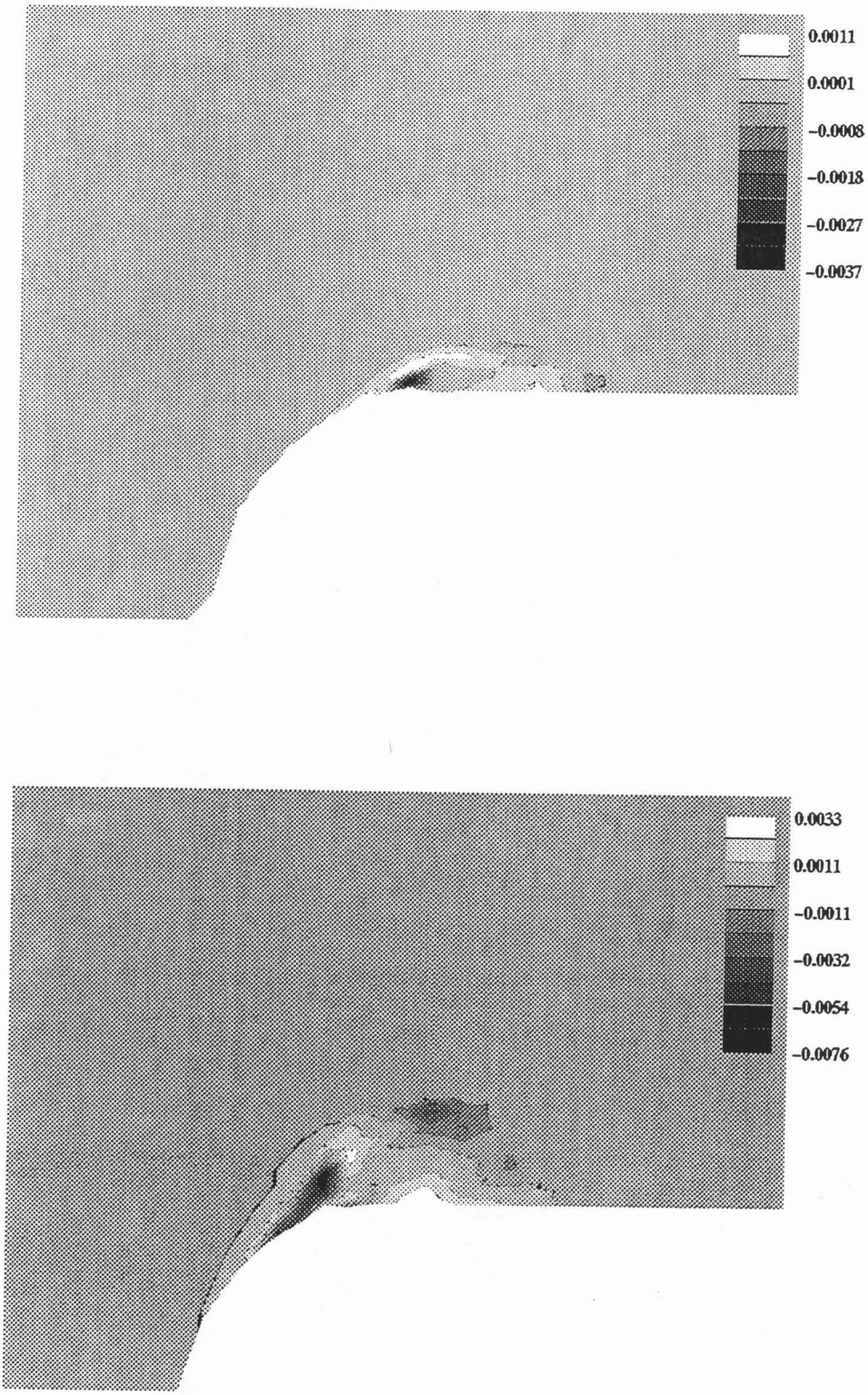

Figure 3.21a,b Contours of $\overline{v'w'}$: a) $x/c = -0.394$, b) $x/c = -0.296$

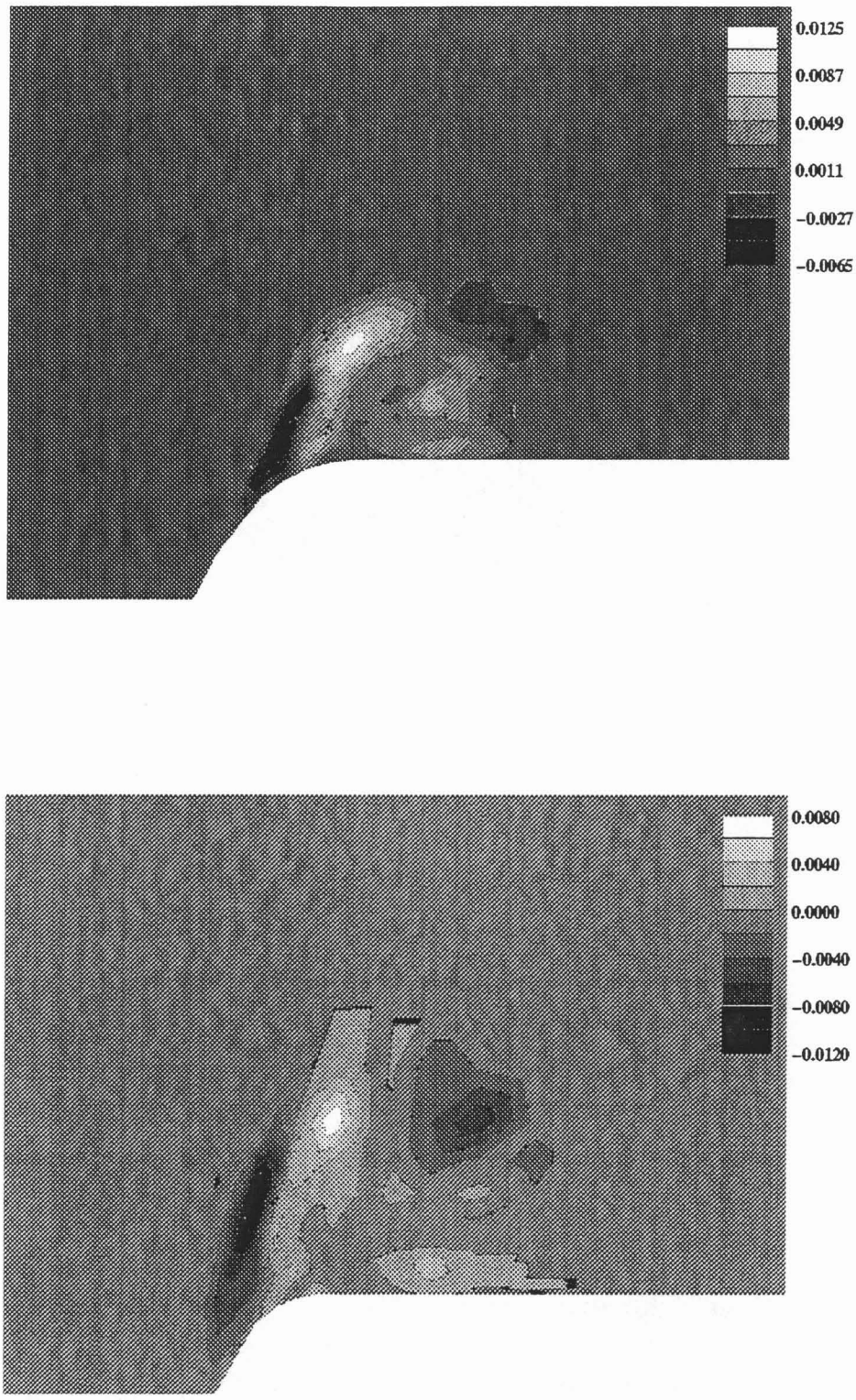

Figure 3.21c,d Contours of $\overline{v'w'}$: c) $x/c = -0.197$, d) $x/c = -0.114$

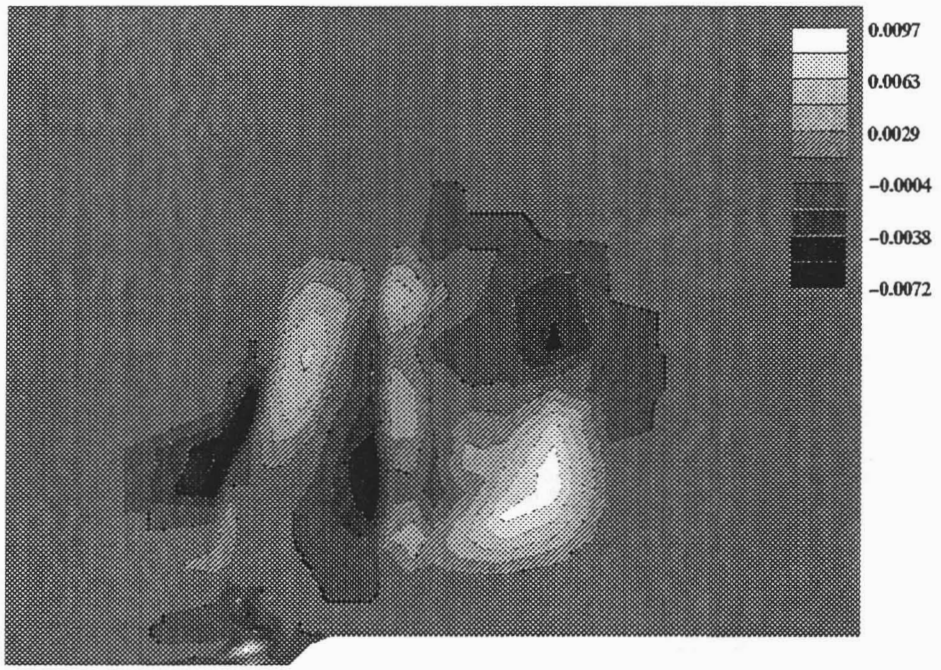

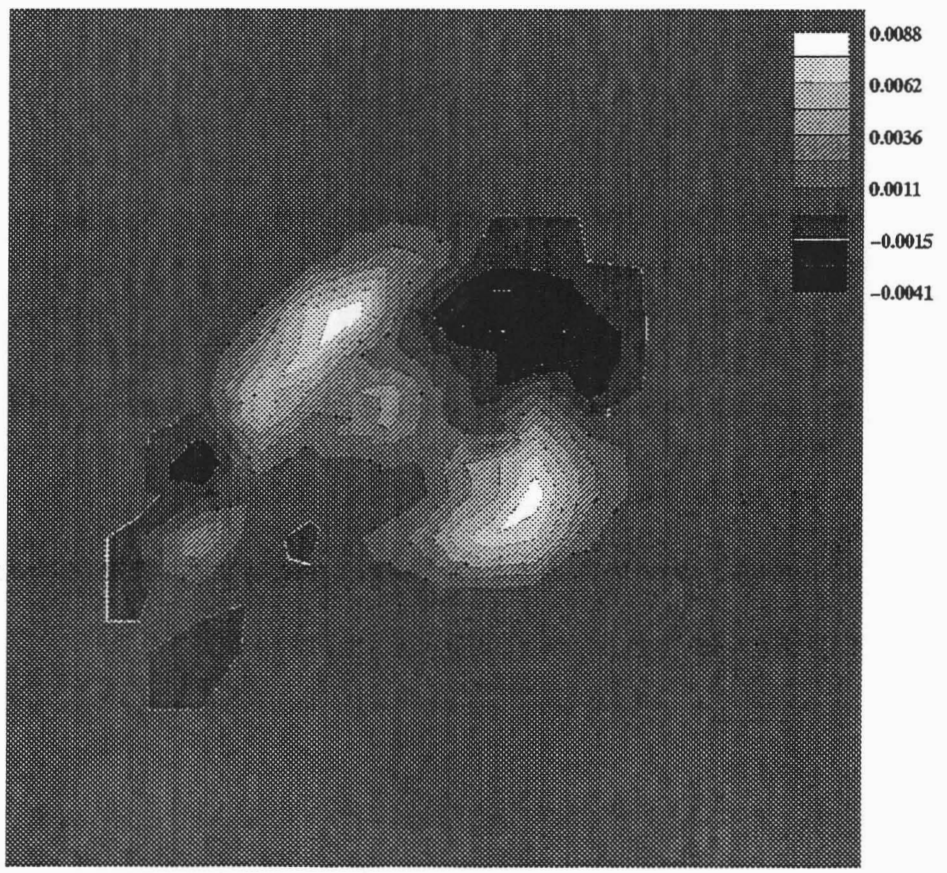

Figure 3.21e,f Contours of $\overline{v'w'}$: e) $x/c = -0.010$, f) $x/c = 0.005$

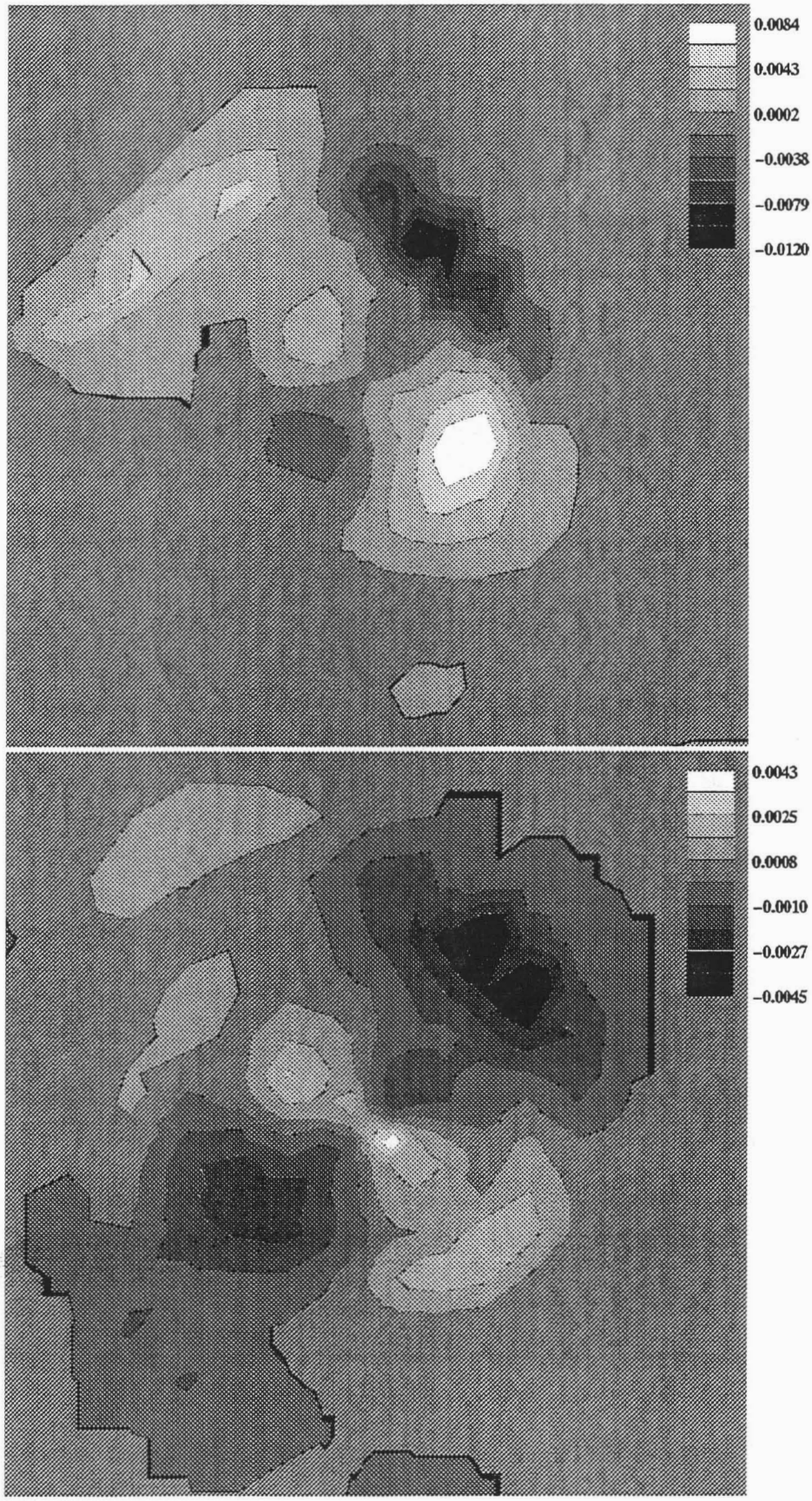

Figure 3.21g,h Contours of $\overline{v'w'}$: g) $x/c = 0.125$, h) $x/c = 0.246$

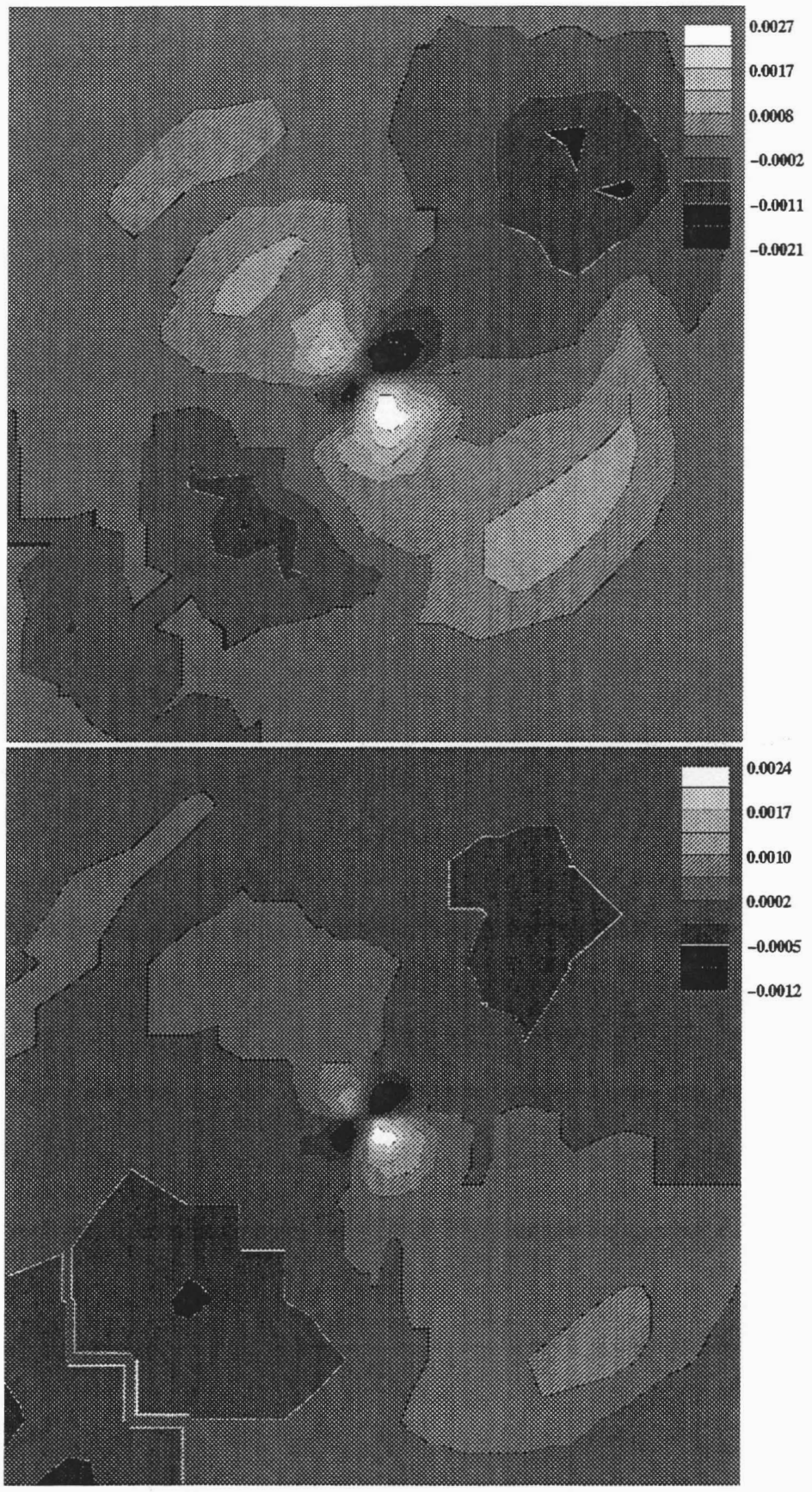

Figure 3.21i,j Contours of $\overline{v'w'}$: i) $x/c = 0.452$, j) $x/c = 0.678$

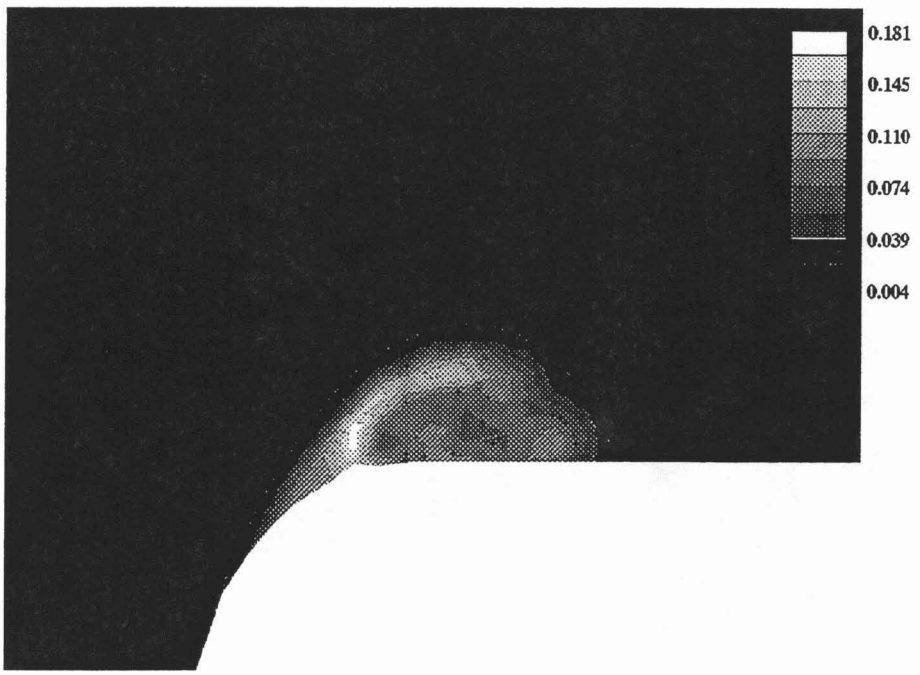

Figure 3.22a,b Contours of $\hat{v}_r$: a) $x/c = -0.394$, b) $x/c = -0.296$

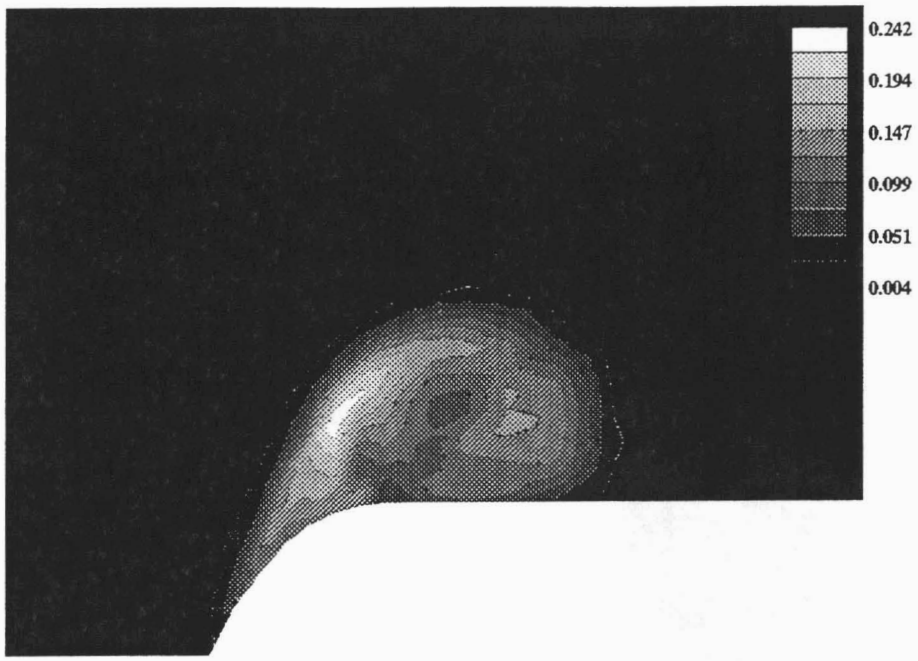

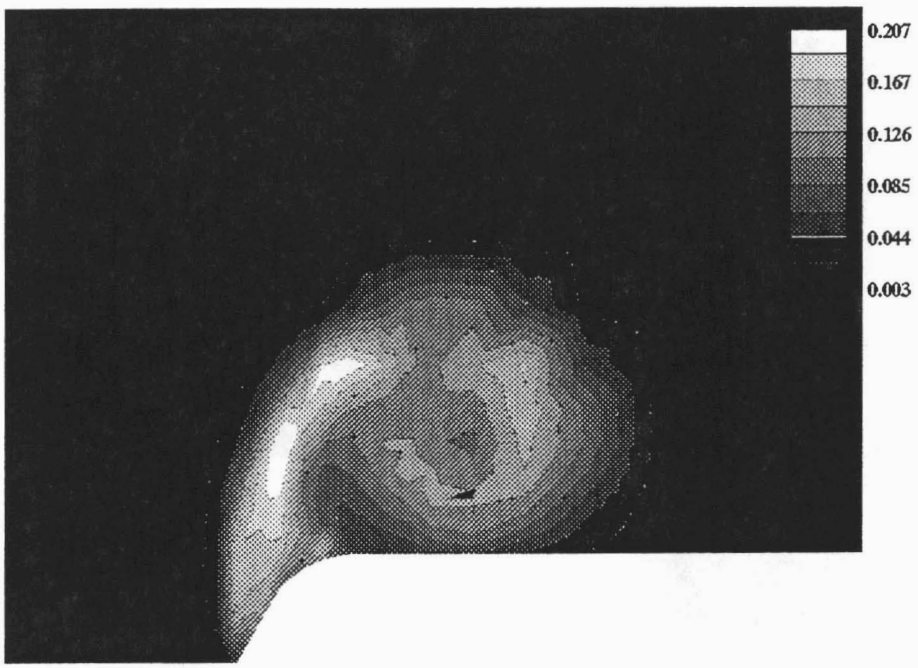

Figure 3.22c,d Contours of $\hat{v}_r$: c) $x/c = -0.197$, d) $x/c = -0.114$

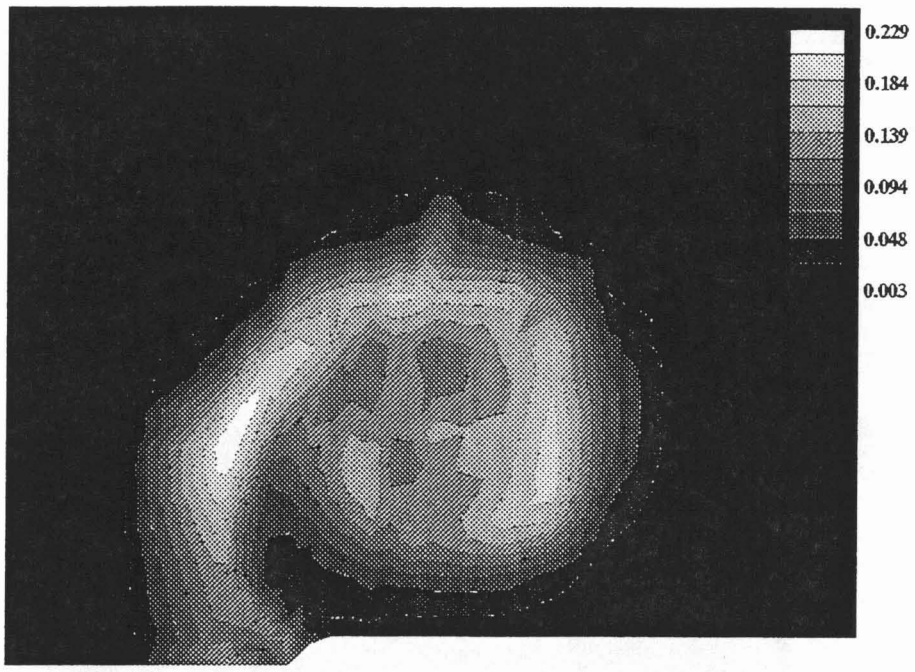

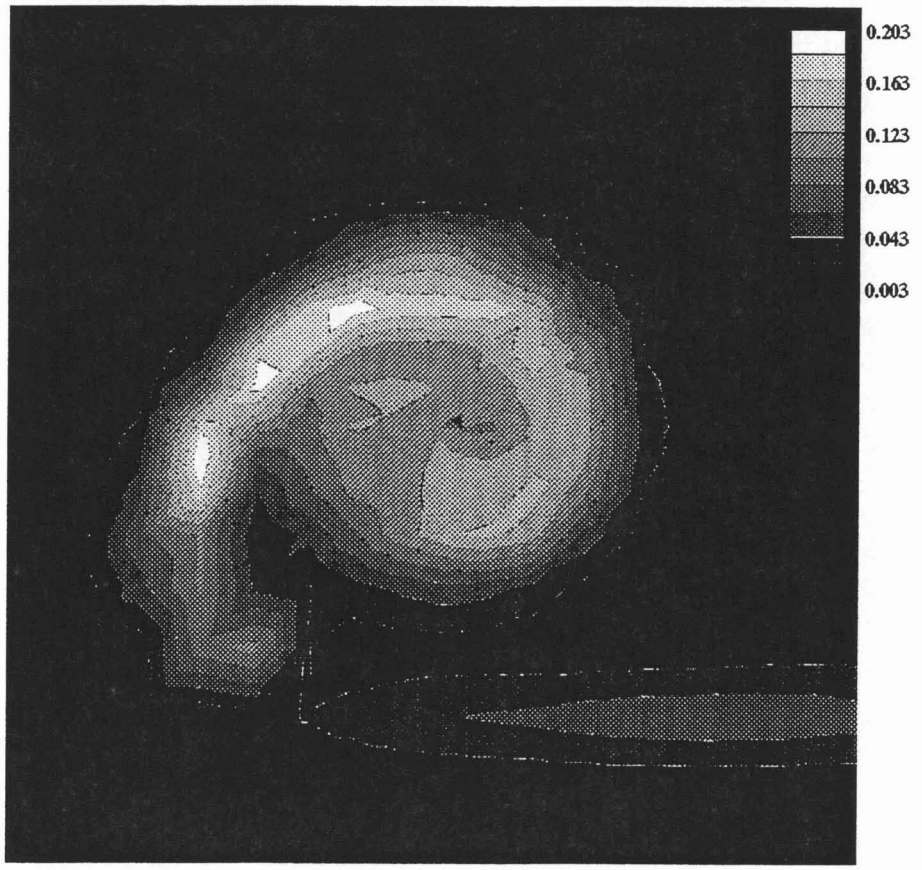

Figure 3.22e,f Contours of $\hat{v}_r$: e) $x/c = -0.010$, f) $x/c = 0.005$

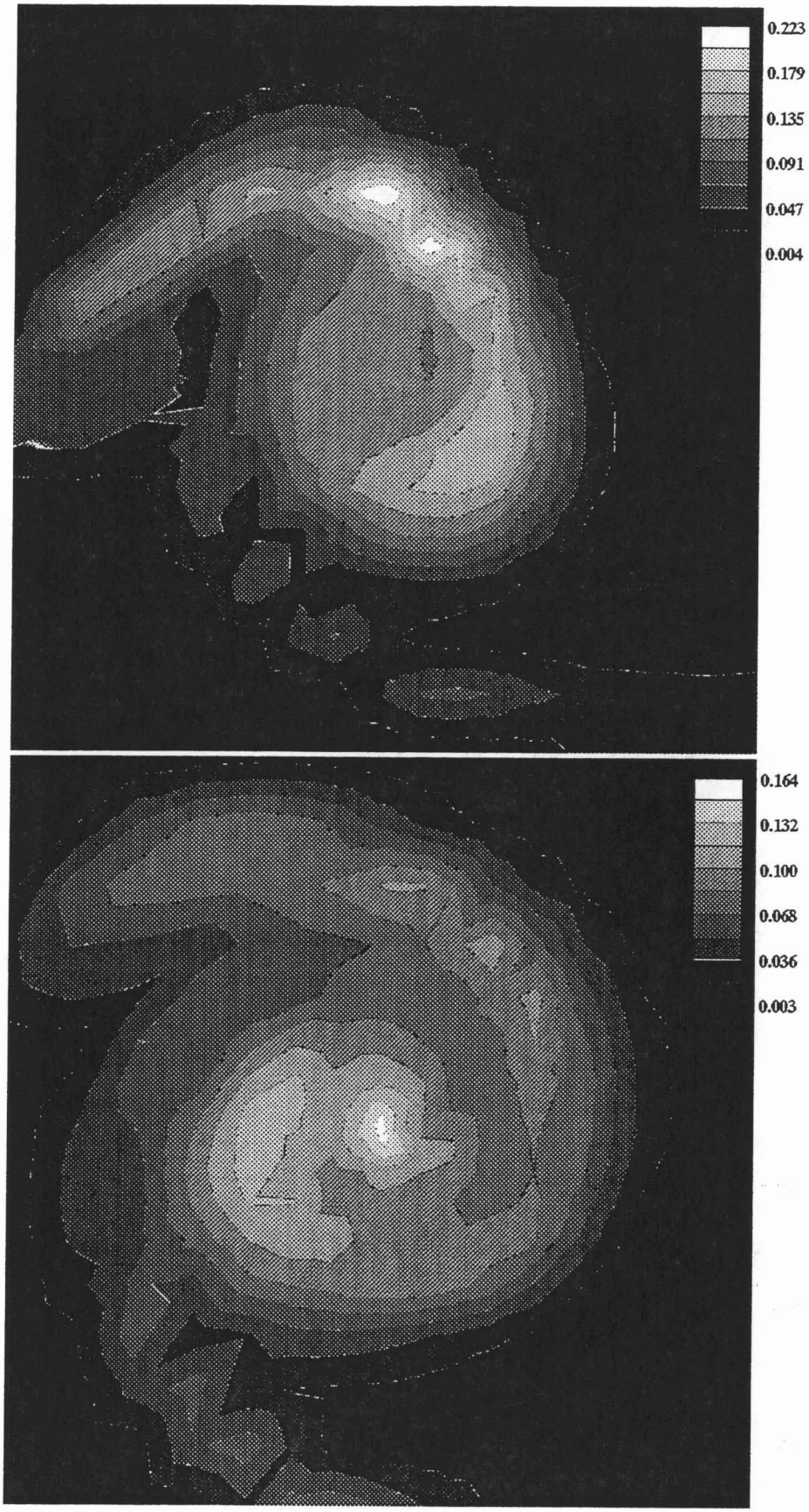

Figure 3.22g,h Contours of $\hat{v}_r$: g) $x/c = 0.125$, h) $x/c = 0.246$

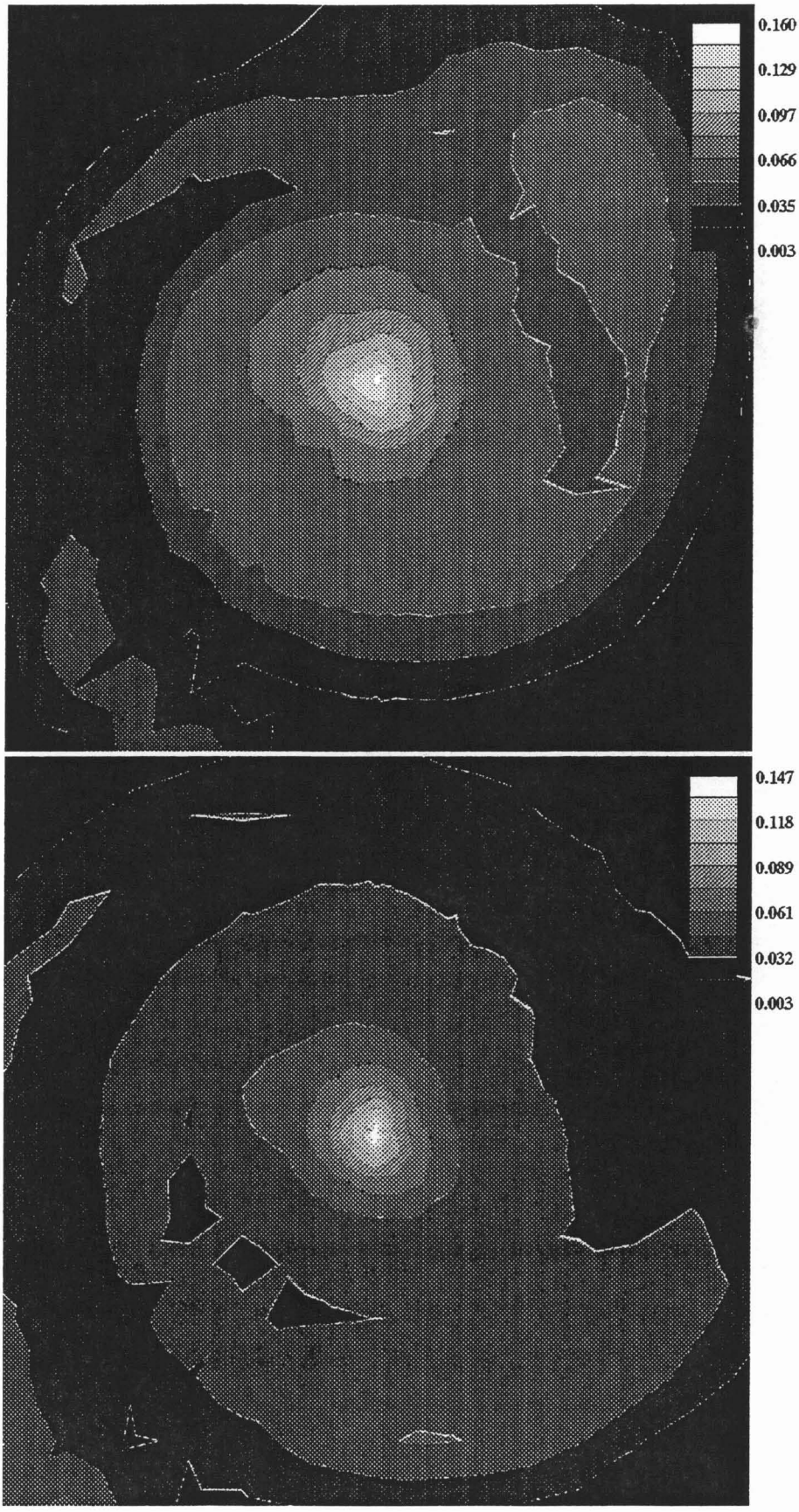

Figure 3.22i,j Contours of $\hat{v}_r$: i) $x/c = 0.452$, j) $x/c = 0.678$

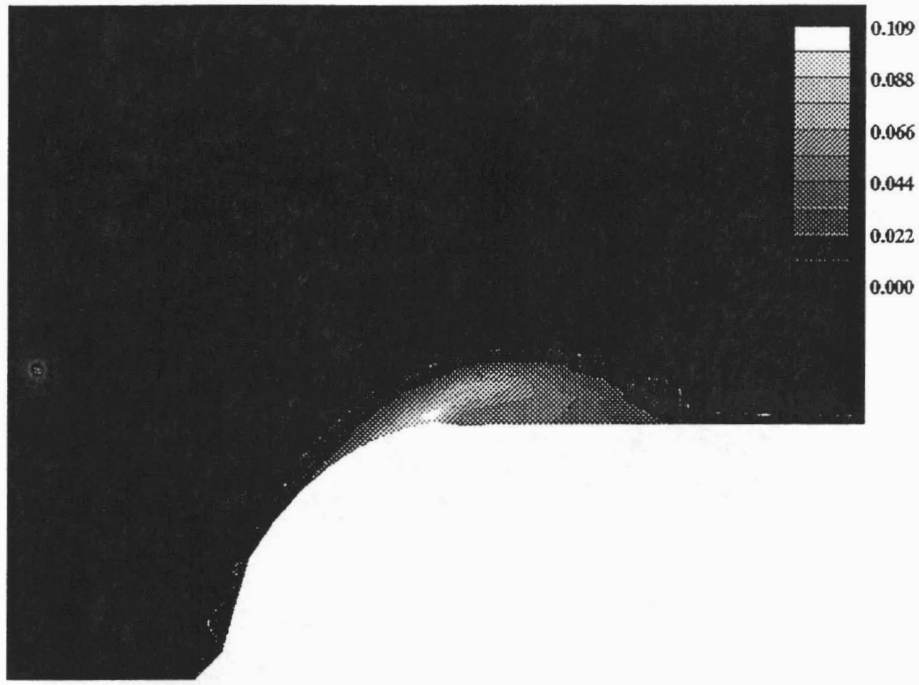

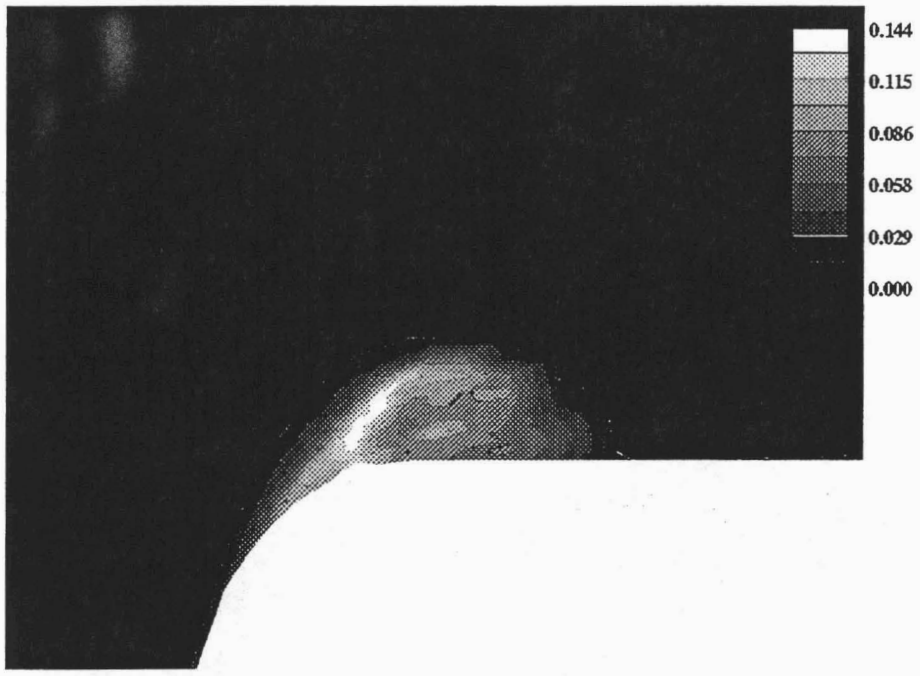

Figure 3.23a,b Contours of $\hat{v}_\theta$: a) $x/c = -0.394$, b) $x/c = -0.296$

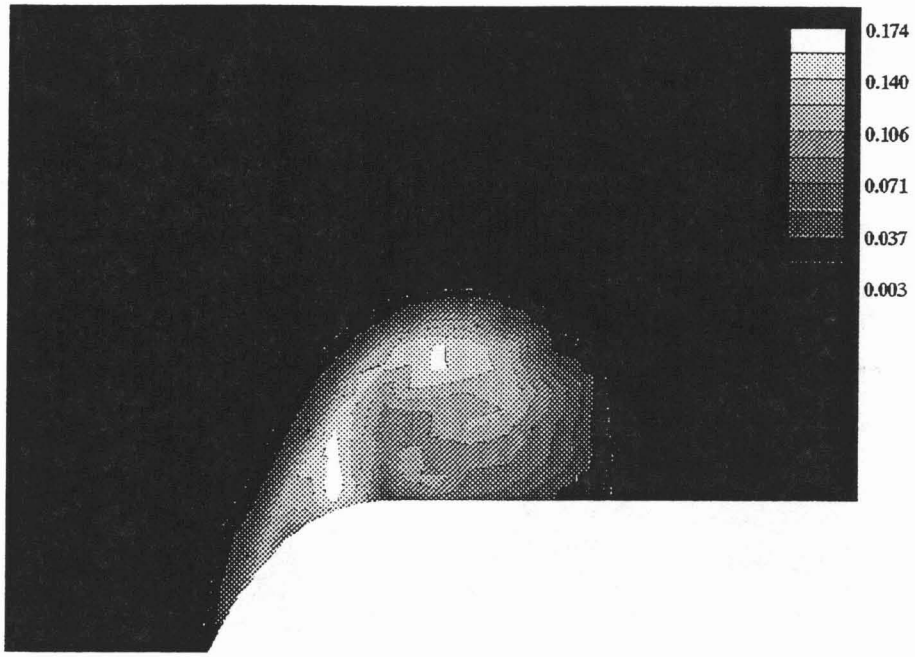

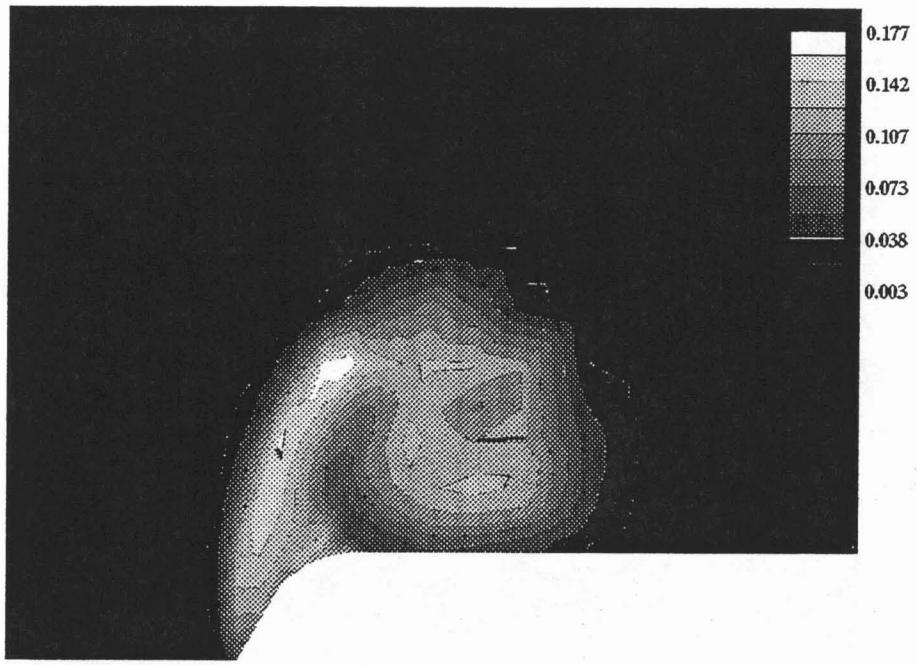

Figure 3.23c,d Contours of $\hat{v}_\theta$: c) $x/c = -0.197$, d) $x/c = -0.114$

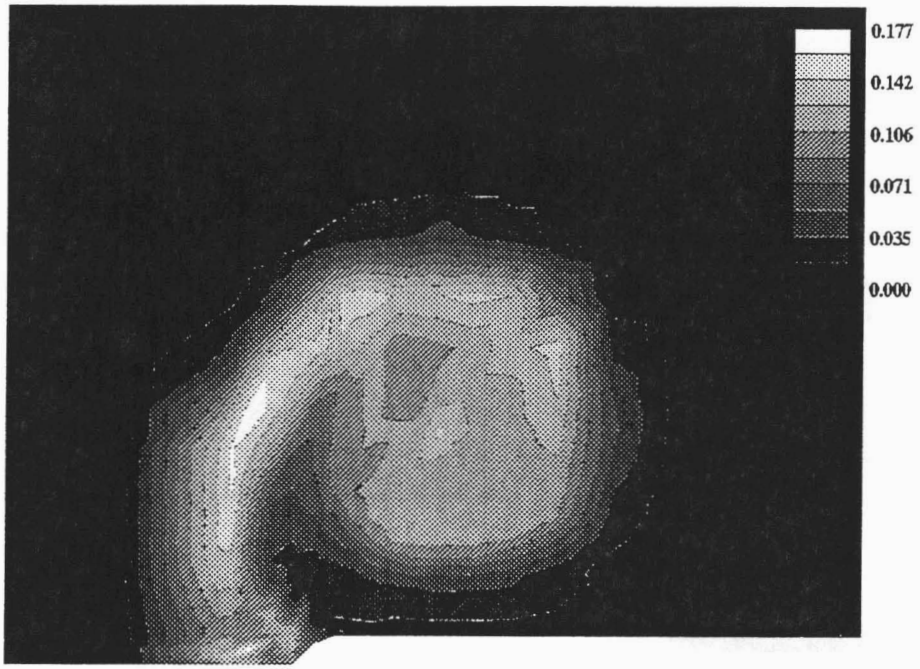

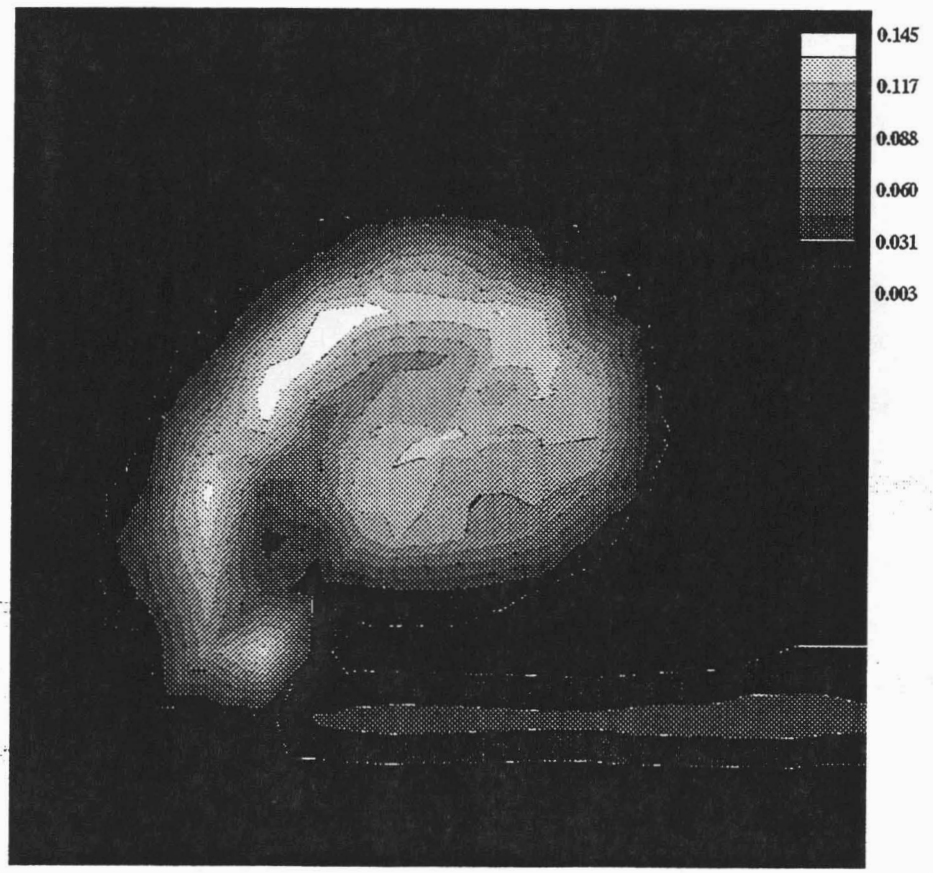

Figure 3.23e,f Contours of $\hat{v}_\theta$: e) $x/c = -0.010$, f) $x/c = 0.005$

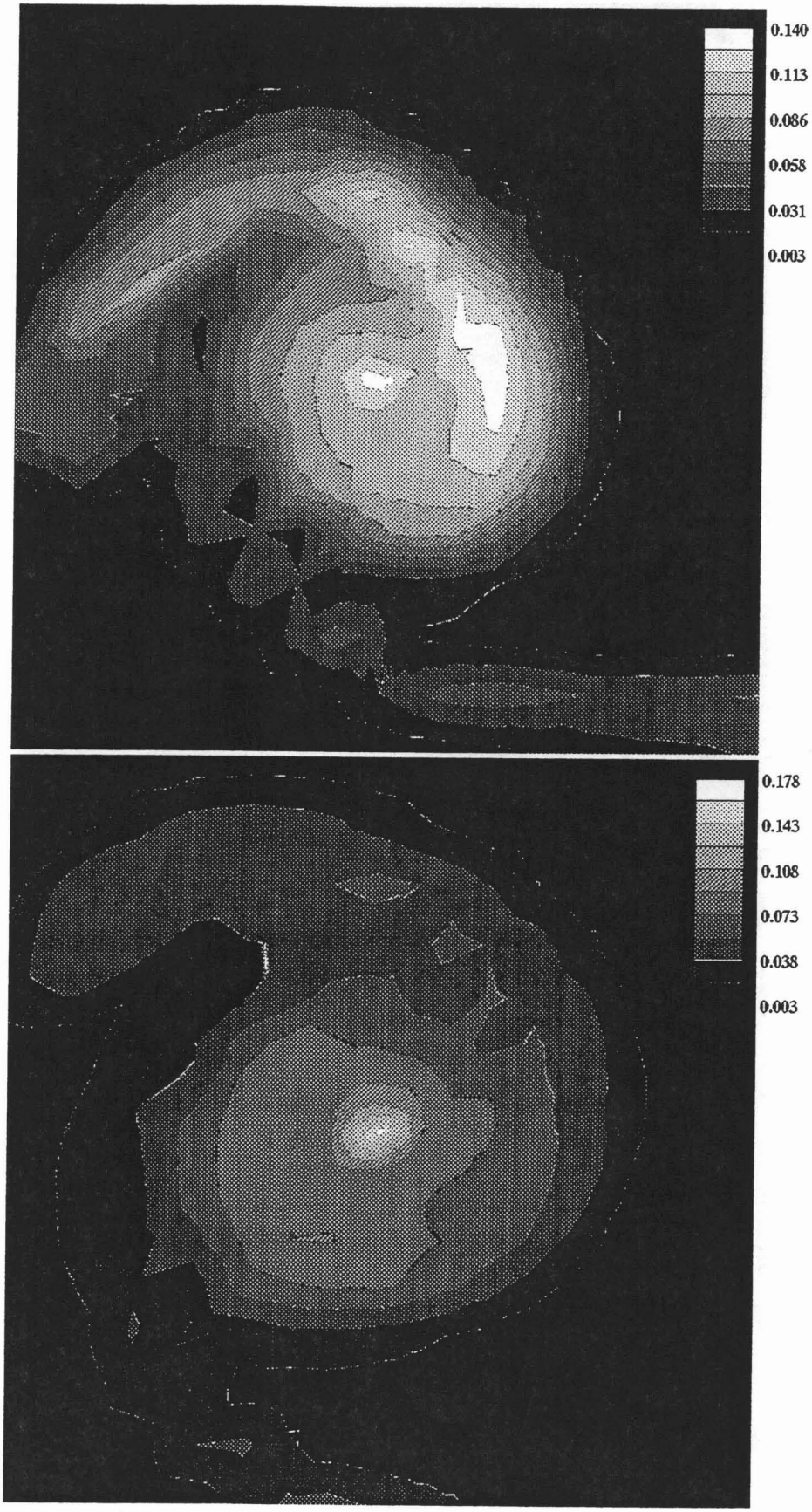

Figure 3.23g,h Contours of $\hat{v}_\theta$: g) $x/c = 0.125$, h) $x/c = 0.246$

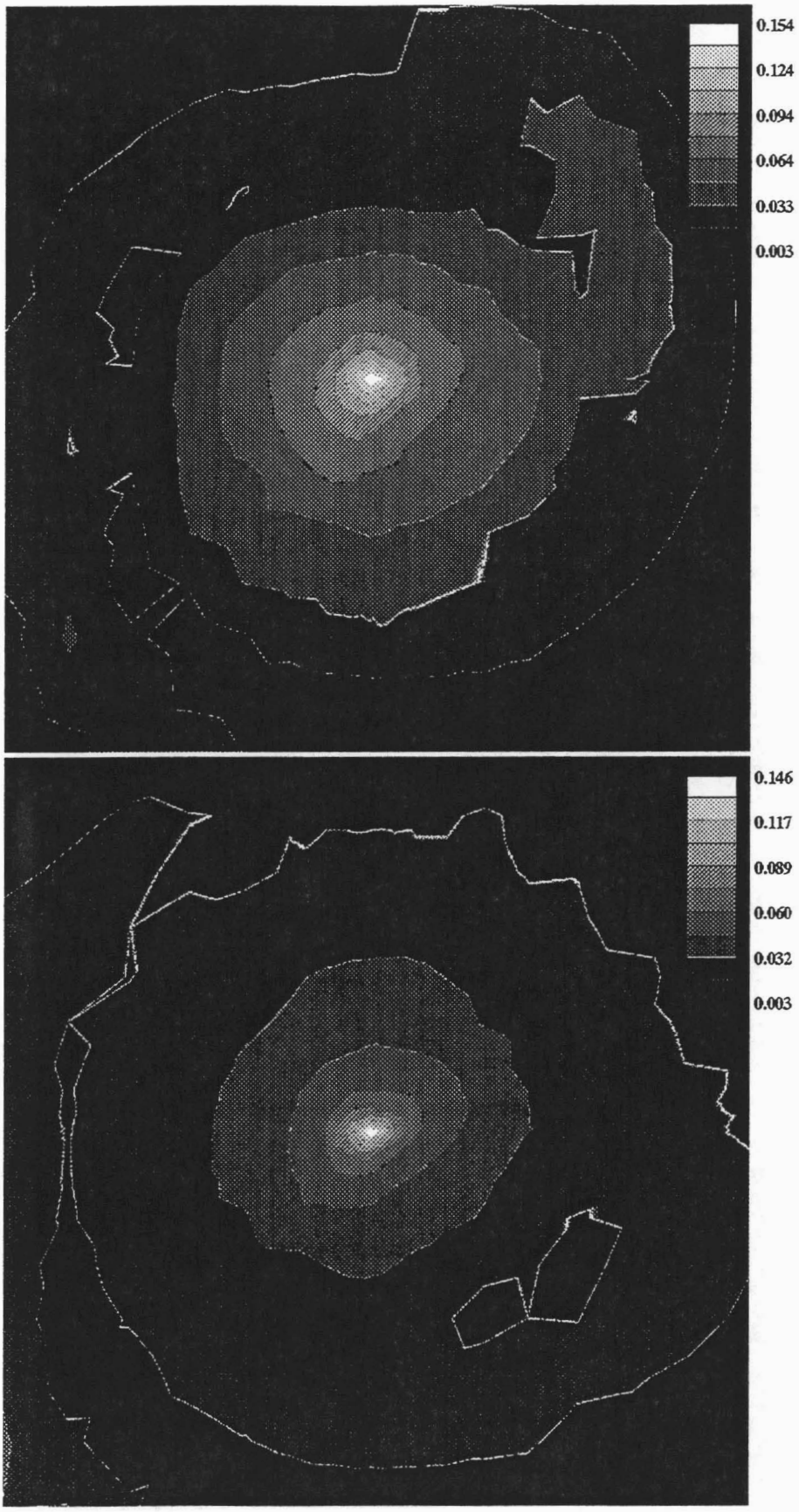

Figure 3.23i,j Contours of $\hat{v}_\theta$: i) $x/c = 0.452$, j) $x/c = 0.678$

4. FURTHER ANALYSIS OF RESULTS

Whereas the previous chapter gave an in-depth analysis of the mean flow and touched briefly upon the turbulence results, this chapter presents further analysis with particular attention to the turbulence results. In the first section, the transport equations for mean x-component vorticity, Reynolds stress, and turbulent kinetic energy are derived and discussed, as are approximations and simplifications appropriate to the present study. In the second section, key terms in the momentum, turbulent kinetic energy, and Reynolds stress transport equations are discussed as well as the balances that were performed on these equations at selected locations of the flow. In the final section, an analysis is performed on key parameters which may influence the development of an axial velocity excess in the core, by compiling the present data with previous experimental work by other researchers.

It should be noted that the text refers several times to Reynolds stresses, but for brevity's sake only writes out the factors of the stress containing the velocity correlations instead of the full term (e.g. $\overline{v'w'}$ rather than $-\rho\overline{v'w'}$).

4.1 TRANSPORT EQUATIONS

In the present state of the art, direct numerical simulations (DNS) of the Navier-Stokes equations are still limited to a small number of flows. Because of the wide range of eddy wavelengths involved, order of magnitude improvements in computational technology are required before practical applications of DNS can be made. The whole range of flow scales is effectively lumped together in the Reynolds averaged Navier-Stokes equations, which reduces computational effort by a large margin: however, accuracy of the various modeling assumptions has been hotly debated. The Reynolds stress transport equations allow for closure of the Reynolds averaged Navier-Stokes equations though to use these equations additional terms must be modeled instead of the Reynolds stresses. The transport equations can also give qualitative insight into the behavior of turbulence and its contributing factors.

4.1.1 Mean x-Component Vorticity Transport Equation

It is useful to look at the x-component vorticity transport equation in the present tip vortex flow because it is the main component of vorticity which is generated in the roll-up process. It is derived by taking the y-derivative of the z-component momentum equation and subtracting from it the z-derivative of the y-component of the momentum equation, giving:

$$\frac{D}{Dt}(\Omega_x) = \Omega_x \frac{\partial U}{\partial x} + \Omega_y \frac{\partial U}{\partial y} + \Omega_z \frac{\partial U}{\partial z} + \nu \nabla^2 \Omega_x + \left(\frac{\partial^2}{\partial y^2} - \frac{\partial^2}{\partial z^2} \right) (-\overline{v'w'}) + \frac{\partial^2}{\partial y \partial z} (\overline{v^2} - \overline{w^2}) \tag{4.1.1}$$

A discussion on a balance of this equation at two locations is given in a following section.

4.1.2 Reynolds Stress Transport Equations

The Reynolds stress transport equations in cartesian coordinates may be derived by multiplying the instantaneous momentum equation in the x_i direction by u'_j and the x_j equation by u'_i and adding the two results together. This result is then time-averaged to give the following relation written in tensor notation for rectangular coordinates:

$$\begin{aligned} \frac{D}{Dt}(\overline{u'_i u'_j}) = & -\left[\overline{u'_j u'_k} \frac{\partial U_i}{\partial x_k} + \overline{u'_i u'_k} \frac{\partial U_j}{\partial x_k} \right] \\ & - 2\nu \overline{\frac{\partial u'_i}{\partial x_k} \frac{\partial u'_j}{\partial x_k}} \\ & + \overline{\frac{p'}{\rho} \left[\frac{\partial u'_i}{\partial x_j} + \frac{\partial u'_j}{\partial x_i} \right]} \\ & - \frac{\partial}{\partial x_k} \left[\overline{u'_i u'_j u'_k} - \nu \frac{\partial \overline{u'_i u'_j}}{\partial x_k} + \overline{\frac{p'}{\rho} (\delta_{jk} u'_i + \delta_{ik} u'_j)} \right] \end{aligned} \tag{4.1.2}$$

The transport equation for each individual Reynolds stress in rectangular and axisymmetric cylindrical coordinates is written out in Appendix equations B.7-B.19.

4.1.2.1 Discussion of Terms

The Reynolds stress transport equations (Equation 4.1.2) can be broken down into the following contributions (going from left to right of the equation): Mean flow transport, generation, dissipation, pressure-strain, and turbulent (viscous transport included in this last group) transport.

The mean flow transport term represents the rate of change of a scalar quantity (in this case a Reynolds stress) along a mean flow streamline. The production term represents the generation rate of Reynolds stress due to the interaction of the mean velocity gradients with the Reynolds stresses. The dissipation rate is the correlation of the product of various velocity fluctuation gradients. The name is a slight misnomer in that the term can actually be positive in rare instances (such as transitional flow), however, in the present case, the term should be negative. The pressure-strain term redistributes the turbulence such that the turbulence becomes more isotropic. It does not generate or destroy Reynolds stresses, however it tends to equalize the levels of normal stress while reducing the levels of shear stress. The diffusion rate term is actually a combination of three terms. They represent the transport of stress due to velocity fluctuations, pressure fluctuations, and viscous diffusion respectively. The pressure fluctuation transport term is usually small in comparison to the triple-product transport term while the viscous diffusion term is usually considered to be negligible, except in the wall region of viscous flows.

4.1.3 Turbulent Kinetic Energy Transport Equation

The turbulent kinetic energy relation can be derived by letting $j = i$ in Equation 4.1.2, summing over the repeated index, and then dividing by two. This relation may be written in indicial notation as:

$$\begin{aligned}\frac{1}{2}\frac{D}{Dt}(\overline{u_i'u_i'}) = &-\overline{u_i'u_k'}\frac{\partial U_i}{\partial x_k} \\ &- \nu\overline{\frac{\partial u_i'}{\partial x_k}\frac{\partial u_i'}{\partial x_k}} \\ &- \frac{\partial}{\partial x_k}\left[\overline{u_i'u_i'u_k'} - \nu\frac{\partial\overline{u_i'u_i'}}{\partial x_k} + 2\overline{\frac{p'}{\rho}\delta_{ik}u_i'}\right] \qquad (4.1.3a)\end{aligned}$$

Written out in full, this becomes:

$$\begin{aligned}\frac{Dk}{Dt} = &- \left[\overline{u'^2}\frac{\partial U}{\partial x} + \overline{u'v'}\left(\frac{\partial U}{\partial y} + \frac{\partial V}{\partial x}\right) + \overline{v'^2}\frac{\partial V}{\partial y}\right. \\ &\left. + \overline{v'w'}\left(\frac{\partial V}{\partial z} + \frac{\partial W}{\partial y}\right) + \overline{w'^2}\frac{\partial W}{\partial z} + \overline{u'w'}\left(\frac{\partial U}{\partial z} + \frac{\partial W}{\partial x}\right)\right] \\ &- \nu\left[\overline{\left(\frac{\partial u'}{\partial x}\right)^2} + \overline{\left(\frac{\partial u'}{\partial y}\right)^2} + \overline{\left(\frac{\partial u'}{\partial z}\right)^2} + \overline{\left(\frac{\partial v'}{\partial x}\right)^2} + \overline{\left(\frac{\partial v'}{\partial y}\right)^2} + \overline{\left(\frac{\partial v'}{\partial z}\right)^2}\right. \\ &\left. + \overline{\left(\frac{\partial w'}{\partial x}\right)^2} + \overline{\left(\frac{\partial w'}{\partial y}\right)^2} + \overline{\left(\frac{\partial w'}{\partial z}\right)^2}\right] \\ &- \frac{1}{2}\left(\frac{\partial(\overline{u'^3} + \overline{u'v'^2} + \overline{u'w'^2})}{\partial x} + \frac{\partial(\overline{u'^2v'} + \overline{v'^3} + \overline{v'w'^2})}{\partial y} + \frac{\partial(\overline{u'^2w'} + \overline{v'^2w'} + \overline{w'^3})}{\partial z}\right) \\ &+ \frac{\nu}{2}\nabla^2(\overline{u'^2} + \overline{v'^2} + \overline{w'^2}) - \frac{1}{\rho}\left(\frac{\partial(\overline{p'u'})}{\partial x} + \frac{\partial(\overline{p'v'})}{\partial y} + \frac{\partial(\overline{p'w'})}{\partial z}\right) \qquad (4.1.3b)\end{aligned}$$

Like the Reynolds stress transport equations, the turbulent kinetic energy transport equation can be broken down into the following sections: advection, production, dissipation, and turbulent transport. Note that the redistribution term (pressure-strain) drops out because $\partial u_i'/\partial x_i = 0$ by the continuity equation for incompressible flow.

4.1.4 Turbulence Parameters

The total dissipation rate may be defined as:

$$\epsilon \equiv \nu\overline{u_{i,j}'(u_{i,j}' + u_{j,i}')} \qquad (4.1.4)$$

A good approximation to the total dissipation rate is the homogeneous dissipation rate defined as:

$$D \equiv \nu\overline{u_{i,j}'u_{i,j}'} \qquad (4.1.5)$$

which is equal to one-half the trace of the viscous destruction term. It was assumed that the dissipation rate of turbulent kinetic energy was isotropic such that the viscous destruction term may be modeled as:

$$2\nu\overline{u'_{i,k}u'_{j,k}} \equiv \frac{2}{3}\epsilon\delta_{i,j} \tag{4.1.6}$$

4.2 IMPORTANT TERMS AND EQUATION BALANCES

4.2.1 Ω_x, Axial Vorticity

Along the vortex centerline, the vorticity increases rapidly in planes over the wing and continues to increase in planes in the wake albeit at a much slower rate. The continued increase of vorticity in the wake indicates that roll-up is not complete even at the farthest wake plane. A balance of equation 4.1.1 was done on the core centerline points at $x/c = -0.010$ and 0.452 and the breakdown of the balances is displayed in Figure 4.1. Note that in this coordinate system, vorticity is negative, and that vorticity was calculated by differencing the normalized velocity so that the units of the vorticity rate are 1/inch-sec. The dominant terms on the right-hand-side of the balance were the mean "stretching" (production) terms. Production at $x/c = -0.010$ was -0.21 and at $x/c = 0.452$ it was -0.0075. The marked difference in production levels at the 2 stations indicates that although roll-up is not complete in the near-wake, the bulk of the axial vorticity production occurs at stations over the wing. The viscous dissipation term was negligible in both cases while the turbulence terms were only slightly more significant. Clearly, in the far wake, these terms will become more dominant, but it seems that while the vortex is still developing, the production terms are of much larger magnitude.

4.2.2 Reynolds Stress

Balances of the individual Reynolds stresses were possible after the dissipation term in the transport of TKE equation was found by difference. Equation 4.1.6 was used to approximate the viscous destruction term. It was noted in the previous chapter that none of the Reynolds shear stresses were aligned with the mean strain

rate, whereas for an isotropic eddy viscosity turbulence model the shear stresses would align themselves with the mean strain rate (i.e. $\overline{u_i' u_j'} \propto \frac{\partial U_i}{\partial x_j} + \frac{\partial U_j}{\partial x_i}$). Figure 4.2 shows contours of (negative) mean strain rate and the corresponding component of Reynolds shear stress and demonstrates quite vividly the 'lag' in the shear stress. It was shown in Chapter 3 and in Appendix C that the orientation of the extrema of the $\overline{v'w'}$ stress found in the present experiment (roughly a $\pm$ 45 degree orientation off the y and z axes) is decided kinematically by $\overline{v_r'^2} > \overline{v_\theta'^2}$ and relatively small levels of $\overline{v_r' v_\theta'}$. In confirmation of these kinematics, the contours for $\hat{v}$ and $\hat{w}$ were found to be elliptical. The next questions and perhaps the real physical questions that arise are: Why is there an inequality of radial and tangential normal stresses and why are there relatively small levels of $\overline{v_r' v_\theta'}$?

The answer to the second question, which has been proposed before by several authors, is that the approximately solid body rotation of the vortex core mean flow minimizes production of $\overline{v_r' v_\theta'}$. The production of stress is not equal to zero however, and indeed it will be shown later that a small level of production of $\overline{v_r' v_\theta'}$ can help explain the answer to the first question. The answer to the first question prompts a further investigation into the transport equations of $\overline{v_r'^2}$, $\overline{v_\theta'^2}$, and $\overline{v_r' v_\theta'}$, shown in Equations B.17, B.18, and B.15 respectively. The production terms in the $\overline{v_r'^2}$ transport equation (Equation B.17) are $-2\overline{v_r'^2}\frac{\partial V_r}{\partial r}$, $-2\overline{v_x' v_r'}\frac{\partial V_r}{\partial x}$, and $+2\overline{v_r' v_\theta'}\frac{V_\theta}{r}$. In the vortex core, the mean flow factor $\frac{V_\theta}{r}$ is orders of magnitude greater than the other mean flow factors, which makes the last term a significant term. The first term may also be significant because the turbulence stress factor is a normal stress (in the present experiment, normal stresses are much larger than the shear stresses). The mean flow factor in this first term however is small. The second term has a small mean flow factor and a small turbulence factor (a shear stress) and may be ignored. The important production terms in the the transport equation for $\overline{v_r'^2}$ and the other Reynolds stresses (with the exception of $\overline{v_x'^2}$) are shown in Table 4.1. The production terms in the $\overline{v_\theta'^2}$ transport equation (Equation B.18) are $-2\overline{v_\theta'^2}\frac{\partial V_r}{\partial r}$, $-2\overline{v_x' v_\theta'}\frac{\partial V_\theta}{\partial x}$, and $-2\overline{v_r' v_\theta'}\frac{\partial V_\theta}{\partial r}$. The mean flow factor $\frac{\partial V_\theta}{\partial r}$, which is approximately equal to $\frac{V_\theta}{r}$ in the vortex core region, is orders of magnitude greater

than the other mean flow factors. Hence, $-2\overline{v_r' v_\theta'}\frac{\partial V_\theta}{\partial r}$ is a significant production term for $\overline{v_\theta'^2}$. The first production term is also significant because of the normal stress factor contained in it. In fact, this first term is nearly identical in form to the first production term in the $\overline{v_r'^2}$ transport equation. The second term may be ignored because of the small shear stress factor and the small mean flow gradient. The significant production terms in 5 of the 6 Reynolds stress transport equations (including the two just mentioned) are summarized in Table 4.1. The significant terms in the production of $\overline{v_r'^2}$ and $\overline{v_\theta'^2}$ are almost identical in the vortex core region with a couple of exceptions. First and most importantly, the last term is opposite in sign (positive in the $\overline{v_r'^2}$ equation and negative in the $\overline{v_\theta'^2}$ equation). Secondly, the normal stress factor in the first term is different for each equation ($\overline{v_r'^2}$ in the $\overline{v_r'^2}$ equation and $\overline{v_\theta'^2}$ in the $\overline{v_\theta'^2}$ equation). Considering the relatively small differences in $\overline{v_r'^2}$ and $\overline{v_\theta'^2}$, the different sign of the last production term for each equation is the key to explaining the anisotropy in normal stress levels.

The orientation of the present coordinate system and the sense of the vortex rotation resulted in negative vorticity in the vortex core, negative tangential velocity, V_θ, and approximately constant negative $\frac{\partial V_\theta}{\partial r}$ in the vortex core region. In analyzing the last production term of the $\overline{v_r'^2}$ and $\overline{v_\theta'^2}$ transport equations, it is necessary to find the sign of the $\overline{v_r' v_\theta'}$ factor. This may be determined by analyzing the $\overline{v_r' v_\theta'}$ transport equation. Ignoring terms with small mean flow gradient factors and shear stresses, the significant production terms in the $\overline{v_r' v_\theta'}$ transport equation are: $-\frac{V_\theta}{r}(\overline{v_r'^2} - \overline{v_\theta'^2})$ and $-r\overline{v_r'^2}\frac{\partial}{\partial r}(\frac{V_\theta}{r})$. Figure 4.3 shows a plot of the (not entirely obvious) mean flow gradient, $\frac{\partial}{\partial r}(\frac{V_\theta}{r})$. It can be seen that this quantity, which is initially zero on the vortex centerline, becomes increasingly negative towards the edge of the vortex core. This is due to the rolling off of the mean tangential velocity profile, initially $V_\theta \approx C_1 r$, as the edge of the vortex core is approached. Hence, the second production term is negative in sign. The first production term can be looked upon as a term which tends to return the normal stresses to an isotropic state. Isotropy of the normal stresses will eliminate this term. Anisotropy of the normal stresses such that $\overline{v_r'^2} > \overline{v_\theta'^2}$ will make this first production term positive

(remember $V_\theta < 0$), which will counter the effects of the second term. The reactive nature of this first production term means that the anisotropy of the normal stresses will be driven by the second production term. Imagine an initially isotropic state of the normal stresses such that the first production term is equal to zero. The production of $\overline{v_r' v_\theta'}$ will be governed almost entirely by the $-r\overline{v_r'^2}\frac{\partial}{\partial r}(\frac{V_\theta}{r})$ term, which will be negative. It may be expected then that negative levels of $\overline{v_r' v_\theta'}$ will develop. Negative levels of $\overline{v_r' v_\theta'}$ mean that the third production term in the $\overline{v_r'^2}$ equation will be positive and that the third production term in the $\overline{v_\theta'^2}$ equation will be negative. Hence production of $\overline{v_r'^2}$ is enhanced relative to production of $\overline{v_\theta'^2}$. This result should hold for a turbulent vortex in the far-wake also and indeed computational studies by Zeman (1994) have corroborated this belief. Zeman (1994) studied a time-evolving line vortex with initially isotropic turbulence levels using a full Reynolds stress model. He found almost identical orientation of the $\overline{v'w'}$ stress compared with the present experiment, a low level of $\overline{v_r' v_\theta'}$ stress, and $\overline{v_r'^2} > \overline{v_\theta'^2}$. Contours of his computed $\overline{v'w'}$ are plotted along with the experimental contours of $\overline{v'w'}$ in Figure 4.4.

Figure 4.5a shows levels of $\overline{v_x' v_r'}$ at $x/c = 0.125$. As expected, the contours are far from axisymmetric except in the vortex core. More importantly, the level of $\overline{v_x' v_r'}$ was positive in the vortex core region, with a maximum of 0.009 (normalized by U_∞^2) measured on the edge of the core. The level of $\overline{v_x' v_r'}$ was reduced as the centerline was approached. Figure 4.5b shows contours of $\overline{v_x' v_\theta'}$ at $x/c = 0.125$. Again, the contours do not appear axisymmetric and positive levels of stress were measured. A maximum (normalized by U_∞^2) of 0.008 was measured on the edge of the core and the levels of stress were reduced as the centerline was approached. A plot of these two shear stresses against vertical distance from the vortex centerline is shown in Figure 4.6. Keeping these shear stresses in cylindrical axes in mind, an explanation for the behavior of the shear stresses in rectangular coordinates (hereafter called "cylindrical" or "rectangular" shear stresses), $\overline{u'v'}$ and $\overline{u'w'}$, will now be offered.

As was shown in the previous chapter, contours of $\overline{u'v'}$ were aligned so that positive peaks of $\overline{u'v'}$ occurred at $\theta = -30$ to -60 degrees, depending upon axial

station. Upstream stations had peaks at around $\theta = -30$ degrees and the θ peaks became progressively smaller with axial station. Negative peaks of stress were aligned +180 degrees relative to the positive peak. At $x/c = 0.125$, the positive peak of $\overline{u'v'}$ stress was aligned at approximately $\theta = -45$ degrees. Appendix C includes a derivation of the relationship between $\overline{u'v'}$ and the cylindrical shear stresses, $\overline{v'_x v'_r}$ and $\overline{v'_x v'_\theta}$. Using the maximum levels shown in Figures 4.5a and 4.5b, a distribution of $\overline{u'v'}$ as a function of θ was calculated and is plotted in Figure 4.7a. Note that the peaks shown in Figure 4.7a correspond roughly to the θ at which the peaks are roughly displayed in Figure 3.19. All this really demonstrates is that the kinematics correctly predict the orientation of the $\overline{u'v'}$ stress. The real question here is: why are $\overline{v'_x v'_r}$ and $\overline{v'_x v'_\theta}$ both positive in the vortex core region and why are they roughly of the same order of magnitude? Again, to answer these questions, the production terms of the respective transport equations are analyzed.

The production terms in the transport of $\overline{v'_x v'_r}$ equation (Equation B. 13) are: $\frac{V_\theta}{r}\overline{v'_x v'_\theta}$, $-\overline{v'^2_x}\frac{\partial V_x}{\partial x}$, $-\overline{v'^2_r}\frac{\partial V_x}{\partial r}$, and $-\overline{v'_x v'_r}(\frac{\partial V_x}{\partial x} + \frac{\partial V_r}{\partial r})$. The last term can be ignored because the mean flow gradient factors are small and the shear stress factor is relatively small. The second production term can also be ignored even though the turbulence factor is a normal stress, because the mean flow gradient factor is particularly small. It is particularly small because the radial velocity is small and the axial gradient of this velocity is even smaller. This leaves the first and third terms as the dominant production terms in the transport equation. A comparison of these terms for a $y-$cut through the vortex centerline at $x/c = 0.125$ and $x/c = 0.452$ is shown in Figures 4.8a and 4.8b. The $-\overline{v'^2_r}\frac{\partial V_x}{\partial r}$ term clearly dominates and the sum of the two production terms is positive, which corresponds to the sign of $\overline{v'_x v'_r}$ measured. An unsurprising result; physically this means that positive radial fluctuations of the fluid near the vortex centerline bring a positive $x-$momentum flux to the relatively lower $x-$momentum fluid nearby. This result also demonstrates that the presence of a velocity excess in the vortex core creates levels of $\overline{v'_x v'_r}$ that would not be apparent in a 2-D vortex.

The sign of the $\overline{v'_x v'_\theta}$ can be explained using a similar order-of-magnitude anal-

ysis on the production terms of its transport equation. The significant terms are: $-\overline{v_x'^2}\frac{\partial V_\theta}{\partial x}$, $-\overline{v_x' v_r'}\frac{\partial V_\theta}{\partial r}$, and $-\overline{v_r' v_\theta'}\frac{\partial V_x}{\partial r}$. The magnitude of the first of these terms was difficult to ascertain because measurement of the axial gradient was fairly inaccurate. It may be fair to assume that in planes over the wing, $\frac{\partial V_\theta}{\partial x} > 0$ and in planes in the wake, $\frac{\partial V_\theta}{\partial x} < 0$. If so, the first production term can be assumed to be negative in planes over the wing and positive in plane in the wake. The relative magnitudes of the second and third production terms are shown in Figure 4.9a and 4.9b. The second and third terms are generally both positive, and are of the same order of magnitude. Again, the presence of gradients of the axial velocity in the vortex core is the cause of measurable levels of $\overline{v_x' v_\theta'}$. At the very least, in the wake, the sum of all three production terms is positive, which corresponds to the sign of stress measured in the experiment. The production of $\overline{v_x' v_r'}$ is greater than that of $\overline{v_x' v_\theta'}$. The fact that roughly equal levels of stress were measured may be due to the pressure-strain (redistribution) term.

It is interesting that Figures 4.8a, b show that the peaks of the production of $\overline{v_x' v_r'}$ occur at $r/r_1 \approx 0.40$ and Figures 4.9a, b show that the peaks of the production of $\overline{v_x' v_\theta'}$ occur at $r/r_1 \approx 0.33$. These are approximately the locations at which the peak levels of the Reynolds shear stresses were measured at $x/c = 0.452$ and 0.678. As was discussed in Chapter 3, the peak levels of the shear stresses had shifted from near the outer edge of the vortex core ($r/r_1 \approx 0.67$) at $x/c = 0.125$, to a radius of approximately $r/r_1 = 0.33$ at $x/c = 0.452$. In addition, in general, the peak turbulence levels had shifted from the viscous core edge towards the core center. The fact that the peak production rates were found at $r/r_1 \approx 0.33 - 0.4$ at $x/c = 0.452$, where the peak stresses were measured at $r/r_1 \approx 0.33$ might be expected. However the fact that similar results were found at $x/c = 0.125$, where the peak stresses were measured at $r/r_1 \approx 0.67$, indicate that there really is something to this. Figures 4.10a,b show V_θ and $\frac{\partial V_x}{\partial r}$ vs. y-distance from the vortex centerline at $x/c = 0.125$ and 0.452 respectively. V_θ is plotted only to aid in figuring out where r_1 is. The peak levels of $\frac{\partial V_x}{\partial r}$ also occur at $r/r_1 \approx 0.40$. The radial gradient of the mean axial velocity in the vortex core is the main cause of turbulent production in

the near wake.

The positive and roughly equal levels of $\overline{v'_x v'_r}$ and $\overline{v'_x v'_\theta}$ are also kinematically consistent with the orientation of $\overline{u'w'}$. Appendix C shows its relationship to the cylindrical stresses. A plot of $\overline{u'w'}$ as a function of θ is shown in Figure 4.7b for the cylindrical stresses found at $x/c = 0.125$ and $r \approx r_1$.

4.2.3 Momentum

Now that the orientation of the Reynolds stresses can be explained, what is the significance of these orientations?

The three Reynolds averaged momentum equations, which are written in tensor notation in Appendix B, each contain three additional terms due to the turbulent stresses. The turbulence terms in the $x-$momentum equation are: $-\frac{\partial \overline{u'^2}}{\partial x}$, $-\frac{\partial \overline{u'v'}}{\partial y}$, and $-\frac{\partial \overline{u'w'}}{\partial z}$.

A plot of $\overline{u'v'}$ vs. $y-$distance to the vortex centerline is shown in Figure 4.11, and a plot of $\overline{u'w'}$ vs $z-$distance to the vortex centerline is shown in Figure 4.12. The slopes of these plots represents the rate per unit mass at which the turbulence is transferring $x-$momentum. A positive slope indicates that the turbulence is slowing down the fluid element. As would be expected, these plots indicate that the turbulence is diffusing the peak of axial velocity in the vortex core.

An $x-$momentum equation balance was done on the core centerline at $x/c = 0.125$ and 0.452 to look at the relative effect of the turbulent diffusion, and the results are displayed in Figure 4.13. The $x-$momentum equation written out in full is:

$$U\frac{\partial U}{\partial x} + V\frac{\partial U}{\partial y} + W\frac{\partial U}{\partial z} = -\frac{1}{\rho}\frac{\partial P}{\partial x} + \nu\nabla^2 U - \frac{\partial \overline{u'^2}}{\partial x} - \frac{\partial \overline{u'v'}}{\partial y} - \frac{\partial \overline{u'w'}}{\partial z} \qquad (4.1.7)$$

At $x/c = 0.125$, the core centerline fluid is being decelerated rather slowly and almost entirely by the core turbulence. The gradients of $\overline{u'v'}$ contributed the most to the deceleration, followed by $\overline{u'w'}$ and then by $\overline{u'^2}$. Laminar dissipation was negligible and was not plotted. The pressure force acted as a rather substantial accelerating force. The favorable pressure gradient may be due to the incomplete

roll-up of the vortex. At $x/c = 0.452$, the core centerline fluid is still being decelerated but at a faster rate. Inspection of the terms indicate that this was primarily due to a drop in the accelerating pressure forces. The shear stress gradients were again the prime decelerating forces, with the $\overline{u'w'}$ gradient contributing relatively more to the total force than at the $x/c = 0.125$ station. The axial decay of the axial normal stress at $x/c = 0.452$ created a very slight accelerating force to the balance.

4.2.4 Influence of Parameters on Core Axial Velocity

It had been mentioned in the previous chapter that the tip shape, angle of attack and Reynolds number might be expected to have an influence on the core axial velocity. The simplest possible formula describing the axial velocity on the vortex core centerline as a function of these parameters (excluding tip shape) could be written as:

$$U/U_\infty = a_1 Re_c^{a_2} (\alpha/deg)^{a_3} (x/c + 1)^{a_4} AR^{a_5} \tag{4.2.1}$$

This formula includes dependence upon x/c and AR in addition to the parameters described previously. A non-linear least squares fit was performed (using the IMSL routine, UNLSF) on Equation 4.2.1 with data compiled from the reference list shown in Table 1.1. Some data in Table 1.1 were not included because of the suspicion of probe intereference contaminating the data. Some of the peculiarities of the data from Chiger and Corsiglia (1971) were pointed out in Chapter 1, and only a single data point was used from that study. The data used in the fits are shown in Table 4.2. A plot of the fit is shown in Figure 4.14. Square-tipped wings and round-tipped wings were denoted with square and round symbols respectively. The constants found for Equation 4.2.1 were: $a1 = 0.56$, $a2 = 0.041$, $a3 = 0.25$, $a4 = -0.13$, $a5 = -0.14$. The standard deviation of the fit was determined to be $0.10\ U_\infty$. From the fit, it may be determined that the centerline axial velocity increases with Re_c and α, but decreases with x/c and AR. Using the determined constants and Equation 4.2.1, Figures 4.15 and 4.16 show centerline axial velocity

vs. Re_c and α respectively for the wing used in the present experiment. Figure 4.16 demonstrates that angle of attack is the key parameter that influences the centerline axial velocity. Upon general inspection of the data in Table 1.1 and Table 4.2, the round-tipped wings showed slightly higher levels of axial velocity compared to the square-tipped wings. Variation due to tip and airfoil shape may be buried within the standard deviation of the fit of Equation 4.2.1. The range of applicability of the fit was: $4.1e5 < Re_c < 4.6e6$, $4.0 < \alpha < 12.0$, $0.005 < x/c < 15.0$, and $1.5 < AR < 6.6$. The variation with aspect ratio should be looked upon with some caution because there were a limited number of samples with different aspect ratios (see Table 4.2).

Table 4.1 Important Production Terms

Reynolds Stress Factor	Important Production Terms
$\overline{v_r'^2}$	$-2\overline{v_r'^2}\frac{\partial V_r}{\partial r}$, $+2\overline{v_r' v_\theta'}\frac{V_\theta}{r}$
$\overline{v_\theta'^2}$	$-2\overline{v_\theta'^2}\frac{\partial V_r}{\partial r}$, $-2\overline{v_r' v_\theta'}\frac{\partial V_\theta}{\partial r}$
$\overline{v_r' v_\theta'}$	$-\frac{V_\theta}{r}(\overline{v_r'^2} - \overline{v_\theta'^2})$, $-r\overline{v_r'^2}\frac{\partial}{\partial r}(\frac{V_\theta}{r})$
$\overline{v_x' v_r'}$	$\frac{V_\theta}{r}\overline{v_x' v_\theta'}$, $-\overline{v_r'^2}\frac{\partial V_x}{\partial r}$
$\overline{v_x' v_\theta'}$	$-\overline{v_x' v_r'}\frac{\partial V_\theta}{\partial r}$, $-\overline{v_r' v_\theta'}\frac{\partial V_x}{\partial r}$

Table 4.2 Experimental Data Used in Least-Squares Fit

Study	u/U_∞	Re_c	α (deg)	x/c	AR
1	1.772	4.6e6	10.0	0.005	1.5
1	1.770	4.6e6	10.0	0.125	1.5
1	1.756	4.6e6	10.0	0.246	1.5
1	1.725	4.6e6	10.0	0.452	1.5
1	1.699	4.6e6	10.0	0.678	1.5
1	1.492	1.16e6	10.0	0.678	1.5
2	1.62	6.8e5	10.0	2.0	2.3
2	1.33	6.8e5	5.0	2.0	2.3
2	1.17	4.1e5	6.2	2.0	3.7
2	1.12	6.8e5	10.0	10.0	2.3
2	0.71	6.8e5	5.0	10.0	2.3
2	1.04	4.1e5	6.2	6.0	3.7
2	0.96	4.1e5	6.2	15.0	3.7
3	0.880	7.6e5	8.0	2.0	5.33
3	1.05	7.6e5	10.0	2.0	5.33
3	1.18	7.6e5	12.0	2.0	5.33
4	1.40	9.5e5	12.0	0.005	5.33
5	1.53	1.5e6	12.0	0.1	6.6
5	1.55	1.5e6	12.0	0.2	6.6
5	1.49	1.5e6	12.0	0.5	6.6
5	1.32	1.5e6	12.0	1.0	6.6
5	1.29	1.5e6	12.0	2.0	6.6
5	1.18	1.5e6	12.0	4.0	6.6
5	1.16	1.5e6	12.0	6.0	6.6
5	1.28	1.5e6	8.0	0.1	6.6
5	1.08	1.5e6	4.0	0.1	6.6
5	1.05	1.5e6	8.0	4.0	6.6
5	1.00	1.5e6	4.0	4.0	6.6
5	1.08	3.0e6	4.0	0.1	6.6
5	1.18	1.7e6	7.0	0.1	6.6
5	1.40	1.1e6	10.0	0.1	6.6
5	1.00	3.0e6	4.0	4.0	6.6
5	1.06	1.7e6	7.0	4.0	6.6
5	1.16	1.7e6	10.0	4.0	6.6

1 Experimental results in present study.
2 Green and Acosta(1991)
3 Orloff (1974)
4 Chiger and Corsiglia (1971)
5 McAlister and Takahashi (1991)

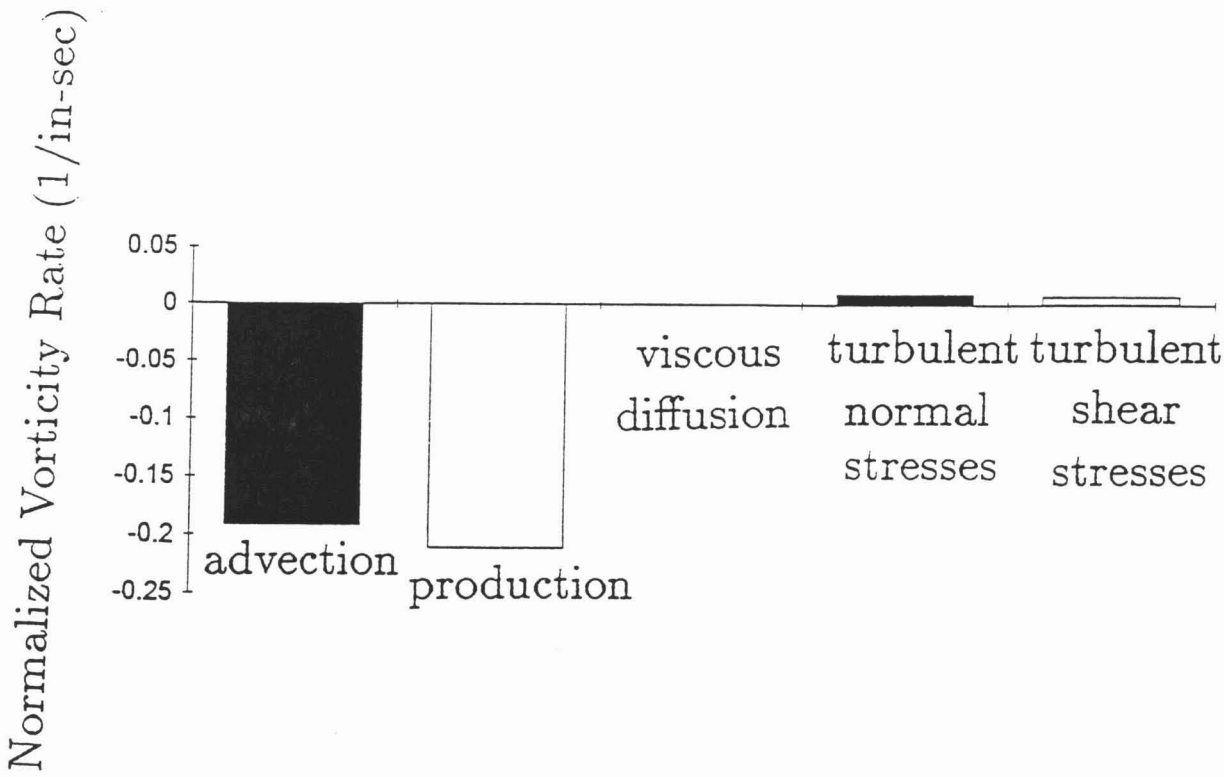

Figure 4.1a Balance of Axial Vorticity Eqn on Vortex Centerline
x/c = -0.010

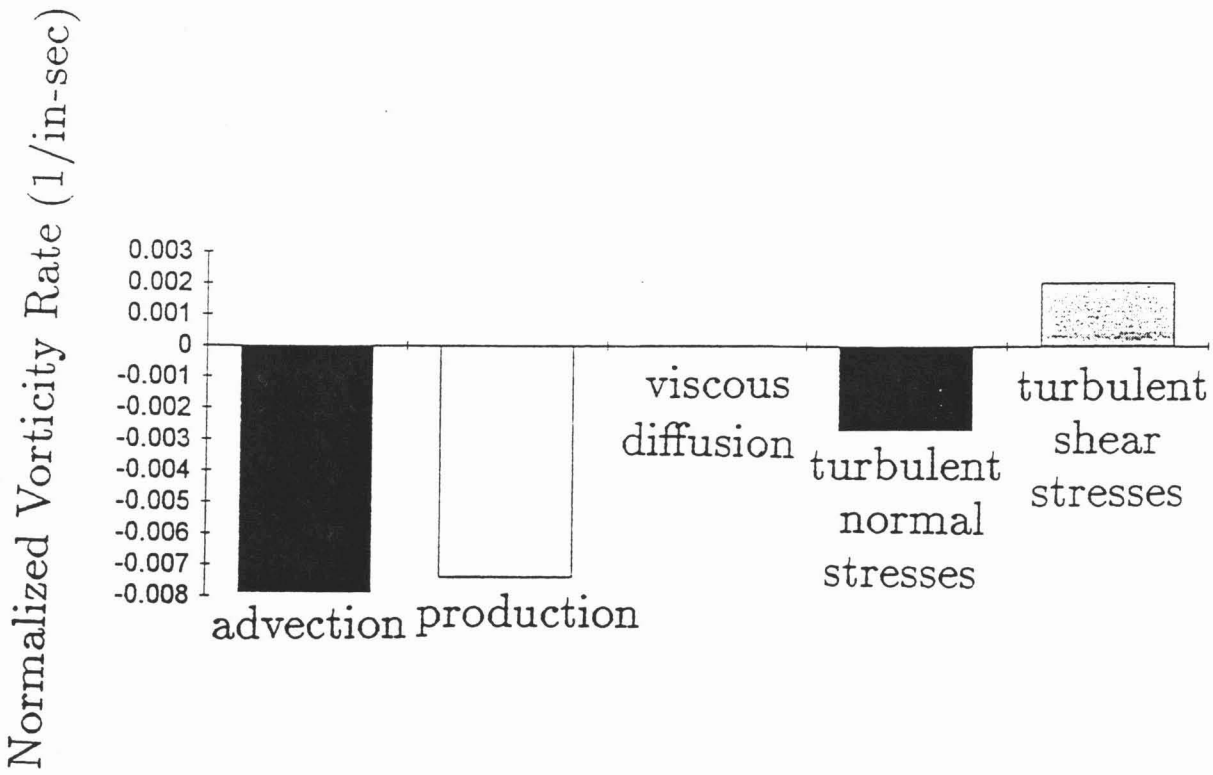

Figure 4.1b Balance of Axial Vorticity Eqn on Vortex Centerline
x/c = 0.452

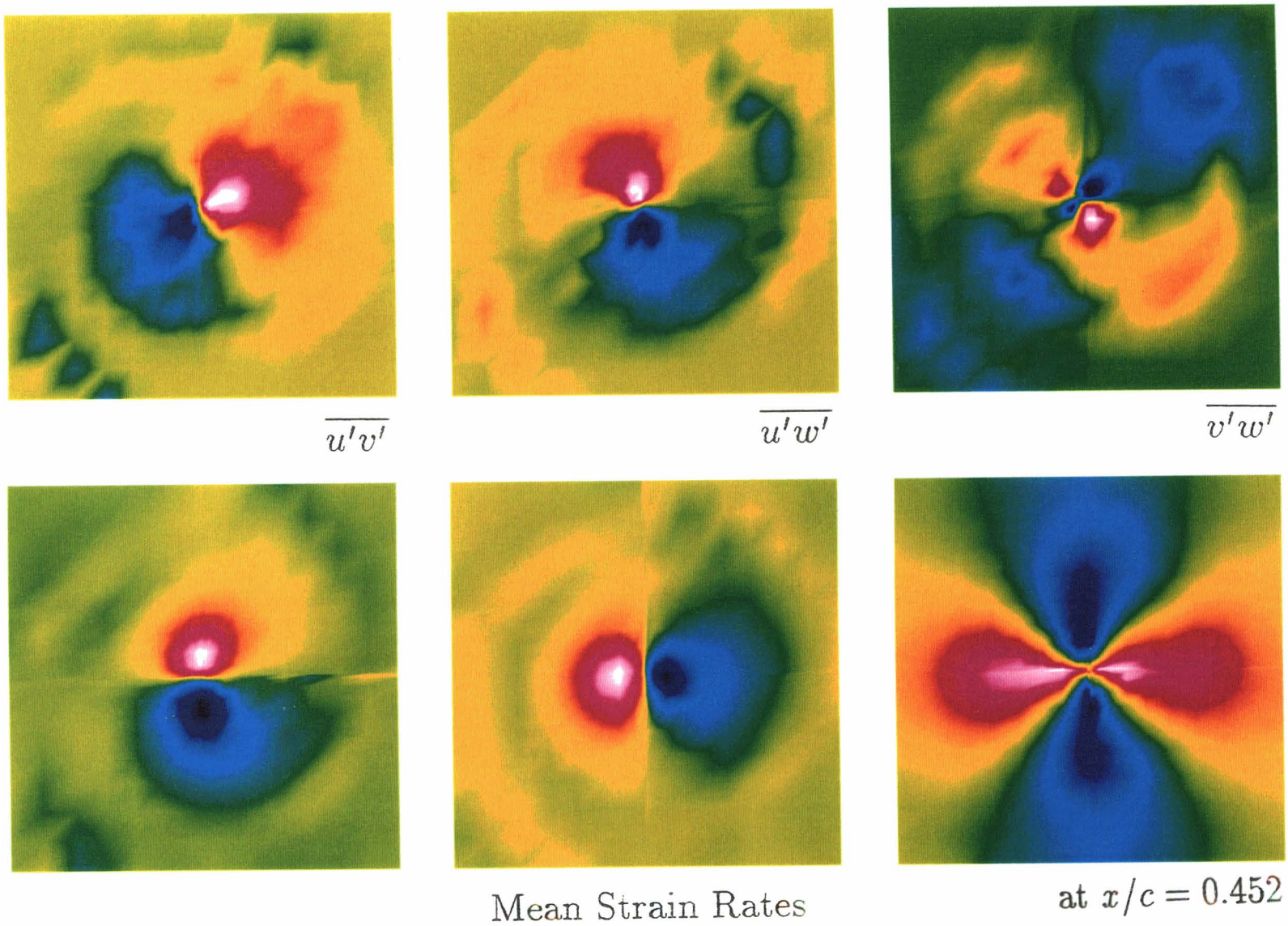

Figure 4.2 Contours of Mean Strain Rate and Respective Reynolds Stress

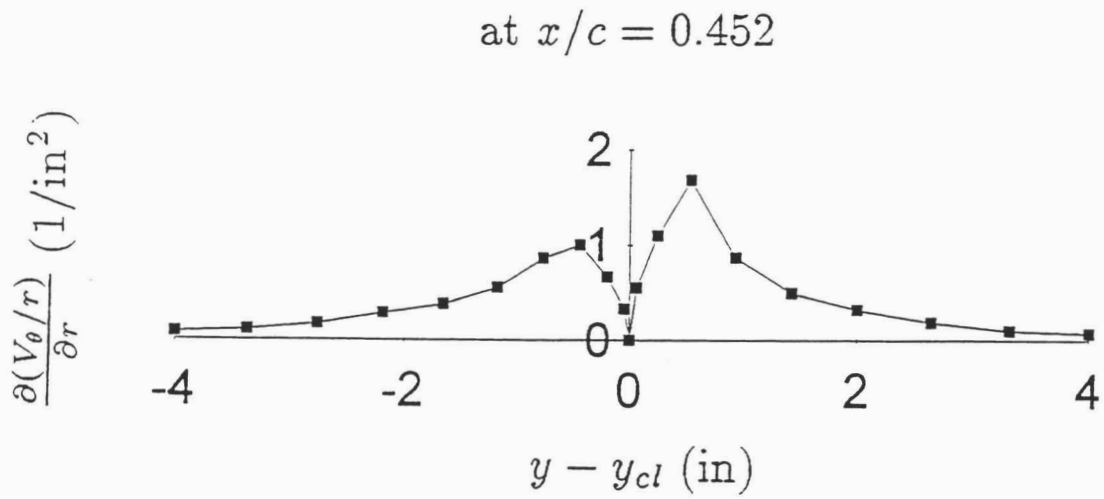

Figure 4.3 $\frac{\partial(V_\theta/r)}{\partial r}$ **vs.** y**-Distance From Vortex Centerline**

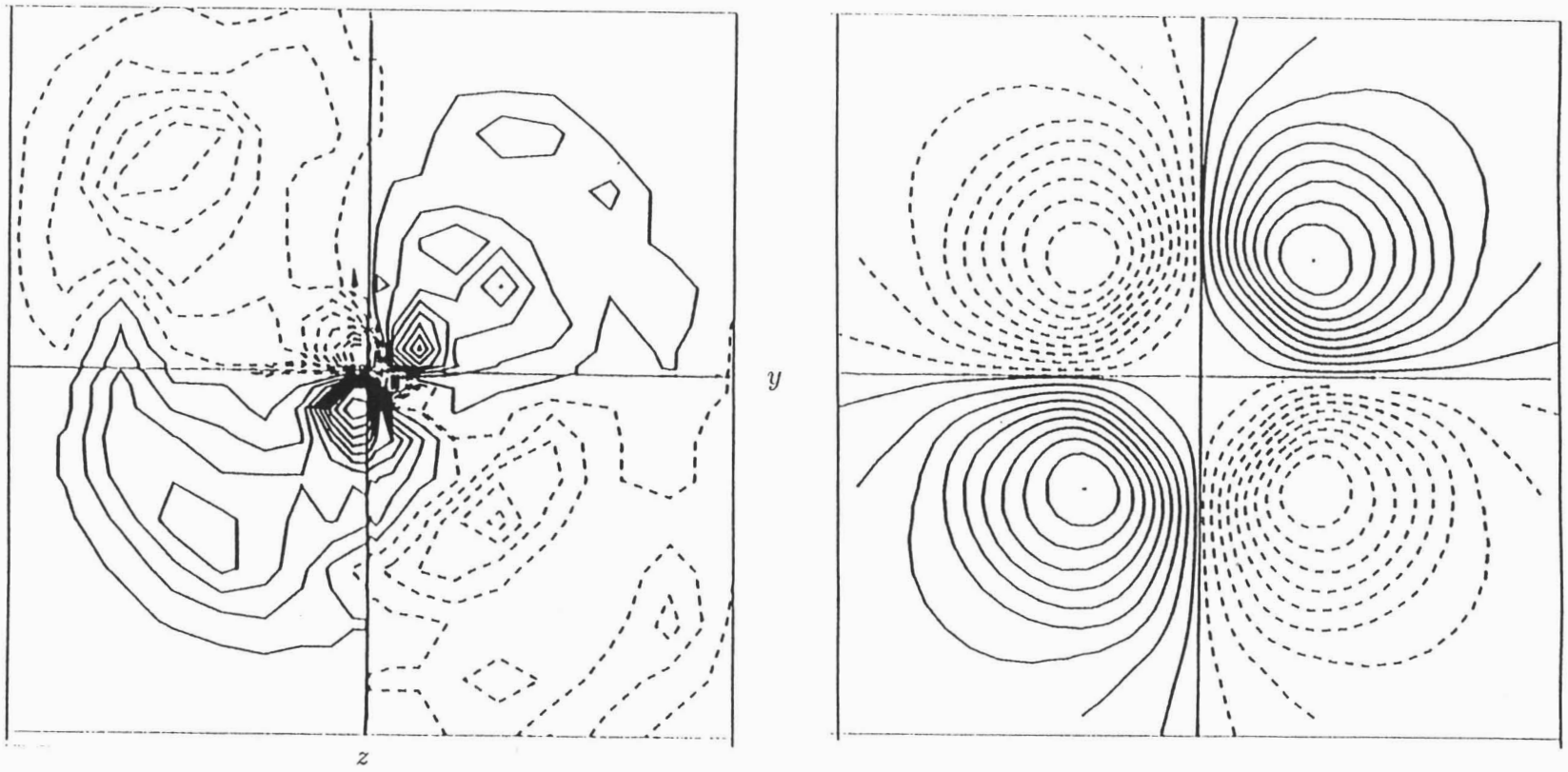

$\overline{v'w'}$, experimental

$\overline{v'w'}$, computed (Zeman, 1994)

Figure 4.4 Computed vs. Experimental Contours of $\overline{v'w'}$

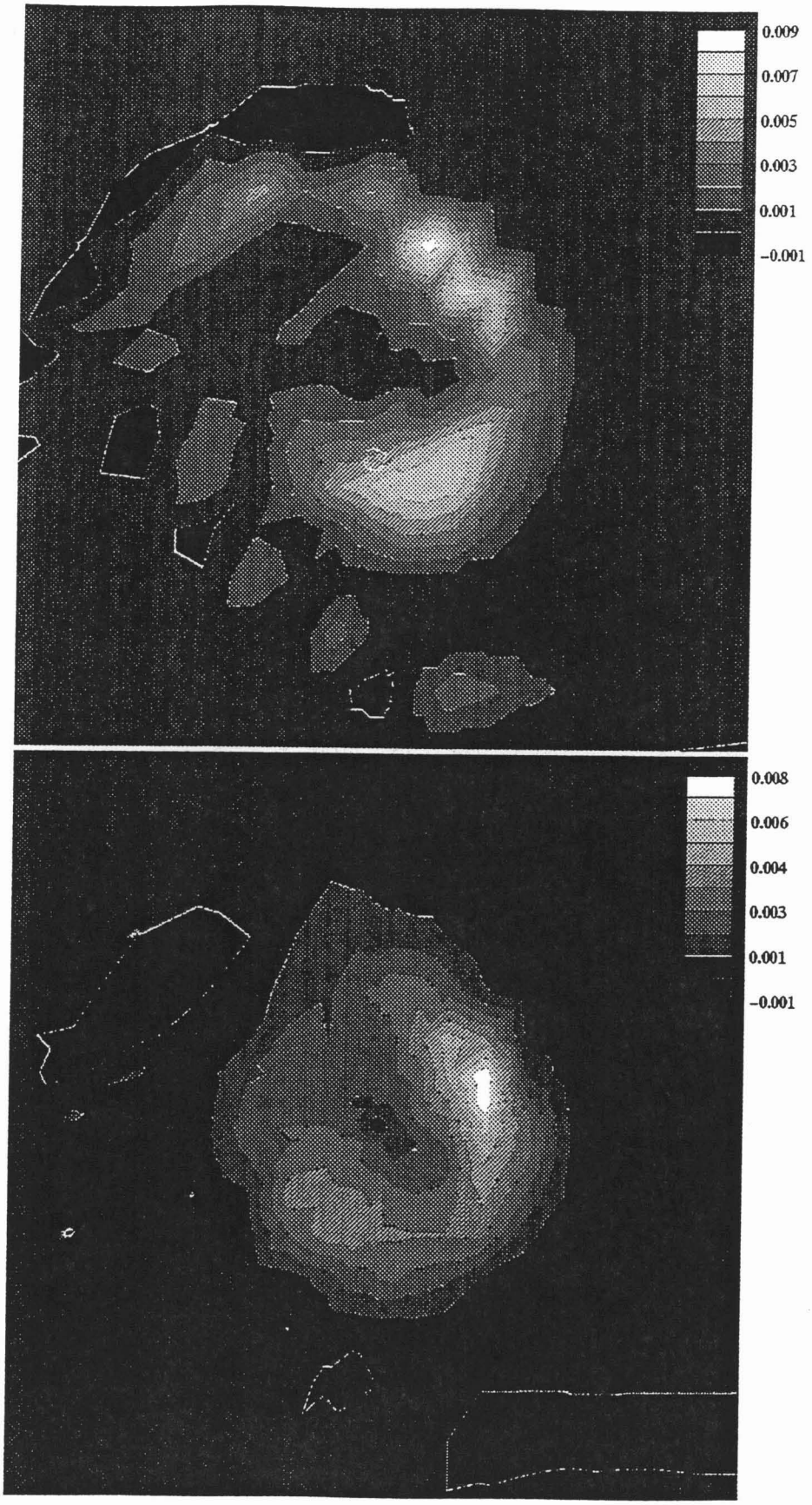

Figure 4.5a,b, Contours of: a) $\overline{v_x' v_r'}$ at $x/c = 0.125$, b) $\overline{v_x' v_\theta'}$ at $x/c = 0.125$

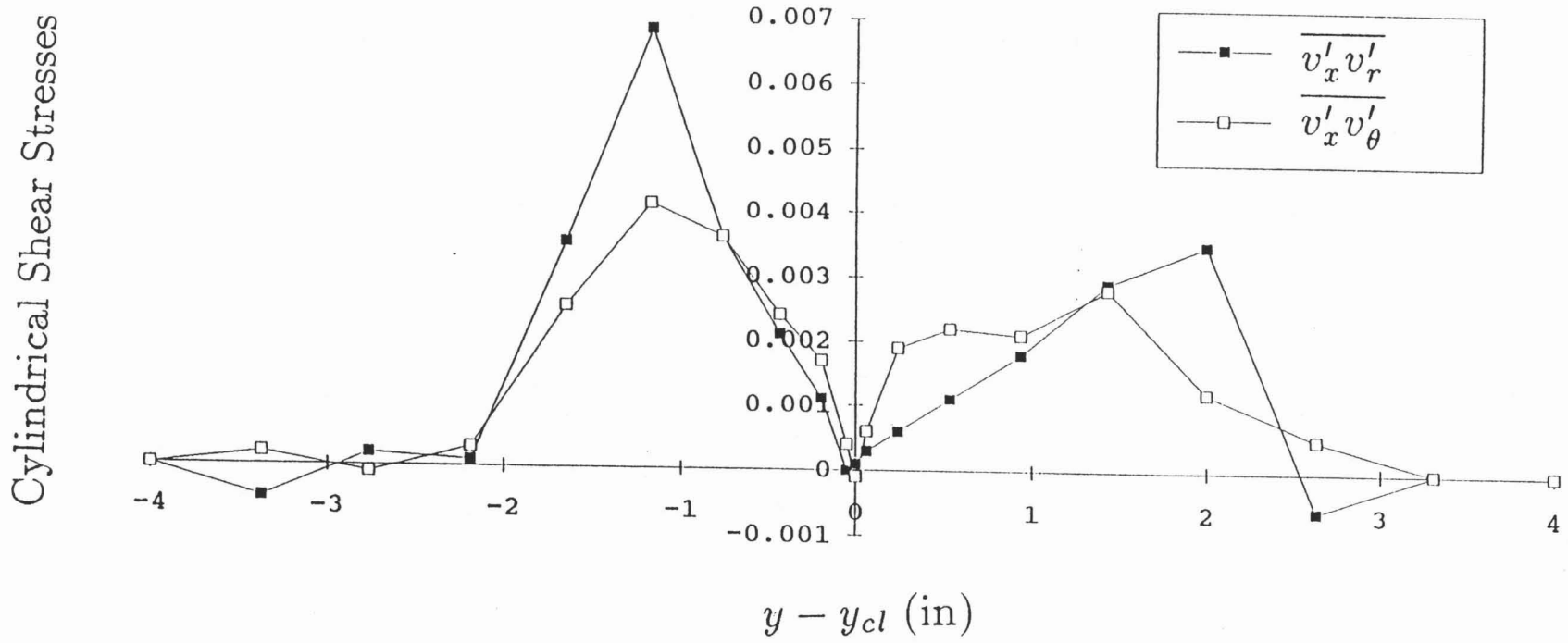

Figure 4.6 Line Plot of Reynolds Shear Stresses in Cylindrical Coordinates

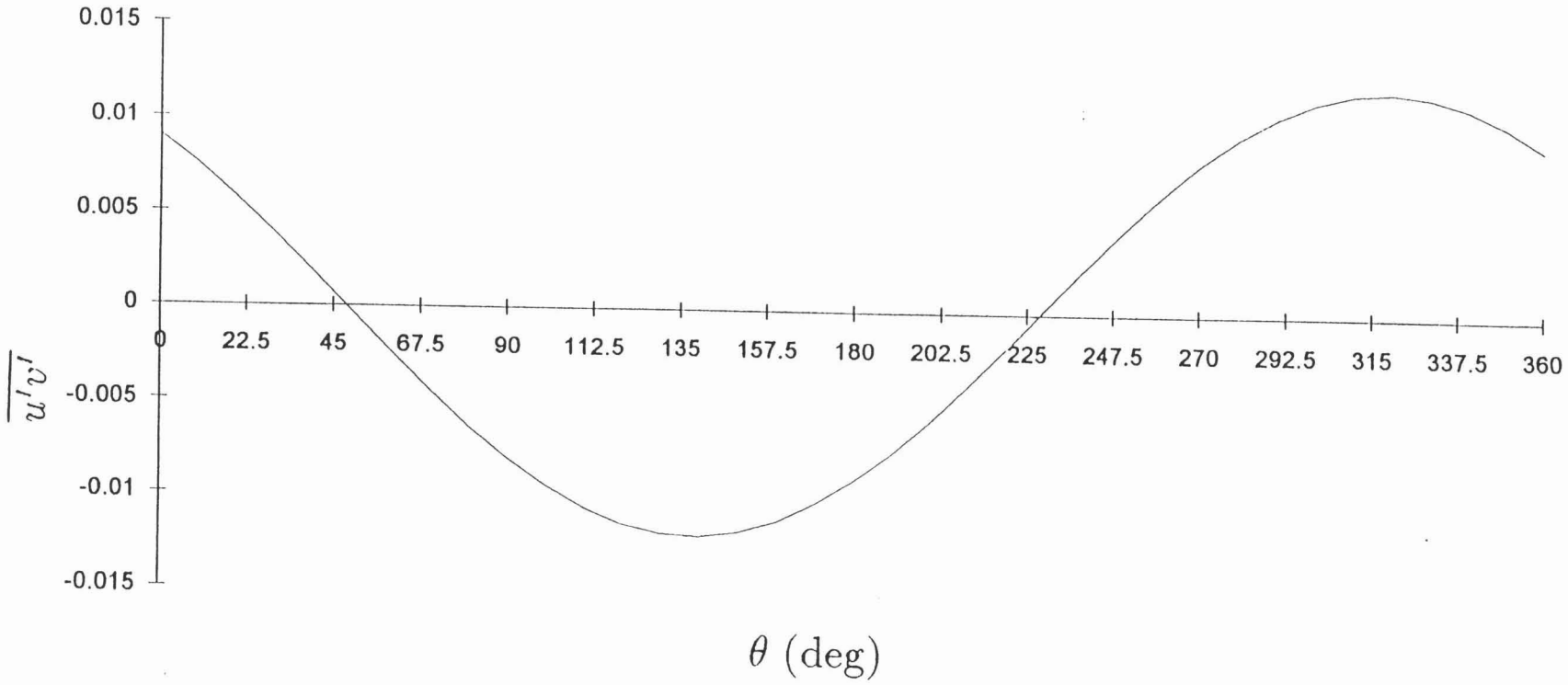

Figure 4.7a $\overline{u'v'}$ vs. θ With Assumed Axisymmetric Cylindrical Shear Stresses

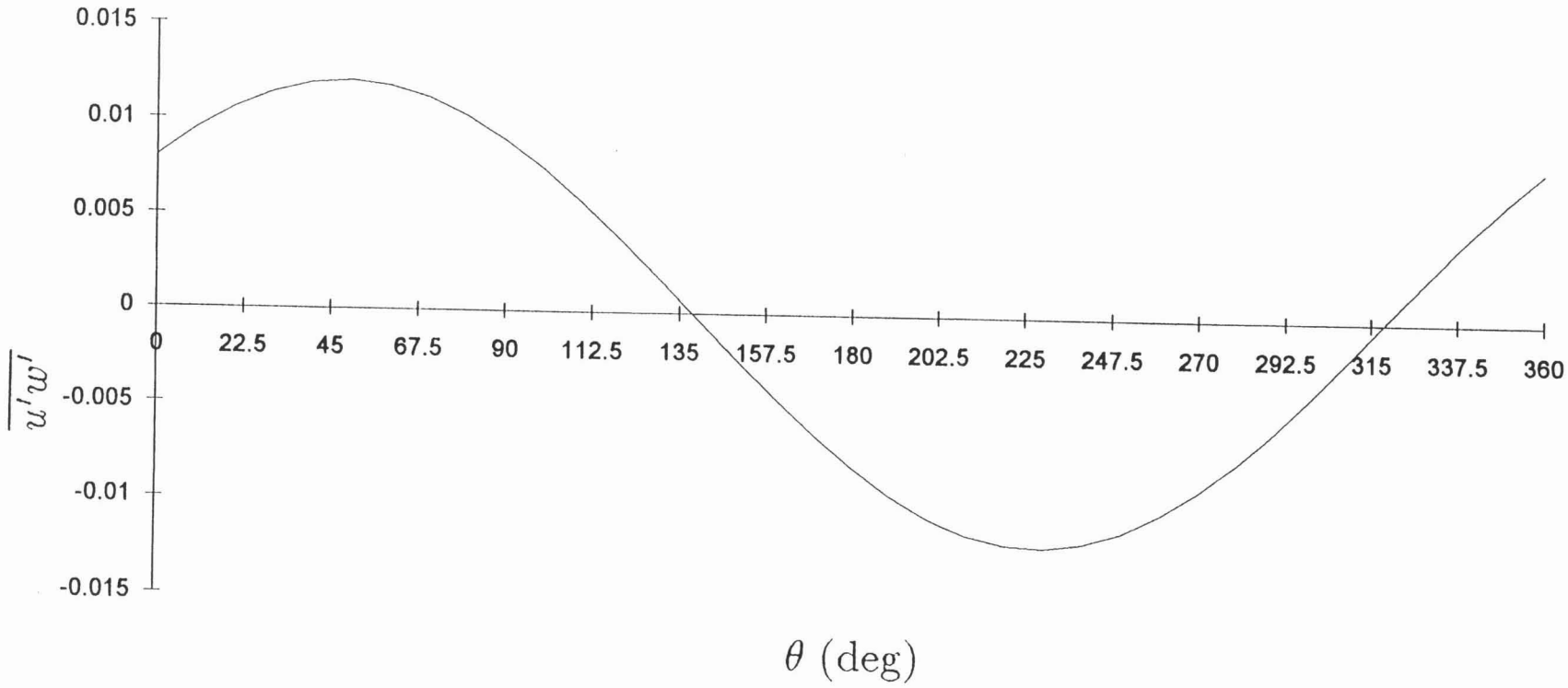

Figure 4.7b $\overline{u'w'}$ vs. θ With Assumed Axisymmetric Cylindrical Shear Stresses

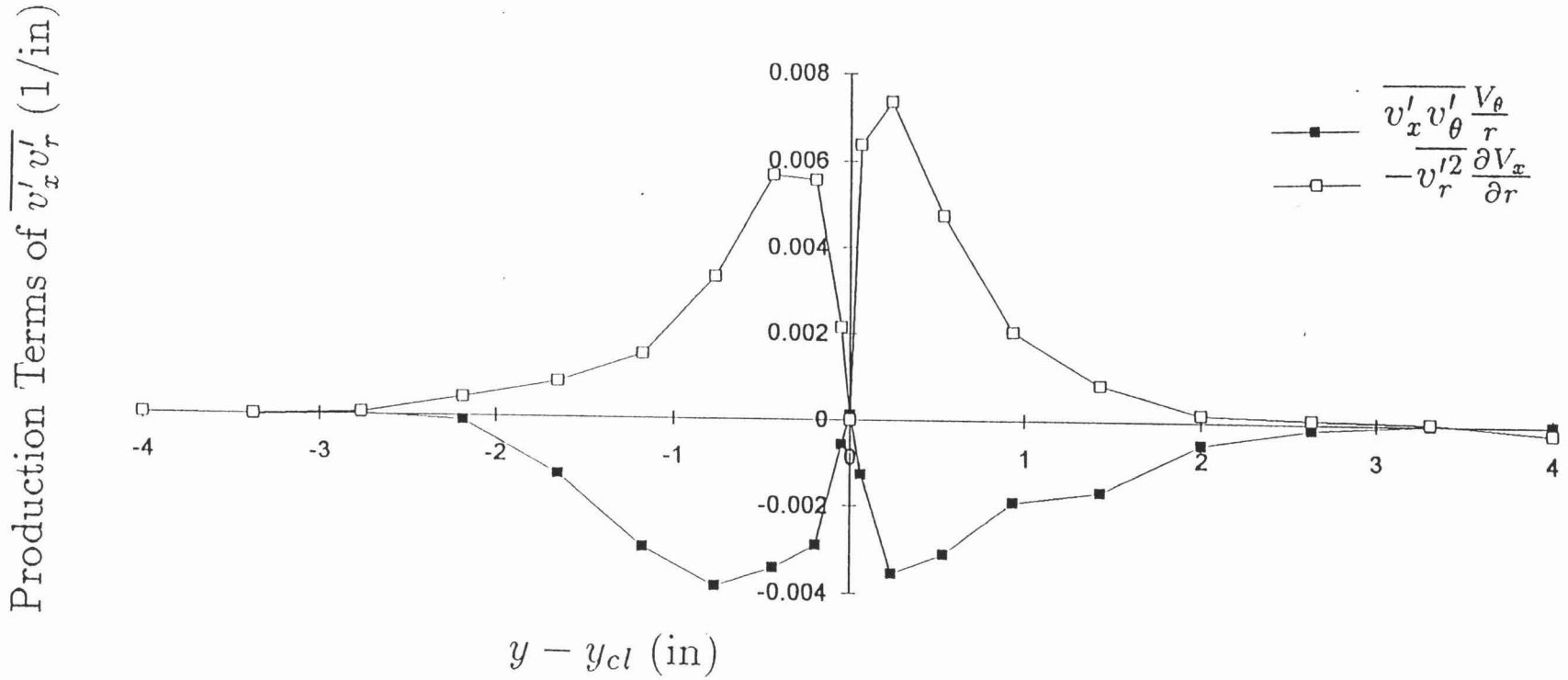

Figure 4.8a Key Production Terms of $\overline{v'_x v'_r}$ vs. y-Distance From Vortex Centerline: $x/c = 0.125$

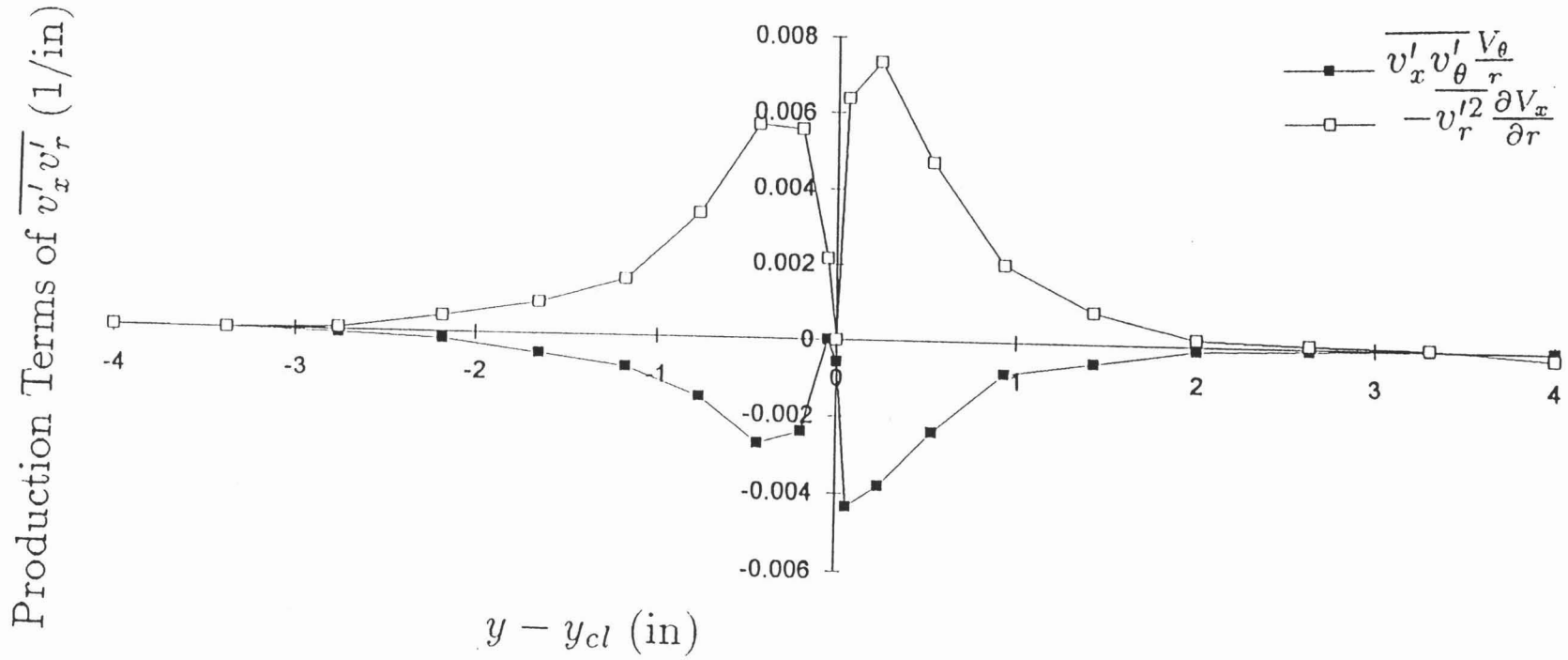

Figure 4.8b Key Production Terms of $\overline{v'_x v'_r}$ vs. y-Distance From Vortex Centerline: $x/c = 0.452$

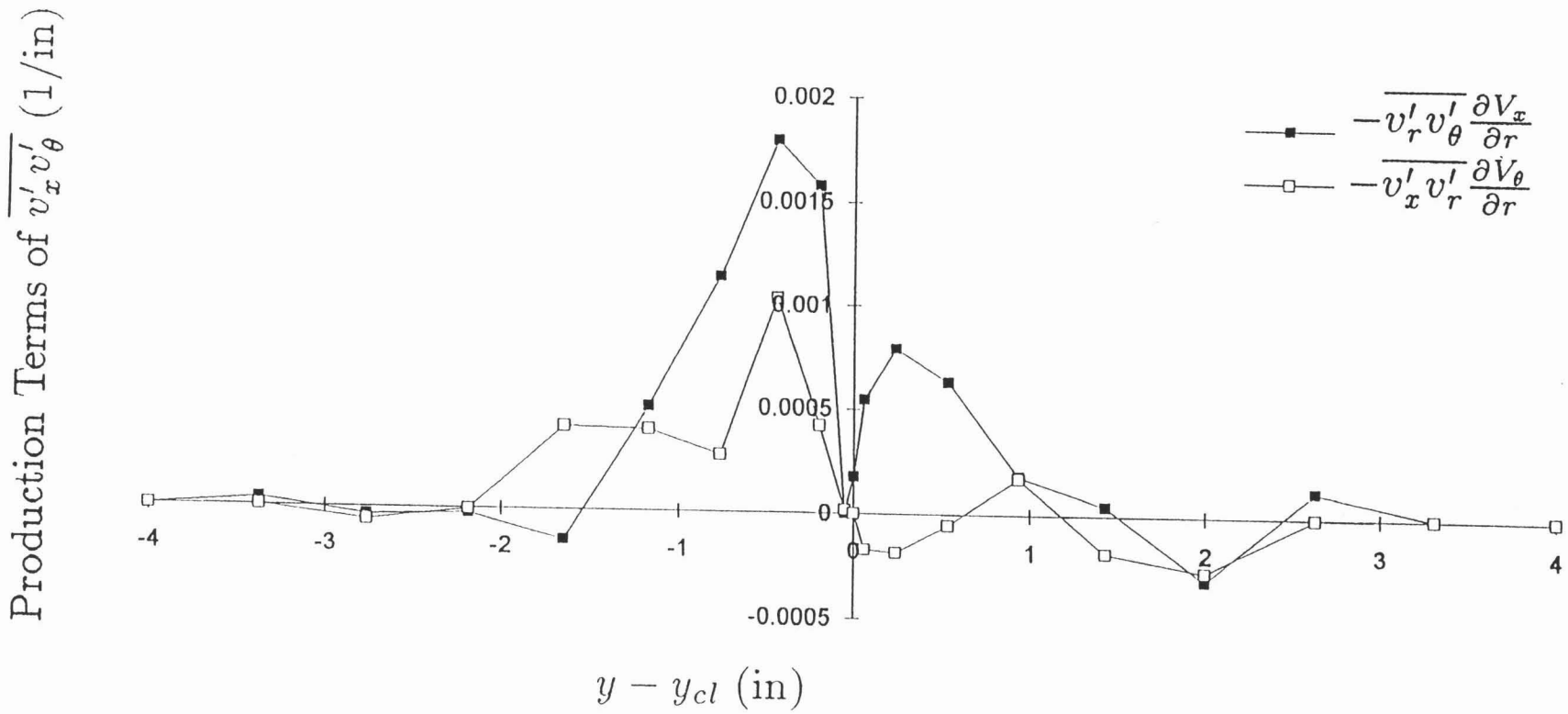

Figure 4.9a Key Production Terms of $\overline{v'_x v'_\theta}$ vs. y-Distance From Vortex Centerline: $x/c = 0.125$

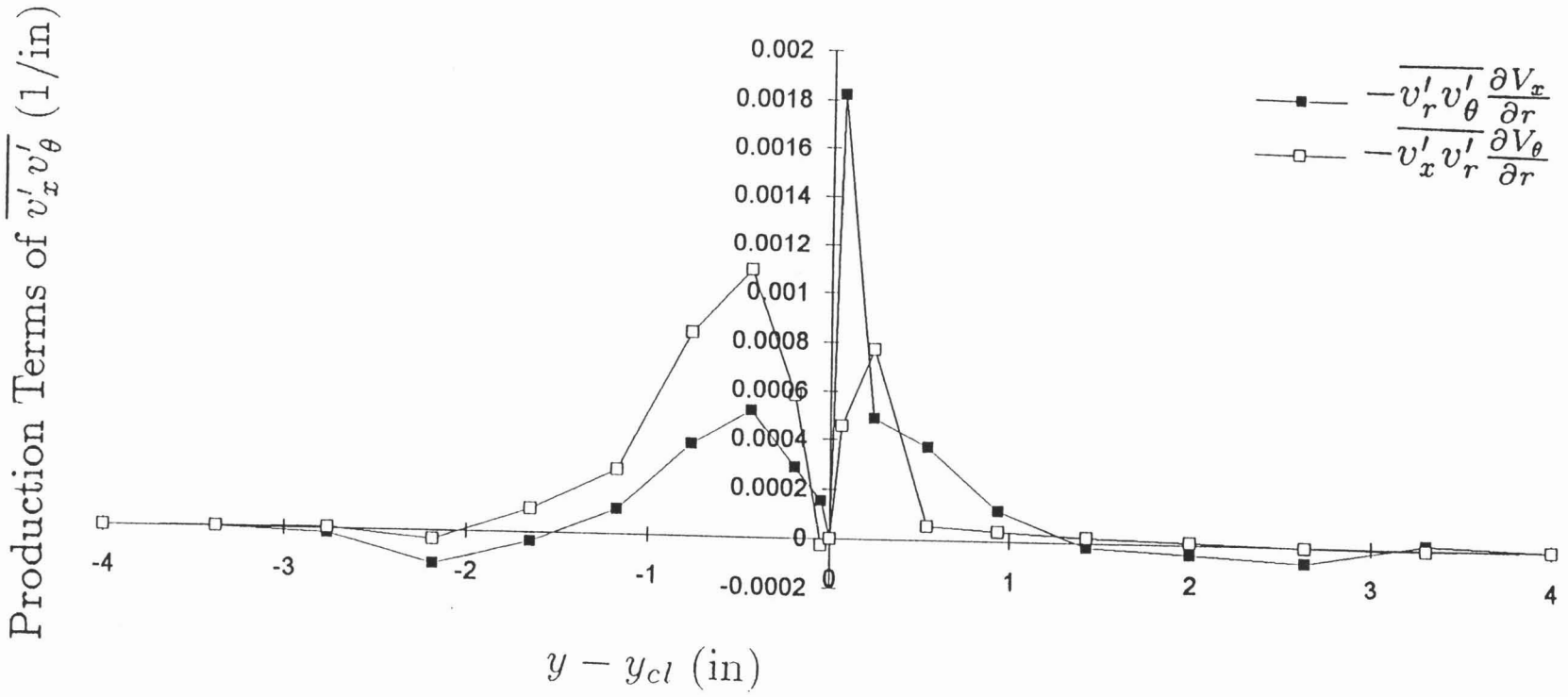

Figure 4.9b Key Production Terms of $\overline{v'_x v'_\theta}$ vs. y-Distance From Vortex Centerline: $x/c = 0.452$

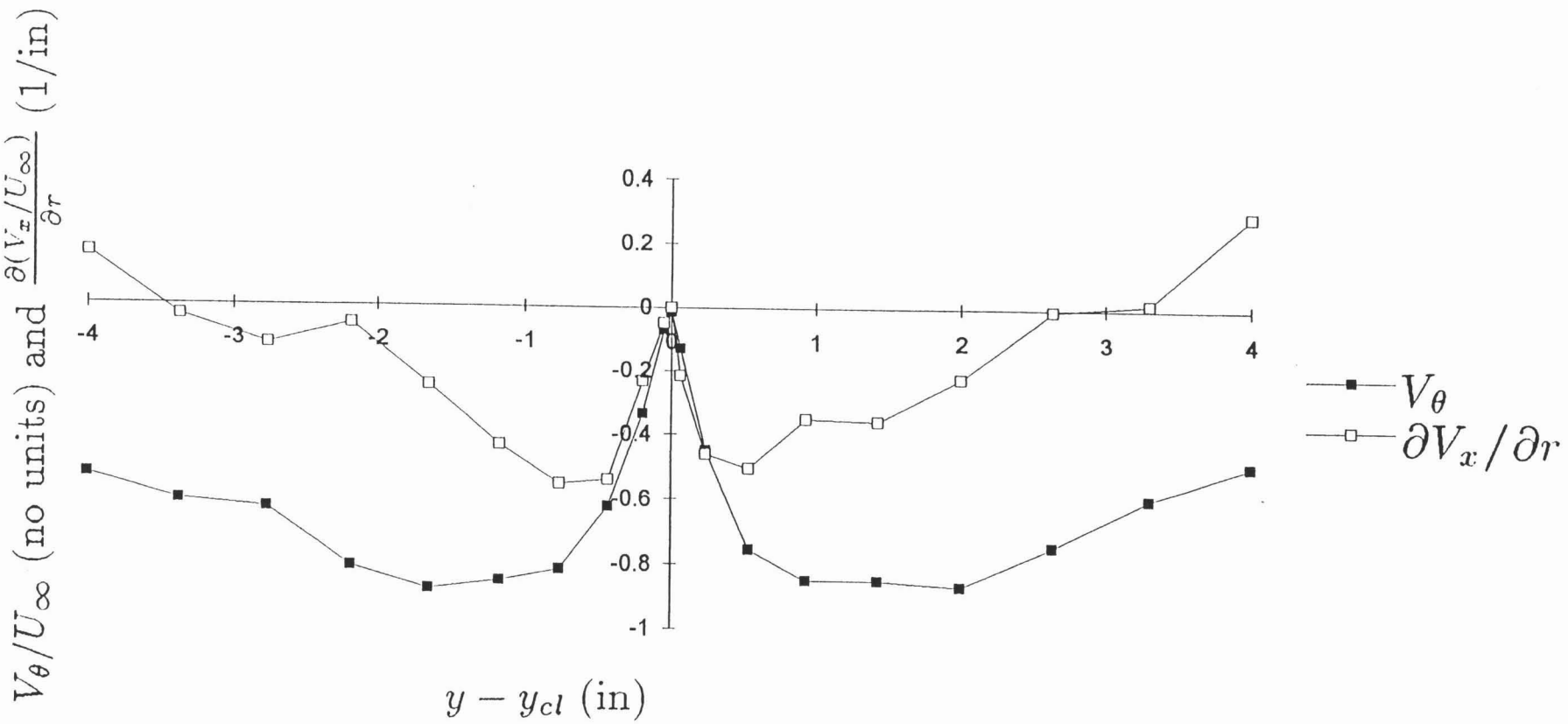

Figure 4.10a V_θ/U_∞ and $\partial V_x/\partial r$ vs. y-Distance From Vortex Centerline, $x/c = 0.125$

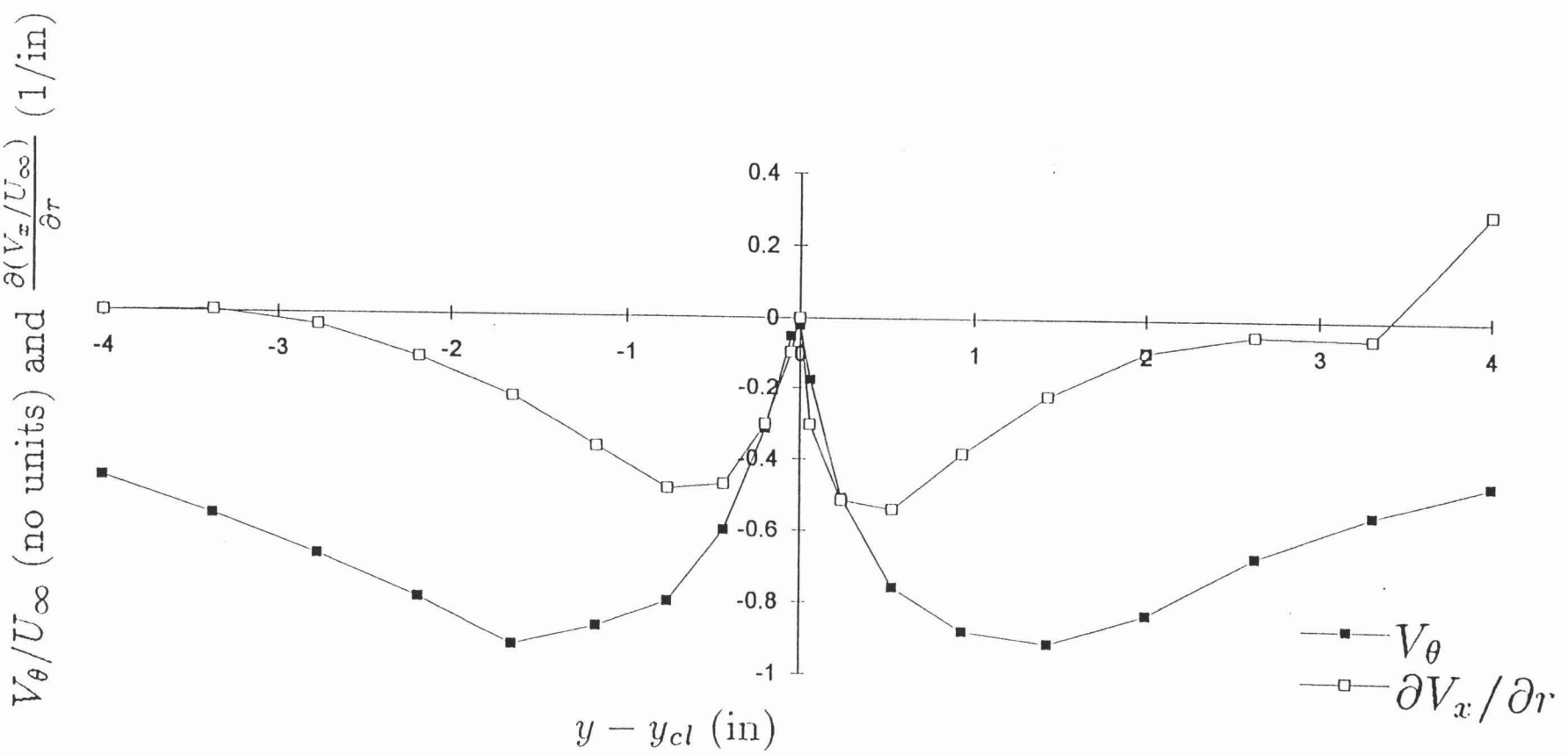

Figure 4.10b V_θ/U_∞ and $\partial V_x/\partial r$ vs. y-Distance From Vortex Centerline, $x/c = 0.452$

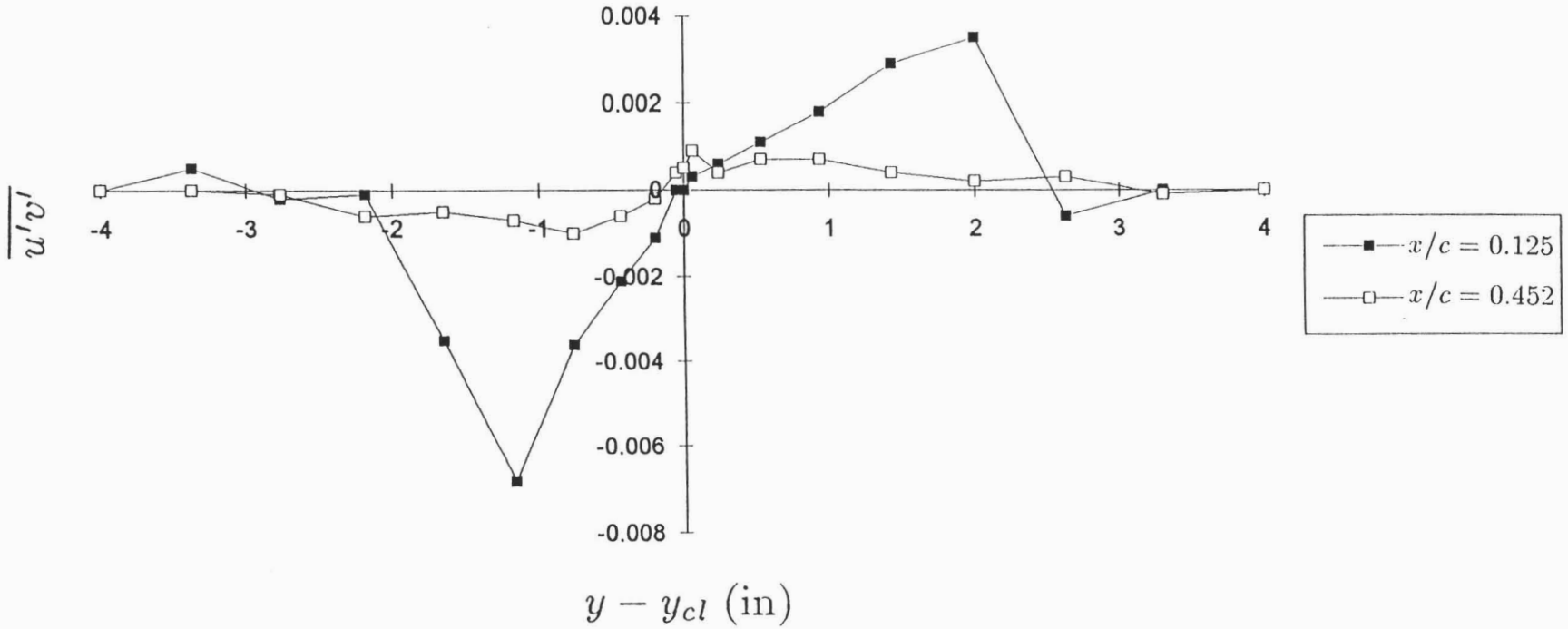

Figure 4.11 $\overline{u'v'}$ **vs.** y**-Distance From Vortex Centerline**

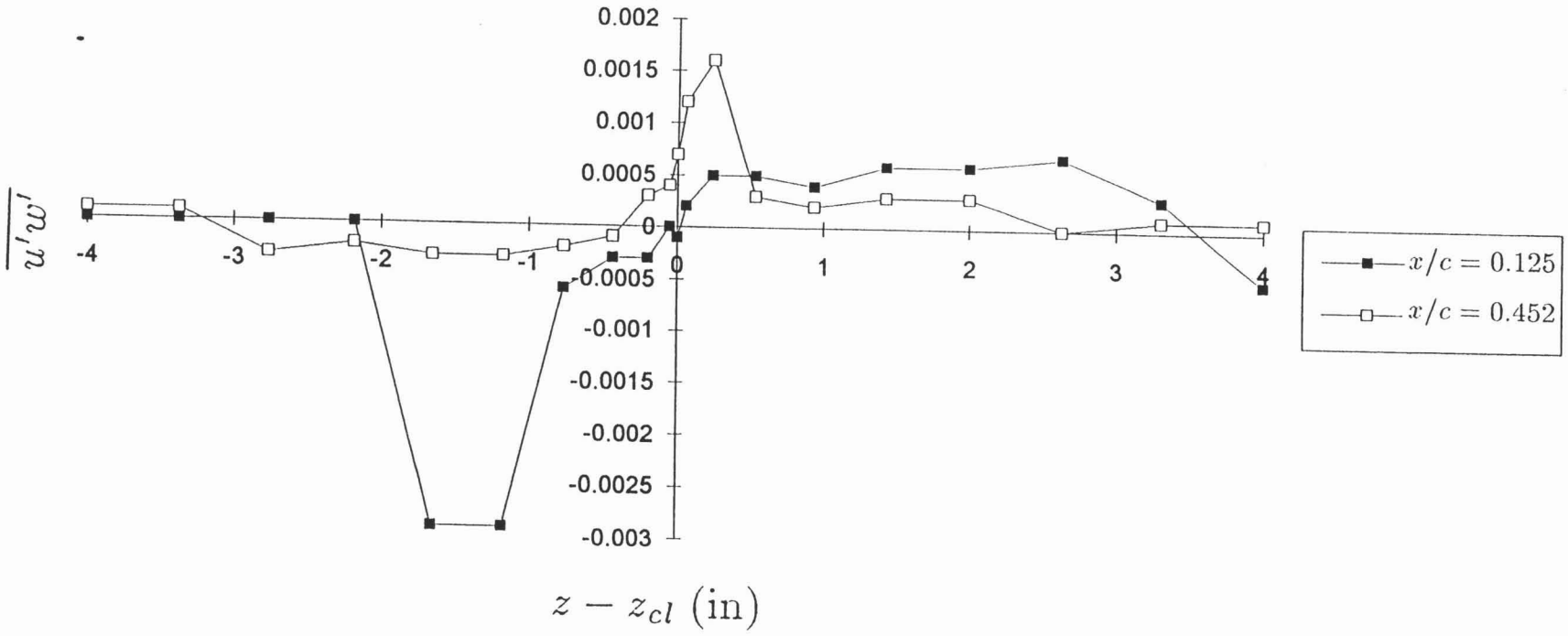

Figure 4.12 $\overline{u'w'}$ **vs.** y**-Distance From Vortex Centerline**

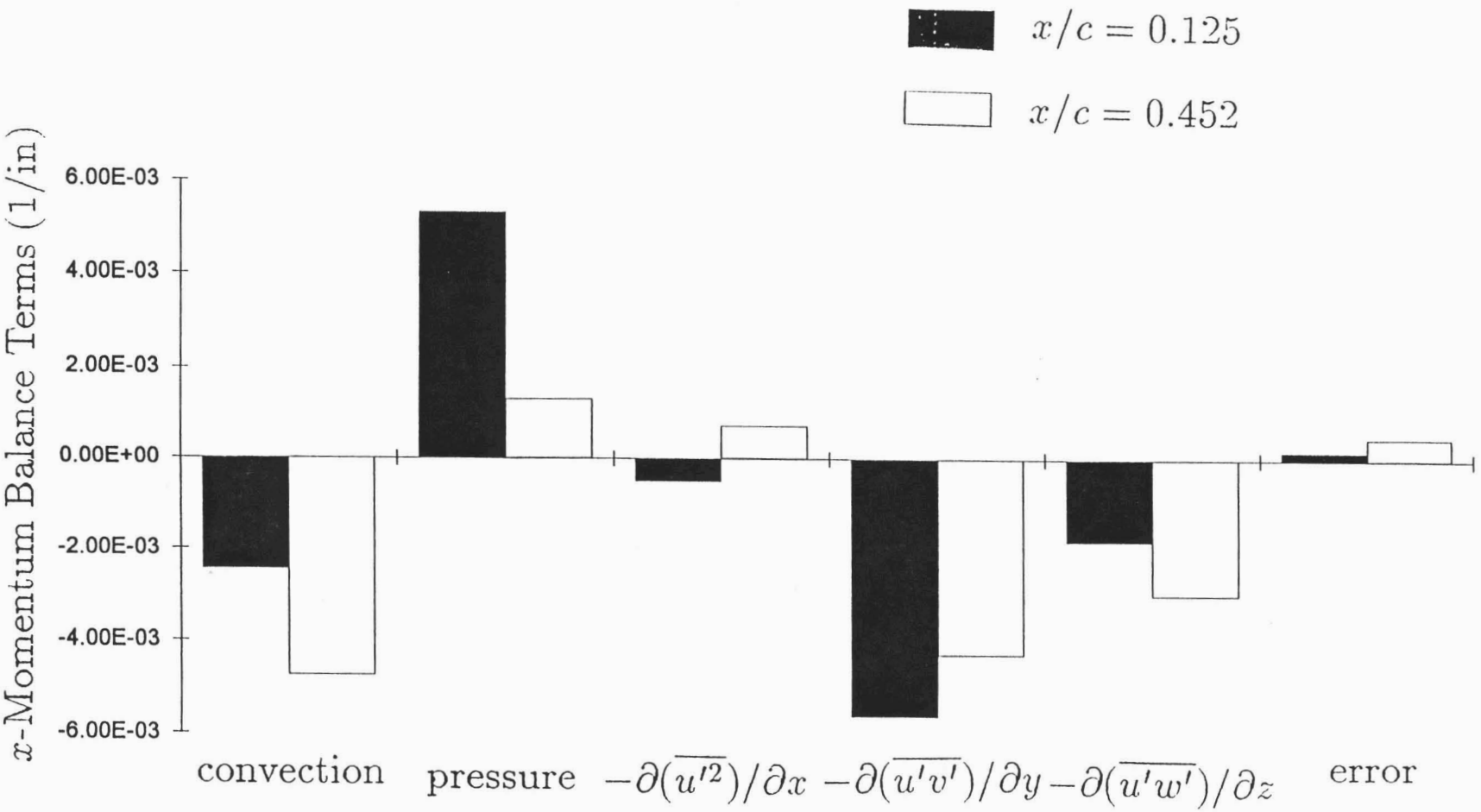

Figure 4.13 Terms of Momentum Balance at $x/c = 0.125$ and 0.452

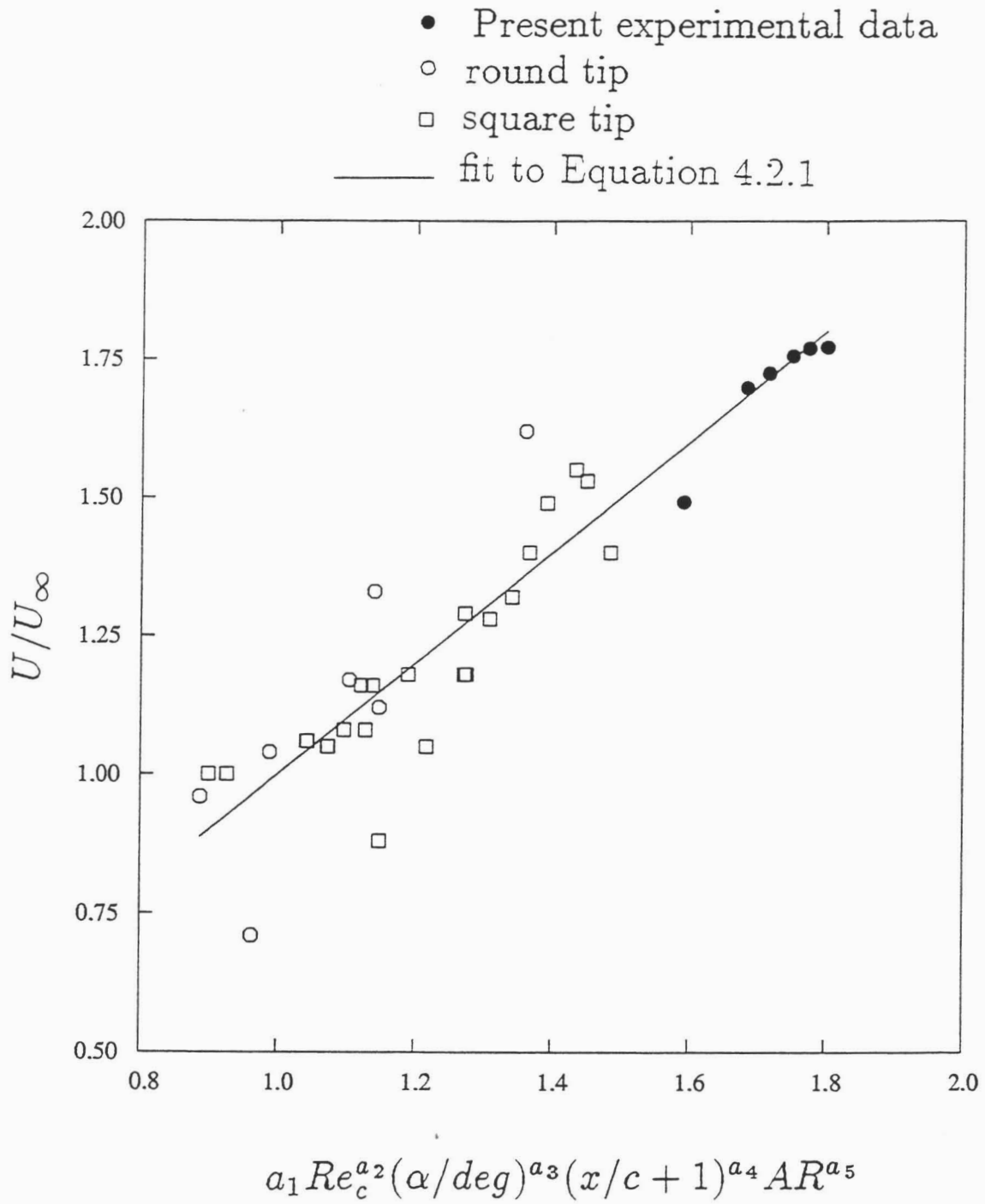

Figure 4.14 Non-Linear Least Squares Fit of Past Experimental Data

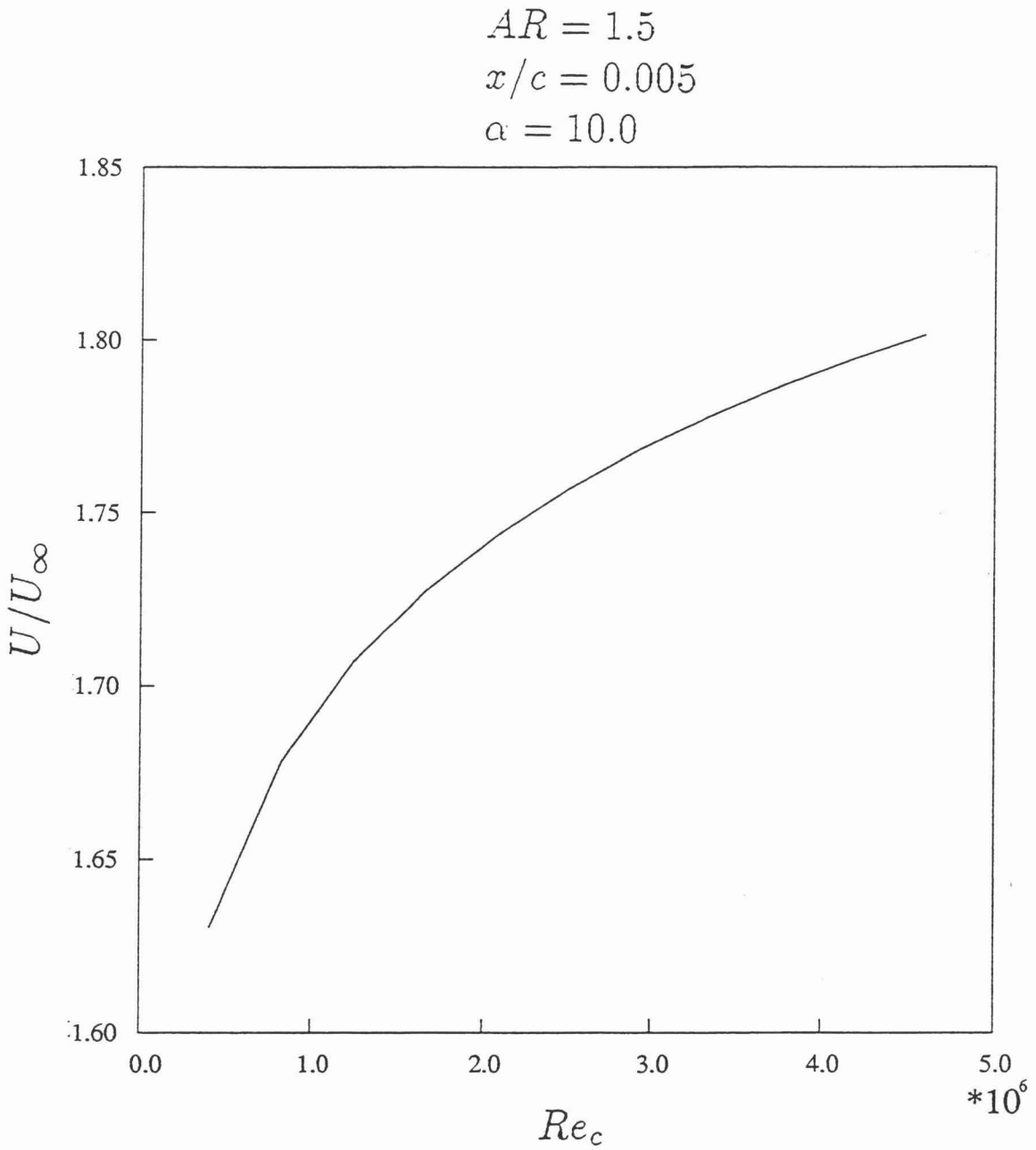

Figure 4.15 U/U_∞ **vs.** Re_c

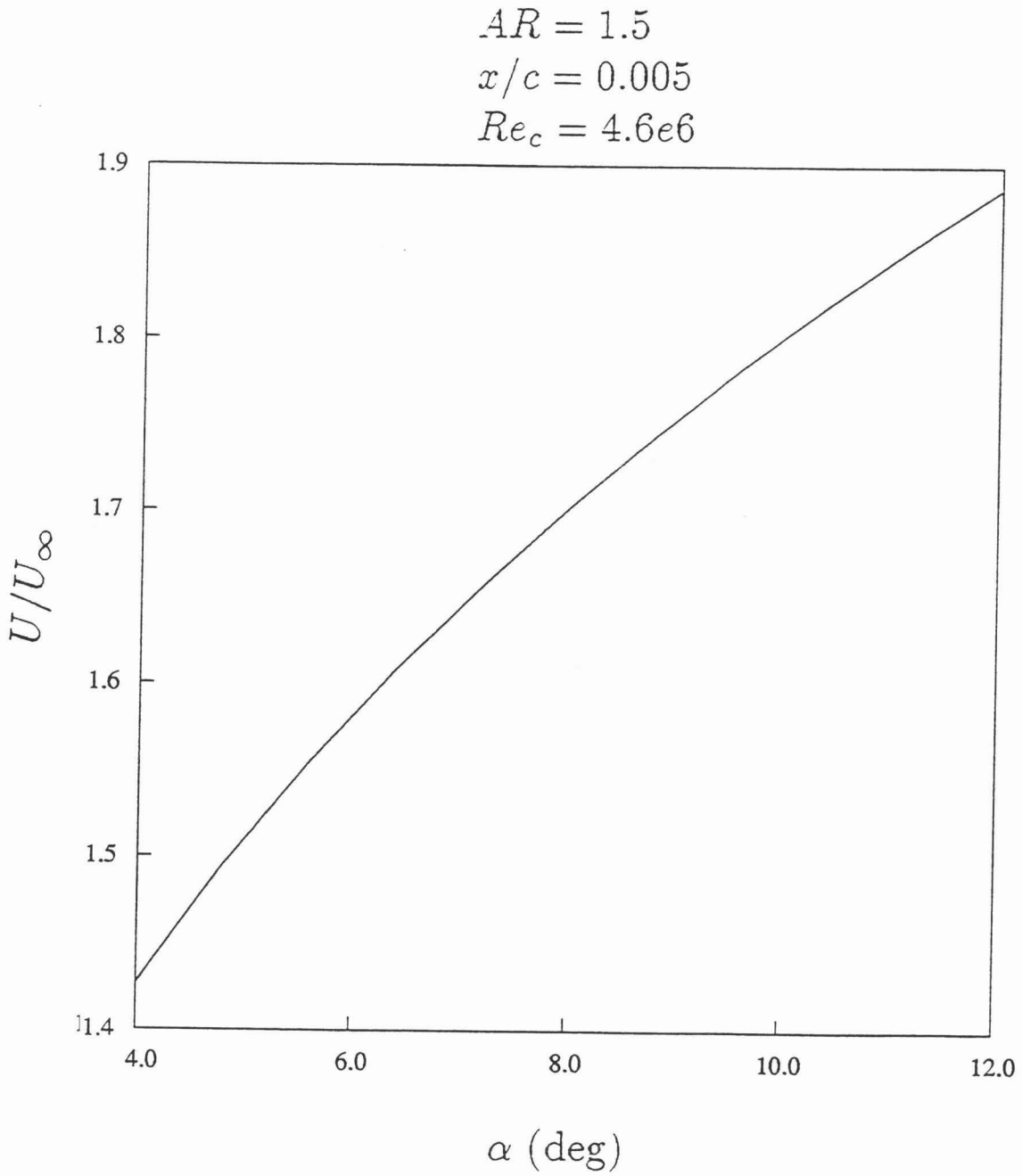

Figure 4.16 U/U_∞ **vs.** α

5. CONCLUSIONS AND RECOMMENDATIONS

The following chapter summarizes the major findings of the present study and discusses some of their implications. In addition, recommendations are made for future research related to the wingtip vortex flow.

5.1 CONCLUSIONS

The complete mean flow field and the complete Reynolds stress tensor have been measured in the near-field of a turbulent wingtip vortex. The tip vortex was generated by a tripped, low aspect ratio NACA 0012 wing with rounded wingtip set at 10 degrees angle of attack and tested at a Reynolds number in full-scale range for a helicopter blade tip. The topology of the skin friction patterns has been observed by surface oil flow. The surface pressure on the entire wing surface has been measured. Measurements of the mean flow field and of extensive turbulence statistics were made at data planes extending from 0.591 chords upstream of the trailing edge to 0.678 chords downstream of the trailing edge. These measurements were performed using a 7-hole pressure probe and a triple-wire probe, which were both ideal for the high flow angle environment of the tip-vortex flowfield. A much better understanding of the initial roll-up has been gained as well as a better understanding of the behavior of the turbulence in the vortex in the near-field and far-field. The following points are the major discoveries of the present study and a general discussion of some of their implications ensues.

Surface oil flow visualization tests showed a primary converging skin-friction line slightly above the mean chord line of the wingtip. The local separation at this line was caused by an adverse pressure gradient encountered as fluid navigates from the suction side of the wing to the pressure side. Two other converging skin-friction lines were found on the pressure side of the wing, near the wingtip. These were caused by adverse crossflow pressure gradients induced by the formation of the primary and secondary vortices.

Development of the crossflow velocities with chordwise distance induced a fa-

vorable axial pressure gradient in the vortex core (located above the wing surface), resulting in acceleration of the the core centerline fluid to 1.77 times the freestream velocity. Such high levels of mean axial velocity excess have not been measured previously in unswept wing vortices. The reasons for this are many:

1) Relatively high angle of attack: To first degree, lift is proportional to angle of attack. Larger amounts of lift induce larger crossflow velocities wrapping around the wing-tip, which produce greater axial pressure forces.

2) High Reynolds number: Viscous forces played a smaller role in influencing the axial velocity of the core. Whereas the axial pressure forces served to accelerate the axial flow, the low momentum fluid being wrapped into the vortex from the tip boundary layers served to decelerate the axial flow. In addition, the large model of the experiment generated a vortex with a core radius of 1-1.5 inches, which reduced the possibilities of probe-induced vortex breakdown, and reduced probe velocity gradient errors.

3) Near-field nature of the study: Effects of vortex meander were minimized. Dissipation effects on the vortex were still at an early stage.

4) The rounded wingtip provided relatively smooth separation characteristics. The roll-up of the primary vorticity was preceded by the formation of a single local separation line. The roll-up of the primary vorticity around a square tip will be preceded by at least two separation lines (one for each corner). It might be expected that this would effectively weaken the level of crossflow velocity induced and impede the development of the axial pressure forces.

Previous researchers have conjectured that helicopter blade slap was caused by transonic flow being induced on blade tips 'running into' the preceding blade-tip-vortex. It had been assumed however that the crossflow velocity of the tip vortex was the primary culprit in inducing this local transonic effect. It is entirely possible that instead, it may be the large axial velocity in the core of the blade-tip-vortex that creates the transonic conditions on the following blade.

The axial velocity excess was responsible for some of the interesting behavior of the turbulence structure in the vortex also. Turbulence levels in and around

the vortex core were initially very large. This was primarily due to the highly turbulent tip-boundary layer fluid being wrapped into the roll-up of the vortex. Peak turbulence levels in data planes measured over the wing were near the edge of the viscous core of the vortex. In a short streamwise distance however, peak turbulence levels decayed rapidly. In addition the peak shear stress levels shifted from the edge of the viscous core, $r/r_1 \approx 1$, to a much smaller radius, $r/r_1 \approx 0.33$. Whereas production of $\overline{v'_r v'_\theta}$ was inhibited by the solid body rotation of the vortex mean flow, production of $\overline{v'_x v'_r}$ and $\overline{v'_x v'_\theta}$ was governed by the mean flow gradient, $\frac{\partial V_x}{\partial r}$. The gradient and the production peaked also at $r/r_1 \approx 0.33$, indicating that the primary culprit to the shift in location of the peak levels of turbulence are caused by the radial gradients of the axial velocity in the vortex core.

The conclusion by Bandyopadhyay et al. (1991) that low Rossby numbers promote re-laminarization is not surprising. A vortex flow with either a large axial velocity excess or deficit (high Rossby number) would enhance turbulence production because of the additional velocity gradients. Although additional turbulence was generated by the axial velocity gradients, it does seem that the re-laminarizing influence of the solid body rotation has a much larger effect, resulting in the high decay rate of the overall turbulence in the vortex. Small levels of $\overline{v'_r v'_\theta}$ were produced however and it was discovered that the anisotropy of the normal stresses, $\overline{v'^2_r} > \overline{v'^2_\theta}$ was caused by this production. Computational studies by Zeman (1994) have come to a similar conclusion, even in the far-wake of the vortex flow-field. Kinematically, the anisotropy of the normal stresses and the low levels of $\overline{v'_r v'_\theta}$ stress will result in contours of $\overline{v'w'}$ stress shifted 45 degrees from the corresponding mean strain rate. The fact that the stress 'lags' the strain rate and will never 'catch up' even in the far-field bodes ill for isotropic eddy-viscosity methods.

5.2 SUGGESTIONS FOR FUTURE WORK

The present experiment was limited to a single test condition: Tests were performed only at one angle of attack and one freestream velocity. It would be useful to perform parametric studies for a range of angles of attack and a range of

freestream velocities and to measure their influence. In addition, tests performed on the influence of different of tip shapes would be desirable.

Measurements in data planes over the wing were limited by the proximity to the wing surface at which the triple-wire probe could safely operate without physical harm and without overstepping the limits of the hot-wire angle calibration. More detailed boundary layer measurements would be invaluable in better understanding the initial turbulence that is generated in the roll-up. A 3-D laser doppler anemometer system could possibly perform these measurements in the tip boundary layers, whereas the triple-wire probe may still be necessary to measure the flow in the vortex core because of seeding problems.

Some work is presently being done at the Fluid Mechanics Laboratory of NASA Ames Research Center on a laser-interferometry technique which will allow surface skin-friction measurements over the entire wing to be made.

APPENDIX A

Correction to Triple Hot-Wire Data for Mean Velocity Gradients

Correction to the triple-wire reduction from probe gradient errors was done using a first-order expansion on the triple-wire equations. In indicial notation, this is written simply as:

$$U^2_{eff,i,corr} = U^2_{eff,i} + \frac{\partial(U^2_{eff,i})}{\partial x_k}\left[\Delta x_k\right] \qquad (A.1)$$

where the Δx_k terms are the physical distances in cartesian coordinates from the probe center to the $i-$th wire. In the present study, gradients in the $x-$direction were ignored, so that in the previous equation, the summed indices would only include the k =2 and 3 terms. From Equation 2.2.8, the gradient of the square of the effective velocities can be written as:

$$\frac{\partial U^2_{eff,i}}{\partial x_k} = 2(k_i^2 - 1)(U_j \cos\beta_{i,j})\left[\frac{\partial U_j}{\partial x_k}\cos\beta_{i,j}\right] + 2\left(U_j \frac{\partial U_j}{\partial x_k}\right) \qquad (A.2)$$

In use, the true velocities are decoded from the original effective hot-wire velocities. Equation A.2 is used to determine the effective velocity gradients and the corrective effective velocities are recomputed using equation A.1, whereupon the corrected true velocities are decoded again. Care must be taken upon using equation A.2, however. The decoding equation is written in probe-aligned coordinates (not tunnel aligned), and so, before the velocity gradients are computed, the velocity field must be transformed to the probe-aligned coordinate system for that particular point (each data point will have a different probe-aligned coordinate system). The scheme corrects for mean velocity and maximum correction was 0.5 % of freestream velocity.

APPENDIX B

Governing Equations

Effects due to compressibility, heat transfer, body forces, and variations in fluid properties are negligible in the present study, and thus the corresponding terms in the Navier-Stokes equations can be neglected. Because the present study is concerned primarily with time-averaged measurements, the *Reynolds-averaged* form of the Navier-Stokes equations is considered here. This form is obtained by separating the flow variables into their mean and fluctuating components and then time-averaging the equations.

The resulting form of the Navier-Stokes equations in rectangular coordinates, using summation indices is:

Continuity:

$$\frac{\partial U_i}{\partial x_i} = 0 \tag{B.1}$$

Momentum:

$$U_j \frac{\partial U_i}{\partial x_j} = -\frac{1}{\rho}\frac{\partial P}{\partial x_i} + \nu \nabla^2 U_i - \frac{\partial \overline{u_i' u_j'}}{\partial x_j}, \tag{B.2}$$

The use of cylindrical coordinates in vortical flows can be useful, especially if axisymmetry can be assumed. The resulting form of the axisymmetric Navier-Stokes equations in cylindrical coordinates is:

Continuity:

$$\frac{1}{r}\frac{\partial (r V_r)}{\partial r} + \frac{\partial V_x}{\partial x} = 0 \tag{B.3}$$

r-Momentum:

$$\begin{aligned} V_r \frac{\partial V_r}{\partial r} + V_x \frac{\partial V_r}{\partial x} - \frac{V_\theta^2}{r} = &-\frac{1}{\rho}\frac{\partial P}{\partial r} + \nu\left[\frac{\partial}{\partial r}\left(\frac{1}{r}\frac{\partial}{\partial r}(r V_r)\right) + \frac{\partial^2 V_r}{\partial x^2}\right] \\ &- \frac{1}{r}\frac{\partial}{\partial r}(r\overline{v_r'^2}) - \frac{\partial}{\partial x}(\overline{v_r' v_x'}) + \frac{\overline{v_\theta'^2}}{r} \end{aligned} \tag{B.4}$$

θ-Momentum:

$$V_r \frac{\partial V_\theta}{\partial r} + V_x \frac{\partial V_\theta}{\partial x} + \frac{V_r V_\theta}{r} = \nu\left[\frac{1}{r^2}\frac{\partial}{\partial r}\left(r^3 \frac{\partial}{\partial r}\left(\frac{V_\theta}{r}\right)\right) + \frac{\partial^2 V_\theta}{\partial x^2}\right]$$

$$- \frac{1}{r^2}\frac{\partial}{\partial r}(r^2\overline{v_r' v_\theta'}) - \frac{\partial}{\partial x}(\overline{v_x' v_\theta'}) \qquad (B.5)$$

x-Momentum:

$$V_r\frac{\partial V_x}{\partial r} + V_x\frac{\partial V_x}{\partial x} = -\frac{1}{\rho}\frac{\partial P}{\partial x} + \nu\left[\frac{1}{r}\frac{\partial}{\partial r}(r\frac{\partial V_x}{\partial r}) + \frac{\partial^2 V_x}{\partial x^2}\right] - \frac{1}{r}\frac{\partial}{\partial r}(r\overline{v_r' v_x'}) - \frac{\partial}{\partial x}(\overline{v_x'^2}) \qquad (B.6)$$

Presented below are the Reynolds Stress Transport Equations written out in full for each $\overline{u_i' u_j'}$ in cartesian coordinates:

$\overline{u'v'}$:

$$\begin{aligned}\frac{D}{Dt}(\overline{u'v'}) = &-\left[\overline{u'^2}\frac{\partial V}{\partial x} + \overline{v'^2}\frac{\partial U}{\partial y} + \overline{u'v'}(\frac{\partial U}{\partial x} + \frac{\partial V}{\partial y}) + \overline{u'w'}\frac{\partial V}{\partial z} + \overline{v'w'}\frac{\partial U}{\partial z}\right] \\ &- 2\nu\left[\overline{\frac{\partial u'}{\partial x}\frac{\partial v'}{\partial x}} + \overline{\frac{\partial u'}{\partial y}\frac{\partial v'}{\partial y}} + \overline{\frac{\partial u'}{\partial z}\frac{\partial v'}{\partial z}}\right] \\ &+ \overline{\frac{p'}{\rho}\left[\frac{\partial u'}{\partial y} + \frac{\partial v'}{\partial x}\right]} \\ &- \left[\frac{\partial}{\partial x}(\overline{u'^2 v'}) + \frac{\partial}{\partial y}(\overline{u'v'^2}) + \frac{\partial}{\partial z}(\overline{u'v'w'})\right] \\ &+ \nu\nabla^2\overline{u'v'} - \frac{1}{\rho}\left[\frac{\partial}{\partial x}(\overline{p'v'}) + \frac{\partial}{\partial y}(\overline{p'u'})\right]\end{aligned} \qquad (B.7)$$

$\overline{u'w'}$:

$$\begin{aligned}\frac{D}{Dt}(\overline{u'w'}) = &-\left[\overline{u'^2}\frac{\partial W}{\partial x} + \overline{w'^2}\frac{\partial U}{\partial z} + \overline{u'w'}(\frac{\partial U}{\partial x} + \frac{\partial W}{\partial z}) + \overline{u'v'}\frac{\partial W}{\partial y} + \overline{v'w'}\frac{\partial U}{\partial y}\right] \\ &- 2\nu\left[\overline{\frac{\partial u'}{\partial x}\frac{\partial w'}{\partial x}} + \overline{\frac{\partial u'}{\partial y}\frac{\partial w'}{\partial y}} + \overline{\frac{\partial u'}{\partial z}\frac{\partial w'}{\partial z}}\right] \\ &+ \overline{\frac{p'}{\rho}\left[\frac{\partial u'}{\partial z} + \frac{\partial w'}{\partial x}\right]} \\ &- \left[\frac{\partial}{\partial x}(\overline{u'^2 w'}) + \frac{\partial}{\partial y}(\overline{u'v'w'}) + \frac{\partial}{\partial z}(\overline{u'w'^2})\right] \\ &+ \nu\nabla^2\overline{u'w'} - \frac{1}{\rho}\left[\frac{\partial}{\partial x}(\overline{p'w'}) + \frac{\partial}{\partial z}(\overline{p'u'})\right]\end{aligned} \qquad (B.8)$$

$\overline{v'w'}$:

$$\frac{D}{Dt}(\overline{v'w'}) = -\left[\overline{v'^2}\frac{\partial W}{\partial y} + \overline{w'^2}\frac{\partial V}{\partial z} + \overline{v'w'}(\frac{\partial V}{\partial y} + \frac{\partial W}{\partial z}) + \overline{u'v'}\frac{\partial W}{\partial x} + \overline{u'w'}\frac{\partial V}{\partial x}\right]$$

$$
\begin{aligned}
&- 2\nu\left[\overline{\frac{\partial v'}{\partial x}\frac{\partial w'}{\partial x}} + \overline{\frac{\partial v'}{\partial y}\frac{\partial w'}{\partial y}} + \overline{\frac{\partial v'}{\partial z}\frac{\partial w'}{\partial z}}\right] \\
&+ \overline{\frac{p'}{\rho}\left[\frac{\partial v'}{\partial z} + \frac{\partial w'}{\partial y}\right]} \\
&- \left[\frac{\partial}{\partial x}(\overline{u'v'w'}) + \frac{\partial}{\partial y}(\overline{v'^2w'}) + \frac{\partial}{\partial z}(\overline{v'w'^2})\right] \\
&+ \nu\nabla^2\overline{v'w'} - \frac{1}{\rho}\left[\frac{\partial}{\partial y}(\overline{p'w'}) + \frac{\partial}{\partial z}(\overline{p'v'})\right] \qquad (B.9)
\end{aligned}
$$

$\overline{u'^2}$:

$$
\begin{aligned}
\frac{D}{Dt}(\overline{u'^2}) = &-\left[2\overline{u'^2}\frac{\partial U}{\partial x} + 2\overline{u'v'}\frac{\partial U}{\partial y} + 2\overline{u'w'}\frac{\partial U}{\partial z}\right] \\
&- 2\nu\left[\overline{\left(\frac{\partial u'}{\partial x}\right)^2} + \overline{\left(\frac{\partial u'}{\partial y}\right)^2} + \overline{\left(\frac{\partial u'}{\partial z}\right)^2}\right] \\
&+ \overline{\frac{p'}{\rho}\left[2\frac{\partial u'}{\partial x}\right]} \\
&- \left[\frac{\partial}{\partial x}(\overline{u'^3}) + \frac{\partial}{\partial y}(\overline{u'^2v'}) + \frac{\partial}{\partial z}(\overline{u'^2w'})\right] \\
&+ \nu\nabla^2\overline{u'^2} - \frac{2}{\rho}\left[\frac{\partial}{\partial x}(\overline{p'u'})\right] \qquad (B.10)
\end{aligned}
$$

$\overline{v'^2}$:

$$
\begin{aligned}
\frac{D}{Dt}(\overline{v'^2}) = &-\left[2\overline{u'v'}\frac{\partial V}{\partial x} + 2\overline{v'^2}\frac{\partial V}{\partial y} + 2\overline{v'w'}\frac{\partial V}{\partial z}\right] \\
&- 2\nu\left[\overline{\left(\frac{\partial v'}{\partial x}\right)^2} + \overline{\left(\frac{\partial v'}{\partial y}\right)^2} + \overline{\left(\frac{\partial v'}{\partial z}\right)^2}\right] \\
&+ \overline{\frac{p'}{\rho}\left[2\frac{\partial v'}{\partial y}\right]} \\
&- \left[\frac{\partial}{\partial x}(\overline{u'v'^2}) + \frac{\partial}{\partial y}(\overline{v'^3}) + \frac{\partial}{\partial z}(\overline{v'^2w'})\right] \\
&+ \nu\nabla^2\overline{v'^2} - \frac{2}{\rho}\left[\frac{\partial}{\partial y}(\overline{p'v'})\right] \qquad (B.11)
\end{aligned}
$$

$\overline{w'^2}$:

$$
\frac{D}{Dt}(\overline{w'^2}) = -\left[2\overline{u'w'}\frac{\partial W}{\partial x} + 2\overline{v'w'}\frac{\partial W}{\partial y} + 2\overline{w'^2}\frac{\partial W}{\partial z}\right]
$$

$$
\begin{aligned}
&- 2\nu\left[\overline{\left(\frac{\partial w'}{\partial x}\right)^2} + \overline{\left(\frac{\partial w'}{\partial y}\right)^2} + \overline{\left(\frac{\partial w'}{\partial z}\right)^2}\right] \\
&+ \overline{\frac{p'}{\rho}\left[2\frac{\partial w'}{\partial z}\right]} \\
&- \left[\frac{\partial}{\partial x}(\overline{u'w'^2}) + \frac{\partial}{\partial y}(\overline{v'w'^2}) + \frac{\partial}{\partial z}(\overline{w'^3})\right] \\
&+ \nu\nabla^2\overline{w'^2} - \frac{2}{\rho}\left[\frac{\partial}{\partial z}(\overline{p'w'})\right] \qquad (B.12)
\end{aligned}
$$

Presented below are the Reynolds Stress Transport Equations written out for each stress in axisymmetric cylindrical coordinates (from Rodi, 1970):

$\overline{v'_x v'_r}$:

$$
\begin{aligned}
V_x\frac{\partial\overline{v'_x v'_r}}{\partial x} + V_r\frac{\partial\overline{v'_x v'_r}}{\partial r} - \frac{V_\theta}{r}\overline{v'_x v'_\theta} = &\left[\frac{V_\theta}{r}\overline{v'_x v'_\theta} - \overline{v'^2_x}\frac{\partial V_r}{\partial x} - \overline{v'^2_r}\frac{\partial V_x}{\partial r} - \overline{v'_x v'_r}\left(\frac{\partial V_x}{\partial x} + \frac{\partial V_r}{\partial r}\right)\right] \\
&- 2\nu\left[\overline{\frac{\partial v'_x}{\partial x}\frac{\partial v'_r}{\partial x}} + \overline{\frac{\partial v'_x}{\partial r}\frac{\partial v'_r}{\partial r}} + \frac{1}{r^2}\overline{\frac{\partial v'_x}{\partial\theta}\frac{\partial v'_r}{\partial\theta}} - \frac{1}{r^2}\overline{v'_\theta\frac{\partial v'_x}{\partial\theta}}\right] \\
&+ \overline{\frac{p'}{\rho}\left[\frac{\partial v'_x}{\partial r} + \frac{\partial v'_r}{\partial x}\right]} + \nu\left(\nabla^2\overline{v'_x v'_r} - \frac{\overline{v'_x v'_r}}{r^2}\right) \\
&- \left[\frac{\partial}{\partial x}(\overline{v'^2_x v'_r}) + \frac{1}{r}\frac{\partial}{\partial r}(r\overline{v'_x v'^2_r}) - \frac{\overline{v'_x v'^2_\theta}}{r}\right] \\
&- \frac{1}{\rho}\left[\frac{\partial}{\partial x}(\overline{p'v'_r}) + \frac{\partial}{\partial r}(\overline{p'v'_x})\right] \qquad (B.13)
\end{aligned}
$$

$\overline{v'_x v'_\theta}$:

$$
\begin{aligned}
V_x\frac{\partial\overline{v'_x v'_\theta}}{\partial x} + V_r\frac{\partial\overline{v'_x v'_\theta}}{\partial r} + \frac{V_\theta}{r}\overline{v'_x v'_\theta} = &\left[-\frac{V_r}{r}\overline{v'_x v'_\theta} - \overline{v'^2_x}\frac{\partial V_\theta}{\partial x} - \overline{v'_x v'_\theta}\frac{\partial V_x}{\partial x} - \overline{v'_x v'_r}\frac{\partial V_\theta}{\partial r} - \overline{v'_r v'_\theta}\frac{\partial V_x}{\partial r}\right] \\
&- 2\nu\left[\overline{\frac{\partial v'_x}{\partial x}\frac{\partial v'_\theta}{\partial x}} + \overline{\frac{\partial v'_x}{\partial r}\frac{\partial v'_\theta}{\partial r}} + \frac{1}{r^2}\overline{\frac{\partial v'_x}{\partial\theta}\frac{\partial v'_\theta}{\partial\theta}} + \frac{1}{r^2}\overline{v'_r\frac{\partial v'_x}{\partial\theta}}\right] \\
&+ \overline{\frac{p'}{\rho}\left[\frac{1}{r}\frac{\partial v'_x}{\partial\theta} + \frac{\partial v'_\theta}{\partial x}\right]} \\
&- \left[\frac{\partial}{\partial x}(\overline{v'^2_x v'_\theta}) + \frac{1}{r}\frac{\partial}{\partial r}(r\overline{v'_x v'_r v'_\theta}) + \frac{\overline{v'_x v'_r v'_\theta}}{r}\right]
\end{aligned}
$$

$$+\nu(\nabla^2\overline{v'_x v'_\theta}-\frac{\overline{v'_x v'_\theta}}{r^2})-\frac{1}{\rho}\left[\frac{\partial}{\partial x}(\overline{p' v'_\theta})\right] \qquad (B.14)$$

$\overline{v'_r v'_\theta}$:

$$\begin{aligned}
V_x\frac{\partial\overline{v'_r v'_\theta}}{\partial x}+V_r\frac{\partial\overline{v'_r v'_\theta}}{\partial r}+\frac{V_\theta}{r}(\overline{v'^2_r}-\overline{v'^2_\theta}) = \Bigg[&-\frac{V_\theta}{r}(\overline{v'^2_r}-\overline{v'^2_\theta})-r\overline{v'^2_r}\frac{\partial}{\partial r}(\frac{V_\theta}{r})-\overline{v'_r v'_\theta}\frac{V_r}{r}\\
&-\overline{v'_x v'_r}\frac{\partial V_\theta}{\partial x}-\overline{v'_x v'_\theta}\frac{\partial V_r}{\partial x}-\overline{v'_r v'_\theta}\frac{\partial V_r}{\partial r}\Bigg]\\
&-2\nu\Bigg[\overline{\frac{\partial v'_r}{\partial x}\frac{\partial v'_\theta}{\partial x}}+\overline{\frac{\partial v'_r}{\partial r}\frac{\partial v'_\theta}{\partial r}}\\
&+\frac{1}{r^2}\left(\overline{\frac{\partial v'_r}{\partial\theta}\frac{\partial v'_\theta}{\partial\theta}}+\overline{v'_r\frac{\partial v'_r}{\partial\theta}}-\overline{v'_\theta\frac{\partial v'_\theta}{\partial\theta}}-\overline{v'_r v'_\theta}\right)\Bigg]\\
&+\overline{\frac{p'}{\rho}\left[\frac{1}{r}\frac{\partial v'_r}{\partial\theta}+\frac{\partial v'_\theta}{\partial r}-\frac{1}{r}v'_\theta\right]}\\
&-\left[\frac{1}{r}(\overline{v'^2_r v'_\theta}-\overline{v'^3_\theta})+\frac{\partial}{\partial x}(\overline{v'_x v'_r v'_\theta})+\frac{1}{r}\frac{\partial}{\partial r}(r\overline{v'^2_r v'_\theta})+\frac{\overline{v'_x v'_r v'_\theta}}{r}\right]\\
&+\nu(\nabla^2\overline{v'_r v'_\theta}-\frac{\overline{v'_r v'_\theta}}{r^2})-\frac{1}{\rho}\left[\frac{\partial}{\partial r}(\overline{p' v'_\theta})-\frac{1}{r}\overline{p' v'_\theta}\right] \qquad (B.15)
\end{aligned}$$

$\overline{v'^2_x}$:

$$\begin{aligned}
V_x\frac{\partial\overline{v'^2_x}}{\partial x}+V_r\frac{\partial\overline{v'^2_x}}{\partial r} = &-2\left[\overline{v'^2_x}\frac{\partial V_x}{\partial x}+\overline{v'_x v'_r}\frac{\partial V_x}{\partial r}\right]\\
&-2\nu\left[\overline{(\frac{\partial v'_x}{\partial x})^2}+\overline{(\frac{\partial v'_x}{\partial r})^2}+\frac{1}{r^2}\overline{(\frac{\partial v'_x}{\partial\theta})^2}\right]\\
&+2\overline{\frac{p'}{\rho}\left[\frac{\partial v'_x}{\partial x}\right]}\\
&-\left[\frac{1}{r}\frac{\partial}{\partial r}(r\overline{v'^2_x v'_r})+\frac{\partial}{\partial x}(\overline{v'^3_x})\right]\\
&+\nu\nabla^2\overline{v'^2_x}-\frac{2}{\rho}\left[\frac{\partial}{\partial x}(\overline{p' v'_x})\right] \qquad (B.16)
\end{aligned}$$

$\overline{v'^2_r}$:

$$V_x\frac{\partial\overline{v_r'^2}}{\partial x}+V_r\frac{\partial\overline{v_r'^2}}{\partial r}-2\frac{V_\theta}{r}\overline{v_r'v_\theta'}=-2\left[\overline{v_r'^2}\frac{\partial V_r}{\partial r}+\overline{v_x'v_r'}\frac{\partial V_r}{\partial x}-\frac{V_\theta}{r}\overline{v_r'v_\theta'}\right]$$
$$-2\nu\left[\overline{\left(\frac{\partial v_r'}{\partial x}\right)^2}+\overline{\left(\frac{\partial v_r'}{\partial y}\right)^2}+\overline{\left(\frac{\partial v_r'}{\partial z}\right)^2}-\frac{2}{r^2}\overline{v_\theta'\frac{\partial v_r'}{\partial\theta}}+\frac{1}{r^2}\overline{v_\theta'^2}\right]$$
$$+2\overline{\frac{p'}{\rho}\left[\frac{\partial v_r'}{\partial r}\right]}$$
$$-\left[\frac{1}{r}\frac{\partial}{\partial r}(r\overline{v_r'^3})+\frac{\partial}{\partial x}(\overline{v_x'v_r'^2})-\frac{2}{r}\overline{v_r'v_\theta'^2}\right]$$
$$+\nu\left(\nabla^2\overline{v_r'^2}-\frac{2}{r^2}(\overline{v}_r'^2-\overline{v}_\theta'^2)\right)-\frac{2}{\rho}\left[\frac{\partial}{\partial r}(\overline{p'v_r'})\right]\qquad(B.17)$$

$\overline{v_\theta'^2}$:

$$V_x\frac{\partial\overline{v_\theta'^2}}{\partial x}+V_r\frac{\partial\overline{v_\theta'^2}}{\partial r}+2\frac{V_\theta}{r}\overline{v_r'v_\theta'}=-2\left[\overline{v_\theta'^2}\frac{\partial V_r}{\partial r}+\overline{v_x'v_\theta'}\frac{\partial V_\theta}{\partial x}+\overline{v_r'v_\theta'}\frac{\partial V_\theta}{\partial r}\right]$$
$$-2\nu\left[\overline{\left(\frac{\partial v_\theta'}{\partial x}\right)^2}+\overline{\left(\frac{\partial v_\theta'}{\partial y}\right)^2}+\overline{\left(\frac{\partial v_\theta'}{\partial z}\right)^2}+\frac{2}{r^2}\overline{v_r'\frac{\partial v_\theta'}{\partial\theta}}+\frac{1}{r^2}\overline{v_r'^2}\right]$$
$$+\frac{2}{r}\overline{\frac{p'}{\rho}\left[\frac{\partial v_\theta'}{\partial\theta}+v_r'\right]}$$
$$-\left[\frac{1}{r}\frac{\partial}{\partial r}(r\overline{v_r'v_\theta'^2})+\frac{\partial}{\partial x}(\overline{v_x'v_\theta'^2})+\frac{2}{r}\overline{v_r'v_\theta'^2}\right]$$
$$+\nu\left(\nabla^2\overline{v_\theta'^2}-\frac{2}{r^2}(\overline{v}_\theta'^2-\overline{v}_r'^2)\right)-\frac{2}{r\rho}\left[(\overline{p'v_r'})\right]\qquad(B.18)$$

APPENDIX C

Coordinate Systems

Although the flow in the present study cannot be considered to be strictly axisymmetric, it is useful to observe trends in some scalar quantities to see if they are tending towards axisymmetry.

Display of the various fluid scalar quantities of a rotating flow in cartesian coordinates and cylindrical coordinates can be related by the use of the following equations:

Position:

$$x = x$$

$$y = r\cos\theta$$

$$z = r\sin\theta$$

Velocity:

$$U = V_x$$

$$V = V_r\cos\theta - V_\theta\sin\theta$$

$$W = V_r\sin\theta + V_\theta\cos\theta$$

Separating instantaneous velocities into mean and fluctuating parts and taking the time average, the various Reynolds Stresses may be converted between coordinate systems by the following equations:

Reynolds Stresses:

$$\overline{u'^2} = \overline{v_x'^2}$$

$$\overline{v'^2} = \overline{v_\theta'^2}\sin^2\theta + \overline{v_r'^2}\cos^2\theta - 2\overline{v_r'v_\theta'}\sin\theta\cos\theta$$

$$\overline{w'^2} = \overline{v_\theta'^2}\cos^2\theta + \overline{v_r'^2}\sin^2\theta + 2\overline{v_r'v_\theta'}\sin\theta\cos\theta$$

$$\overline{u'v'} = -\overline{v_x'v_\theta'}\sin\theta + \overline{v_x'v_r'}\cos\theta$$

$$\overline{u'w'} = \overline{v_x'v_\theta'}\cos\theta + \overline{v_x'v_r'}\sin\theta$$

$$\overline{v'w'} = (\overline{v_r'^2} - \overline{v_\theta'^2})\sin\theta\cos\theta + \overline{v_r'v_\theta'}(\cos^2\theta - \sin^2\theta)$$

Figures C.1, C.2, and C.3 plot $\overline{u'v'}$, $\overline{u'w'}$, and $\overline{v'w'}$ as a function of θ at some r, given

an axisymmetric distribution of the Reynolds stresses in cylindrical coordinates. Figures C.1 and C.2 plots $\overline{u'v'}$ and $\overline{u'w'}$ for four cases:

1) The limiting case of $\overline{v'_x v'_r} = 0$.

2) The limiting case of $\overline{v'_x v'_\theta} = 0$.

3) $\overline{v'_x v'_r} = \overline{v'_x v'_\theta}$

4) Cylindrical stress distribution from Phillips and Graham (1981).

For Case 1, $\overline{u'v'}$ has peaks at 0 and 180 degrees and zeroes at 90 and 270 degrees, while $\overline{u'w'}$ has peaks at 90 and 270 degrees and zeroes at 0 and 180 degrees. These trends are reversed for Case 2. For Case 3, $\overline{u'v'}$ has peaks at 135 and 315 degrees and zeroes at 45 and 225 degrees, while $\overline{u'w'}$ has peaks at 45 and 225 degrees and zeroes at 135 and 315 degrees.

Figure C.3 plots $\overline{v'w'}$ for three cases:

1) The limiting case of $v'_r = v'_\theta$.

2) The limiting case of $v'_r > v'_\theta$, and $\overline{v'_r v'_\theta}$ 0.

3) Cylindrical stress distribution from Phillips and Graham (1981).

It can be seen for all cases that the four-leaf clover pattern of $\overline{v'w'}$ stress is merely a result of the four quadrant cartesian coordinate system. The orientation of the positive and negative regions of stress depends however upon the levels of $\overline{v'^2_r}, \overline{v'^2_\theta}$, and $\overline{v'_r v'_\theta}$. For case 1, the peak absolute stresses occur at $\theta = 0$, 90, 180, and 270 degrees. For case 2, the peak absolute stresses occur at $\theta = 45$, 135, 225, and 315 degrees. The cylindrical stress distribution from Phillips and Graham give peaks at locations similar to case 2.

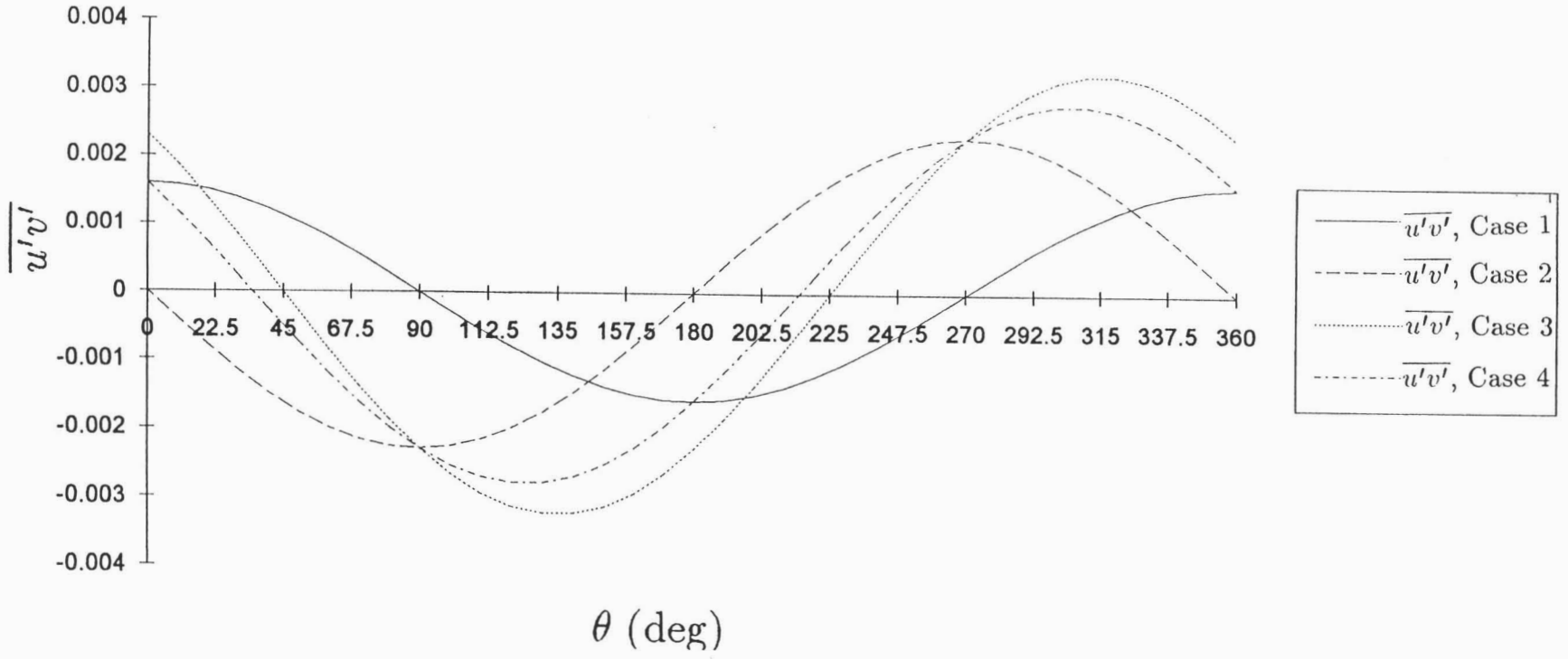

Figure C.1 $\overline{u'v'}$ **as a function of** θ

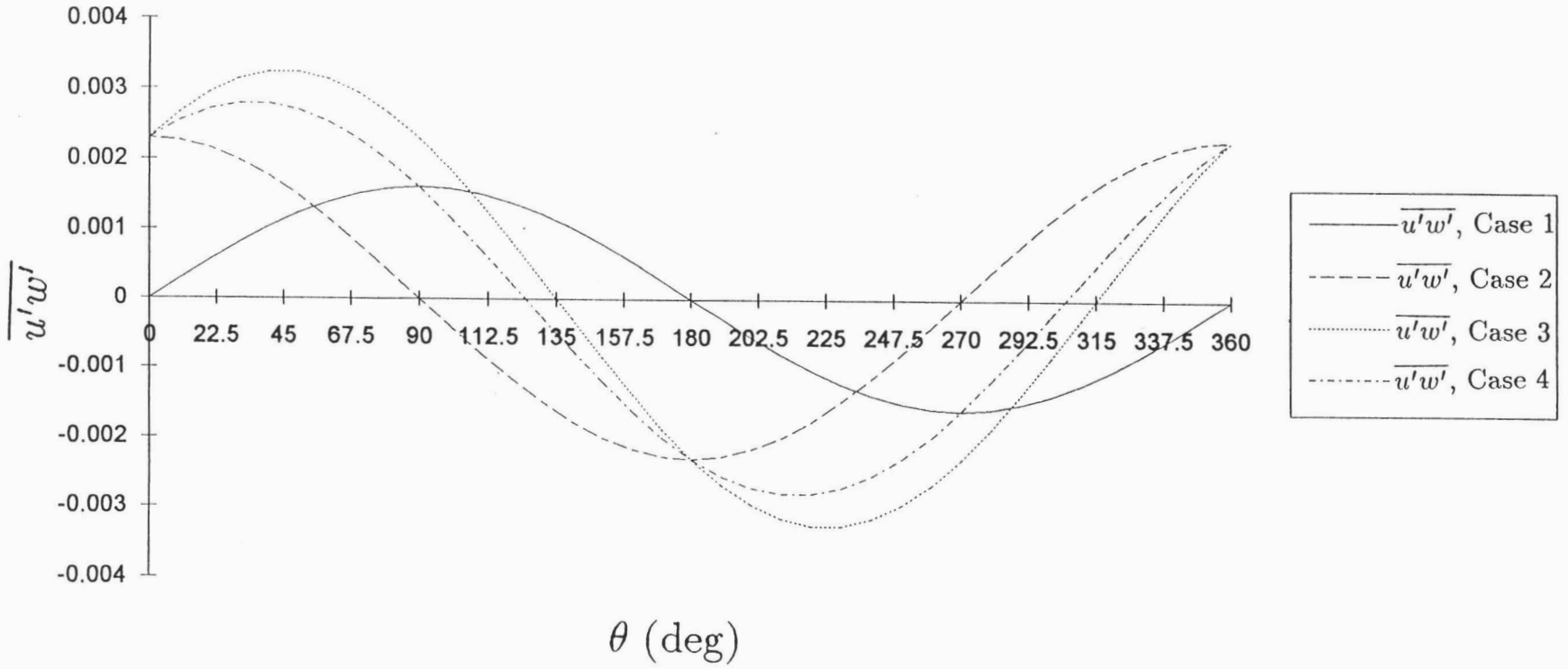

Figure C.2 $\overline{u'w'}$ as a function of θ

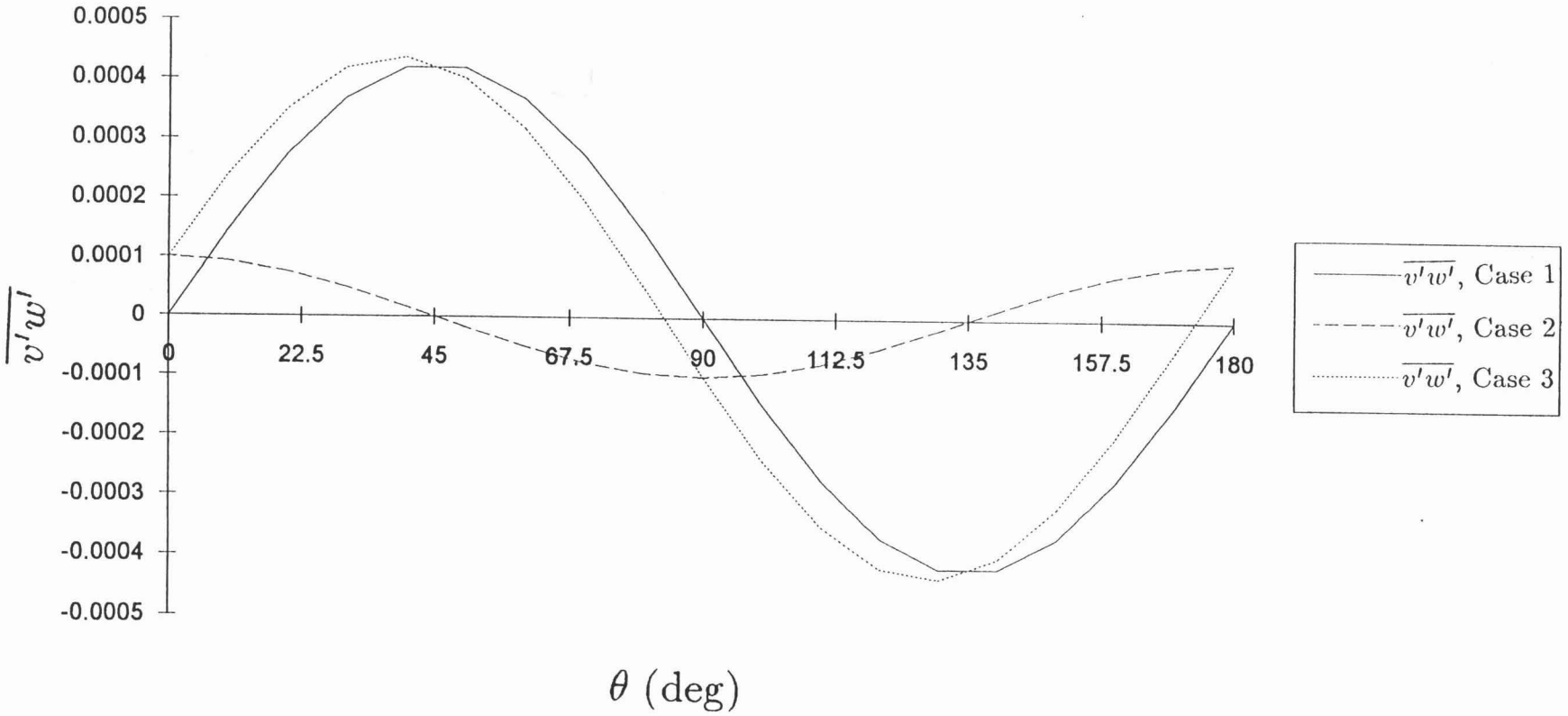

Figure C.3 $\overline{v'w'}$ as a function of θ

Appendix Table D.1 Surface Pressure Coefficient Quantities

x/c	z/b_o or γ (deg)	Upper/Lower Surface	C_p
-0.250	0.181	Lower	−1.048
-0.245	0.181	Lower	0.942
-0.237	0.181	Lower	1.022
-0.225	0.181	Lower	0.885
-0.200	0.181	Lower	0.640
-0.175	0.181	Lower	0.496
-0.150	0.181	Lower	0.401
-0.100	0.181	Lower	0.285
-0.050	0.181	Lower	0.211
0.000	0.181	Lower	0.158
0.050	0.181	Lower	0.125
0.150	0.181	Lower	0.077
0.350	0.181	Lower	0.022
0.550	0.181	Lower	0.062
0.600	0.181	Lower	0.078
0.625	0.181	Lower	0.084
0.675	0.181	Lower	0.106
0.700	0.181	Lower	0.117
0.725	0.181	Lower	0.141
-0.250	0.181	Upper	−1.033
-0.245	0.181	Upper	−2.642
-0.237	0.181	Upper	−2.621
-0.225	0.181	Upper	−2.236
-0.200	0.181	Upper	−1.753
-0.175	0.181	Upper	−1.527
-0.150	0.181	Upper	−1.370
-0.100	0.181	Upper	−1.143
-0.050	0.181	Upper	−0.984
0.000	0.181	Upper	−0.855
0.050	0.181	Upper	−0.736
0.150	0.181	Upper	−0.540
0.350	0.181	Upper	−0.247
0.550	0.181	Upper	−0.024
0.600	0.181	Upper	0.027
0.625	0.181	Upper	0.053
0.675	0.181	Upper	0.106
0.700	0.181	Upper	0.133
0.725	0.181	Upper	0.158

Appendix Table D.1 (Continued)

x/c	z/b_o or γ (deg)	Upper/Lower Surface	C_p
-0.250	0.362	Lower	−0.905
-0.245	0.362	Lower	0.943
-0.237	0.362	Lower	1.017
-0.225	0.362	Lower	0.872
-0.200	0.362	Lower	0.623
-0.175	0.362	Lower	0.478
-0.150	0.362	Lower	0.379
-0.100	0.362	Lower	0.259
-0.050	0.362	Lower	0.181
0.000	0.362	Lower	0.133
0.050	0.362	Lower	0.097
0.150	0.362	Lower	0.046
0.350	0.362	Lower	0.008
0.550	0.362	Lower	0.040
0.600	0.362	Lower	0.056
0.625	0.362	Lower	0.066
0.675	0.362	Lower	0.091
0.700	0.362	Lower	0.110
0.725	0.362	Lower	0.135
-0.250	0.362	Upper	−0.858
-0.245	0.362	Upper	−2.456
-0.237	0.362	Upper	−2.463
-0.225	0.362	Upper	−2.126
-0.200	0.362	Upper	−1.689
-0.175	0.362	Upper	−1.465
-0.150	0.362	Upper	−1.318
-0.100	0.362	Upper	−1.106
-0.050	0.362	Upper	−0.954
0.000	0.362	Upper	−0.823
0.050	0.362	Upper	−0.713
0.150	0.362	Upper	−0.524
0.350	0.362	Upper	−0.246
0.550	0.362	Upper	−0.034
0.600	0.362	Upper	0.017
0.625	0.362	Upper	0.043
0.675	0.362	Upper	0.098
0.700	0.362	Upper	0.129
0.725	0.362	Upper	0.159

Appendix Table D.1 (Continued)

x/c	z/b_o or γ (deg)	Upper/Lower Surface	C_p
-0.250	0.725	Lower	−0.430
-0.245	0.725	Lower	0.998
-0.237	0.725	Lower	0.973
-0.225	0.725	Lower	0.785
-0.200	0.725	Lower	0.520
-0.175	0.725	Lower	0.372
-0.150	0.725	Lower	0.275
-0.100	0.725	Lower	0.158
-0.050	0.725	Lower	0.083
0.000	0.725	Lower	0.035
0.050	0.725	Lower	−0.001
0.150	0.725	Lower	−0.044
0.350	0.725	Lower	−0.080
0.550	0.725	Lower	−0.043
0.600	0.725	Lower	−0.018
0.625	0.725	Lower	−0.007
0.675	0.725	Lower	0.034
0.700	0.725	Lower	0.065
0.725	0.725	Lower	0.106
-0.250	0.725	Upper	−0.350
-0.245	0.725	Upper	−1.842
-0.237	0.725	Upper	−1.940
-0.225	0.725	Upper	−1.697
-0.200	0.725	Upper	−1.386
-0.175	0.725	Upper	−1.215
-0.150	0.725	Upper	−1.097
-0.100	0.725	Upper	−0.914
-0.050	0.725	Upper	−0.793
0.000	0.725	Upper	−0.689
0.050	0.725	Upper	−0.602
0.150	0.725	Upper	−0.453
0.350	0.725	Upper	−0.246
0.550	0.725	Upper	−0.105
0.600	0.725	Upper	−0.066
0.625	0.725	Upper	−0.050
0.675	0.725	Upper	0.000
0.700	0.725	Upper	0.038
0.725	0.725	Upper	0.089

Appendix Table D.1 (Continued)

x/c	z/b_o or γ (deg)	Upper/Lower Surface	C_p
-0.250	0.845	Lower	−0.142
-0.245	0.845	Lower	1.014
-0.237	0.845	Lower	0.927
-0.225	0.845	Lower	0.721
-0.200	0.845	Lower	0.442
-0.175	0.845	Lower	0.300
-0.150	0.845	Lower	0.207
-0.100	0.845	Lower	0.094
-0.050	0.845	Lower	0.025
0.000	0.845	Lower	−0.019
0.050	0.845	Lower	−0.052
0.150	0.845	Lower	−0.098
0.350	0.845	Lower	−0.131
0.550	0.845	Lower	−0.100
0.600	0.845	Lower	−0.076
0.625	0.845	Lower	−0.063
0.675	0.845	Lower	−0.030
0.700	0.845	Lower	−0.003
0.725	0.845	Lower	0.032
-0.250	0.845	Upper	−0.109
-0.245	0.845	Upper	−1.534
-0.237	0.845	Upper	−1.690
-0.225	0.845	Upper	−1.465
-0.200	0.845	Upper	−1.226
-0.175	0.845	Upper	−1.071
-0.150	0.845	Upper	−0.966
-0.100	0.845	Upper	−0.812
-0.050	0.845	Upper	−0.705
0.000	0.845	Upper	−0.617
0.050	0.845	Upper	−0.543
0.150	0.845	Upper	−0.427
0.350	0.845	Upper	−0.251
0.550	0.845	Upper	−0.180
0.600	0.845	Upper	−0.171
0.625	0.845	Upper	−0.166
0.675	0.845	Upper	−0.143
0.700	0.845	Upper	−0.101
0.725	0.845	Upper	−0.036

Appendix Table D.1 (Continued)

x/c	z/b_o or γ (deg)	Upper/Lower Surface	C_p
-0.250	0.906	Lower	0.004
-0.245	0.906	Lower	1.013
-0.237	0.906	Lower	0.886
-0.225	0.906	Lower	0.664
-0.200	0.906	Lower	0.385
-0.175	0.906	Lower	0.247
-0.150	0.906	Lower	0.155
-0.100	0.906	Lower	0.051
-0.050	0.906	Lower	−0.014
0.000	0.906	Lower	−0.057
0.050	0.906	Lower	−0.090
0.150	0.906	Lower	−0.137
0.350	0.906	Lower	−0.176
0.550	0.906	Lower	−0.154
0.600	0.906	Lower	−0.131
0.625	0.906	Lower	−0.120
0.675	0.906	Lower	−0.083
0.700	0.906	Lower	−0.060
0.725	0.906	Lower	−0.050
-0.250	0.906	Upper	0.061
-0.245	0.906	Upper	−1.337
-0.237	0.906	Upper	−1.506
-0.225	0.906	Upper	−1.312
-0.200	0.906	Upper	−1.103
-0.175	0.906	Upper	−0.972
-0.150	0.906	Upper	−0.885
-0.100	0.906	Upper	−0.748
-0.050	0.906	Upper	−0.654
0.000	0.906	Upper	−0.581
0.050	0.906	Upper	−0.520
0.150	0.906	Upper	−0.417
0.350	0.906	Upper	−0.260
0.550	0.906	Upper	−0.257
0.600	0.906	Upper	−0.300
0.625	0.906	Upper	−0.337
0.675	0.906	Upper	−0.389
0.700	0.906	Upper	−0.365
0.725	0.906	Upper	−0.291

Appendix Table D.1 (Continued)

x/c	z/b_o or γ (deg)	Upper/Lower Surface	C_p
-0.250	0.936	Lower	0.123
-0.245	0.936	Lower	1.006
-0.237	0.936	Lower	0.853
-0.225	0.936	Lower	0.626
-0.200	0.936	Lower	0.348
-0.175	0.936	Lower	0.213
-0.150	0.936	Lower	0.127
-0.100	0.936	Lower	0.027
-0.050	0.936	Lower	−0.034
0.000	0.936	Lower	−0.080
0.050	0.936	Lower	−0.116
0.150	0.936	Lower	−0.162
0.350	0.936	Lower	−0.209
0.550	0.936	Lower	−0.198
0.600	0.936	Lower	−0.180
0.625	0.936	Lower	−0.168
0.675	0.936	Lower	−0.123
0.700	0.936	Lower	−0.103
0.725	0.936	Lower	−0.103
-0.250	0.936	Upper	0.157
-0.245	0.936	Upper	−1.206
-0.237	0.936	Upper	−1.399
-0.225	0.936	Upper	−1.211
-0.200	0.936	Upper	−1.036
-0.175	0.936	Upper	−0.911
-0.150	0.936	Upper	−0.831
-0.100	0.936	Upper	−0.708
-0.050	0.936	Upper	−0.626
0.000	0.936	Upper	−0.564
0.050	0.936	Upper	−0.510
0.150	0.936	Upper	−0.415
0.350	0.936	Upper	−0.247
0.550	0.936	Upper	−0.443
0.600	0.936	Upper	−0.626
0.625	0.936	Upper	−0.723
0.675	0.936	Upper	−0.816
0.700	0.936	Upper	−0.775
0.725	0.936	Upper	−0.629

Appendix Table D.1 (Continued)

x/c	z/b_o or γ (deg)	Upper/Lower Surface	C_p
-0.250	0.966	Lower	0.194
-0.245	0.966	Lower	0.983
-0.237	0.966	Lower	0.799
-0.225	0.966	Lower	0.569
-0.200	0.966	Lower	0.299
-0.175	0.966	Lower	0.170
-0.150	0.966	Lower	0.092
-0.100	0.966	Lower	−0.005
-0.050	0.966	Lower	−0.066
0.000	0.966	Lower	−0.115
0.050	0.966	Lower	−0.152
0.150	0.966	Lower	−0.201
0.350	0.966	Lower	−0.264
0.550	0.966	Lower	−0.280
0.600	0.966	Lower	−0.269
0.625	0.966	Lower	−0.262
0.675	0.966	Lower	−0.214
0.700	0.966	Lower	−0.180
0.725	0.966	Lower	−0.163
-0.250	0.966	Upper	0.238
-0.245	0.966	Upper	−1.080
-0.237	0.966	Upper	−1.239
-0.225	0.966	Upper	−1.089
-0.200	0.966	Upper	−0.939
-0.175	0.966	Upper	−0.840
-0.150	0.966	Upper	−0.767
-0.100	0.966	Upper	−0.672
-0.050	0.966	Upper	−0.603
0.000	0.966	Upper	−0.551
0.050	0.966	Upper	−0.508
0.150	0.966	Upper	−0.453
0.350	0.966	Upper	−0.617
0.550	0.966	Upper	−1.247
0.600	0.966	Upper	−1.309
0.625	0.966	Upper	−1.290
0.675	0.966	Upper	−1.178
0.700	0.966	Upper	−1.074
0.725	0.966	Upper	−0.836

Appendix Table D.1 (Continued)

x/c	z/b_o or γ (deg)	Upper/Lower Surface	C_p
-0.245	10.0°	Lower	0.721
-0.237	10.0°	Lower	0.509
-0.225	10.0°	Lower	0.314
-0.200	10.0°	Lower	0.083
-0.175	10.0°	Lower	−0.019
-0.150	10.0°	Lower	−0.088
-0.100	10.0°	Lower	−0.176
-0.050	10.0°	Lower	−0.239
0.000	10.0°	Lower	−0.287
0.050	10.0°	Lower	−0.331
0.150	10.0°	Lower	−0.413
0.350	10.0°	Lower	−0.586
0.550	10.0°	Lower	−0.913
0.625	10.0°	Lower	−1.112
0.675	10.0°	Lower	−1.142
0.700	10.0°	Lower	−1.004
0.725	10.0°	Lower	−0.533
-0.245	10.0°	Upper	−0.694
-0.237	10.0°	Upper	−0.914
-0.225	10.0°	Upper	−0.780
-0.200	10.0°	Upper	−0.765
-0.175	10.0°	Upper	−0.711
-0.150	10.0°	Upper	−0.688
-0.100	10.0°	Upper	−0.648
-0.050	10.0°	Upper	−0.621
0.000	10.0°	Upper	−0.595
0.050	10.0°	Upper	−0.576
0.150	10.0°	Upper	−0.561
0.350	10.0°	Upper	−0.677
0.550	10.0°	Upper	−0.858
0.625	10.0°	Upper	−0.845
0.675	10.0°	Upper	−0.832
0.700	10.0°	Upper	−0.791
0.725	10.0°	Upper	−0.521

Appendix Table D.1 (Continued)

x/c	z/b_o or γ (deg)	Upper/Lower Surface	C_p
-0.245	22.5°	Lower	0.570
-0.237	22.5°	Lower	0.342
-0.225	22.5°	Lower	0.179
-0.200	22.5°	Lower	−0.038
-0.175	22.5°	Lower	−0.127
-0.150	22.5°	Lower	−0.191
-0.100	22.5°	Lower	−0.269
-0.050	22.5°	Lower	−0.338
0.000	22.5°	Lower	−0.388
0.050	22.5°	Lower	−0.436
0.150	22.5°	Lower	−0.533
0.350	22.5°	Lower	−0.757
0.550	22.5°	Lower	−1.187
0.600	22.5°	Lower	−1.382
0.625	22.5°	Lower	−1.508
0.675	22.5°	Lower	−1.701
0.700	22.5°	Lower	−1.391
-0.245	22.5°	Upper	−0.621
-0.237	22.5°	Upper	−0.830
-0.225	22.5°	Upper	−0.715
-0.200	22.5°	Upper	−0.730
-0.175	22.5°	Upper	−0.696
-0.150	22.5°	Upper	−0.686
-0.100	22.5°	Upper	−0.656
-0.050	22.5°	Upper	−0.648
0.000	22.5°	Upper	−0.637
0.050	22.5°	Upper	−0.626
0.150	22.5°	Upper	−0.609
0.350	22.5°	Upper	−0.668
0.550	22.5°	Upper	−0.844
0.600	22.5°	Upper	−0.859
0.625	22.5°	Upper	−0.843
0.675	22.5°	Upper	−0.838
0.700	22.5°	Upper	−0.804

Appendix Table D.1 (Continued)

x/c	z/b_o or γ (deg)	Upper/Lower Surface	C_p
-0.245	45.0°	Lower	0.314
-0.237	45.0°	Lower	0.091
-0.225	45.0°	Lower	−0.048
-0.200	45.0°	Lower	−0.234
-0.175	45.0°	Lower	−0.309
-0.150	45.0°	Lower	−0.361
-0.100	45.0°	Lower	−0.438
-0.050	45.0°	Lower	−0.500
0.000	45.0°	Lower	−0.554
0.050	45.0°	Lower	−0.600
0.150	45.0°	Lower	−0.720
0.350	45.0°	Lower	−0.998
0.550	45.0°	Lower	−1.541
0.600	45.0°	Lower	−1.719
0.625	45.0°	Lower	−1.840
0.675	45.0°	Lower	−1.897
0.700	45.0°	Lower	−1.367
0.725	45.0°	Lower	−0.559
-0.245	45.0°	Upper	−0.489
-0.237	45.0°	Upper	−0.707
-0.225	45.0°	Upper	−0.644
-0.200	45.0°	Upper	−0.688
-0.175	45.0°	Upper	−0.681
-0.150	45.0°	Upper	−0.681
-0.100	45.0°	Upper	−0.688
-0.050	45.0°	Upper	−0.700
0.000	45.0°	Upper	−0.710
0.050	45.0°	Upper	−0.727
0.150	45.0°	Upper	−0.750
0.350	45.0°	Upper	−0.742
0.550	45.0°	Upper	−0.846
0.600	45.0°	Upper	−0.856
0.625	45.0°	Upper	−0.845
0.675	45.0°	Upper	−0.861
0.700	45.0°	Upper	−0.817
0.725	45.0°	Upper	−0.516

Appendix Table D.1 (Continued)

x/c	z/b_o or γ (deg)	Upper/Lower Surface	C_p
-0.245	67.5°	Lower	0.074
-0.237	67.5°	Lower	−0.166
-0.225	67.5°	Lower	−0.231
-0.200	67.5°	Lower	−0.412
-0.175	67.5°	Lower	−0.477
-0.150	67.5°	Lower	−0.517
-0.100	67.5°	Lower	−0.581
-0.050	67.5°	Lower	−0.638
0.000	67.5°	Lower	−0.688
0.150	67.5°	Lower	−0.857
0.350	67.5°	Lower	−1.155
0.550	67.5°	Lower	−1.658
0.600	67.5°	Lower	−1.783
0.625	67.5°	Lower	−1.793
0.675	67.5°	Lower	−1.590
0.700	67.5°	Lower	−0.964
0.725	67.5°	Lower	−0.550
-0.245	67.5°	Upper	−0.353
-0.237	67.5°	Upper	−0.579
-0.225	67.5°	Upper	−0.549
-0.200	67.5°	Upper	−0.639
-0.175	67.5°	Upper	−0.655
-0.150	67.5°	Upper	−0.671
-0.100	67.5°	Upper	−0.702
-0.050	67.5°	Upper	−0.730
0.000	67.5°	Upper	−0.762
0.150	67.5°	Upper	−0.862
0.350	67.5°	Upper	−1.024
0.550	67.5°	Upper	−0.879
0.600	67.5°	Upper	−0.865
0.625	67.5°	Upper	−0.858
0.675	67.5°	Upper	−0.870
0.700	67.5°	Upper	−0.822
0.725	67.5°	Upper	−0.516

Appendix Table D.1 (Continued)

x/c	z/b_o or γ (deg)	Upper/Lower Surface	C_p
-0.245	90.0°	Lower	−0.161
-0.237	90.0°	Lower	−0.390
-0.225	90.0°	Lower	−0.418
-0.200	90.0°	Lower	−0.559
-0.175	90.0°	Lower	−0.600
-0.150	90.0°	Lower	−0.629
-0.100	90.0°	Lower	−0.681
-0.050	90.0°	Lower	−0.732
0.000	90.0°	Lower	−0.776
0.050	90.0°	Lower	−0.826
0.150	90.0°	Lower	−0.924
0.350	90.0°	Lower	−1.207
0.550	90.0°	Lower	−1.467
0.600	90.0°	Lower	−1.341
0.625	90.0°	Lower	−1.192
0.675	90.0°	Lower	−0.973
0.700	90.0°	Lower	−0.886
0.725	90.0°	Lower	−0.564
-0.245	90.0°	Upper	−0.174
-0.237	90.0°	Upper	−0.396
-0.225	90.0°	Upper	−0.442
-0.200	90.0°	Upper	−0.551
-0.175	90.0°	Upper	−0.590
-0.150	90.0°	Upper	−0.619
-0.100	90.0°	Upper	−0.669
-0.050	90.0°	Upper	−0.714
0.000	90.0°	Upper	−0.760
0.050	90.0°	Upper	−0.807
0.150	90.0°	Upper	−0.899
0.350	90.0°	Upper	−1.155
0.550	90.0°	Upper	−1.394
0.600	90.0°	Upper	−1.267
0.625	90.0°	Upper	−1.163
0.675	90.0°	Upper	−0.916
0.700	90.0°	Upper	−0.806
0.725	90.0°	Upper	−0.505

REFERENCES

Bandyopadhyay, P.R., Stead, D.J., Ash, R.L., "The Organized Nature of a Turbulent Trailing Vortex,"21st Fluid Dynamics, Plasma Dynamics and Lasers Conference, June 18-20, 1990, Seattle, WA.

Batchelor, G.K., "Axial Flow in Trailing Line Vortices," *Journal of Fluid Mechanics*, Vol. 20, 1964, pp. 645-658.

Bell, J.H. and Mehta, R.D., "Contraction Design for Small Low-Speed Wind Tunnels," JIAA Report TR-84, Dept. of Aeronautics and Astronautics, Stanford University, 1988.

Carlin, G., Dadone, L., Spencer, R., "Results of an Experimental Investigation of Blade Tip Vortex Modification Devices,"NASA CR-181853.

Cebeci, T. and Bradshaw, P., "*Momentum Transfer in Boundary Layers*," McGraw-Hill, London, 1977.

Chigier, N.A., Corsiglia, V.R., "Tip Vortices - Velocity Distributions,"NASA TM X-62,087, September 1971.

Chigier, N.A., Corsiglia, V.R., "Wind-Tunnel Studies of Wing Wake Turbulence,"*Journal of Aircraft*, Vol. 9, Number 12, December 1972, pp. 820-825.

Corsiglia, V.R., Schwind, R.G., Chigier, N.A., "Rapid Scanning, Three-Dimensional Hot-Wire Anemometer Surveys of Wing-Tip Vortices,"*Journal of Aircraft*, Vol. 10, Number 12, December 1973, pp. 752-757.

Crow, S.C., "Stability Theory for a Pair of Trailing Vortices, "*AIAA Journal*, Vol. 8, Number 12, 1970, pp. 2172.

Cutler, A.D., Bradshaw, P., "Strong Vortex/Boundary Layer Interactions: Part I. Vortices High," *Experiments in Fluids*, Vol. 14, 1993, pp. 321-332.

Cutler, A.D., Bradshaw, P., "Strong Vortex/Boundary Layer Interactions: Part II. Vortices Low," *Experiments in Fluids*, Vol. 14, 1993, pp. 393-401.

Dacles-Mariani, J., Rogers, S., Kwak, D., Zilliac, G.G, Chow J., "A Computational Study of Wingtip Vortex Flowfield," AIAA 24th Fluid Dynamics Conference, July 6-9, 1993, Orlando, Florida.

Dacles-Mariani, D., Zilliac, G.G, Chow J., Bradshaw, P., "A Computational/Experimental Study of a Wingtip Vortex Flowfield," To appear in *AIAA Journal*, 1994.

De Jong, F.J., Govindan, T.R., Levy, R., Shamroth, S.J., "Validation of a Forward Marching Procedure to Compute Tip Vortex Generation Process for Ship Propeller Blades," Scientific Research Associates, Inc., Report R88-920023-F, August 1988.

Dunham, J., "The Static Pressure in a Vortex Core," *Aeronautical Journal*, Vol. 83, No. 8, pp. 402-406.

Francis, T.B., Katx, J., "Observations on the Development of a Tip Vortex on a Rectangular Hydrofoil." *Journal of Fluids Engineering*, Vol. 110, June 1988, pp. 208-215.

Gieseke, T.J., Guezennec, Y.G., "An Experimental Approach to the Calibration and Use of Triple-Wire Probes," *Experiments in Fluids*, Vol. 14, 1993, pp. 305-315.

Govindaraju, S.P., Saffman, P.G., "Flow in a Turbulent Trailing Vortex, " *Physics of Fluids*, Vol. 14, Number 10, October 1971, pp. 2074-2080.

Green, S.I., "Correlating Single Phase Flow Measurements With Observations of Trailing Vortex Cavitation," *Journal of Fluids Engineering*, Vol. 113, 1991, pp. 125-129.

Green, S.I., Acosta, A.J., "Unsteady Flow in Trailing Vortices," *Journal of Fluid Mechanics*, Vol. 227, 1991, pp. 107-134.

Grow, T.L., "Effect of a Wing on Its Tip Vortex," *Journal of Aircraft*, Vol. 6, No.1, January-February 1969, pp. 37-41.

Heffernan, K.G., "Trailing Vortex Attenuation Devices," Ph.D. Dissertation, Naval Postgraduate School, 1985.

Higuchi, H., Quadrell, J.C., Farell, C., "Vortex Roll-up for an Elliptically-Loaded Wing at Moderately Low Reynolds Numbers," AIAA 24th Aerospace Sciences Meeting, January 6-9, 1986, Reno, Nevada.

Hoffman, E.R., Joubert, J., "Turbulent Line Vortices," *Journal of Fluid Mechanics*, Vol. 16, 1963, pp. 395-411.

Hooper, C. and Saunders, D., "FMDAS: Fluid Mechanics Data Acquisition Sys-

tem," Tech. Report 7104-307, 13, Informatics General Corporation, February 1985.

Hooper, C., and Saunders, D., "FMDAS: Fluid Mechanics Data Acquisition System User's Guide," Technical Report 7104-3-7, 13, Sterling Software, September 1986.

Hooper, C., "Use of the IRIS for Animation and Still Graphics Hardcopies," Sterling Software Project 7104-7, Technical Note no. 1, October 1988.

Hopfinger, E.J., Browand, F.K., Gagne, Y., "Turbulence and Waves in a Rotating Tank," *Journal of Fluid Mechanics*, Vol. 125, 1982. pp. 505-534.

Ikohagi, T., Higuchi, H., Arndt, R.E.A., "The Structure of Trailing Vortices,"in Advancement in Aerodynamics, Fluid Mechanics and Hydraulics, Joint AIAA, ASME and ASCE Symposium, Univ. of Minnesota, June 1986.

Lamb, H., Sect. 334a, "*Hydrodynamics*," Dover, New York, 1945.

LeBoeuf, R.L., "Application of the Proper Orthogonal Decomposition Techniques to an Annular Cascade Flowfield," Ph.D. Dissertation, SUNY at Buffalo, 1991.

Lee, H., Schetz, J.A., "Experimental Results for Reynolds Number Effects on Trailing Vortices," *Journal of Aircraft*, Vol. 22, No. 2, February 1985, pp. 158-160.

Lezius, D.K., "Water Tank Study of the Decay of Trailing Vortices," *AIAA Journal*, Vol. 12, No. 8, August 1974, pp. 1065-1071.

Lezius, D.K., "Unstable Wing Vortex Rollup Induced by Lift Tailoring in the Wing-Tip Region," Lockheed Report, 1991.

Logan, A.H., "Vortex Velocity Distributions at Large Downstream Distances," *Journal of Aircraft*, Vol. 8, November 1971, No. 11, *pp.* 930-932.

McAlister, K.W., Takahashi, R.K., " NACA 0015 Wing Pressure and Trailing Vortex Measurements," NASA TP-3151, November 1991.

McCormick, B.W., Tangler, J.L., Sherrieb, H.E., "Structure of Trailing Vortices," *Journal of Aircraft*, Vol. 5, No. 3, May-June 1968, pp. 260-267.

Mehta, R.D. and Bradshaw, P., 1979, "Design Rules for Small Low Speed Wind Tunnels," *Aeronaut. J., vol.* 83, *no.* 827, *pp.* 443-449.

Mehta, R.D., Cantwell, E.R., " Mean Flow and Turbulent Measurements in a Half-

Delta Wing Vortex," *Fluid Dynamics Research*, Vol. 4, 1988, pp. 123-137.

Moore, D.W., and Saffman, P.G., "Axial Flow in Laminar Trailing Vortices," *Proceedings Royal Society London*, Vol. 333, June 1973, pp. 491-508.

Muller, U.R., "Comparison of Turbulence Measurements with Single, X, and Triple Hot-Wire Probes," *Experiments in Fluids*, Vol. 13, 1992, pp. 208-216.

Orloff, K.L., " Trailing Vortex Wind-Tunnel Diagnostics with a Laser Velocimeter," *Journal of Aircraft*, Vol. 11, No. 8, August 1974, pp. 477-482.

Paulsen, L., "Triple Hot-Wire Technique for Simultaneous Measurements of Instantaneous Velocity Components in Turbulent Flows," *Journal of Physics E.: Scientific Instruments*, 1983, pp. 554-562.

Phillips, W.R.,"Turbulent Trailing Vortex During Roll-Up,"
Journal of Fluid Mechanics, Vol. 105, 1981, pp. 451-467.

Phillips, W.R., Graham, J.A., "Reynolds-Stress Measurements in a Turbulent Trailing Vortex," *Journal of Fluid Mechanics*, Vol. 147, 1984, pp. 353-371.

Pompeo, L.P., "An Experimental Study of Three-Dimensional Turbulent Boundary Layers," Ph.D. Dissertation, Swiss Federal Institute of Technology Zurich, 1992.

Poppleton, "Effect of Air Injection into the Core of a Trailing Vortex," *Journal of Aircraft*, Vol. 8, No. 8, August 1971, pp. 672-673.

Prandtl, L., "Applications of Modern Hydrodynamics to Aeronautics," NACA Report No. 116, 1921.

Rodi, W., "Basic Equations for Turbulent Flow in Cartesian and Cylindrical Coordinates," Imperial College, Department of Mechanical Engineering Report, BL/TN/A/36, 1970.

Shekarriz, A., Fu, T.C., Katz, J., "Near-Field Behavior of a Tip Vortex," *AIAA Journal*, Vol. 31, No. 1, January 1993, pp. 112-118.

Singh, P.I., "The Structure and Stability of a Vortex," Ph.D. Dissertation, University of Colorado, 1974.

Spivey, R.F., "Blade Tip Aerodynamics, Profile and Planform Effects,"24th Annual National Forum of the American Helicopter Society, May 1968.

Spivey, W.A., Morehouse, G.G., "New Insights Into the Design of Swept-Tip Rotor Blades", 26th Annual National Forum of the American Helicopter Society, June 1970.

Squire, H.B., "The Growth of a Vortex in Turbulent Flow," *The Aeronautical Quarterly*, Vol. 16, Part 3, August 1965, pp. 302-306.

Srinivasan, G.R., McCroskey, W.J., Baeder, J.D., Edwards, T.A., "Numerical Simulation of Tip Vortices of Wings in Subsonic and Transonic Flows," *AIAA Journal*, Vol. 26, Number 10, October 1988, pp. 1153-1162.

Stinebring, D.R., Farrell, K.J., Billet, M.L, "The Structure of a Three-Dimensional Tip Vortex at High Reynolds Number," *Journal of Fluids Engineering*, Vol. 113, September 1991, pp. 496-503.

Thompson, D.H., "A Flow Visualization Study of Tip Vortex Formation," ARL-Aero-Note-421, 1983.

Tobak, M., Peake, D.J., "Three-Dimensional Separated Flows," *Annual Review Fluid Mechanics*, Vol. 14, 1982, pp. 61-85.

Van Den Berg, B., "A European Collaborative Investigation of the Three-Dimensional Turbulent Shear Layers of a Swept Wing,"AGARD-CP-438, 25, 1989.

Walatka, P.P., Clucas, J., McCabe, R.K., Plessel, T., "FAST User Guide," NASA Ames WAO/RND-92-013, 1992.

Westphal, R.V., Eaton, J.K. and Pauley, W.R., "Interaction Between a Vortex and a Turbulent Boundary Layer - Part 1: Mean Flow Evolution and Turbulence Properties," NASA TM-88361, 1987.

Westphal, R.V., Mehta, R.D., " Interaction of an Oscillating Vortex With a Turbulent Boundary Layer," *Experiments in Fluids*, Vol. 7, 1989, pp. 405-411.

Widnall, S.E., Wolf, T.L., " Effect of Tip Vortex Structure on Helicopter Noise Due to Blade-Vortex Interaction," *Journal of Aircraft*, Vol. 17, No. 10, 1980, pp. 705-711.

Zeman, O., Private Communication, 1994.

Zilliac, G., "Calibration of Seven-Hole Pressure Probes for Use in Fluid Flows with Large Angularity,"NASA TM 102200, December 1989.

Zilliac, G., "32 by 48 inch Design Summary," NASA Ames Internal Report, 1988, available upon request.

Zilliac, G., "Computational/Experimental Study of the Flowfield on a Body of Revolution at Incidence," *AIAA Journal*, Vol. 27, No. 8, 1989, pp. 1008-1016.

Zsoldos, J.S., Devenport, W.J., " An Experimental Investigation of Interacting Wing-Tip Vortex Pairs," VPI-AOE-191, June 1992.

REPORT DOCUMENTATION PAGE

Form Approved
OMB No. 0704-0188

1. AGENCY USE ONLY *(Leave blank)*	2. REPORT DATE	3. REPORT TYPE AND DATES COVERED
	February 1997	Technical Memorandum

4. TITLE AND SUBTITLE

Turbulence Measurements in the Near Field of a Wingtip Vortex

5. FUNDING NUMBERS

505-59-53

6. AUTHOR(S)

Jim Chow,* Greg Zilliac, and Peter Bradshaw†

7. PERFORMING ORGANIZATION NAME(S) AND ADDRESS(ES)

Ames Research Center
Moffett Field, CA 94035-1000

8. PERFORMING ORGANIZATION REPORT NUMBER

A-961558

9. SPONSORING/MONITORING AGENCY NAME(S) AND ADDRESS(ES)

National Aeronautics and Space Administration
Washington, DC 20546-0001

10. SPONSORING/MONITORING AGENCY REPORT NUMBER

NASA TM-110418

11. SUPPLEMENTARY NOTES

Point of Contact: Greg Zilliac, Ames Research Center, MS 260-1, Moffett Field, CA 94035-1000; (415) 604-3904
*Institute for Defense Analyses, Alexandria, VA 22311
†Stanford University, Stanford, CA 94305

12a. DISTRIBUTION/AVAILABILITY STATEMENT

Unclassified-Unlimited
Subject Category – 01

12b. DISTRIBUTION CODE

13. ABSTRACT ***(Maximum 200 words)***

The roll-up of a wingtip vortex, at Reynolds number based on chord of 4.6 million was studied with an emphasis on suction side and near wake measurements. The research was conducted in a 32 in. × 48 in. low-speed wind tunnel. The half-wing model had a semi-span of 36 in. a chord of 48 in. and a rounded tip.

Seven-hole pressure probe measurements of the velocity field surrounding the wingtip showed that a large axial velocity of up to 1.77 U_∞ developed in the vortex core. This level of axial velocity has not been previously measured. Triple-wire probes have been used to measure all components of the Reynolds stress tensor. It was determined from correlation measurements that meandering of the vortex was small and did not appreciably contribute to the turbulence measurements.

The flow was found to be turbulent in the near-field (as high as 24 percent RMS w – velocity on the edge of the core) and the turbulence decayed quickly with streamwise distance because of the nearly solid body rotation of the vortex core mean flow. A streamwise variation of the location of peak levels of turbulence, relative to the core centerline, was also found. Close to the trailing edge of the wing, the peak shear stress levels were found at the edge of the vortex core, whereas in the most downstream wake planes they occurred at a radius roughly equal to one-third of the vortex core radius. The Reynolds shear stresses were not aligned with the mean strain rate, indicating that an isotropic-eddy-viscosity based prediction method cannot accurately model the turbulence in the cortex. In cylindrical coordinates, with the origin at the vortex centerline, the radial normal stress was found to be larger than the circumferential.

14. SUBJECT TERMS

Vortex, Turbulence, Wing

15. NUMBER OF PAGES

241

16. PRICE CODE

A11

17. SECURITY CLASSIFICATION OF REPORT	18. SECURITY CLASSIFICATION OF THIS PAGE	19. SECURITY CLASSIFICATION OF ABSTRACT	20. LIMITATION OF ABSTRACT
Unclassified	Unclassified		